GOLD CATALYSTS FOR SUSTAINABLE CHEMICAL PROCESSING

XIAODONG WANG

A dissertation submitted for the degree of Doctor of Philosophy

Heriot-Watt University

School of Engineering and Physical Sciences

January 2014

ABSTRACT

The focus of this thesis is the development of supported gold catalysts with application in selective hydrogenation directed at sustainable chemical processing. The gas phase hydrogenation of nitrobenzene (to aniline), *p*- and *o*-chloronitrobenzene (to *p*- and *o*-chloroaniline), *p*-nitrobenzonitrile (to *p*-aminobenzonitrile), nitrocyclohexane (to cyclohexanone oxime) and phenylacetylene (to styrene) have been examined. Utilisation of an array of complementary characterisation techniques has facilitated an explicit correlation of catalyst performance with structure/performance that is underpinned by detailed thermodynamic and mechanistic kinetic analysis. Taking the conversion of *p*-chloronitrobenzene as a model system, it is established that reaction temperature has little effect on equilibrium composition whereas an increase in H_2/*p*-chloronitrobenzene ratio results in *p*-chloroaniline hydrodechlorination/hydrogenation to aniline, benzene and cyclohexane. Gold on non-reducible oxides (Al_2O_3 and ZrO_2) is 100% selective in catalysing the hydrogenation of nitrobenzene, *p*-chloronitrobenzene and *p*-nitrobenzonitrile to the target amine product. Use of reducible oxides, notably $Ce_{0.62}Zr_{0.38}O_2$, resulted in hydrodechlorination (of *p*-chloronitrobenzene) through the catalytic action of oxygen vacancies generated during catalyst activation. The use of Mo_2C as Au carrier serves to enhance activity (relative to Al_2O_3) as a result of increased surface reactive hydrogen associated with the carbide. Incorporation of Pd with Au on both Al_2O_3 and Mo_2C further increases rate while retaining product exclusivity Selectivity is particularly challenging in the conversion of nitrocyclohexane as an aliphatic nitro-compound and sensitive to the support where preferential oxime formation (selectivity as high as 95%) over Au/Al_2O_3 while Au/TiO_2, Au/ZrO_2 and Au/CeO_2 are non-selective, promoting cyclohexylamine and cyclohexanone formation. Moreover, application of Au/Al_2O_3 in phenylacetylene hydrogenation delivers full selectivity to the target styrene. Process sustainability has been examined in terms of hydrogen utilisation and productivity in moving from batch to continuous processing. Hydrogenation rate also shows a dependence on reactant carrier where a switch from an alcoholic to an aqueous feed serves to increase turnover. The results in this thesis can be applied in the development of cleaner alternative routes to a range of fine chemicals.

DEDICATION

To my grandparents

Chengyin Li and Yulian Liu

Guoqing Wang and Guilan Zhang

Acknowledgements

I would like to express my sincere appreciation to my supervisor Professor Mark A. Keane for his guidance, patience and encouragement throughout the development of this thesis. His commitment to science, rich experience in research and various ways of directing projects have helped me reach a completely new level. I have also learnt a lot from his integrity as a result of many conversations that we had in the past four years. Thanks for being such an inspiration to me. I also wish to thank my previous supervisor Professor Xinbin Ma while I studied in Tianjin University for his continuous trust, support and encouragement, without which I may not reach this stage.

I would like to acknowledge my colleagues at Heriot-Watt University who have created a pleasant environment and provided direct help in research. Thanks to Dr. Humphrey Yiu, Dr. Fernando Cárdenas-Lizana, Dr. Santiago Gómez Quero, Dr. Alexander Foster, Dr. Cameron Brown, Gregor Sneddon, Craig Callahan, Dalila Capao and Natalie Falenta *et al.* Many thanks to the staff in the Chemical Engineering Department, Marian Millar, Curtis Abbott and Cameron Smith *et al.* for the support. Moreover, special thanks to my labmates as well as good friends, Dr. Noémie Perret, soon to be Dr. Yufen Hao and Dr. Maoshuai Li for our talks, discussion and dinners. I am also grateful to my close friends, to name just a few, Lin Wang, Zhe Liu, Rui Ma, Dr. Yan Zhuang and Dr. Ling Qin *et al.* They have made life in the UK wonderful.

Finally, I would like to give a special place for my family. Sincere gratitude to my wife Na Wang for looking after and always being with me at each stage in the UK. Thanks for always putting me and family (relative to her) at priority. I am forever grateful to my parents, Chen Wang and Xiumei Li, for your education and day-to-day example that have built me a kind-hearted (good) character/personality and a way of handling things properly. I am sorry for not seeing you many times since I lived abroad. Special thanks also to other members of the family for your support to me and my parents.

Financial support from the Scottish Overseas Research Student Awards Scheme, Heriot-Watt University, China Scholarship Council and Great Britain-China Educational Trust are also acknowledged.

Table of Contents

List of Tables

List of Figures

Glossary

Acronyms

AAS	Atomic Absorption Spectroscopy
p-ABN	*p*-Aminobenzonitrile
AN	Aniline
p-ATL	*p*-Aminotoluene
BE	Binding Energy
BET	S. Brunauer, P. H. Emmett and E. Teller theory; measurements of surface area
BZ	Benzene
o-CAN	*ortho*-Chloroaniline
p-CAN	*para*-Chloroaniline
CB	Chlorobenzene
CCA	Cyclohexyl-Cyclohexylidene Amine
CHA	Cyclohexane
CHE	Cyclohexene
o-CNB	*ortho*- Chloronitrobenzene
p-CNB	*para*-Chloronitrobenzene
CZ	$Ce_{0.62}Zr_{0.38}O_2$
DCA	Dicyclohexylamine
D-P	Deposition-Precipitation
FID	Flame Ionisation Detector
FTIR	Fourier Transform Infrared Spectroscopy
GHSV	Gas Hourly Space Velocity
ICP	Inductively Coupled Plasma
JCPDS-ICDD	Joint Committee on Powder Diffraction Standards-International Centre for Diffraction Data
NB	Nitrobenzene
p-NBN	*p*-Nitrobenzonitrile
NC	Nitrocyclohexane
OSC	Oxygen Storage Capacity
(HAADF) SEM	(High-Angle Annular Dark-Field) Scanning Electron Microscopy
TCD	Thermal Conductivity Detector
TGA-DSC	Thermogravimetric Analysis-Differential Scanning Calorimetry
(HR)TEM	(High Resolution) Transmission Electron Microscopy
TOF	Turnover Frequency
TOF_{max}	Maximum Turnover Frequency
TPD	Temperature Programmed Desorption
TPR	Temperature Programmed Reduction
XRD	Powder X-ray Diffraction
XPS	X-ray Photoelectron Spectroscopy

Symbols

a_{ik}	Number of atoms of the *k*th element present in each molecule of species *i*
A_k	Total mole of *k*th element in the feed
D_{eff}	Effective diffusivity
d_p	Mean catalyst particle diameter
$D_{p\text{-CNB},H_2}$	Molecular diffusivity of *p*-CNB in hydrogen
d_r	Reactor diameter (mm)
$d_{\text{(S)TEM}}$	Mean metal diameter
F	Inlet organic reactant molar flow
$\hat{f}_i$	The fugacity of species *i* in system
f_i^0	The standard-state fugacity of species *i*
$\bar{G}_i$	Partial molar Gibbs free energy of species *i*
G^t	Total Gibbs free energy
G_i^0	Standard Gibbs free energy of species *i*
ΔG^0	Standard Gibbs function of molar reaction
$\Delta G_{f_i}^0$	Standard Gibbs function of formation of species *i*
I	Integrated intensity
k_{eff}	Effective thermal conductivity of the catalysts bed
L	Catalyst bed length
Mw_{i}	Molecular weight of compound
N	Number of species in the reaction system
N	Moler fraction of compent *i*
n	Number of moles of Au or Pd in the catalyst bed; Reaction order
n_{i}	Number of moles of component *i*; Number of au particles with diameter "d_{i}"
P	Pressure of the system
P^0	Standard-state pressure of 1 atm
P_{c}	Critical pressure
P_{H_2}	Hydrogen partial pressure
R	Universal gas constant, 8.314 J mol^{-1} K^{-1}
r_0	Initial reaction rate
$r_{8\text{h}}$	Reaction rate after 8 h on-stream
Re_p	Reynolds number
S	Selectivity (%)
T	Temperature of the system
T_{c}	Critical temperature
T_{max}	Temperature of maximum H_2 consumption during TPR

ΔT_{max}	Maximum temperature differential in the catalyst particle
TOF	Turn over frequency
Δt	Time-on-stream
u	Superficial gas velocity
v_H	Kinematic viscosity of hydrogen
V_c	Critical volume
V_m	Fraction of monoclinic ZrO_2
W	Catalyst mass
x	Fractional conversion
X_m	Intensity ratio of monoclinic ZrO_2
x_0, X_0	Initial fractional conversion
x_{3h}	Fractional conversion after 3 h time-on-stream
y_i	Mole fraction of species i
Z_c	Critical compressibility factor
λ_k	Lagrange multiplier
$\bar{\mu}_i$	Chemical potential of species i
$\hat{\phi}_i$	Fugacity coefficient of species i
β	Time scale fitting parameter
βe	Prater number
σ_I	Characteristic length of component "i"
$\sigma_{i,j}$	Binary pair characteristic length
ε_{Al2O3}	Porosity of Al_2O_3 support
$(\varepsilon/k)_{H2}$	Lenard-Jones potential
ρ_{Al2O3}	Density of Al_2O_3 support
τ	Contact time
τ_{Al2O3}	Tortuosity of the Al_2O_3 support
Ω_D	Collision integral

List of Publications:

[1] F. Cárdenas-Lizana, **X. Wang**, D. Lamey, M. Li, M.A. Keane, L. Kiwi-Minsker. *An examination of catalyst deactivation in nitroarene hydrogenation over supported gold*, Chem. Eng. J., submitted for publication. (**Chapter 4**)

[2] **X. Wang**, M. Li, M.A. Keane. *Harnessing the selective catalytic action of supported gold in hydrogenation applications*, In Heterogeneous Gold Catalysts and Catalysis, Z. Ma and S. Dai, eds., Royal Society of Chemistry, Cambridge, 2014.

[3] N. Perret, **X. Wang**, T. Onfroy, C. Calers, M.A. Keane. *Selectivity in the gas phase hydrogenation of 4-nitrobenzaldehyde over supported Au catalysts*, J. Catal., **309**, 333–342 (2014).

[4] M. Li, **X. Wang**, N. Perret, M.A. Keane, *Enhanced production of benzyl alcohol in the gas phase continuous hydrogenation of benzaldehyde over* Au/Al_2O_3, Catal. Commun., **46**, 187–191 (2014).

[5] **X. Wang**, N. Perret, M.A. Keane, *Gas phase hydrogenation of nitrocyclohexane over supported gold catalysts*, Appl. Catal. A: Gen., **467**, 575–584 (2013). (**Chapter 8**)

[6] **X. Wang**, N. Perret, J.J. Delgado, G. Blanco, X. Chen, C.M. Olmos, S. Bernal, M.A. Keane, *Reducible support effects in the gas phase hydrogenation of p-chloronitrobenzene over gold*, J. Phys. Chem. C, **117**, 994–1005 (2013). (**Chapter 3**)

[7] F. Cárdenas-Lizana, Y. Hao, M. Crespo-Quesada, I. Yuranov, **X. Wang**, M.A. Keane, L. Kiwi-Minsker, *Selective hydrogenation of p-chloronitrobenzene over supported Pd catalysts*, ACS Catal., **3**, 1386–1396 (2013).

[8] **X. Wang**, N. Perret, M.A. Keane, *The role of hydrogen partial pressure in the gas phase hydrogenation of p-chloronitrobenzene over alumina supported Au and Pd: a consideration of reaction thermodynamics and kinetics*, Chem. Eng. J., **210**, 103–113 (2012). (**Chapter 2**)

[9] N. Perret, **X. Wang**, L. Delannoy, C. Potvin, C. Louis, M.A. Keane, *Enhanced selective nitroarene hydrogenation over Au supported on* β-Mo_2C *and*

β-Mo_2C/Al_2O_3, J.Catal. **286**, 172−183 (2012).

[10] C. Amorim, **X. Wang**, M.A. Keane, *Application of hydrodechlorination in environmental pollution control: comparison of the performance of supported and unsupported Pd and Ni catalysts*, Chin. J. Catal., 32, (2011) 746−755.

[11] **X. Wang**, Y. Hao, M.A. Keane, *Selective gas phase hydrogenation of p-nitrobenzonitrile to p-aminobenzonitrile over zirconia supported gold*, manuscript ready for submission. (**Chapter 6**)

[12] **X. Wang**, M.A. Keane, *Gas phase selective hydrogenation of phenylacetylene to styrene over Au/Al_2O_3*, manuscript ready for submission. (**Chapter 9**)

[13] **X. Wang**, N. Perret, L. Delannoy, C. Louis, M.A. Keane, *Selective gas phase hydrogenation of nitroarenes over Mo_2C supported Au-Pd*, manuscript in preparation. (**Chapter 7**)

[14] **X. Wang**, F. Cárdenas-Lizana, M.A. Keane, *Towards sustainable chemoselective nitroarene hydrogenation using supported gold*, manuscript in preparation. (**Chapter 5**)

[15] N. Perret, **X. Wang**, J.J. Delgado, G. Blanco, X. Chen, C.M. Olmos, S. Bernal, M.A. Keane, *Selective hydrogenation of benzoic acid over Au supported on CeO_2 and $Ce_{0.62}Zr_{0.38}O_2$: formation of benzyl alcohol*, manuscript ready for submission.

List of Presentation:

[1] Oral presentation at SURCAT ECOSSE Conference, Edinburgh (2010)

Awards:

[1] Great Britain-China Educational Trust “Chinese Student Award” **2013**.

[2] Chinese Government Award for Outstanding Self-Financed Students Abroad **2012**.

[3] The 2nd Year Research Student Prize (Heriot-Watt University) **2011**.

CHAPTER 1

Introduction and Scope of the Thesis

This chapter presents an overview of sustainable chemical processes, focusing on selective hydrogenation of nitro-compounds over gold catalysts and highlighting the significance of achieving high (or exclusive) selectivity to the target amine in gas phase continuous operation. The objectives of this PhD research are defined and the approach taken is described.

1.1 Sustainable Chemical Processing and Selective Hydrogenation

The fast pace of industrial development and excessive dependence on fossil fuel energy has resulted in serious environmental damage [1]. The role of the chemical sector in contributing to negative environmental impact is now recognised, notably with respect to waste production, energy consumption and chemical toxicity [2]. This has resulted in the introduction of increasingly stringent environmental policies and legislation with the pressing requirement for the development of sustainable chemical processing [3]. The concept of green chemistry is a key principle in the design and conduct of modern chemical technologies, where sustainability must be considered from the outset in terms of process design and operation through to product purification and utilisation [4]. Wherever possible, chemical synthesis should incorporate all materials used in the process (atom efficiency), circumventing by-product/waste production to minimise treatment and/or disposal. Hydrogenation is a critical component in a wide range of processes across the chemical sector, where selective hydrogenation has been the subject of appreciable research over the past decade [5]. For example, selective $–NO_2$ hydrogenation in the presence of other reactive functional groups is an alternative and progressive route to a range of high value functionalised amines. Likewise, selective reduction of acid (to aldehyde) [6], carbonyl (to alcohol) [7] and C≡C (to C=C) functions [8] underpins a diversity of commercial processes. Catalysis holds the key in delivering chemo-selectivity and high target product output. A number of metals (Pd, Pt,

Rh, Ru, Ir, Ni and Co) have exhibited hydrogenation activity with varying selectivity [3,9,10]. The critical role of catalysis in 21st century chemical processing is to achieve maximum selectivity rather than high reactant turnover [11]. Exclusivity to a target product and atom efficiency with energy savings are the overarching goals of a modern chemical process.

1.2 Gold Catalysis

The renaissance in gold catalysis research can be traced to the work of Haruta *et al.* dating from 1987 where appreciable activity in CO oxidation was recorded at sub ambient temperatures [12]. However, Bond has unveiled a rich and varied literature, predating Haruta's work, which demonstrated the catalytic properties of gold [13]. The catalytic response associated with nano-scale Au in CO oxidation has led to a number of studies directed at oxidation applications, which have been the subject of recent reviews [14-16]. In addition, use of Au catalysts has been extended to a series of organic syntheses [3], including carbon–heteroatom bond formation, C-C bond activation, water gas shift and hydrogenation, the topic of this thesis. While the published work has largely dealt with selective oxidation, use in hydrogenation is now the subject of a burgeoning literature [17]. This has been driven by the enhanced selectivity exhibited by Au systems (relative to Pd, Pt and Ni) in the hydrogenation of aromatic nitroarenes, unsaturated aldehydes and ketones, acetylene, propyne and 1,3-butadiene [3,17]. Previous work that formed the basis for this thesis established 100% selectivity in the gas phase hydrogenation of nitroarenes to the target amine over oxide supported Au [18]. However, the catalytic activity of Au was significantly lower than the non-selective catalysts, which can be ascribed to a less effective dissociation/activation of hydrogen [3]. To date, hydrogenation reactions using Au catalysts have been conducted in batch liquid phase at elevated operating T (up to 542 K [19]) and P (up to 40 atm [20]) – the switch to continuous processes at ambient pressure can close the existing sustainability gap.

1.3 Scope and Organisation of the Thesis

The aim of this thesis is to exploit the catalytic selectivity exhibited by gold catalysis to develop hydrogenation processes for the sustainable synthesis of commercially important products. The work has involved reaction thermodynamic and mechanistic kinetic analysis, catalyst synthesis, characterisation and process optimisation. Catalyst characterisation has involved ICP, AAS, elemental analysis, TPR, H_2/O_2 chemisorption, TPD, BET/pore volume/pore size distribution, XRD, TEM/(HAADF-)STEM, FTIR, TGA-DSC, and XPS measurements. A move from batch liquid to continuous gas flow operation avoids down time and the use of additional chemicals as solvents/hydrogen donors/derivatisation agents. Moreover, economies of scale in continuous processing favour higher throughput, which enhances overall sustainability [21]. Gold supported on Al_2O_3 was employed as the model or benchmark catalyst where chloronitrobenzene (*p*-CNB or *o*-CNB) was used as a representative reactant (**Chapters 2-5**) to probe fundamental features of nitro-group reduction. The thesis organisation and scope of the work that has been conducted are illustrated in **Figure 1.1**. The conventional route to haloamines *via* reduction of the corresponding nitro-compound by Fe promoted reaction in acid media (the Bechamp process) suffers major drawbacks, notably low product yields with the generation of significant amounts of toxic Fe/FeO sludge waste [19,22,23]. The work presented in **Chapter 2** (see publication No. 8) examines reaction thermodynamics and kinetics as a function of hydrogen partial pressure, where the catalytic action of Pd/Al_2O_3 was used for comparative purposes. This is the first thermodynamic and kinetic analysis for Au promoted gas phase nitroarene hydrogenation. The work was extended to consider a new catalyst formulation where Au was supported on a reducible carrier ($Ce_{0.62}Zr_{0.38}O_2$) (**Chapter 3**, see publication No. 6) and the performance is compared with Au/Al_3O_3. Catalyst lifetime is an important parameter in terms of commercial application and temporal deactivation of Au/Al_2O_3 is addressed **Chapter 4** (see publication No. 1), where the possible causes of activity loss are assessed. The focus of **Chapter 5** (see publication No. 14) is on process sustainability, comparing the performance of

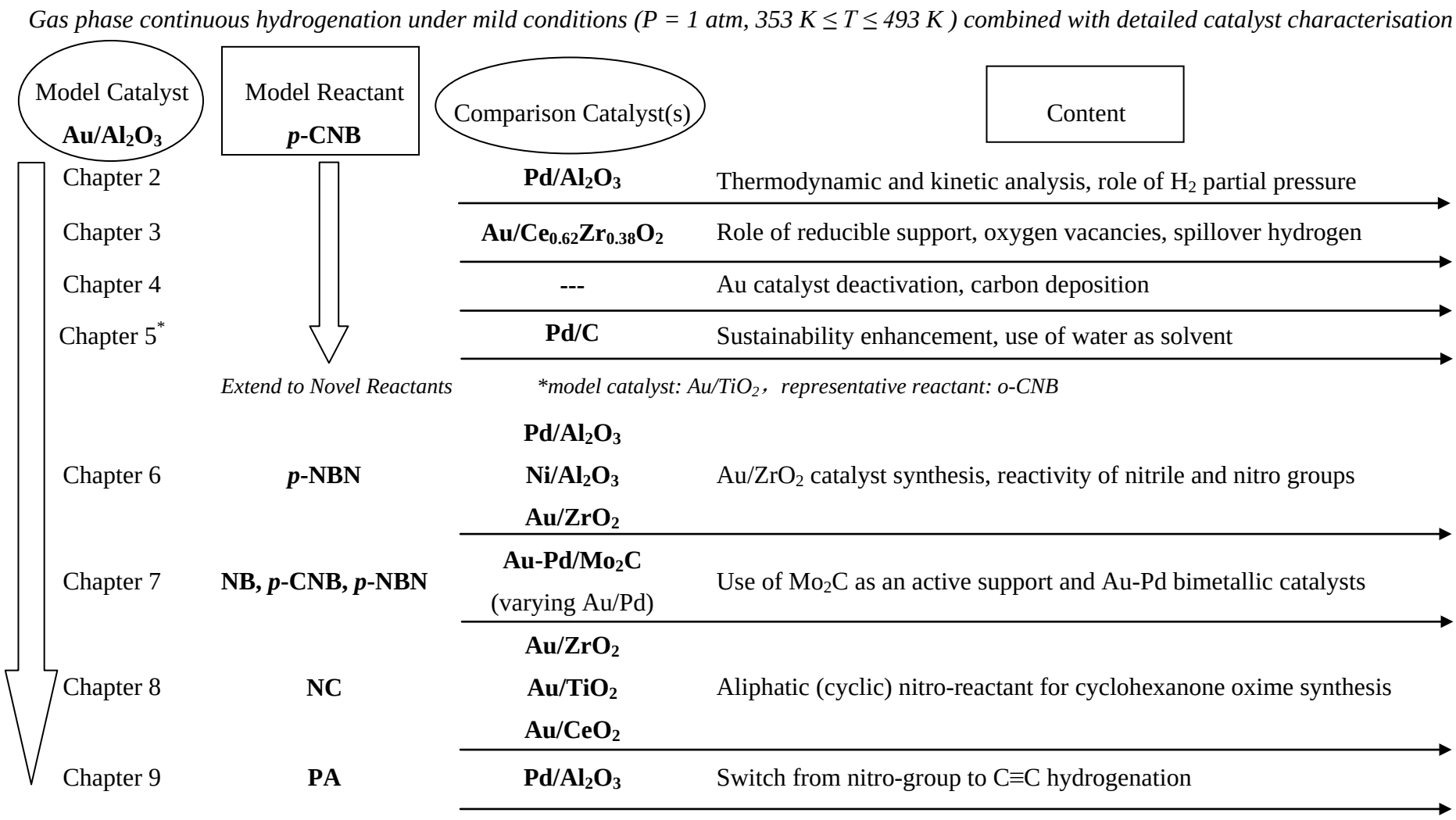

Note: *p*-CNB: *p*-chloronitrobenzene, *p*-NBN: *p*-nitrobenzonitrile, NB: nitrobenzene, NC: nitrocyclohexane and PA: phenylacetylene

Figure 1.1: Scope of the studies undertaken in this thesis.

supported Au and Pd in batch liquid phase and gas phase continuous modes with a consideration of the effects of hydrogen partial pressure and solvent (ethanol *vs.* water). The work to this point has dealt with the conversion of (*p*-/*o*-) CNB. In order to further explore the full potential of Au catalysts, additional reactants are introduced in **Chapter 6** (see publication No. 11), with the selective conversion of *p*-nitrobenzonitrile (*p*-NBN) to *p*-aminobenzonitrile (*p*-ABN) over laboratory synthesised Au/ZrO_2, coupling catalyst testing with comprehensive characterisation. Catalyst development is taken further in **Chapter 7** (see publication No. 13) with the use of Mo_2C as support and the combination of Pd with Au in bimetallic systems. A switch from aromatic to aliphatic (cyclic) nitro-compounds (nitrocyclohexane (NC)) is developed in **Chapter 8** (see publication No. 5) for reaction over a range (Au/Al_2O_3, Au/CeO_2, Au/TiO_2 and Au/ZrO_2) of catalysts where the target product is cyclohexanone oxime. The final study (in **Chapter 9** see publication No. 12) takes the range of reactants further with a consideration of C≡C reactivity in phenylacetylene (PA) hydrogenation. The thesis closes (**Chapter 10**) with a final overview, concluding remarks and suggested future work.

1.4 References

[1.1] S.H. Park, C.L. Walter, *Industrial development and environmental degradation*, Edward Publ., Inc., Cheltenham, 1998

[1.2] M. Gavrilescu, Y. Chisti, *Biotechnology-a sustainable alternative for chemical industry*, Biotechnol. Adv., **23**, 471-499 (2005)

[1.3] F. Cárdenas-Lizana, M.A. Keane, *The development of gold catalysts for use in hydrogenation reactions*, J. Mater. Sci., **48**, 543-564 (2013)

[1.4] P.T. Anastas, M.M. Kirchhoff, T.C. Williamson, *Catalysis as a foundational pillar of green chemistry*, Appl. Catal. A: Gen., **221**, 3-13 (2001)

[1.5] M. Pietrowski, *Recent developments in heterogeneous selective hydrogenation of halogenated nitroaromatic compounds to halogenated anilines*, Curr. Org. Synth., **9**, 470-487 (2012)

[1.6] M. Chong, D.-G. Cheng, L. Liu, F. Chen, X. Zhan, *Deactivation of CeO_2 catalyst*

in the hydrogenation of benzoic acid to benzaldehyde, Catal. Lett., **114**, 198-201 (2007)

[1.7] N. Perret, F. Cardenas-Lizana, M.A. Keane, *Selective hydrogenation of benzaldehyde to benzyl alcohol over Au/Al_2O_3*, Catal. Commun., **16**, 159-164 (2011)

[1.8] S. Nikolaev, V. Smirnov, *Selective hydrogenation of phenylacetylene on gold nanoparticles*, Gold Bull., **42**, 182-189 (2009)

[1.9] B. Zhao, Y.-W. Chen, *Hydrogenation of p-chloronitrobenzene on Mo, La, Fe, and W-modified NiCoB nanoalloy catalysts*, J. Non-cryst. Solids, **356**, 839-847 (2010)

[1.10] H.-U. Blaser, C. Malan, B. Pugin, F. Spindler, H. Steiner, M. Studer, *Selective hydrogenation for fine chemicals: Recent trends and new developments*, Adv. Synth. Catal., **345**, 103-151 (2003)

[1.11] G. Somorjai, C. Kliewer, *Reaction selectivity in heterogeneous catalysis*, React. Kinet. Catal. Lett., **96**, 191-208 (2009)

[1.12] M. Haruta, T. Kobayashi, H. Sano, N. Yamada, *Novel gold catalysts for the oxidation of carbon-monoxide at a temperature far below 0 ^oC*, Chem. Lett., 405-408 (1987)

[1.13] G. Bond, *The early history of catalysis by gold*, Gold Bull., **41**, 235-241 (2008)

[1.14] C. Della Pina, E. Falletta, L. Prati, M. Rossi, *Selective oxidation using gold*, Chem. Soc. Rev., **37**, 2077-2095 (2008)

[1.15] C.D. Pina, E. Falletta, M. Rossi, *Update on selective oxidation using gold*, Chem. Soc. Rev., **41**, 350-369 (2012)

[1.16] G.J. Hutchings, J.K. Edwards, L.J. Roy, J.P. Wilcoxon, *Application of gold nanoparticles in catalysis*, Front. Nanosci., **3**, 249-293 (2012)

[1.17] L. McEwan, M. Julius, S. Roberts, J. Fletcher, *A review of the use of gold catalysts in selective hydrogenation reactions*, Gold Bull., **43**, 298-306 (2010)

[1.18] F. Cardenas-Lizana, S. Gomez-Quero, N. Perret, M.A. Keane, *Support effects in the selective gas phase hydrogenation of p-chloronitrobenzene over gold*, Gold Bull., **42**, 124-132 (2009)

[1.19] F. Cárdenas-Lizana, S. Gómez-Quero, M.A. Keane, *Clean production of*

chloroanilines by selective gas phase hydrogenation over supported Ni catalysts, Appl. Catal. A: Gen., **334**, 199-206 (2008)

[1.20] B. Zuo, Y. Wang, Q. Wang, J. Zhang, N. Wu, L. Peng, L. Gui, X. Wang, R. Wang, D. Yu, *An efficient ruthenium catalyst for selective hydrogenation of ortho-chloronitrobenzene prepared via assembling ruthenium and tin oxide nanoparticles*, J. Catal., **222**, 493-498 (2004)

[1.21] X. Wang, N. Perret, M.A. Keane, *The role of hydrogen partial pressure in the gas phase hydrogenation of p-chloronitrobenzene over alumina supported Au and Pd: A consideration of reaction thermodynamics and kinetics*, Chem. Eng. J., **210**, 103-113 (2012)

[1.22] B. Coq, A. Tijani, F. Figuéras, *Influence of alloying platinum for the hydrogenation of p-chloronitrobenzene over PtM/Al_2O_3 catalysts with Mn, Pb, Ge, Al, Zn*, J. Mol. Catal., **71**, 317-333 (1992)

[1.23] Y.D. Smirnov, L.A. Fedorova, A.P. Tomilov, *Improvement of the electrochemical synthesis of p-chloroaniline*, Russ. J. Electrochem., **33**, 1168-1170 (1997)

CHAPTER 2

The Role of Hydrogen Partial Pressure in the Gas Phase Hydrogenation of *p*-Chloronitrobenzene over Alumina Supported Au and Pd: A Consideration of Reaction Thermodynamics and Kinetics

In this chapter, thermodynamic equilibrium analysis of gas phase *p*-chloronitrobenzene hydrogenation is studied first, where Au/Al_2O_3 and Pd/Al_2O_3 catalysts have then been employed to probe reaction kinetics considering hydrogen partial as an important parameter. This chapter has been published in Chemical Engineering Journal (see publication No. 8). Co-author N.P. participated in the discussion and co-wrote the chapter. M.A.K. directed the project and co-wrote the chapter.

2.1 Introduction

Catalysis plays a critical role in the chemical industry and, given pressing eco-efficient and financial demands, it is estimated that over 90% of commercial chemical processes involve a catalytic component [1]. Catalyst fabrication continues to be crucial and a relatively recent development has seen the use of gold as catalytic material, building on the pioneering work of Haruta [2,3] and Hutchings [4]. Although bulk Au is essentially non-reactive, Au particles at the nano-scale, when dispersed on oxide supports, have proven to be effective in CO oxidation [5], NO_x treatment [6] and the water gas shift reaction [7]. However, gold catalysis has had limited application in hydrogenation, due to the low capacity for H_2 activation/chemisorption [8]. Nevertheless, we have demonstrated high selectivity in the hydrogenation of nitroarenes over Au/Al_2O_3 [9,10], Au/TiO_2 [11,12], Au/CeO_2 [13] and Au/Fe_2O_3 [13]. The catalytic activity of Au in hydrogen mediated reactions is significantly lower than that of standard transition metal (Ni, Pd, or Pt) catalysts [14]. Palladium, as a representative Group VIII metal, has been widely used to promote steam reforming [15,16], oxidation [17,18], combustion [19,20],

hydrogenolysis [21,22], hydrogenation [10,23] and dehydrogenation [24,25]. In previous work, we have reported that supported Pd delivers higher reaction rates than Au catalysts but is non-selective in the gas phase hydrogenation of functionalised nitroarenes [10]. The existing literature on the hydrogenation of chloronitrobenzenes has focused on batch liquid systems operated at elevated pressure [26-28], where by-products including aniline (AN) [26,27], nitrobenzene (NB) [26], dichlorohydrazobenzene [28], dichloroazoxybenzene [29], dichloroazobenzene [29] and *N*-ethyl-chloroaniline [29] have been reported. A move from batch liquid to continuous gas phase operation has immediate benefits in terms of increased throughput where economies of scale favour continuous processes for high throughput.

Nitroarene hydrogenation reactions have been conducted where the H_2/nitroarene ratio was maintained far in excess (up to 3200) in both liquid and gas phase operation [30,31]. There is currently a dearth of literature dealing with reactions conducted at the H_2/nitroarene reaction stoichiometry and at sub-atmospheric pressure. In this chapter, the catalytic action of alumina supported Au and Pd in gas phase *p*-chloronitrobenzene (*p*-CNB) hydrogenation is compared where the inlet H_2 has been varied from excess (H_2/*p*-CNB up to 2300) to lean (stoichiometric) conditions. Alumina was chosen as support because its acid-base character has been shown to enhance H_2 activation on supported Au sites [32]. The target product (*p*-chloroaniline, *p*-CAN) is commercially important as an intermediate in the production of a diversity of pharmaceuticals and agrochemicals [33]. In terms of process development, use of a dilute H_2 reaction stream is an important consideration with regard to cost and atom efficiency. A search through the literature did not unearth any comprehensive thermodynamic analysis of nitroarene hydrogenation. In order to explicitly establish the catalytic response, we consider the thermochemical features of this reaction system. Moreover, we could not find any published mechanistic kinetic treatment of gas phase hydrogenation over Au. We propose here a kinetic model that can account for the dependence of *p*-CNB hydrogenation rate on H_2 partial pressure over Au/Al_2O_3 and Pd/Al_2O_3, which we link to critical catalyst characteristics.

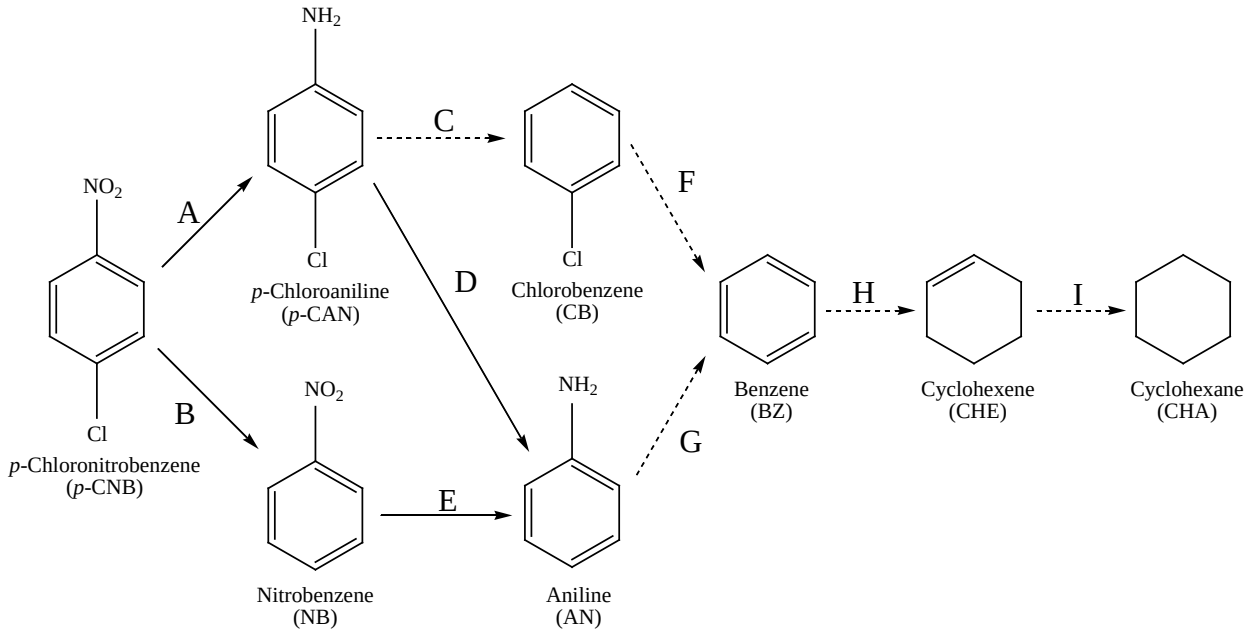

Figure 2.1: Reaction pathways associated with the hydrogen mediated conversion of *p*-CNB. Note: solid arrows identify steps observed in the catalytic reaction; dashed arrows identify additional steps considered in the thermochemical calculations.

Table 2.1: Stoichiometric requirement, corresponding reactions (see Figure 2.1) and associated (calculated) changes in enthalpy and Gibbs free energy of formation for each product.

Product	Stoichi-ometry[a]	Reaction path(s)	ΔH_{423K} (kJ mol^{-1})	ΔG_{423K} (kJ mol^{-1})
NB	1	B: $C_6H_4ClNO_2 + H_2 \rightleftharpoons C_6H_5NO_2 + HCl$	–63.7	–81.1
p-CAN	3	A: $C_6H_4ClNO_2 + 3H_2 \rightleftharpoons C_6H_4ClNH_2 + 2H_2O$	–467.7	–452.0
CB	4	C: $C_6H_4ClNH_2 + H_2 \rightleftharpoons C_6H_5Cl + NH_3$	–52.2	–51.6
AN	4	D: $C_6H_4ClNH_2 + H_2 \rightleftharpoons C_6H_5NH_2 + HCl$ E: $C_6H_5NO_2 + 3H_2 \rightleftharpoons C_6H_5NH_2 + 2H_2O$	–64.7 –468.7	–70.4 –441.4
BZ	5	F: $C_6H_5Cl + H_2 \rightleftharpoons C_6H_6 + HCl$ G: $C_6H_5NH_2 + H_2 \rightleftharpoons C_6H_6 + NH_3$	–64.7 –52.1	–73.6 –54.8
CHE	7	H: $C_6H_6 + 2H_2 \rightleftharpoons C_6H_{10}$	–91.9	6.2
CHA	8	I: $C_6H_{10} + H_2 \rightleftharpoons C_6H_{12}$	–121.2	–57.2

[a]moles of hydrogen required per mol of *p*-CNB

2.2 Methodology: Thermodynamic Analysis

Chemical thermodynamics provide a critical measure of the maximum conversion/selectivity that is possible under given reaction conditions as an essential initial consideration in the design of a catalytic process [34,35]. The possible pathways in the hydrogen mediated conversion of *p*-CNB are identified in **Figure 2.1**. Aniline (AN) can result from $-NO_2$ group reduction (step A) with subsequent hydrodechlorination (step D) or *via* sequential hydrodechlorination to give nitrobenzene (NB, step B) and hydrogenation (step E). Hydrodenitrogenation of *p*-CAN generates chlorobenzene (CB, step C) while benzene (BZ) can be formed from either CB hydrodechlorination (step F) or AN hydrodenitrogenation (step G). Subsequent hydrogenation of BZ generates cyclohexene (CHE) and cyclohexane (CHA) *via* steps H and I. Each organic intermediate/product and inorganic component (H_2, HCl, NH_3 and H_2O) was considered in the thermodynamic calculations (see **Table 2.1**). Setting the inlet *p*-CNB at 1 mol, product distribution at equilibrium was determined with varying reaction temperature (373-473 K) and H_2/*p*-CNB ratio (1-50) at a total pressure of 1 atm. The equilibrium calculations were carried out using CHEMCAD (Version 6) where the Gibbs reactor facility was applied to obtain product composition under the conditions of minimised Gibbs free energy [36]. The equation of state for fugacity employed the Soave–Redlich–Kwong approach [34]. The total Gibbs function is given by

$$G^t = \sum_{i=1}^{N} n_i \bar{G}_i = \sum_{i=1}^{N} n_i \bar{\mu}_i = \sum n_i G_i^0 + RT \sum n_i \ln \frac{\hat{f}_i}{f_i^0} \tag{2.1}$$

For reaction equilibrium in the gas phase, $\hat{f}_i = \hat{\phi}_i y_i P$, $f_i^0 = P^0$, $\Delta G^0 = \Delta G_{f_i}^0$ and the minimum Gibbs free energy of each gaseous species and the total for the system can be expressed by

$$\Delta G_{f_i}^0 + RT \ln \frac{\hat{\phi}_i y_i P}{P^0} + \sum_k \lambda_k a_{ik} = 0 \tag{2.2}$$

$$\sum_{i=1}^{N} n_i (\Delta G_{f_i}^0 + RT \ln \frac{\hat{\phi}_i y_i P}{P^0} + \sum_k \lambda_k a_{ik}) = 0 \tag{2.3}$$

according to the Lagrange undetermined multiplier method [37] with the elemental balance constraint

$$\sum_{i=1}^{N} n_i a_{ik} = A_k \qquad (2.4)$$

2.3 Experimental: Materials and Methods

2.3.1 Catalyst Preparation

A 1.1% w/w Au/γ-Al_2O_3 was prepared by deposition-precipitation (DP). Urea (Riedel-de Häen, ≥ 99%), used as basification agent, was added (100-fold excess) to a solution of $HAuCl_4$ (7.3×10^{-3} M), the γ-Al_2O_3 support (Puralox, Condea Vista Co.) was introduced and the suspension stirred and heated to 353 K (2 K min^{-1}) for 3 h. The pH progressively increased to reach *ca.* 7 as a result of urea decomposition

$$NH_2\text{-}CO\text{-}NH_2 + 3H_2O \xrightarrow{T=353K} 2NH_4^+ + 2OH^- + CO_2 \qquad (2.5)$$

The resultant solid was separated by centrifugation, washed repeatedly with deionised water (with centrifugation between each washing) until the washing water was Cl-free (based on the $AgNO_3$ test) and dried in He (45 cm^3 min^{-1}) at 373 K (2 K min^{-1}) for 5 h. For comparison purposes, a commercial (Sigma-Aldrich) 1.2 % w/w Pd/Al_2O_3 catalyst was employed and used as received. The catalysts were sieved to 75 μm average particle diameter (ATM fine test sieves) and the Au and Pd loadings determined by inductively coupled plasma-optical emission spectrometry (ICP-OES, Vista-PRO, Varian Inc.) from the diluted extract in aqua regia.

2.3.2 Catalyst Characterisation

Nitrogen adsorption-desorption isotherms were obtained at 77 K using the commercial automated Micromeritics Gemini 2390 system. Specific surface areas were calculated from the isotherms using the standard BET method. The average pore sizes, cumulative pore volumes and pore size distributions were obtained by BJH analysis from the desorption isotherms; samples were outgassed at 423 K under N_2 for 1 h prior to analysis. Temperature programmed reduction (TPR) and H_2 chemisorption were recorded using the commercial CHEMBET 3000 (Quantachrome Instrument) unit; data acquisition/manipulation employed the TPR Win^{TM} software. The samples were loaded into a U-shaped quartz cell (100 mm × 3.76 mm i.d.) and heated in 17 cm^3 min^{-1} (Brooks

mass flow controlled) 5% v/v H_2/N_2 to 473-573 K at 2 K min^{-1}. The effluent gas passed through a liquid N_2 trap and H_2 consumption was monitored by a thermal conductivity detector. Post-TPR, the samples were swept with 65 cm^3 min^{-1} N_2 for 1.5 h, cooled to ambient or reaction (423 K) temperature and subjected to H_2 chemisorption using a pulse (10-50 μl) titration procedure. Hydrogen pulse introduction was repeated until the signal area was constant, indicating surface saturation. The sample was then thoroughly flushed in N_2 and subjected to a temperature-programmed desorption (TPD) at 50 K min^{-1} to 1173 K. Powder x-ray diffractograms (XRD) were recorded on a Bruker/Siemens D500 incident x-ray diffractometer using Cu Kα radiation. The sample was scanned at a rate of 0.02º $step^{-1}$ over the range $20º \leq 2\theta \leq 85º$ and the diffractograms were compared with JCPDS-ICDD reference standards (Au (Card No. 04-0784), Pd (05-0681) and γ-Al_2O_3 (10-0425)). Transmission electron microscopy (TEM) analysis was conducted using a JEOL JEM 2011 HRTEM unit with a UTW energy dispersive X-ray detector (EDX) detector (Oxford Instruments) operated at an accelerating voltage of 200 kV; Gatan DigitalMicrograph 3.4 was used for data acquisition/manipulation. Samples for analysis were prepared by dispersion in acetone and deposited on a holey carbon/Cu grid (300 Mesh). The number weighted mean metal particle size (d_{TEM}) was obtained from

$$d_{TEM} = \frac{\sum_i n_i d_i}{\sum_i n_i} \tag{2.6}$$

where n_i is the number of particles of diameter d_i and $\Sigma n_i > 300$. X-ray photoelectron spectroscopy (XPS) analysis was conducted on an Axis Ultra instrument (Kratos Analytical) under ultra-high vacuum condition (< 10^{-8} Torr) using a monochromatic Al Kα X-ray source (1486.6 eV). The source power was maintained at 150 W and the emitted photoelectrons were sampled from a 750 × 350 μm^2 area at a take-off angle = 90°. The analyser pass energy was 80 eV for survey spectra (0–1000 eV), 40 eV (Pd $3d_{5/2}$) and 20 eV (Au $4f_{7/2}$) for high resolution spectra. Bulk Pd obtained from the reduction of PdO (Aldrich) was employed as a reference for metallic Pd. The adventitious carbon 1*s* peak was calibrated at 284.5 eV and used as an internal standard to compensate for any charging effects. Spectra curve fitting and quantification were performed with the Casa XPS software, using relative sensitivity factors provided by Kratos.

2.3.3 Catalytic Procedure

Reactions were carried out at H_2 partial pressures in the range 0.8×10^{-3}–0.92 atm (varied by dilution in He, total pressure = 1 atm), immediately after *in situ* activation (at 2 K min^{-1} to 473-573 K in 60 cm^3 min^{-1} H_2 for 1h) in a continuous flow fixed bed vertical glass reactor (60 cm × 15 mm i.d.) at 373-473 K. The catalytic reactor and operating conditions to ensure negligible heat/mass transport limitations have been fully described elsewhere [38,39] but some features, pertinent to this study, are given below. A layer of borosilicate glass beads served as preheating zone, ensuring that the inlet *p*-CNB (or *p*-CAN) was vaporised and reached reaction temperature before contacting the catalyst. Isothermal conditions (±1 K) were ensured by diluting the catalyst bed with ground glass (75 μm); the ground glass was mixed thoroughly with catalyst before insertion into the reactor. Reaction using physical mixtures of catalyst with support ($Au/Al_2O_3+Al_2O_3$ and $Pd/Al_2O_3+Al_2O_3$) was also examined. Temperature was continuously monitored by a thermocouple inserted in a thermowell within the catalyst bed. *p*-CNB (or *p*-CAN) was delivered *via* a glass/teflon air-tight syringe and teflon line using a microprocessor controlled infusion pump (Model 100 kd Scientific) at a fixed calibrated flow rate. A co-current flow in H_2 (or H_2/He) was maintained at $GHSV = 2\times10^4$ h^{-1} with an inlet $–NO_2$ (or $–NH_2$) molar flow (F) of 6.3×10^{-5}–3.8×10^{-4} mol h^{-1}; molar metal (n) to F ratio spanned the range 3×10^{-4}–4.2×10^{-2} h. In a series of blank tests, passage of *p*-CNB (or *p*-CAN) in H_2 through the empty reactor or over the support alone, *i.e.* in the absence of Au or Pd, did not result in any detectable conversion. The reactor effluent was frozen in a liquid N_2 trap for subsequent analysis, using a Perkin-Elmer Auto System XL gas chromatograph equipped with a programmed split/splitless injector and a flame ionization detector, employing a DB-1 50 m × 0.20 mm i.d. 0.33 μm film thickness capillary column (J&W Scientific), as described elsewhere [40]. Quantitative analysis was based on relative peak area where analytical repeatability was better than ± 1 % and the detection limit corresponded to a feedstock conversion less than 0.1 mol %. *p*-CNB (Aldrich, ≥ 99%), *p*-CAN (Aldrich, ≥ 98%) and the 1-butanol solvent (Riedel-de Häen, ≥ 99.5%) were used without further purification. All the gases used in this study (H_2, N_2 and He) were of ultra high purity (≥ 99.99 %, BOC). Repeated reactions with different samples from the same batch of

catalyst delivered raw conversion and selectivity data that were reproducible to within ±3 %. The turnover frequency (*TOF*) of *p*-CNB (or *p*-CAN) was calculated based on Au and Pd dispersion obtained from TEM analysis. Fractional hydrogenation ($x_{p\text{-}CNB}$) was obtained from

$$x_{p-CNB} = \frac{[p-CNB]_{in} - [p-CNB]_{out}}{[p-CNB]_{in}} \tag{2.7}$$

where selectivity with respect to *p*-CAN ($S_{p\text{-}CAN}$) is given by

$$S_{p-CAN}(\%) = \frac{[p-CAN]_{out}}{[p-CNB]_{in} - [p-CNB]_{out}} \times 100 \tag{2.8}$$

2.4 Results and Discussion

The stoichiometric requirements for each step in the reaction pathway shown in **Figure 2.1** are given in **Table 2.1**. The formation of *p*-CAN *via* the hydrogenation of *p*-CNB (path A) has been demonstrated previously for supported Au [9-13] and Ni [41] catalysts. Subsequent hydrodenitrogenation to CB (path C) has been reported for Pt/Al_2O_3 [42]. NB and AN are produced by hydrodechlorination of *p*-CNB with further hydrogenation (paths B and E), as proposed for Pd/Al_2O_3 [9,11,41], Ni/Al_2O_3 [41] and bimetallic Pd-Rh and Pd-Fe [43] catalysts. Path D was observed over palladised charcoal when using *p*-CAN as reactant [44]. There is, however, no available literature regarding the production of benzene (BZ) or additional hydrogenation to cyclohexene (CHE) or cyclohexane (CHA), *i.e.* from path F to I. All the steps shown in **Figure 2.1** have been taken into account in the thermodynamic calculations.

2.4.1 Reaction Thermodynamics

The calculated change in reaction enthalpy (ΔH_{423K}) and Gibbs free energy (ΔG_{423K}) of formation at 423 K (median temperature in this study) for each reaction step are presented in **Table 2.1**. The negative values of ΔH_{423K} indicate that all the reactions are exothermic with paths A and E releasing the greatest amount of heat (*ca.* 470 kJ mol^{-1}). The ΔG_{423K} values serve as an indicator of possible thermodynamic limitations, where reactions can occur spontaneously when $\Delta G_{423K} < 0$. With the exception of path H (hydrogenation of BZ to CHE), the reaction steps exhibit negative ΔG_{423K}, indicating that

CHE is a thermodynamically unfavourable product. The analysis also considered the effect of reaction temperature (373–473 K) at two H_2/*p*-CNB ratios, *i.e.* H_2/*p*-CNB = 50 (H_2 far in excess) and 4 (stoichiometric ratio for the production of AN). The results at H_2/*p*-CNB = 50 can be taken to be representative as product distribution is invariant at H_2/*p*-CNB $\geq$ 10. Complete conversion is achieved at equilibrium for both H_2/*p*-CNB ratios, irrespective of reaction temperature. As shown in **Table 2.2**, CHA is the sole product for reaction in excess H_2 regardless of temperature, indicating that there is no

Table 2.2: Effect of temperature on product selectivity (calculated) at equilibrium for selected H_2/*p*-CNB ratios.

H_2/*p*-CNB	Temperature (K)	Selectivity (%)					
		p-CAN	NB	AN	CB	BZ	CHA
50	373	-	-	-	-	-	100
	423	-	-	-	-	-	100
	473	-	-	-	-	-	100
4	373	11	-	70	8	11	-
	423	12	-	67	9	12	-
	473	13	-	64	10	13	-

thermodynamic barrier for full hydrogenation (with hydrogenolysis) of *p*-CNB. At H_2/*p*-CNB = 4, a combination of *p*-CAN, AN, CB and BZ is generated at equilibrium with AN as the predominant product. The occurrence of CB is consistent with reaction along paths A and C and the formation of AN *via* path D. Furthermore, BZ can arise from the conversion of CB (path F, hydrodechlorination) and/or AN (path G, hydrodenitrogenation). An increase in temperature serves to lower selectivity with respect to AN but the effect is slight in comparison with the sensitivity of equilibrium composition to H_2/*p*-CNB ratio. Reaction selectivity (*S* %) under thermodynamic control (at 423 K) as a function H_2/*p*-CNB ratio can be assessed from the entries in **Figure 2.2**. Hydrogenation of *p*-CNB produced *p*-CAN as the only product where H_2/*p*-CNB $\leq$ 3, which is the stoichiometric requirement for path A (**Table 2.1**). Under these conditions, *p*-CAN is the only thermodynamically favoured product and NB is not formed at equilibrium even though the H_2/*p*-CNB ratio exceeds the stoichiometry for path B. An

increase in H_2/*p*-CNB results in a decrease in *p*-CAN selectivity, favouring principally the formation of AN (path D) with CB (path C) as a secondary product. The AN and CB hydrogenolysis products pass through a selectivity maximum at H_2/*p*-CNB = 4 (stoichiometric requirement, see **Table 2.1**) with the exclusive formation of BZ at H_2/*p*-CNB = 5.

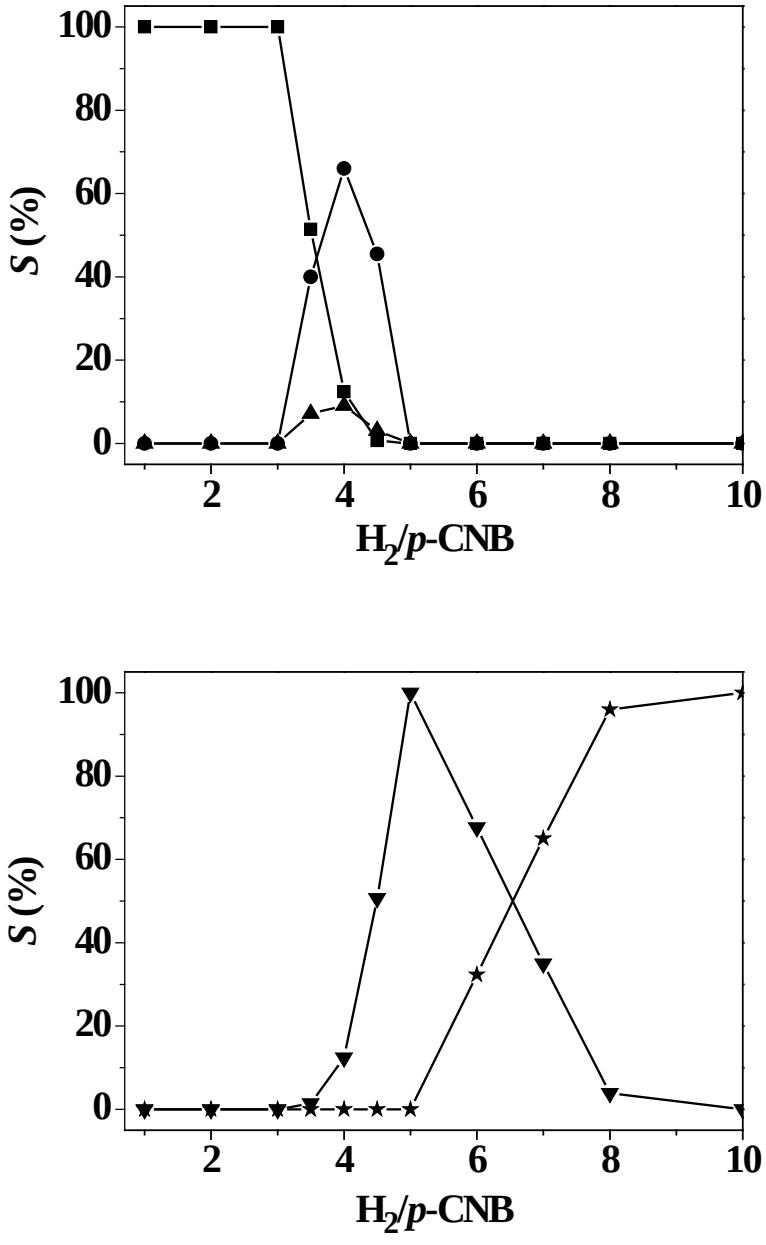

Figure 2.2: Product selectivity (calculated) at equilibrium as a function of the inlet H_2/*p*-CNB at 423 K: *p*-CAN (■); AN (●); CB (▲); BZ (▼); CHA (★).

The hydrogenation of BZ is thermodynamically favoured where H_2/*p*-CNB > 5 with the sole formation of CHA. CHE is not generated at the H_2/*p*-CNB stoichiometry (= 7),

suggesting a single step BZ→CHA transformation. In summary, for a given H_2/*p*-CNB, reaction temperature has a negligible influence on equilibrium composition but product selectivity is sensitive to H_2/*p*-CNB ratio in the range 1-8.

2.4.2 Catalyst Characteristics

Critical catalyst characteristics are given in **Table 2.3**. The BET surface areas (156-166 m^2 g^{-1}) and total pore volumes (0.36-0.46 cm^3 g^{-1}) are within the range (150–250 m^2 g^{-1} and 0.27–0.75 cm^3 g^{-1}) reported for γ-Al_2O_3 supported metal systems [45]. The N_2 adsorption/ desorption isotherms (see **Figure 2.3**) show type IV behaviour in terms of the IUPAC classification, characteristic of mesoporous materials [46-49], consistent with the average pore size obtained for Au/Al_2O_3 (29 Å) and Pd/Al_2O_3 (46 Å).

Table 2.3: Physicochemical characteristics of Au/Al_2O_3 and Pd/Al_2O_3.

	Au/Al_2O_3	Pd/Al_2O_3
Metal loading (% w/w)	1.1	1.2
TPR T_{max} (K)	453	355[a]
BET area (m^2 g^{-1})	166	156
Pore volume (cm^3 g^{-1})	0.36	0.46
Mean pore radius (Å)	29	46
H_2 chemisorption[b] (μmol_{H2} μmol_{metal}^{-1})	7×10^{-3}	0.3
H_2 chemisorption[c] μmol_{H2} μmol_{metal}^{-1})	8×10^{-2}	0.2
Metal particle size range (nm)	1-13	1-6
d_{TEM} (nm)	4.5	2.4
XPS binding energy (eV)	84.1[d]	334.9[e]

[a]negative peak due to decomposition of β-Pd hydride
[b]at ambient temperature
[c]at 423 K
[d]Au $4f_{7/2}$
[e]Pd $3d_{5/2}$

The temperature programmed reduction (TPR) profiles for Al_2O_3 (I), Au/Al_2O_3 (II) and Pd/Al_2O_3 (III) are shown in **Figure 2.4(A)**. The TPR response for the Al_2O_3 support was featureless with no evidence of H_2 uptake or release, a response that is expected and in

agreement with the literature [45]. A positive peak at 453 K was observed for Au/Al_2O_3 where the associated H_2 consumption matched that required for the reduction of the precursor to the metallic form, *i.e.* $Au^{3+} \rightarrow Au^0$. A single TPR peak has been reported previously for Au/Al_2O_3 at 436 K [50] and 503 K [51]. We accordingly adopted an activation temperature of 473 K to fully reduce the supported Au precursor. The profile for Pd/Al_2O_3 presents a single negative (H_2 release) peak at 355 K. This response is in line with published TPR results and can be ascribed to the decomposition of β-Pd hydride resulting from H_2 absorption, which is known to occur at room temperature where the H_2

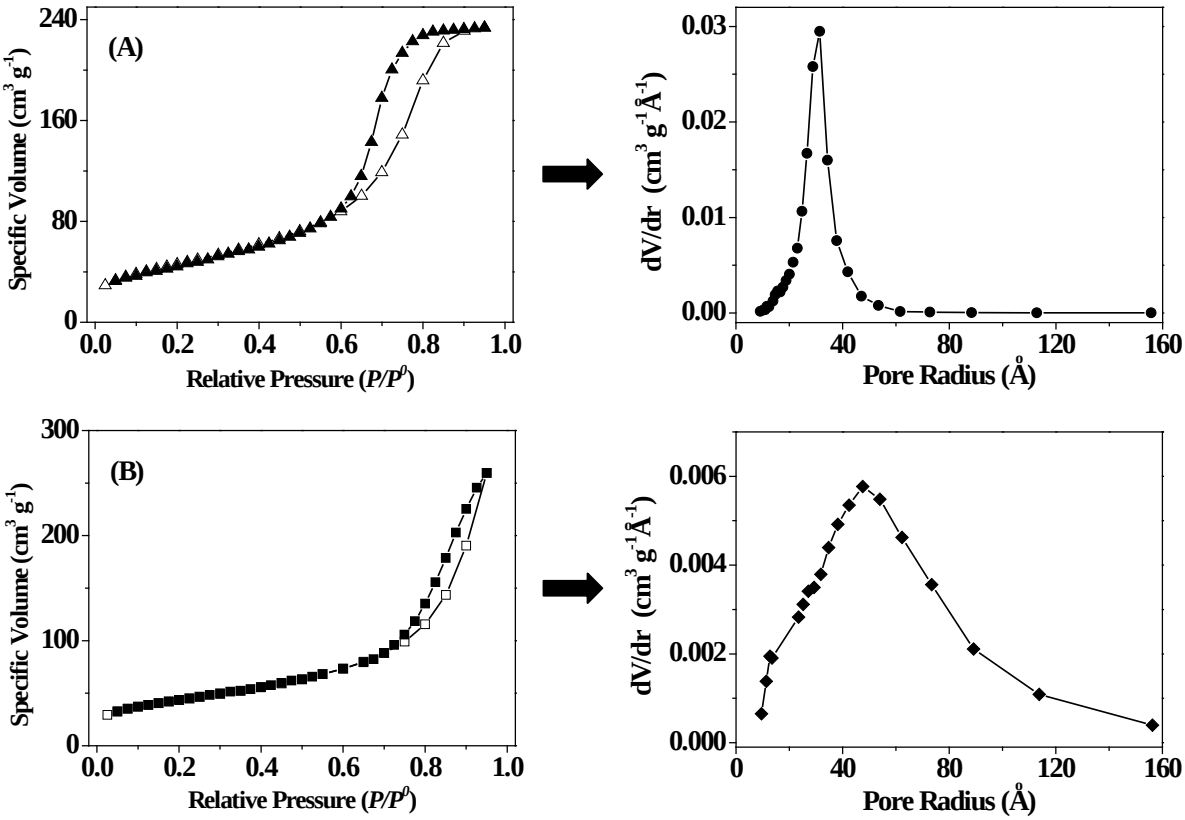

Figure 2.3: Nitrogen adsorption (open symbols) and desorption (solid symbols) isotherms with associated pore size distributions for (A) Au/Al_2O_3 and (B) Pd/Al_2O_3.

partial pressure exceeds 0.02 atm [52-54]; a pressure of 0.05 atm was used in this study. Hydride composition can be represented by the atomic ratio H_{ab}/Pd (H_{ab} = number of absorbed H atoms), which has been shown to decrease with decreasing Pd particle size [55,56]. The H_{ab}/Pd ratio for bulk Pd (*ca.* 0.69 $\mu mol_H\ \mu mol_{Pd}^{-1}$ [52]) is significantly greater than that (0.1 $\mu mol_H\ \mu mol_{Pd}^{-1}$) recorded in this study for Pd/Al_2O_3. We should flag

the work of Mendez *et al.* [57] who obtained an equivalent hydride composition for 0.66% w/w Pd/Al_2O_3 with a mean Pd particle size of 2.0 nm.

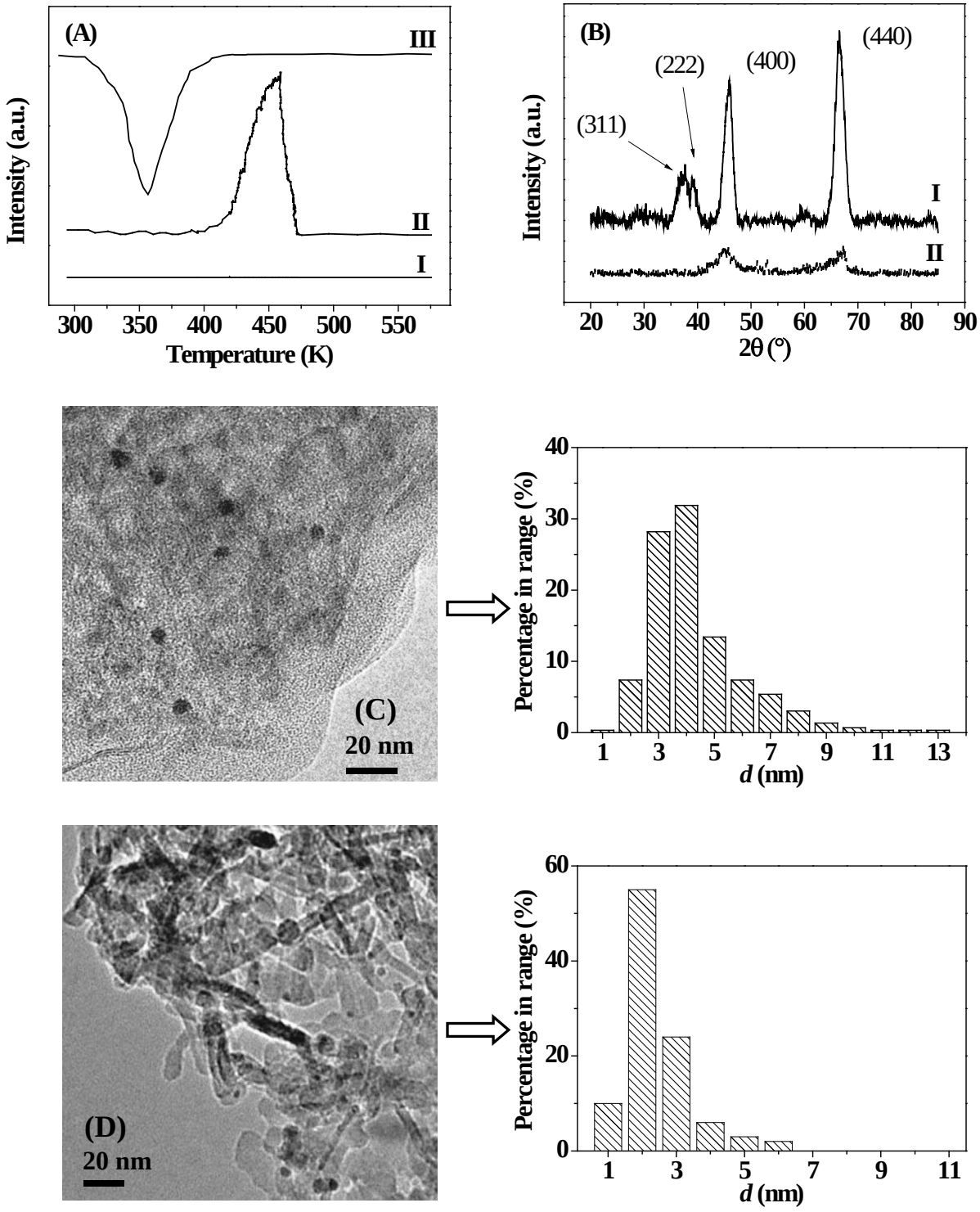

Figure 2.4: (A) TPR profiles for (I) Al_2O_3, (II) Au/Al_2O_3 and (III) Pd/Al_2O_3; (B) XRD patterns for (I) Au/Al_2O_3 and (II) Pd/Al_2O_3 including peak assignments for γ-Al_2O_3 based on JCPDS-ICDD 10-0425; Representative TEM images and particle size histograms for (C) Au/Al_2O_3 and (D) Pd/Al_2O_3.

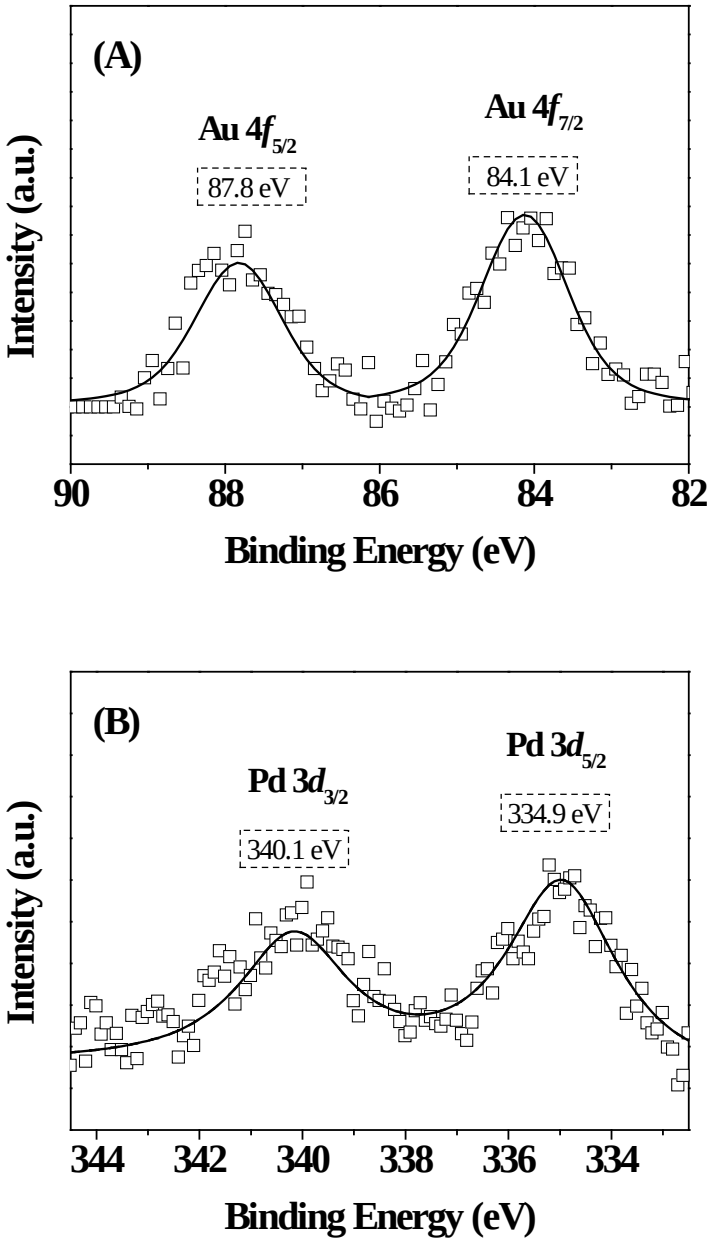

Figure 2.5 XPS spectra over (A) Au 4*f* (Au/Al_2O_3) and (B) Pd 3*d* (Pd/Al_2O_3) regions. Note: the XPS experimental data are represented by symbols (□) while the lines are the result of spectra curve fitting.

The XRD for Pd/Al_2O_3 (**Figure 2.4(B)II**) did not exhibit any characteristic peak for Pd metal, suggesting a well dispersed metal phase (< 5 nm) [58]. The XRD pattern for Au/Al_2O_3 (**Figure 2.4(B)I**) likewise only presents peaks due to the support. We have applied TEM analysis to explicitly determine metal particle size and the representative TEM images, shown in **Figure 2.4(C) and (D)**, demonstrate the occurrence of pseudo-spherical Au and Pd particles in the size range 1-13 and 1-6 nm, respectively. The

particle size distribution histograms in **Figure 2.4** were used to generate number weighted mean values for Au/Al_2O_3 (4.5 nm) and Pd/Al_2O_3 (2.4 nm). The latter is consistent with our H_{ab}/Pd ratio.

Selectivity in hydrogenation over supported Au [59] and Pd [60] is influenced by both metal particle size (geometric effect) and electronic structure where variations in metal charge can affect reactant adsorption/activation. XPS measurements were conducted to provide insight into the electronic character of the supported Pd and Au phases. The resulting spectra over the Pd 3*d* and Au 4*f* binding energy (BE) regions are shown in **Figure 2.5**; the associated BE values are given in **Table 2.3**. The Pd $3d_{5/2}$ core level has a value of 334.9 eV, which is 0.4 eV lower than that for the metallic Pd reference (335.3 eV) measured in this work, suggesting electron transfer from the support to generate $Pd^{\delta-}$, as has been proposed elsewhere for nano-scale Pd on Al_2O_3 [61]. The Au $4f_{7/2}$ BE (84.1 eV) recorded for Au/Al_2O_3 is close to the value reported for metallic Au (84.0 eV) [62], suggesting limited electron transfer to the support with a negligible net charge on Au. Ambient temperature H_2 chemisorption on Pd/Al_2O_3 was appreciably greater than that recorded for Au/Al_2O_3 (**Table 2.3**). This agrees with the general consensus that Au exhibits a high activation energy barrier for dissociative H_2 adsorption [8,63], which is favoured at low coordinated corner and edge atom sites [64]. The Pd size (2.0 nm) calculated from H_2 chemisorption agrees with the value (2.4 nm) from TEM analysis. Chemisorption at the median reaction temperature (423 K) revealed a significantly higher (by a factor of 10) uptake on Au/Al_2O_3 relative to the ambient temperature measurement. van Bokhoven *et al.* have reported increased capacity for H_2 activation on Au with increasing temperature (from 298 to 373 K) [65,66]. In contrast, H_2 chemisorption on Pd/Al_2O_3 decreased at the higher adsorption temperature. A lower capacity for H_2 uptake on supported noble metal catalysts has been noted in the literature [67,68].

2.4.3 Catalytic Response

Fractional *p*-CNB conversion ($x_{p\text{-}CNB}$) is illustrated as a function of time on-stream for representative cases in **Figure 2.6(A)**. The temporal decline in activity can be expressed in terms of the empirical relationship [69,70]

$$\frac{(x_{p-CNB} - x_0)}{(x_{3h} - x_0)} = \frac{\Delta t}{(\beta + \Delta t)} \tag{2.9}$$

where x_{3h} represents conversion after 3 h on-stream and β is a time scale fitting parameter. Fit convergence yields values for x_0, the initial fractional conversion, used here as a measure of activity. The effect of varying the inlet H_2/*p*-CNB ratio was examined at 423 K in order to facilitate a direct comparison with the thermochemical calculations. Under conditions of excess H_2, complete conversion of *p*-CNB can be achieved over both Au/Al_2O_3 and Pd/Al_2O_3 by increasing the catalyst to reactant ratio (*n*/*F*) in order to converge with the thermodynamic response. Complete conversion required a higher *n*/*F* for Au/Al_2O_3 (4.2×10^{-2} h) relative to Pd/Al_2O_3 (2.7×10^{-2} h), demonstrating lower catalytic efficiency for Au/Al_2O_3. While CHA is the only product at thermodynamic equilibrium, Au/Al_2O_3 generated exclusively *p*-CAN and Pd/Al_2O_3 produced AN as the predominant product with NB as secondary product. This means that under conditions of complete conversion, Au/Al_2O_3 directed *p*-CNB conversion *via* path A (see **Figure 2.1**), whereas reaction over Pd/Al_2O_3 followed path B with the further involvement of path E. It should be noted that reaction in batch liquid phase over supported Au (notably Au/SiO_2 and Au/ZrO_2) can generate 100% selective chloroaniline production at close to complete conversion but this necessitates high operating pressures (up to 4 MPa at 413-423 K), as discussed in the recent review by Zhang *et al*. [71]. Both catalytic transformations in this study are quite distinct from that which results from thermodynamic control.

The dependence of selectivity on H_2/*p*-CNB (up to 8, which meets the stoichiometric requirement for each possible product, **Table 2.1**) is shown in **Figure 2.6(B)**. The H_2 content in the feed did not influence product composition over Au/Al_2O_3 and reaction exclusivity to *p*-CAN was maintained at each H_2/*p*-CNB. In the case of Pd/Al_2O_3, a decrease in H_2/*p*-CNB from 8 to 1 resulted in increased selectivity to NB at the expense of AN; at H_2/*p*-CNB = 1, NB was the sole product. This is consistent with a sequential reaction over Pd/Al_2O_3 (path B→path E, **Figure 2.1**) where a decrease in H_2/*p*-CNB limits the involvement of path E. The dependence of selectivity on fractional conversion is presented in **Figure 2.6(C)** where selectivity (to *p*-CAN) invariance characterises Au/Al_2O_3. Product distribution was sensitive to conversion for reaction over Pd/Al_2O_3 with NB as sole product at low fractional conversion (< 0.09) and a switch to a

preferential AN formation at higher conversion (> 0.25). The effect of reaction temperature at a fixed H_2/*p*-CNB (= 4) can be assessed from the entries in **Table 2.4**.

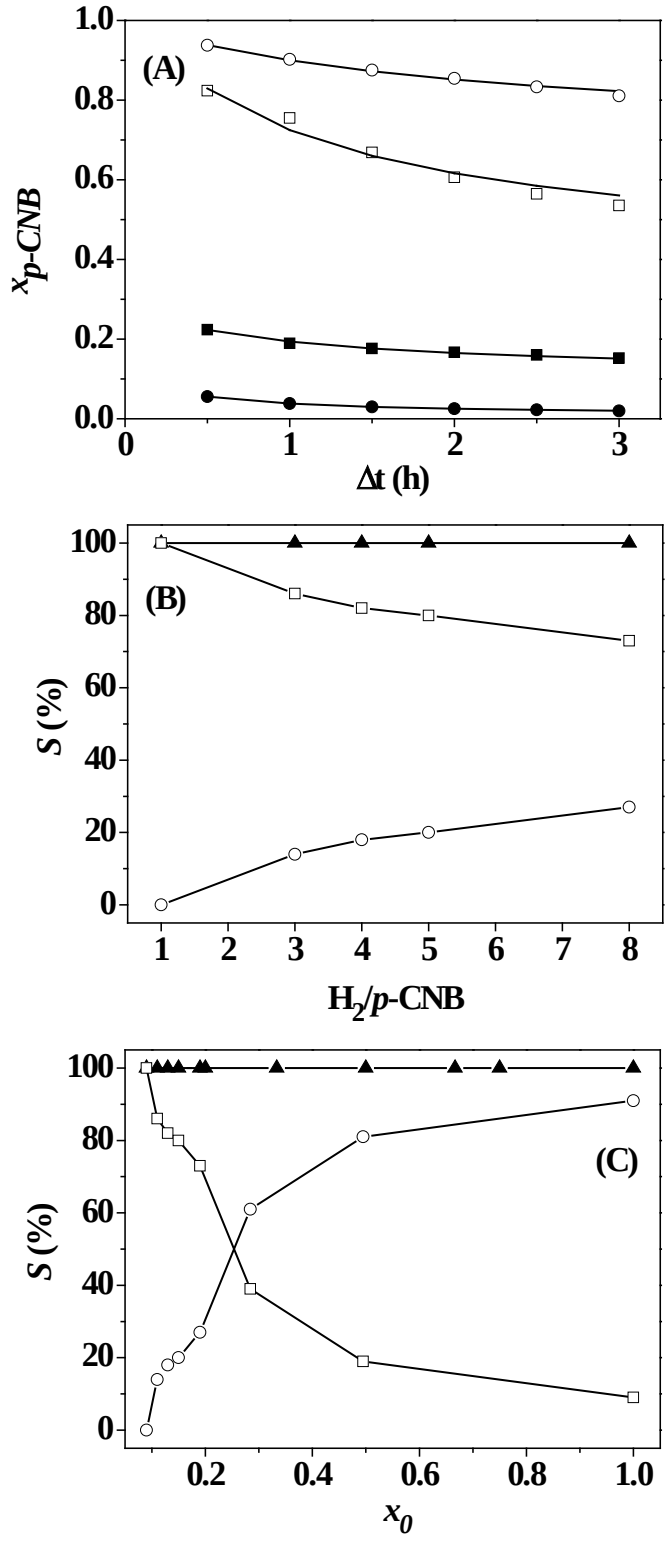

Figure 2.6: (A) Variation of *p*-CNB fractional conversion ($x_{p\text{-}CNB}$) with time-on-stream over Au/Al_2O_3 (○: $n/F = 4.2 \times 10^{-2}$ h, H_2/*p*-CNB = 2322; ●: $n/F = 1.7 \times 10^{-2}$ h, H_2/*p*-CNB = 4) and Pd/Al_2O_3 (□: $n/F = 2.7 \times 10^{-2}$ h, H_2/*p*-CNB = 1161; ■: $n/F = 2.9 \times 10^{-3}$ h, H_2/*p*-CNB = 386). (B) Effect of inlet H_2/*p*-CNB on product selectivity (*S*) over Au/Al_2O_3 (▲: *p*-CAN) and Pd/Al_2O_3 (□: NB, ○: AN) at x_0 between 0.10 and 0.15. (C) Variation of AN (○), NB (□) and *p*-CAN (▲) selectivity (*S*) with *p*-CNB conversion (x_0) over Au/Al_2O_3 (solid symbol) and Pd/Al_2O_3 (open symbols) where H_2/*p*-CNB > 390; *T* = 423 K.

In both cases, activity was raised at higher temperature but remained far below the complete conversion achieved at the thermochemical equilibrium. Reaction exclusivity to *p*-CAN over Au/Al_2O_3 was unaffected by temperature. Sole hydrodechlorination to NB over Pd/Al_2O_3 was observed at 373 K and subsequent hydrogenation to AN (Path E) was promoted at higher temperatures. An explicit comparison of Au/Al_2O_3 with Pd/Al_2O_3 can only be made at an equivalent fractional *p*-CNB conversion, as presented in **Table 2.4**. The results clearly demonstrate that the catalytic action of both metals (Au *vs.* Pd) exerted markedly different control over product composition.

Table 2.4: Effect of reaction temperature on catalyst performance: H_2/*p*-CNB = 4; $n/F = 1.8 \times 10^{-2}$ h (Au/Al_2O_3); n/F = 12-15 × 10^{-4} h (Pd/Al_2O_3).

Temperature (K)	Au/Al_2O_3		Pd/Al_2O_3	
	x_0	Product (*S* %)	x_0	Product(s) (*S* %)
373	0.01	*p*-CAN (100)	0.02	NB (100)
423	0.12	*p*-CAN (100)	0.13	NB (82), AN (18)
473	0.18	*p*-CAN (100)	0.17	NB (74), AN (26)

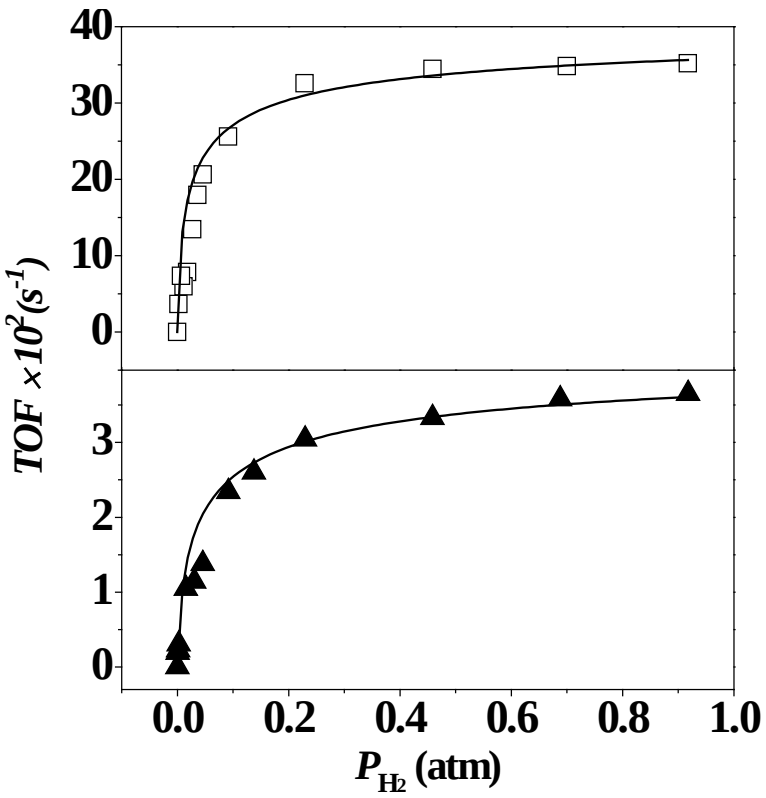

Figure 2.7: *p*-CNB turnover frequency (*TOF*) as a function of H_2 partial pressure for reaction over Au/Al_2O_3 (▲) and Pd/Al_2O_3 (□); T = 423 K; lines represent fits to Eq. (2.16).

2.4.4 Reaction Kinetics

The documented gas phase catalytic nitroarene hydrogenation studies [9-13,30,41,72-74] have all been conducted where H_2 was far in excess of stoichiometric quantities and the effect of H_2 partial pressure on hydrogenation rate has not been considered in any detail. While lower hydrogenation rates have been recorded for supported Au relative to Pd catalysts [10], an explicit kinetic analysis of the catalytic action of the two metals has not been published. The dependence of *p*-CNB turnover frequency (*TOF*) over Au/Al_2O_3 and Pd/Al_2O_3 on H_2 partial pressure is presented in **Figure 2.7**. Considering the interaction of H_2 with the catalyst surface where the partial pressure of *p*-CNB was kept constant

$$2[Cat] + H_2 \underset{k_{des}}{\overset{k_{ads}}{\leftrightarrow}} 2[Cat - H] \tag{2.10}$$

[Cat] denotes all free active surface sites after *p*-CNB adsorption while k_{ads} and k_{des} represent hydrogen adsorption and desorption constants, respectively. Surface reaction between hydrogen and *p*-CNB can be taken as irreversible

$$2[Cat - H] \xrightarrow{k_r} Products \tag{2.11}$$

where k_r (s^{-1}) is the surface rate constant and

$$k_{ads}[Cat]^2 P_{H_2} = k_{des}[Cat - H]^2 + k_r[Cat - H]^2 \tag{2.12}$$

In terms of surface site balance, $[Cat]_0$ represents total active sites after *p*-CNB adsorption

$$[Cat]_0 = [Cat] + [Cat - H] \tag{2.13}$$

and *[Cat-H]* can then be obtained from a combination of Eqs. (2.12) and (2.13)

$$[Cat - H] = \frac{[Cat]_0 P_{H_2}^{\frac{1}{2}}}{\left(P_{H_2}^{\frac{1}{2}} + \left(\frac{k_{des} + k_r}{k_{ads}} \right)^{\frac{1}{2}} \right)} \tag{2.14}$$

where *TOF* is given by

$$TOF = k_r[Cat - H]^2 = \frac{k_r [Cat]_0^2 P_{H_2}}{\left(P_{H_2}^{\frac{1}{2}} + \left(\frac{k_{des} + k_r}{k_{ads}} \right)^{\frac{1}{2}} \right)^2} \tag{2.15}$$

Taking the surface reaction to be rate determining, $k_r << k_{ads}$ and

$$TOF = \frac{k_r [Cat]_0^{\,2} P_{H_2}}{\left(P_{H_2}^{\frac{1}{2}} + (\frac{k_{des}}{k_{ads}})^{\frac{1}{2}} \right)^2} = \frac{TOF_{max} P_{H_2}}{\left(P_{H_2}^{\frac{1}{2}} + A^{\frac{1}{2}} \right)^2} \quad (2.16)$$

where $TOF_{max} = k_r [Cat]_0^{\,2}$ represents the maximum *p*-CNB *TOF* and A^{-1} (= k_{ads}/k_{des}) provides a measure of the surface capacity for H_2 activation. Rate expression (2.16) reproduces the dependence of the experimentally determined *TOF* on H_2 partial pressure, as shown in **Figure 2.7**. In both cases, *TOF* is proportional to pressure where $P_{H2} < 0.2$ atm and attains a limiting value at higher P_{H2}. The values for the kinetic parameters are given in **Table 2.5**, where it can be seen that TOF_{max} for Pd/Al_2O_3 was an order of magnitude higher than that recorded for Au/Al_2O_3. The A^{-1} parameter, reflecting H_2/surface interaction leading to reaction, is also higher for Pd/Al_2O_3. This response is in line with the lower chemisorptive uptake of H_2 on Au/Al_2O_3 compared with Pd/Al_2O_3 (**Table 2.3**). The appreciably higher TOF_{max} delivered by Pd/Al_2O_3 and marked difference in product selectivity suggests critical differences in surface activation of *p*-CNB, which is examined in the following section.

Table 2.5: TOF_{max} and A^{-1} values obtained from fit (using Eq. (2.16)) to the dependence of *p*-CNB *TOF* on hydrogen partial pressure (see Figure 2.7).

	$TOF_{max} \times 10^2$ (s^{-1})	A^{-1} atm^{-1}
Au/Al_2O_3	4.4	100
Pd/Al_2O_3	41.4	166

2.4.5 Reaction Mechanism

From a consideration of product distribution under thermodynamic control, the following steps prevail: *p*-CNB→*p*-CAN→AN (and CB) →BZ→CHA (**Figure 2.1**). Au/Al_2O_3, as a less active catalyst, promotes the reaction according to the thermodynamically favoured route, which is terminated at *p*-CAN, irrespective of inlet H_2/*p*-CNB, temperature or conversion. The exclusive production of *p*-CAN suggests that *p*-CNB/surface interaction results in the preferential activation of the $–NO_2$ group. In the case of Pd/Al_2O_3, the predominance of *p*-CNB hydrodechlorination coupled with

hydrogenation to generate AN suggests surface interaction that activates both C-Cl for hydrogenolytic attack and $-NO_2$ for hydrogen addition. Indeed, Pd/Al_2O_3 is established as an effective hydrodechlorination catalyst with significant activity in the hydrodechlorination of chloroarenes even at sub-ambient temperatures [75]. The kinetic treatment presented in section 4.4 only considered *TOF* dependence on H_2 partial pressure but the dynamics of *p*-CNB (and *p*-CAN) interaction(s) with the surface (metal, support and metal/support interface) can have a major bearing on activity and selectivity. In order to probe these effects, selected reactions were conducted using physical mixtures of catalyst + Al_2O_3. As can be seen from entries in **Table 2.6**, the addition of Al_2O_3 to Au/Al_2O_3 served to increase *p*-CNB conversion while retaining exclusive *p*-CAN production. The contribution due to Al_2O_3 inclusion can result from: (i) increased reactive hydrogen resulting from spillover onto Al_2O_3; (ii) activation of *p*-CNB on Al_2O_3. Spillover involves the migration of atomic hydrogen to the support after H_2 dissociation on the metallic surface and has been reported for combinations of supported Pd [76] and Au [77] with oxide supports. Hydrogen desorption from Au/Al_2O_3 (**Table 2.6**) far exceeded that recorded for pulse chemisorption, suggesting the generation of surface hydrogen during TPR with possible spillover. The occurrence of spillover hydrogen is confirmed by the higher total H_2 released during TPD from $Au/Al_2O_3 + Al_2O_3$ (**Table 2.6**). Appreciably greater H_2 TPD was also recorded for $Pd/Al_2O_3 + Al_2O_3$ relative to Pd/Al_2O_3, which must contribute to the observed increase in *p*-CNB conversion.

Table 2.6: Catalytic performance for reaction over Au/Al_2O_3 ($n/F = 3 \times 10^{-3}$ h) and Pd/Al_2O_3 ($n/F = 3 \times 10^{-4}$ h) with and without the addition of Al_2O_3 as a physical mixture with associated H_2 released during TPD.

Catalyst (mass, g)	x_0	Product (*S* %)	H_2 released during TPD ($\mu mol_{H2}\ \mu mol_{metal}^{-1}$)
Au/Al_2O_3 (0.02)	0.22	*p*-CAN (100)	10.6
Au/Al_2O_3 (0.02) + Al_2O_3 (0.03)	0.29	*p*-CAN (100)	23.9
Pd/Al_2O_3 (0.001)	0.17	NB (84), AN (16)	11.2
Pd/Al_2O_3 (0.001) + Al_2O_3 (0.05)	0.25	NB (62), AN (9), *p*-CAN (29)	159

There is spectroscopic evidence in the literature [32,78,79] for nitro group interaction with alumina Lewis acid (Al^{3+}) sites. Shimizu *et al.* [32] have associated high selectivity in the hydrogenation of nitrostyrene over Au/Al_2O_3 with a preferential interaction of $–NO_2$ with the support. The *p*-CNB reactant can then be activated on Al_2O_3, where Au sites serve to provide reactive (chemisorbed and spillover) hydrogen. The electronegativities of the reactant functional groups decrease in the order $–NO_2$ > –Cl (> –H) > $–NH_2$ with a high electron density at the nitro function that favours interaction with surface Lewis acid sites [26]. Use of *p*-CAN as a reactant (at 423 K) did not result in any conversion over Au/Al_2O_3. It follows that *p*-CAN generated from *p*-CNB does not undergo further reaction to generate AN, resulting in exclusive $–NO_2$ reduction. The inclusion of Al_2O_3 with Pd/Al_2O_3 generated significant quantities of *p*-CAN in the product stream (**Table 2.6**). This suggests activation of $–NO_2$ by Al_2O_3 in the physical mixture and reaction with spillover hydrogen to give *p*-CAN. Interaction with $Pd^{\delta-}$ sites (based on XPS analysis, **Figure 2.5**) must lead to repulsion with respect to $–NO_2$ and –Cl, resulting in adsorption *via* the aromatic nucleus where both substituents can be attacked. The ring carbon bonded to Cl is more susceptible to hydrogenolytic attack as it bears the lowest electron density of all the carbons in the ring [26], leading to NB formation *via* path B (**Figure 2.1**). Moreover, tests established that Pd/Al_2O_3 was also active in promoting *p*-CAN → AN (TOF = 0.12 s^{-1} at 423 K), establishing viability of AN formation *via* path D.

2.5 Conclusions

Thermodynamic equilibrium analysis of *p*-CNB hydrogenation has demonstrated that all the possible hydrogenation and hydrogenolysis reactions are exothermal ($\Delta H_{423K} < 0$). Each step is thermodynamically favourable ($\Delta G_{423K} < 0$) with the exception of CHE production. Under thermodynamic control, reaction temperature (373-473 K) has a negligible effect on product distribution, which is sensitive to H_2/*p*-CNB in the stoichiometric range (1-8) where, at H_2/*p*-CNB ≥ 10, CHA is the preferred product. Reaction over both Au/Al_2O_3 and Pd/Al_2O_3 delivered a product composition far removed from thermodynamic equilibrium where Au/Al_2O_3 promoted sole formation of *p*-CAN at 373-473 K and each inlet H_2/*p*-CNB. Pd/Al_2O_3 generated NB and AN (combined

hydrodechlorination and hydrogenation) with increased selectivity to NB at lower H_2/*p*-CNB. A kinetic treatment has demonstrated a significantly higher maximum *TOF* (by an order of magnitude) for Pd/Al_2O_3 relative to Au/Al_2O_3 and a higher adsorption coefficient for hydrogen that leads to reaction, which is reflected in the chemisorption measurements. Both Au/Al_2O_3 and Pd/Al_2O_3 are characterised by supported metal particles at the nanoscale (1-6 nm Pd, mean = 2.4 nm and 1-13 nm Au, mean = 4.5 nm) with evidence (from XPS analysis) of electron transfer from Al_2O_3 to Pd to generate $Pd^{\delta-}$, an effect that was not a feature of Au/Al_2O_3. The sole production of *p*-CAN over Au/Al_2O_3 is attributed to selective activation of $-NO_2$ at Al_2O_3 Lewis acid sites and reaction with chemisorbed and spillover hydrogen. We account for the formation of AN and NB over Pd/Al_2O_3 in terms of repulsion between $-NO_2$ and –Cl and surface $Pd^{\delta-}$ leading to adsorption *via* the benzene ring, which facilitates hydrogen attack of both substituents.

2.6 References

[2.1] G. Centi, S. Perathoner, *Catalysis, a driver for sustainability and societal challenges*, Catal. Today, **138**, 69-76 (2008)

[2.2] M. Haruta, T. Kobayashi, H. Sano, N. Yamada, *Novel gold catalysts for the oxidation of carbon monoxide at a temperature far below 0 ^oC*, Chem. Lett., 405-408 (1987)

[2.3] M. Haruta, S. Tsubota, T. Kobayashi, H. Kageyama, M.J. Genet, B. Delmon, *Low-temperature oxidation of CO over gold supported on TiO_2, α-Fe_2O_3, and Co_3O_4*, J. Catal., **144**, 175-192 (1993)

[2.4] B. Nkosi, N.J. Coville, G.J. Hutchings, *Reactivation of a supported gold catalyst for acetylene hydrochlorination*, Chem. Commun., 71-72 (1988)

[2.5] A.A. Herzing, C.J. Kiely, A.F. Carley, P. Landon, G.J. Hutchings, *Identification of active gold nanoclusters on iron oxide supports for CO oxidation*, Science, **321**, 1331-1335 (2008)

[2.6] L.Q. Nguyen, C. Salim, H. Hinode, *Performance of nano-sized Au/TiO_2 for selective catalytic reduction of NO_x by propene*, Appl. Catal. A: Gen., **347**, 94-99 (2008)

[2.7] W. Deng, A.I. Frenkel, R. Si, M. Flytzani-Stephanopoulos, *Reaction-relevant gold*

structures in the low temperature water-gas shift reaction on Au-CeO_2, J. Phys. Chem. C, **112**, 12834-12840 (2008)

[2.8] G.C. Bond, D.T. Thompson, Catalysis by gold, Catal. Rev. Sci. Eng. **41**, 319-388, (1999)

[2.9] F. Cárdenas-Lizana, S. Gómez-Quero, M.A. Keane, *Ultra-selective gas phase catalytic hydrogenation of aromatic nitro compounds over Au/Al_2O_3*, Catal. Commun., **9**, 475-481 (2008)

[2.10] F. Cárdenas-Lizana, S. Gómez-Quero, A. Hugon, L. Delannoy, C. Louis, M.A. Keane, *Pd-promoted selective gas phase hydrogenation of p-chloronitrobenzene over alumina supported Au*, J. Catal., **262**, 235-243 (2009)

[2.11] F. Cárdenas-Lizana, S. Gómez-Quero, H. Idriss, M.A. Keane, *Gold particle size effects in the gas-phase hydrogenation of m-dinitrobenzene over Au/TiO_2*, J. Catal., **268**, 223-234 (2009)

[2.12] F. Cárdenas-Lizana, S. Gómez-Quero, M.A. Keane, *Exclusive production of chloroaniline from chloronitrobenzene over Au/TiO_2 and Au/Al_2O_3*, ChemSusChem, **1**, 215-221 (2008)

[2.13] F. Cárdenas-Lizana, S. Gómez-Quero, N. Perret, M. Keane, *Support effects in the selective gas phase hydrogenation of p-chloronitrobenzene over gold*, Gold Bull., **42**, 124-132 (2009)

[2.14] G.C. Bond, *Gold: a relatively new catalyst*, Catal. Today, **72**, 5-9 (2002)

[2.15] N. Iwasa, T. Mayanagi, W. Nomura, M. Arai, N. Takezawa, *Effect of Zn addition to supported Pd catalysts in the steam reforming of methanol*, Appl. Catal. A: Gen., **248**, 153-160 (2003)

[2.16] N. Iwasa, S. Kudo, H. Takahashi, S. Masuda, N. Takezawa, *Highly selective supported Pd catalysts for steam reforming of methanol*, Catal. Lett., **19**, 211-216 (1993)

[2.17] R. Wang, S. Liao, S. Ji, *High performance Pd-based catalysts for oxidation of formic acid*, J. Power Sources, **180**, 205-208 (2008)

[2.18] S. Huang, C. Zhang, H. He, *Complete oxidation of o-xylene over Pd/Al_2O_3 catalyst at low temperature*, Catal. Today, **139**, 15-23 (2008)

[2.19] P. Castellazzi, G. Groppi, P. Forzatti, A. Baylet, P. Marécot, D. Duprez, *Role of Pd*

loading and dispersion on redox behaviour and CH_4 combustion activity of Al_2O_3 supported catalysts, Catal. Today, **155**, 18-26 (2010)

[2.20] K. Sekizawa, M. Machida, K. Eguchi, H. Arai, *Catalytic properties of Pd-supported hexaaluminate catalysts for high-temperature catalytic combustion*, J. Catal., **142**, 655-663 (1993)

[2.21] G. Yuan, M.A. Keane, *Liquid phase hydrodechlorination of chlorophenols over Pd/C and Pd/Al_2O_3: a consideration of HCl/catalyst interactions and solution pH effects*, Appl. Catal. B: Environ., **52**, 301-314 (2004)

[2.22] S. Jujjuri, M.A. Keane, *Catalytic hydrodechlorination at low hydrogen partial pressures: Activity and selectivity response*, Chem. Eng. J., **157**, 121-130 (2010)

[2.23] J.F. Sánchez M, O.J. González Bello, M. Montes, G.M. Tonetto, D.E. Damiani, *Pd/Al_2O_3-cordierite and Pd/Al_2O_3-Fecralloy monolithic catalysts for the hydrogenation of sunflower oil*, Catal. Commun., **10**, 1446-1449 (2009)

[2.24] L. Rodríguez, D. Romero, D. Rodríguez, J. Sánchez, F. Domínguez, G. Arteaga, *Dehydrogenation of n-butane over $Pd-Ga/Al_2O_3$ catalysts*, Appl. Catal. A: Gen., **373**, 66-70 (2010)

[2.25] R.B. Borade, B. Zhang, A. Clearfield, *Selective dehydrogenation of cyclohexene to benzene using Pd-exchanged α-zirconium phosphate*, Catal. Lett., **45**, 233-235 (1997)

[2.26] B. Zhao, Y.-W. Chen, *Hydrogenation of p-chloronitrobenzene on Mo, La, Fe, and W-modified NiCoB nanoalloy catalysts*, J. Non-Cryst. Solids., **356**, 839-847 (2010)

[2.27] X. Meng, H. Cheng, S.-i. Fujita, Y. Yu, F. Zhao, M. Arai, *An effective medium of H_2O and low-pressure CO_2 for the selective hydrogenation of aromatic nitro compounds to anilines*, Green Chem., **13**, 570-572 (2011)

[2.28] G. Zhang, L. Wang, K. Shen, D. Zhao, H.S. Freeman, *Hydrogenation of o-chloronitrobenzene on a Pd/C catalyst doped with metal oxide nanoparticles*, Chem. Eng. J., **141**, 368-374 (2008)

[2.29] D. He, X. Jiao, P. Jiang, J. Wang, B.-Q. Xu, *An exceptionally active and selective $Pt-Au/TiO_2$ catalyst for hydrogenation of the nitro group in chloronitrobenzene*, Green Chem., **14**, 111-116 (2012)

[2.30] F. Cárdenas-Lizana, S. Gómez-Quero, N. Perret, L. Kiwi-Minsker, M.A. Keane, *β-Molybdenum nitride: synthesis mechanism and catalytic response in the gas phase hydrogenation of p-chloronitrobenzene*, Catal. Sci. Tech., **1**, 794-801 (2011)

[2.31] B. Zuo, Y. Wang, Q. Wang, J. Zhang, N. Wu, L. Peng, L. Gui, X. Wang, R. Wang, D. Yu, *An efficient ruthenium catalyst for selective hydrogenation of ortho-chloronitrobenzene prepared via assembling ruthenium and tin oxide nanoparticles*, J. Catal., **222**, 493-498 (2004)

[2.32] K.-i. Shimizu, Y. Miyamoto, T. Kawasaki, T. Tanji, Y. Tai, A. Satsuma, *Chemoselective hydrogenation of nitroaromatics by supported gold catalysts: mechanistic reasons of size- and support-dependent activity and selectivity*, J. Phys. Chem. C, **113**, 17803-17810 (2009)

[2.33] G. Konnecker, A. Boehncke, S. Schmidt, *Ecotoxicological assessment of p-chloroaniline-Fate and effects in aquatic systems*, Fresen. Environ. Bull., **12**, 589-593 (2003)

[2.34] X. Wang, S. Li, H. Wang, B. Liu, X. Ma, *Thermodynamic analysis of glycerin steam reforming*, Energy Fuels, **22**, 4285-4291 (2008)

[2.35] X. Wang, M. Li, M. Wang, H. Wang, S. Li, S. Wang, X. Ma, *Thermodynamic analysis of glycerol dry reforming for hydrogen and synthesis gas production*, Fuel, **88**, 2148-2153 (2009)

[2.36] H. Wang, X. Wang, M. Li, S. Li, S. Wang, X. Ma, *Thermodynamic analysis of hydrogen production from glycerol autothermal reforming*, Int. J. Hydrogen Energy, **34**, 5683-5690 (2009)

[2.37] M. Hazewinkel, Encyclopaedia of mathematics, Springer-Verlag, Berlin, 2002

[2.38] M.A. Keane, *Gas phase hydrogenation/hydrogenolysis of benzaldehyde and o-tolualdehyde over Ni/SiO_2*, J. Mol. Catal. A: Chem., **118**, 261-269 (1997)

[2.39] G. Tavoularis, M.A. Keane, *The gas phase hydrodechlorination of chlorobenzene over nickel/silica*, J. Chem. Technol. Biot., **74**, 60-70 (1999)

[2.40] G. Yuan, M.A. Keane, *Aqueous-phase hydrodechlorination of 2,4-dichlorophenol over Pd/Al_2O_3: Reaction under controlled pH*, Ind. Eng. Chem. Res., **46**, 705-715 (2007)

[2.41] F. Cárdenas-Lizana, S. Gómez-Quero, M.A. Keane, *Clean production of chloroanilines by selective gas phase hydrogenation over supported Ni catalysts*, Appl. Catal. A: Gen., **334**, 199-206 (2008)

[2.42] B. Coq, A. Tijani, R. Dutartre, F. Figuéras, *Influence of support and metallic precursor on the hydrogenation of p-chloronitrobenzene over supported platinum catalysts*, J. Mol. Catal., **79**, 253-264 (1993)

[2.43] Z. Yu, S. Liao, Y. Xu, B. Yang, D. Yu, *Hydrogenation of nitroaromatics by polymer-anchored bimetallic palladium-ruthenium and palladium-platinum catalysts under mild conditions*, J. Mol. Catal. A: Chem., **120**, 247-255 (1997)

[2.44] R. Baltzly, A.P. Phillips, *The catalytic hydrogenolysis of halogen compounds*, J. Am. Chem. Soc., **68**, 261-265 (1946)

[2.45] M. Trueba, S.P. Trasatti, *γ-Alumina as a support for catalysts: A review of fundamental aspects*, Eur. J. Inorg. Chem., **2005**, 3393-3403 (2005)

[2.46] S.J. Gregg, K.S.W. Sing, Adsorption, surface area and porosity, 2nd ed, Academic Press, London, 1982,

[2.47] Z. Zhang, T.J. Pinnavaia, *Mesostructured γ-Al_2O_3 with a lathlike framework morphology*, J. Am. Chem. Soc., **124**, 12294-12301 (2002)

[2.48] B.J. Melde, B.T. Holland, C.F. Blanford, A. Stein, *Mesoporous sieves with unified hybrid inorganic/organic frameworks*, Chem. Mater., **11**, 3302-3308 (1999)

[2.49] M.R. Buchmeiser, Polymeric materials in organic synthesis and catalysis, Wiley-VCH, Weinheim, 2003

[2.50] A. Gluhoi, X. Tang, P. Marginean, B. Nieuwenhuys, *Characterization and catalytic activity of unpromoted and alkali (earth)-promoted Au/Al_2O_3 catalysts for low-temperature CO oxidation*, Top. Catal., **39**, 101-110 (2006)

[2.51] C.K. Costello, J. Guzman, J.H. Yang, Y.M. Wang, M.C. Kung, B.C. Gates, H.H. Kung, *Activation of Au/γ-Al_2O_3 catalysts for CO oxidation: characterization by X-ray absorption near edge structure and temperature programmed reduction*, J. Phys. Chem. B, **108**, 12529-12536 (2004)

[2.52] S. Gómez-Quero, F. Cárdenas-Lizana, M.A. Keane, *Effect of metal dispersion on the liquid-phase hydrodechlorination of 2,4-dichlorophenol over Pd/Al_2O_3*, Ind. Eng. Chem. Res., **47**, 6841-6853 (2008)

[2.53] N.S. Babu, N. Lingaiah, R. Gopinath, P.S. Sankar Reddy, P.S. Sai Prasad, *Characterization and reactivity of alumina-supported Pd catalysts for the room-temperature hydrodechlorination of chlorobenzene*, J. Phys. Chem. C, **111**, 6447-6453 (2007)

[2.54] R. Gopinath, N. Seshu Babu, J. Vinod Kumar, N. Lingaiah, P. Sai Prasad, *Influence of Pd precursor and method of preparation on hydrodechlorination activity of alumina supported palladium catalysts*, Catal. Lett., **120**, 312-319 (2008)

[2.55] N.K. Nag, *A study on the formation of palladium hydride in a carbon-supported palladium catalyst*, J. Phys. Chem. B, **105**, 5945-5949 (2001)

[2.56] G. Fagherazzi, A. Benedetti, S. Polizzi, A. Mario, F. Pinna, M. Signoretto, N. Pernicone, *Structural investigation on the stoichiometry of β-PdH_x in Pd/SiO_2 catalysts as a function of metal dispersion*, Catal. Lett., **32**, 293-303 (1995)

[2.57] C.M. Mendez, H. Olivero, D.E. Damiani, M.A. Volpe, *On the role of Pd β-hydride in the reduction of nitrate over Pd based catalyst*, Appl. Catal. B: Environ., **84**, 156-161 (2008)

[2.58] D.H. Kim, Y.-H. Chin, G.G. Muntean, A. Yezeretz, N.W. Currier, W.S. Epling, H.-Y. Chen, H. Hess, C.H.F. Peden, *Relationship of Pt particle size to the NO_x storage performance of thermally aged $Pt/BaO/Al_2O_3$ lean NO_x trap catalysts*, Ind. Eng. Chem. Res., **45**, 8815-8821 (2006)

[2.59] S. Nikolaev, V. Smirnov, *Selective hydrogenation of phenylacetylene on gold nanoparticles*, Gold Bull., **42**, 182-189 (2009)

[2.60] F.-M. McKenna, R.P.K. Wells, J.A. Anderson, *Enhanced selectivity in acetylene hydrogenation by ligand modified Pd/TiO_2 catalysts*, Chem. Commun., **47**, 2351-2353 (2011)

[2.61] K. Sun, J. Liu, N. Nag, N.D. Browning, *Studying the metal-support interaction in Pd/γ-Al_2O_3 Catalysts by atomic-resolution electron energy-loss spectroscopy*, Catal. Lett., **84**, 193-199 (2002)

[2.62] M. Baron, O. Bondarchuk, D. Stacchiola, S. Shaikhutdinov, H.J. Freund, *Interaction of gold with cerium oxide supports: CeO_2(111) thin films vs CeO_x nanoparticles*, J. Phys. Chem. C, **113**, 6042-6049 (2009)

[2.63] G.C. Bond, *Chemisorption and reactions of small molecules on small gold*

particles, Molecules, **17**, 1716-1743 (2012)

[2.64] P. Claus, *Heterogeneously catalysed hydrogenation using gold catalysts*, Appl. Catal. A: Gen., **291**, 222-229 (2005)

[2.65] E. Bus, J.T. Miller, J.A. van Bokhoven, *Hydrogen chemisorption on Al_2O_3-supported gold catalysts*, J. Phys. Chem. B, **109**, 14581-14587 (2005)

[2.66] C. Kartusch, J.A. van Bokhoven, *Hydrogenation over gold catalysts: The interaction of gold with hydrogen*, Gold Bull., **42**, 343-348 (2009)

[2.67] E. Bus, J.A. van Bokhoven, *Hydrogen chemisorption on supported platinum, gold, and platinum-gold-alloy catalysts*, Phys. Chem. Chem. Phys., **9**, 2894-2902 (2007)

[2.68] C.-M. Lu, I. Wang, S.-C. Chou, C.-T. Yeh, *Hydrogenation of benzene over rhodium-copper alloy crystallites supported on alumina*, Chinyi Journal, **19**, 119-131 (2001)

[2.69] K.V. Murthy, P.M. Patterson, M.A. Keane, *C-X bond reactivity in the catalytic hydrodehalogenation of haloarenes over unsupported and silica supported Ni*, J. Mol. Catal. A: Chem., **225**, 149-160 (2005)

[2.70] S. Jujjuri, E. Ding, E.L. Hommel, S.G. Shore, M.A. Keane, *Synthesis and characterization of novel silica-supported Pd/Yb bimetallic catalysts: Application in gas-phase hydrodechlorination and hydrogenation*, J. Catal., **239**, 486-500 (2006)

[2.71] Y. Zhang, X. Cui, F. Shi, Y. Deng, *Nano-gold catalysis in fine chemical synthesis*, Chem. Rev., **112**, 2467-2505 (2012)

[2.72] F. Cárdenas-Lizana, S. Gómez-Quero, M. Keane, *Gas phase hydrogenation of m-dinitrobenzene over alumina supported Au and Au–Ni alloy*, Catal. Lett., **127**, 25-32 (2009)

[2.73] F. Cárdenas-Lizana, S. Gómez-Quero, C.J. Baddeley, M.A. Keane, *Tunable gas phase hydrogenation of m-dinitrobenzene over alumina supported Au and Au-Ni*, Appl. Catal. A: Gen., **387**, 155-165 (2010)

[2.74] F. Cárdenas-Lizana, S. Gómez-Quero, N. Perret, M.A. Keane, *Gold catalysis at the gas-solid interface: role of the support in determining activity and selectivity in the hydrogenation of m-dinitrobenzene*, Catal. Sci. Tech., **1**, 652-661 (2011)

[2.75] G. Yuan, M.A. Keane, *Liquid phase catalytic hydrodechlorination of chlorophenols at 273 K*, Catal. Commun., **4**, 195-201 (2003)

[2.76] C. Amorim, X. Wang, M.A. Keane, *Application of hydrodechlorination in environmental pollution control: Comparison of the performance of supported and unsupported Pd and Ni catalysts*, Chin. J. Catal., **32**, 746-755 (2011)

[2.77] C.D. M. Lazar, V. Almasan, N. Aldea, B. Barz, P. Marginean, C. Sutan, V. Malinovschi., *Nanostructured gold supported catalysts: Relation between structure and hydrogen catalytic activity*, Rom. Journ. Phys., **51**, 299-304 (2006)

[2.78] M. Boronat, P. Concepción, A. Corma, S. González, F. Illas, P. Serna, *A molecular mechanism for the chemoselective hydrogenation of substituted nitroaromatics with nanoparticles of gold on TiO_2 catalysts: a cooperative effect between gold and the support*, J. Am. Chem. Soc., **129**, 16230-16237 (2007)

[2.79] M. Pietrowski, M. Wojciechowska, *The origin of increased chemoselectivity of platinum supported on magnesium fluoride in the hydrogenation of chloronitrobenzene*, Catal. Today, **169**, 217-222 (2011)

CHAPTER 3

Reducible Support Effects in the Gas Phase Hydrogenation of *p*-Chloronitrobenzene over Gold

In this chapter, the contribution of reducible $Ce_{0.62}Zr_{0.38}O_2$ as a gold carrier has been investigated in the gas phase hydrogenation of *p*-chloronitrobenzene, where Au on non-reducible Al_2O_3 serves as comparison. The oxygen vacancies over $Au/Ce_{0.62}Zr_{0.38}O_2$ formed during activation play a critical role in determining product selectivity. This chapter has been published in Journal of Physical Chemistry C (see publication No. 6). Co-author N.P. participated in the discussion and co-wrote the chapter. J.J.D. conducted the STEM analysis, G.B. performed the XPS measurements, X.C. carried out the FTIR study and C.M.O. worked on the OSC experiments. S.B. and M.A.K. directed the project and co-wrote the chapter.

3.1 Introduction

Following the landmark work of Haruta [1,2] and Hutchings [3] establishing a catalytic response for nanoscale Au, the development of Au catalysts is attracting appreciable research. While bulk Au exhibits negligible catalytic properties [4], Au dispersed on metal oxide supports has been used to promote a range of processes of commercial and environmental remediation importance [5], notably CO oxidation [6], NO_x treatment [7] and the water gas shift (WGS) reaction [8]. The use of Au in hydrogenation reactions has been studied to a lesser extent [9] and the available literature has been compiled and assessed in reviews by Claus [10], Hashmi [11] and McEwan *et al.* [12] Work to date has largely focused on the conversion of carbon oxides, alkenes, alkynes and α,β-unsaturated aldehydes and ketones [10,13]. Catalyst performance has shown a dependence on synthesis [14], Au particle size/shape [15] and support characteristics [16]. Taking the latter, a range of catalytic responses has been observed for Au on different oxides [10,17-20]. The support can affect Au morphology and dispersion

via surface interactions [21,22] where smaller (≤ 10 nm) Au particles exhibit electronic properties distinct from bulk Au [23]. Moreover, the incorporation of Au is known to influence support reducibility, notably in the case of ceria (CeO_2) [24].

Zirconia (ZrO_2) is widely used as a heterogeneous catalyst support due to its adjustable (*via* variation in synthesis, precursor and use of dopants) structural and chemical characteristics [25]. Gold supported on ZrO_2 has been applied in low temperature WGS [26], CO oxidation [27] and the selective hydrogenation of 1,3-butadiene, acrolein and crotonaldehyde [28,29]. Of particular relevance to this study, He *et al.* achieved high selectivities in the liquid phase hydrogenation of *p*- and *o*-chloronitrobenzene and 2,5-dichloronitrobenzene over Au/ZrO_2, limiting the degree of C–Cl bond scission [30]. Ceria supported Au has been the subject of a significant corpus of published work [31-34], with again a particular focus on CO oxidation [31,33] and WGS [32,34]. Incorporation of Zr^{4+} into the CeO_2 lattice increases the oxygen storage capacity (OSC) of the solid solution and improves textural properties (resistance to sintering) [35,36]. The coordination number of the smaller Zr ion is lowered in the mixed oxide, increasing oxygen mobility, which can contribute to the creation of oxygen vacancies.[37] These vacancies serve to promote CO oxidation [38], WGS [34] and hydrogenation reactions [39]. In previous work [40-43], we established reaction exclusivity in the gas phase hydrogenation of *p*-chloronitrobenzene (*p*-CNB) to *p*-chloroaniline (*p*-CAN) over oxide (Al_2O_3, TiO_2, Fe_2O_3 and CeO_2) supported Au. A range of metals (*e.g.* Pd [44], Pt [45], Ir [46], Ni [47] and Co [48]) are active in the hydrogenation of functionalised nitroaromatics with varying degrees of selectivity to the target amine. We could find no published study that has considered the use of Au/ceria-zirconia systems in nitroarene hydrogenation. Taking *p*-CNB as a model reactant, we establish in this report distinct catalytic performance for reaction over Au on reducible ($Ce_{0.62}Zr_{0.38}O_2$) and non-reducible (Al_2O_3) supports that we correlate with critical surface properties.

3.2 Methods

3.2.1 Catalyst Preparation

A 2.6% w/w $Au/Ce_{0.62}Zr_{0.38}O_2$ (Au/CZ) was prepared by deposition-precipitation, applying the procedure described by Zanella *et al.* [49] An aqueous solution of $HAuCl_4$ (Alfa Aesar) served as precursor and the mixed oxide (CZ) support was obtained from Grace Davison. A known mass (50 g) of CZ was suspended in 3 dm^3 (5×10^{-3} mol dm^{-3}) $HAuCl_4$ at room temperature, urea (0.42 mol dm^{-3}) was added, the suspension heated to 353 K and kept under vigorous stirring for 20 h in the complete absence of light. When the pH stabilised at 8.0-8.5, the suspension was aged for 5 h at room temperature under stirring and then filtered. The resulting solid was washed several times with distilled water at room temperature until there was no evidence of chloride ions. The solid was dried overnight at 373 K, sieved to 75 μm mean particle diameter and stored in the dark under Ar. Au/CZ was subjected to an oxidising treatment that was adopted as a standard in this work. The sample as prepared was heated in a flow of 5% v/v O_2/He to 523 K, which was maintained for 1 h with a further contact (1 h) in flowing He and subsequent cooling to 298 K in He. For comparison purposes, the catalytic performance of a 1% w/w Au/Al_2O_3 also prepared by deposition-precipitation [44] was examined. The Au content was measured by inductively coupled plasma-optical emission spectrometry (ICP-OES, Vista-PRO, Varian Inc.) from the diluted extract of aqua regia.

3.2.2 Catalyst Characterisation

The textural, structural and chemical properties of Au/CZ and Au/Al_2O_3 were characterised using a battery of techniques. BET surface areas (63 $m^2\,g^{-1}$ for Au/CZ and 184 $m^2\,g^{-1}$ for Au/Al_2O_3) were determined by volumetric adsorption of N_2 at 77 K. Gold particle size distribution was measured by High Angle Annular Dark Field-Scanning Transmission Electron Microscopy (HAADF-STEM) in combination with X-Ray Energy Dispersive Spectroscopy (X-EDS, Oxford Instrument). Images were recorded on a JEOL2010-F microscope with 0.19 nm spatial resolution at Scherzer defocus conditions. HAADF-STEM images were obtained using an electron probe (0.5 nm diameter) at a diffraction camera length of 12 cm. This imaging mode provides contrast that is directly related to average atomic number (Z) in the region under the electron beam. We have previously demonstrated [50] the applicability of HAADF-STEM to characterise Au nano-particles on CZ. Gold particle size distributions were based on a count of at least

500 particles for each sample. Gold dispersion was determined using a set of truncated cube-octahedron shaped particles where size was increased by discrete steps to cover the range found in the experimental distributions.

The redox characteristics of Au/CZ were evaluated by OSC measurements [51]. Post oxidation at 523 K, Au/CZ was reduced for 1 h in flowing 5% v/v H_2/Ar or pure H_2 at a series of successive isothermal steps over the temperature range 393-973 K. The OSC values were determined from the weight loss recorded at each of the isothermal steps. Temperature programmed reduction (TPR) of Au/Al_2O_3 and temperature programmed desorption (TPD) from Au/Al_2O_3, Au/Al_2O_3+Al_2O_3, Au/CZ and Au/CZ+CZ were recorded using the commercial CHEMBET 3000 (Quantachrome) unit with data acquisition using the TPR Win^{TM} software. Fourier Transform Infrared (FTIR) spectroscopy studies were performed on a Bruker (Vertex 70) spectrometer using a DTGS detector, taking an average of 100 scans. Transmission FTIR spectra of adsorbed CO (at P_{CO} = 40 Torr and 298 K) were recorded using a quartz cell (with CaF_2 windows) attached to a metallic high vacuum manifold equipped with a turbo molecular pump (residual pressure < 10^{-6} Torr). The cell facilitated *in situ* oxidation/reduction of self-supported sample disks under controlled thermo-chemical conditions. X-ray photoelectron spectroscopy (XPS) studies were performed on a Kratos Axis Ultra DLD apparatus equipped with a catalytic cell, allowing transfer of pretreated samples into the analytical chamber under anaerobic conditions. Spectra were recorded using monochromatised AlK_α radiation (1486.6 eV) at an x-ray source power = 150 W. Surface charging effects were compensated for using the Kratos coaxial neutralisation system. A 20 eV pass energy was used to collect the spectra where the energy resolution corresponded to a FWHM of 1.1 eV for the Au $4f_{7/2}$ peak. After charge compensation, the binding energy scale was calibrated with respect to Zr $3d_{5/2}$ at 182.6 eV for Au/CZ and Al $2p_{3/2}$ at 74.6 eV for Au/Al_2O_3.

3.2.3 Catalyst Testing

Prior to catalysis, Au/CZ was subjected to the oxidising pre-treatment described above and then reduced (at 5 K min^{-1}) in a flow (60 cm^3 min^{-1}) of H_2 or 5% v/v H_2/He at 393-673 K for 1 h. The Au/Al_2O_3 sample was activated (at 2 K min^{-1}) directly in 60 cm^3

min^{-1} H_2 or 5% v/v H_2/He at 473-673 K. Reactions were carried out at atmospheric pressure and T = 393 K, *in situ* immediately after activation, in a fixed bed vertical glass reactor (l = 600 mm; i.d. = 15 mm). The catalytic reactor and operating conditions to ensure negligible heat/mass transport limitations have been fully described elsewhere [52] but features pertinent to this study are given below. A layer of borosilicate glass beads served as preheating zone, ensuring that the *p*-CNB (or *p*-CAN) reactant was vaporised and reached reaction temperature before contacting the catalyst. Isothermal conditions (± 1 K) were ensured by diluting the catalyst bed with ground glass (75 μm); the ground glass was mixed thoroughly with catalyst before insertion into the reactor. Reaction temperature was continuously monitored by a thermocouple inserted in a thermowell within the catalyst bed. The organic reactant was delivered to the reactor *via* a glass/teflon air-tight syringe and teflon line using a microprocessor controlled infusion pump (Model 100 kd Scientific) at a fixed calibrated flow rate. A co-current flow of *p*-CNB (or *p*-CAN) and H_2 (or 5% v/v H_2/He) was maintained at $GHSV = 2 \times 10^4$ h^{-1} with an inlet $-NO_2$ (or $-NH_2$) molar flow (F) of 9×10^{-2}–13×10^{-2} mmol h^{-1}, where the H_2 content was from 20 (5% v/v H_2/He) to 400 times (100% H_2) in excess of the stoichiometric requirement; the molar Au (n) to F ratio spanned the range 4.2×10^{-3}–7.5×10^{-2} h. A physical mixture of catalyst and support (1:1.5 on a mass basis) was also examined where the total bed volume was kept constant. The activation and reaction conditions that were considered in this study are given in **Table 3.1**. Catalyst regeneration after reaction was conducted *in situ* by repeating the reduction step. The reactor effluent was frozen in a liquid nitrogen trap for subsequent analysis, which was made using a Perkin-Elmer Auto System XL gas chromatograph equipped with a programmed split/splitless injector and a flame ionisation detector, employing a DB-1 (50 m × 0.20 mm i.d. 0.33 μm film thickness) capillary column (J&W Scientific). *p*-CNB (Aldrich,≥ 99% w/w purity) , *p*-CAN (Aldrich,≥ 98%) and the *1*-butanol solvent (Riedel-de Häen,≥ 99.5%) were used without further purification. Repeated reactions with samples from the same batch of catalyst delivered activity and selectivity values that were reproducible to better than ± 5%. All the samples for off-line analysis were passivated in 1% v/v O_2/He at room temperature for 1 h.

Table 3.1: Activation (393-673 K) and reaction (393 K) conditions in terms of H_2 content in the inlet gas stream.

Activation H_2 content (% v/v)	Reaction H_2 content (% v/v)	Notation
100	100	100-100
100	5	100-5
5	5	5-5

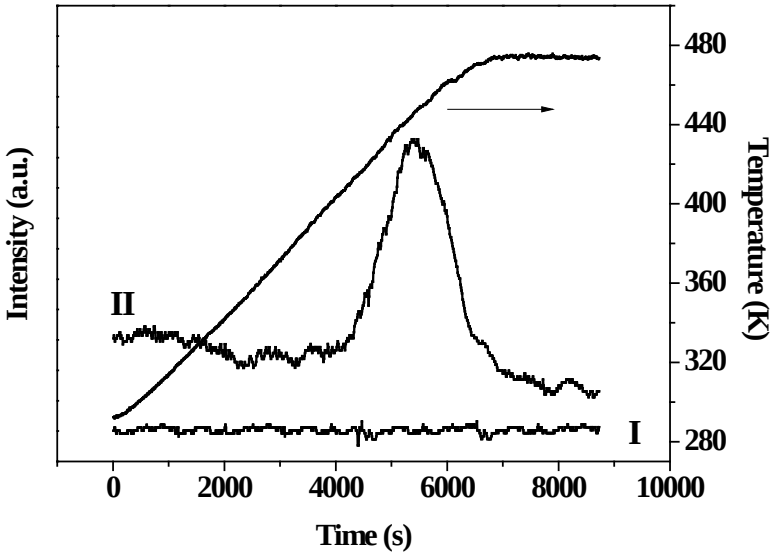

Figure 3.1: TPR profiles generated for (I) Al_2O_3 and (II) Au/Al_2O_3.

3.3 Results and discussion

3.3.1 Au/Al_2O_3: Characteristics

Gold supported on Al_2O_3 as a non-reducible carrier was adopted as a model (or reference) catalyst in this study. The temperature programmed reduction (TPR) response for the Al_2O_3 support (**Figure 3.1(I)**) is featureless with no evidence of H_2 uptake or release, which is consistent with the literature [53]. The TPR profile for the Au/Al_2O_3 precursor is presented in **Figure 3.1(II)** and shows a single peak at 448 K. Hydrogen consumption during TPR matched that required for the reduction of the precursor, *i.e.* $Au^{3+} \rightarrow Au^0$. An equivalent response in terms of Au reduction has been reported previously, with a single reduction peak at 436 K [54] and 503 K [55]. The activation of

Au/Al_2O_3 by TPR to 473 K in 5% v/v H_2 is then sufficient to fully reduce the supported Au precursor to the zero valent state. This was confirmed by XPS analysis and the associated spectrum over the Au 4*f* binding energy (BE) region is shown in **Figure 3.2(A)** with the Au $4f_{7/2}$ BE given in **Table 3.2**. The recorded BE (84.1 eV) is close to that reported for metallic gold (84.0 eV) [56]. We should note the work of Flytzani-Stephanopoulos *et al.* where the occurrence of cationic Au was proposed under reducing conditions with associated activity in the water gas shift reaction [34,57].

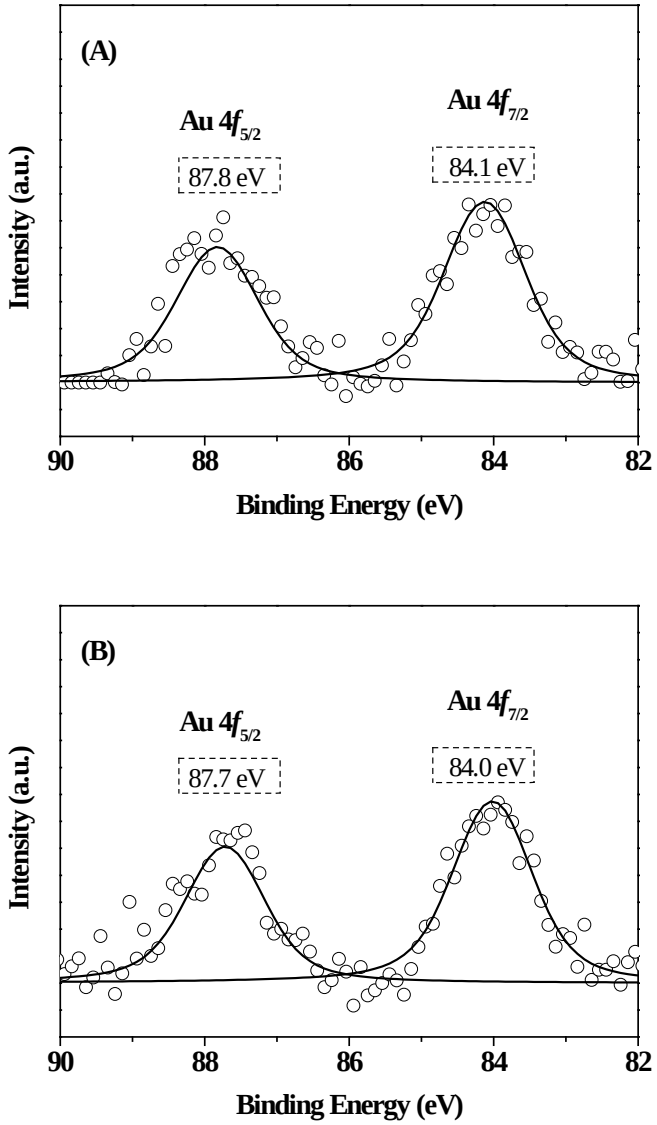

Figure 3.2: XPS spectra over the Au 4*f* region for Au/Al_2O_3 reduced at (A) 473 K and (B) 673 K. Note: the XPS experimental data are represented by symbols (○) while the lines are the result of spectral curve fitting.

Table 3.2: XPS binding energies (BE) associated with the Au $4f_{7/2}$ signal, peak intensity ratios (Au/Al and Au/Zr), Au dispersion (*D*) and mean particle size (*d*) for Au/Al_2O_3 and Au/CZ activated under different conditions.

Sample (activation temperature)	BE Au $4f_{7/2}$ (eV)	Intensity ratio Au/Al	Intensity ratio Au/Zr	Au Dispersion D^a (%)	*d* (nm)
Au/Al_2O_3 (473 K)[b]	84.1	5.0×10^{-3}	-	18.2	5.7
Au/Al_2O_3 (673 K)[b]	84.0	3.6×10^{-3}	-	12.5	8.8
Au/CZ (pre-TPR)	84.5	-	88×10^{-3}	53.0	1.8
Au/CZ (393 K)[b]	84.3	-	89×10^{-3}	52.0	1.8
Au/CZ (393 K)[c]	84.2	-	65×10^{-3}	52.0	1.8
Au/CZ (473 K)[b]	84.3	-	78×10^{-3}	48.0	1.9
Au/CZ (673 K)[b]	84.3	-	55×10^{-3}	48.0	1.9

[a]dispersion, $D = 100\ Au_s/Au$ (Au_s = surface Au atoms; Au = total Au atoms)
[b]activated in 5% v/v H_2
[c]activated in 100% v/v H_2

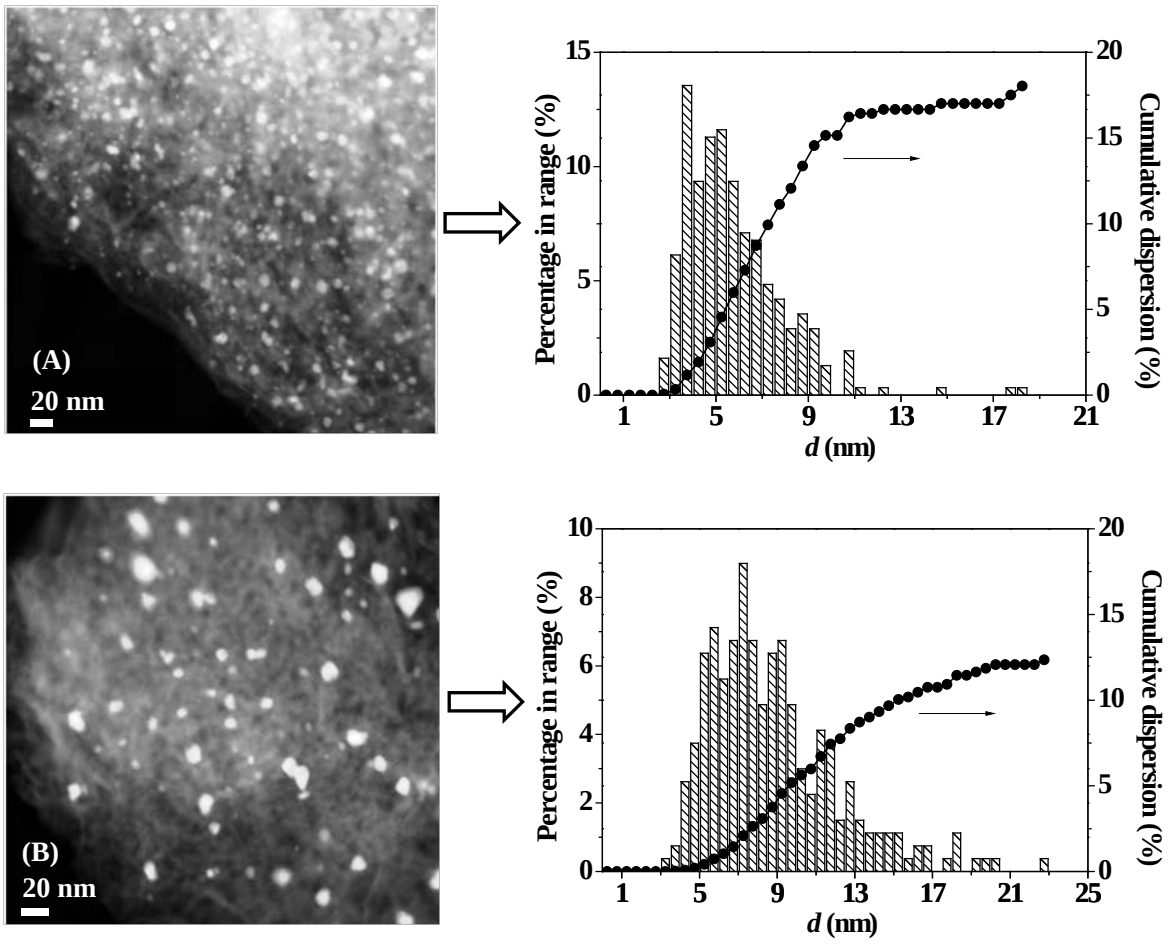

Figure 3.3: Representative HAADF-STEM images and Au particle size distribution for Au/Al_2O_3 activated at (A) 473 K and (B) 673 K.

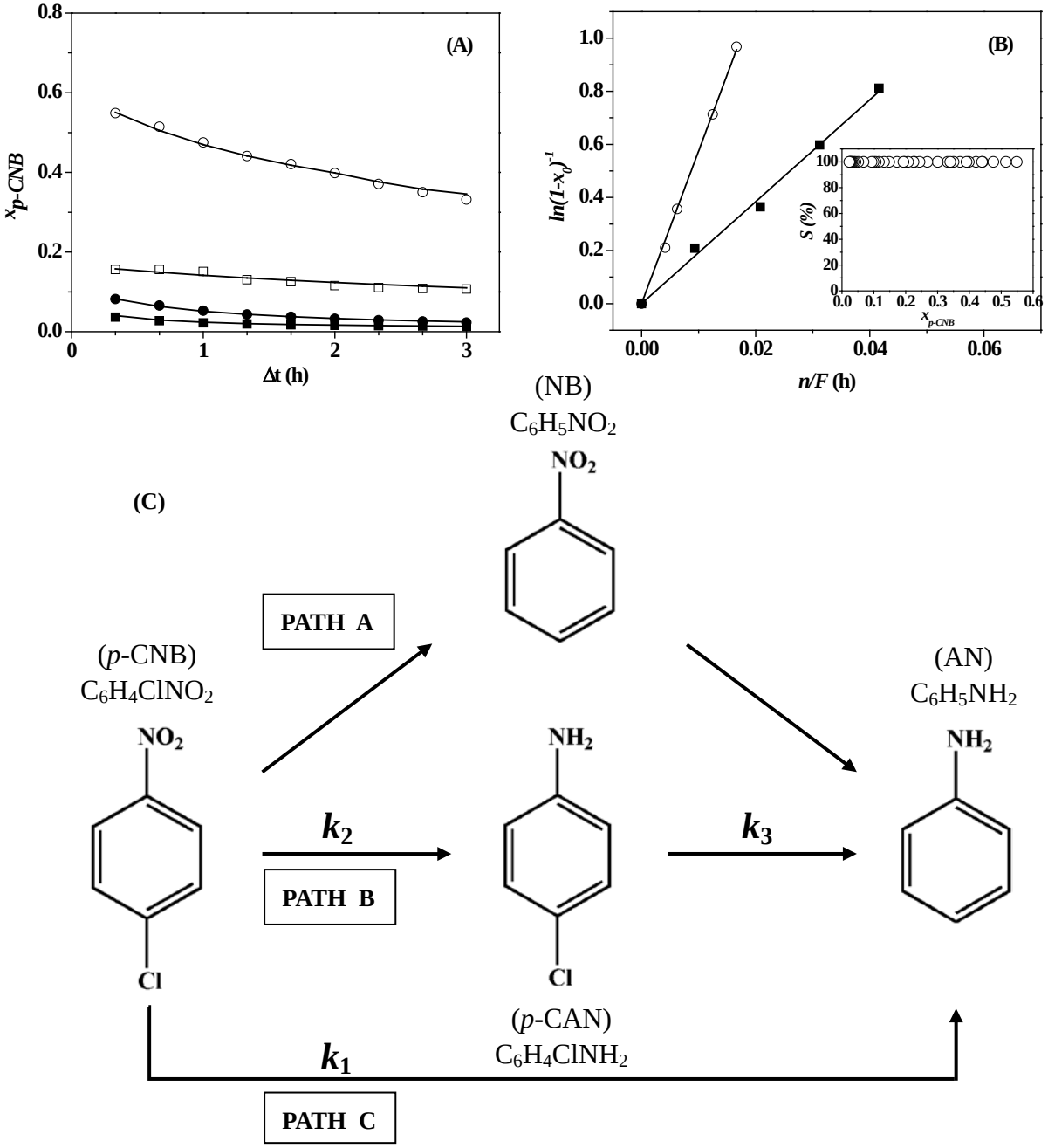

Figure 3.4: (A) Variation of *p*-CNB fractional conversion ($x_{p\text{-}CNB}$) with time-on-stream over Au/Al_2O_3 (●, 5-5, n/F = 8.8×10^{-3} h; ○, 100-100, n/F = 16.6×10^{-3} h) and Au/CZ (■, 5-5, n/F = 7.3×10^{-3} h; □, 100-100, n/F = 10.4×10^{-3} h). (B) Pseudo-first order kinetic plots for the hydrogenation of *p*-CNB over Au/Al_2O_3 (○, 100-100, TPR to 473 K) and Au/CZ (■, 5-5, TPR to 393 K). Inset: *p*-CAN selectivity (*S*) as a function of *p*-CNB fractional conversion ($x_{p\text{-}CNB}$) over Au/Al_2O_3; n/F = 4.2-16.6×10^{-3} h. (C) Reaction pathways associated with the hydrogenation of *p*-CNB.

Extending TPR activation to 673 K resulted in a slight shift in the Au $4f_{7/2}$ signal to lower BE (by 0.1 eV, **Figure 3.2(B)**), with a decrease in the relative (Au/Al) signal intensity (**Table 3.2**), diagnostic of Au particle sintering [56]. This effect was probed by HAADF-STEM analysis and representative images are given in **Figure 3.3** with the resultant Au particle size distribution. It can be seen that TPR to 673 K resulted in a

broadening and shift in the size distribution to higher values. Gold dispersion (*D*), the ratio of surface to total Au atoms, was lower after reduction at 673 K (**Table 3.2**). Sintering of supported Au with increasing temperature (300–800 K) has been reported in the literature [58].

3.3.2 Au/Al_2O_3: Catalytic Response

Fractional *p*-CNB conversion ($x_{p\text{-}CNB}$) is presented as a function of time-on-stream for two representative cases in **Figure 3.4(A)**. The temporal decline in conversion can be expressed in terms of the empirical relationship [59]

$$\frac{(x_{p-CNB} - x_0)}{(x_{3h} - x_0)} = \frac{\Delta t}{(\beta + \Delta t)} \tag{3.1}$$

where x_{3h} represents fractional conversion after 3 h on-stream and β is a time scale fitting parameter. Fit convergence yields x_0 (initial conversion) used to derive the rate constant (k) according to a pseudo-first order kinetic treatment [60]

$$\ln(1 - x_0)^{-1} = k\left(\frac{n}{F}\right) \tag{3.2}$$

where n/F has the physical significance of contact time; a representative linear relationship between $\ln(1\text{-}x_0)^{-1}$ and n/F is shown in **Figure 3.4(B)**. Turnover frequency (*TOF*) values, normalised with respect to Au dispersion are presented in **Table 3.3**, which includes product selectivity obtained at two selected conversions ($x_{p\text{-}CNB}$ = 0.1 and 0.4). The *TOF* generated by Au/Al_2O_3 was unaffected by activation conditions (see 100-5 *vs.* 5-5), *i.e.* H_2 content in the gas flow did not influence the nature of the active catalyst. In contrast, the reactant gas composition had a significant effect on *TOF* (see 100-100 *vs.* 100-5). We can associate this with the low capacity of supported Au to activate/dissociate H_2 [61], where higher H_2 content in the feed must serve to increase surface hydrogen with a consequent elevation of *TOF*. The possible reaction pathways in the conversion of *p*-CNB [41,42] are shown in **Figure 3.4(C)**. Path A involves dechlorination to nitrobenzene (NB), which can be further hydrogenated to aniline (AN). In Path B, the $–NO_2$ group is initially hydrogenated to yield *p*-CAN, which can undergo subsequent dechlorination to AN. In addition, *p*-CNB can be converted directly to AN *via* path C. Reaction over Au/Al_2O_3 proceeded along path B where *p*-CAN was the sole product (see

inset to **Figure 3.4(B)** and entries in **Table 3.3**), *i.e.* reaction exclusivity with respect to $-NO_2$ reduction. The influence of activation temperature was examined, taking 5-5 as a common activation/reaction condition. Reduction at 673 K, resulting in Au sintering, delivered appreciably lower *TOF* (**Table 3.3**). It has been proposed that Au particles < 5 nm are more effective in hydrogenation reactions [40,61,62], which was linked to enhanced H_2 dissociation at corner and edge sites on smaller Au particles [61,63,64]. Exclusive production of *p*-CAN was a feature of Au/Al_2O_3 irrespective of activation/reaction conditions or Au particle size.

Table 3.3: Turnover frequency (*TOF*) and reaction products (with selectivities, *S*) generated at two fractional conversions ($x_{p\text{-CNB}}$ = 0.1 and 0.4) for reaction over Au/Al_2O_3 and Au/CZ.

Catalyst	Activation-reaction conditions	*TOF* (h^{-1})[a]	$S_{0.1}$ (%)	$S_{0.4}$ (%)
Au/Al_2O_3	100-100[b]	315	*p*-CAN (100)	*p*-CAN (100)
	100-5[b]	82	*p*-CAN (100)	*p*-CAN (100)
	5-5[b]	80	*p*-CAN (100)	*p*-CAN (100)
	5-5[c]	29	*p*-CAN (100)	*p*-CAN (100)
Au/CZ	100-100[d]	34	AN (16) *p*-CAN (84)	AN (6) *p*-CAN (94)
	100-5[d]	28	AN (57) *p*-CAN (43)	AN (23) *p*-CAN (77)
	5-5[d]	37	AN (77) *p*-CAN (23)	AN (18) *p*-CAN (82)
	5-5[b]	22	AN (90) *p*-CAN (10)	AN (17) *p*-CAN (83)
	5-5[c]	14	AN (90) *p*-CAN (10)	AN (76) *p*-CAN (24)

[a]Turnover frequency (*TOF*) values normalised with respect to Au dispersion, *i.e.* per Au surface atom; [b]activated at 473 K; [c]activated at 673 K; [d]activated at 393 K

3.3.3 Au/CZ: Characteristics

Gold dispersion on CZ was probed by HAADF-STEM and the resultant mean Au sizes are reported in **Table 3.2** with representative HAADF-STEM images and size histograms presented in **Figure 3.5**.

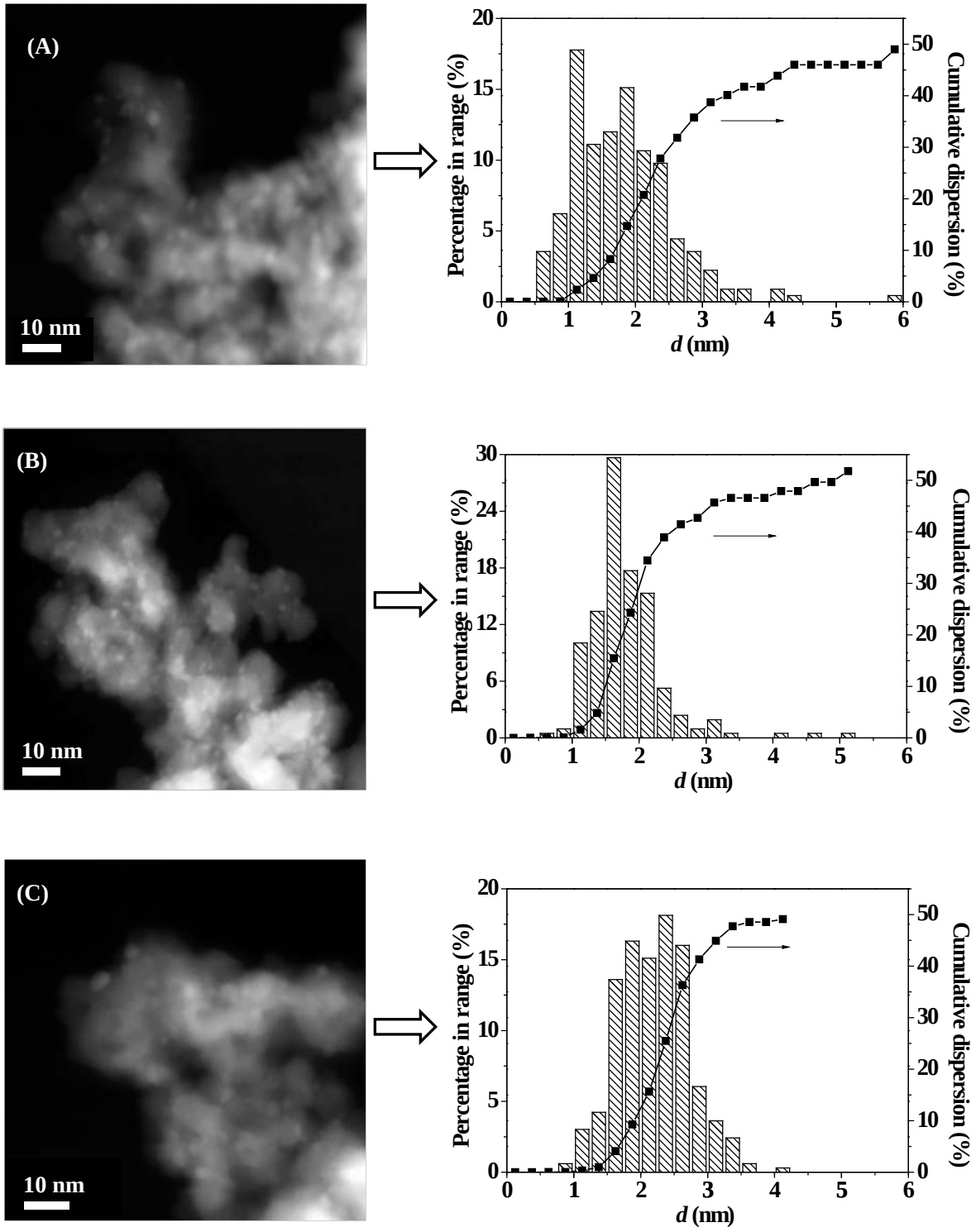

Figure 3.5: Representative HAADF-STEM images and Au particle size distribution for Au/CZ (A) submitted to the standard oxidising treatment at 523 K and following activation in (B) 100% v/v H_2 at 393 K and (C) 5% v/v H_2 at 673 K.

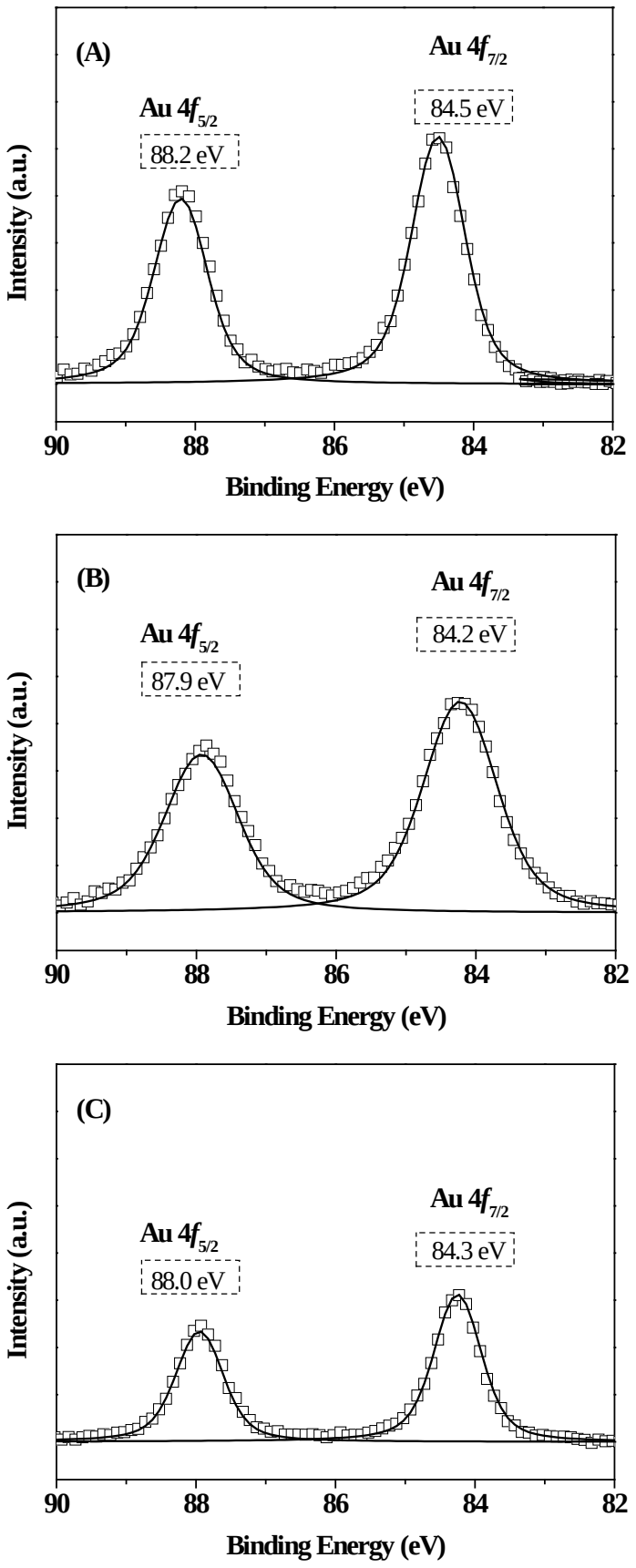

Figure 3.6: XPS spectra over the Au 4*f* region for Au/CZ (A) submitted to the standard oxidising treatment at 523 K, with activation in (B) 100% v/v H_2 at 393 K and (C) 5% v/v H_2 at 673 K. Note: the XPS experimental data are represented by symbols (□) while the lines are the result of spectral curve fitting.

It can be seen that Au size/dispersion on CZ was insensitive to activation conditions, exhibiting a narrower size distribution and smaller mean (1.8-1.9 nm) relative to Au/Al_2O_3. Moreover, the thermal sintering exhibited by Au/Al_2O_3 was not a feature of Au/CZ, suggesting stronger metal/support interactions for the latter. XPS analysis of Au/CZ pre-TPR generated a signal that is consistent with zero valent Au (see **Figure 3.6(A)** and **Table 3.2**). This represents a marked deviation from Au/Al_2O_3 where TPR treatment (**Figure 3.1**) was required to generate metallic Au. However, it has been reported that Au on reducible supports readily undergoes autoreduction at room temperature in Ar and even when heated under oxidising conditions [65,66]. The difference in Au $4f_{7/2}$ BE for Au/CZ (84.5 eV) relative to Au/Al_2O_3 post-TPR (84.0-84.1 eV) can be linked to the enhanced dispersion of Au on CZ that facilitates support interaction. There is a measurable shift in BE to lower values (by 0.2-0.3 eV, **Table 3.2**) post-TPR with essentially equivalent XPS profiles (see **Figure 3.6(B)** and **(C)**) over the range of activation conditions considered.

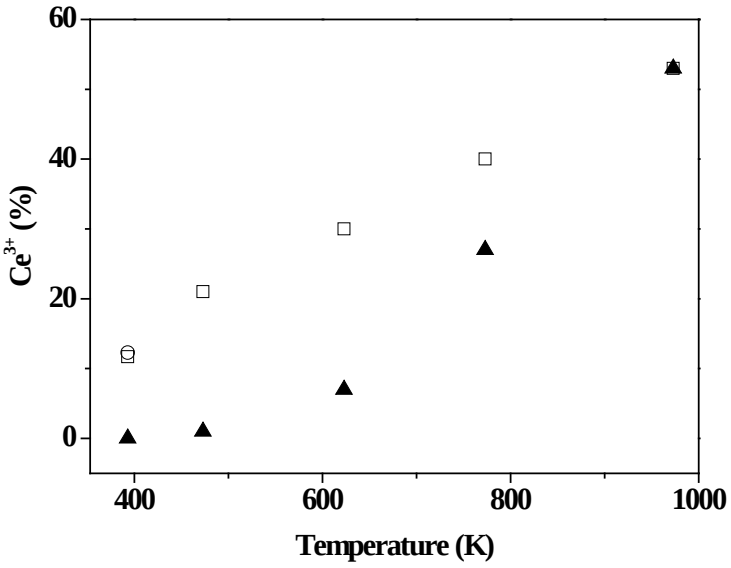

Figure 3.7: Oxygen storage capacity (OSC, expressed in terms of % Ce^{3+}) as a function of activation temperature for the treatment of CZ (▲) and Au/CZ (□) in 5% v/v H_2 and Au/CZ (○) in 100% v/v H_2.

There is evidence in the literature that support oxygen vacancies can stabilise transition metal nano-particles and inhibit sintering [67]. As CZ is a reducible support, treatment in hydrogen can modify the redox state, possibly resulting in (i) incorporation

of chemisorbed hydrogen (reversible reduction) and (ii) formation of oxygen vacancies (irreversible reduction) [68,69]. Atomic hydrogen can "spill over" from Au onto the support to produce oxygen vacancies with the generation of water [69]. We have reported previously [70-73] that CZ redox state is determined by the reduction temperature. TPR-MS analysis of Au/CZ (not shown) coincided with results recorded elsewhere [69] with H_2O release (T_{max} = 400 K) extending to 973 K. Formation of oxygen vacancies is favoured with increasing reduction temperature as demonstrated by the OSC measurements presented in **Figure 3.7**. It is immediately evident that the presence of Au promoted CZ reduction where, at T < 800 K, the degree of Ce^{4+} reduction (to Ce^{3+}) with associated vacancy formation shows a near linear dependence on temperature. Haruta *et al.* [74-76] proposed that CeO_2 oxygen vacancies facilitate Au diffusion on the support surface and into the bulk, which was taken to be irreversible. Our XPS results (**Table 3.2**) reveal a decrease in Au/Zr ratio with increasing reduction temperature. The OSC value for Au/CZ at 393 K was equivalent for TPR in 100% and 5% v/v H_2. An increase in Ce^{4+} reduction with temperature was also observed for the CZ support to converge with Au/CZ at 973 K.

FTIR spectra of CO adsorbed on oxidised Au/CZ and post TPR to 393 K (in 5% and 100% v/v H_2) are presented in **Figure 3.8**. The spectrum recorded for Au/CZ subjected to the standard oxidising pre-treatment at 523 K (**Figure 3.8(A)**) is characterised by a main band at 2114 cm^{-1} assigned to CO-Au(0) [69,77]. The CO-Au bands for the catalyst reduced at 393 K (in 5% and 100% v/v H_2) are less symmetric with appreciable tailing at the low frequency side (**Figure 3.8(B)**). Moreover, a significant shift in band wave number from 2114 cm^{-1} to 2103-2105 cm^{-1} may be observed. We have reported previously a similar red shift for Au/CZ reduced at 473 K [77] and 673 K [69] and attributed this response to electron transfer from the reduced support to nanoscale Au, which is consistent with the Au $4f_{7/2}$ XPS BE shift given in **Table 3.2**. Moreover, a decrease in *v*-CO band intensity was observed following TPR. Weststrate *et al.* [78] have also noted a decrease in CO adsorption on Au/CeO_{2-x} relative to Au/CeO_2. The drop in CO uptake on Au/CZ post TPR can be attributed to an inhibition of the CO adsorption capability of Au nano-particles resulting from the occurrence of strong metal/support interaction [77].

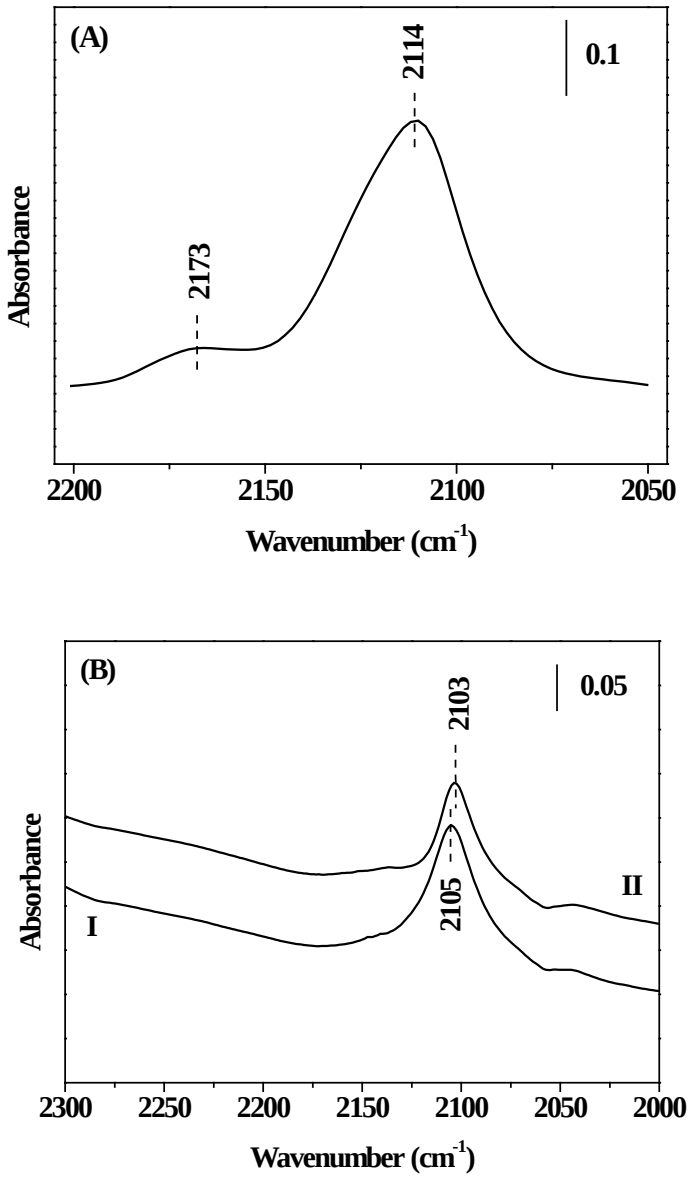

Figure 3.8: FTIR spectra of CO adsorbed on Au/CZ subjected to (A) standard oxidising pre-treatment and (B) and activation (I) in 5% v/v H_2 and (II) 100% v/v H_2 at 393 K.

3.3.4 Au/CZ: Catalytic Response

Conversion of *p*-CNB over Au/CZ also exhibited a temporal decline (**Figure 3.4(A)**) and a pseudo-first order kinetic treatment (**Figure 3.4(B)**) was again applicable; *TOF* and selectivity values are recorded in **Table 3.3**. In common with Au/Al_2O_3, an increase in *TOF* was observed at a higher H_2 content in the feed (100-100 *vs.* 100-5) but this effect was not as marked for reaction over Au/CZ. Reduction of Au/CZ in a H_2 rich stream (100-5 *vs.* 5-5) or increasing temperature (at 5-5) generated lower *TOF* values. This trend matches that of decreasing CO adsorption (from CO-FTIR measurements) and can be linked to variations in Au/support interaction (coincident with the formation of

oxygen vacancies) that serve to modify adsorptive properties and limit the activity of Au [77]. The range of *TOF* values delivered by Au/CZ and Au/Al_2O_3 must reflect differences in Au particle size and electronic character with a possible direct contribution from the support itself. Given the observed structure sensitivity of $–NO_2$ reduction with respect to Au particle size [40], Au/CZ with the higher dispersion should generate enhanced activity relative to Au/Al_2O_3 [79,80]. The higher *TOF* delivered by Au/Al_2O_3 may result from the action of the support to accommodate spillover hydrogen [44] and surface Lewis acidity that can serve to activate *p*-CNB [81-83] and enhance hydrogen dissociation on Au [82,83], contributing to increased efficiency.

Table 3.4: XPS BE associated with the Au $4f_{7/2}$ signal recorded for catalysts post-reaction with peak intensity ratios (Cl/Zr or Cl/Al).

Sample (activation conditions)[a]	BE Au $4f_{7/2}$ (eV)	Intensity ratio
		Cl/Zr
Au/CZ (393 K, 100-100)	84.4	408×10^{-3}
Au/CZ (393 K, 5-5)	84.4	444×10^{-3}
Au/CZ (673 K, 5-5)	84.3	319×10^{-3}
Au/Al_2O_3 (473 K, 100-100)	84.1	(40×10^{-3})[b]

[a]reaction conducted at $n/F = 3\times10^{-2}$ h
[b]Cl/Al

In marked contrast to Au/Al_2O_3, Au/CZ generated *p*-CAN and AN as products; see **Table 3.3**. Baltzly and Phillips [84] concluded, in a very early study, that while aromatically bound Cl is stable under reaction conditions where there is no aromatic ring reduction, amino substitution serves to labilise the halogen. We have reported elsewhere that, under reducing conditions, Cl is readily incorporated into ceria [73]. Indeed, strong Cl interactions have been established for Rh/CeO_2 [85], Pd/CeO_2 [86], Pd/TiO_2 [87] and Rh/CZ [88]. XPS analysis did not reveal any detectable Cl in activated Au/CZ pre-reaction but there was a significant Cl content in the samples post-reaction (see **Table 3.4**), which can be linked to the observed dechlorination and AN formation. The dependence of product selectivity on conversion over Au/CZ for different activation-reaction conditions is presented in **Figure 3.9**. Under 100-100 conditions

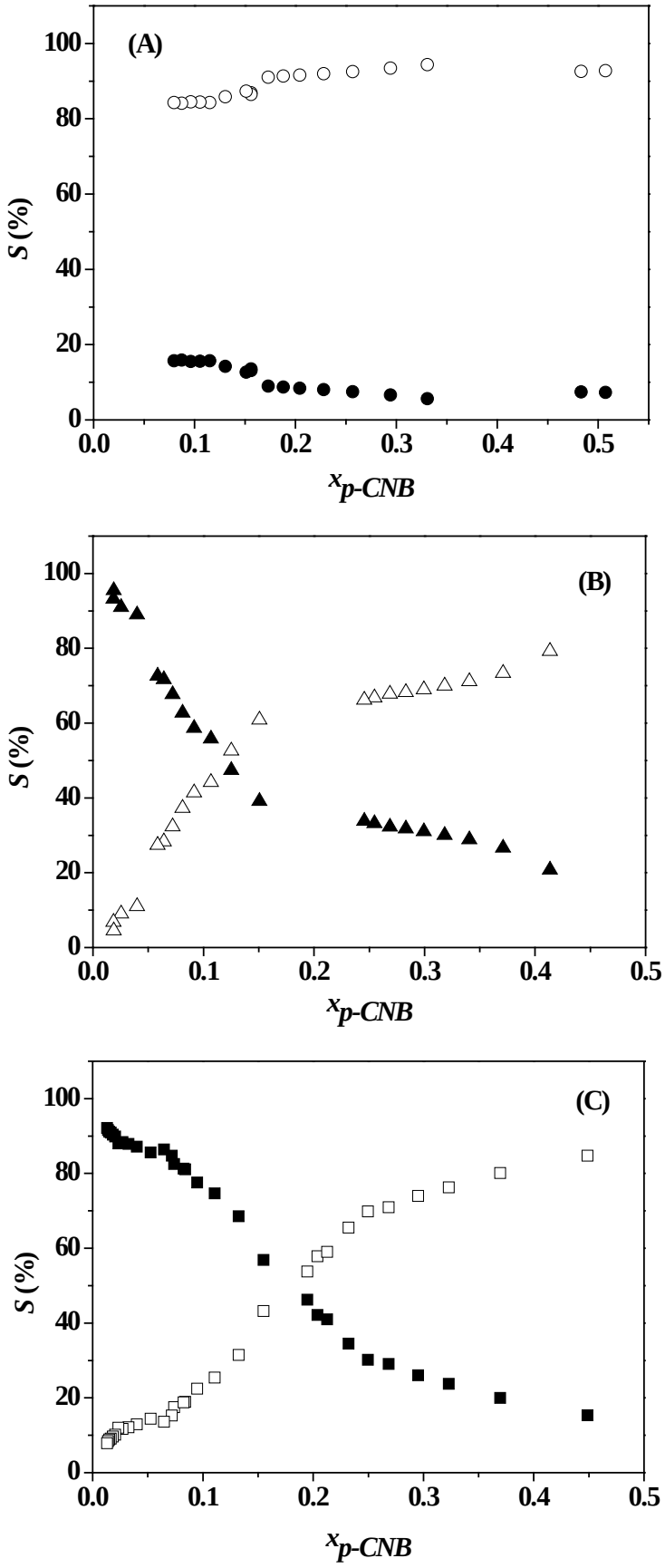

Figure 3.9: Variation of AN (solid symbols) and *p*-CAN (open symbols) selectivity (*S*) with *p*-CNB fractional conversion ($x_{p\text{-}CNB}$) for reaction over Au/CZ activated at 393 K: (A) 100-100, n/F = 10.4-26.3×10^{-3} h; (B) 100-5, n/F = 7.3-46.8×10^{-3} h; (C) 5-5, n/F = 7.3-20.8×10^{-3} h.

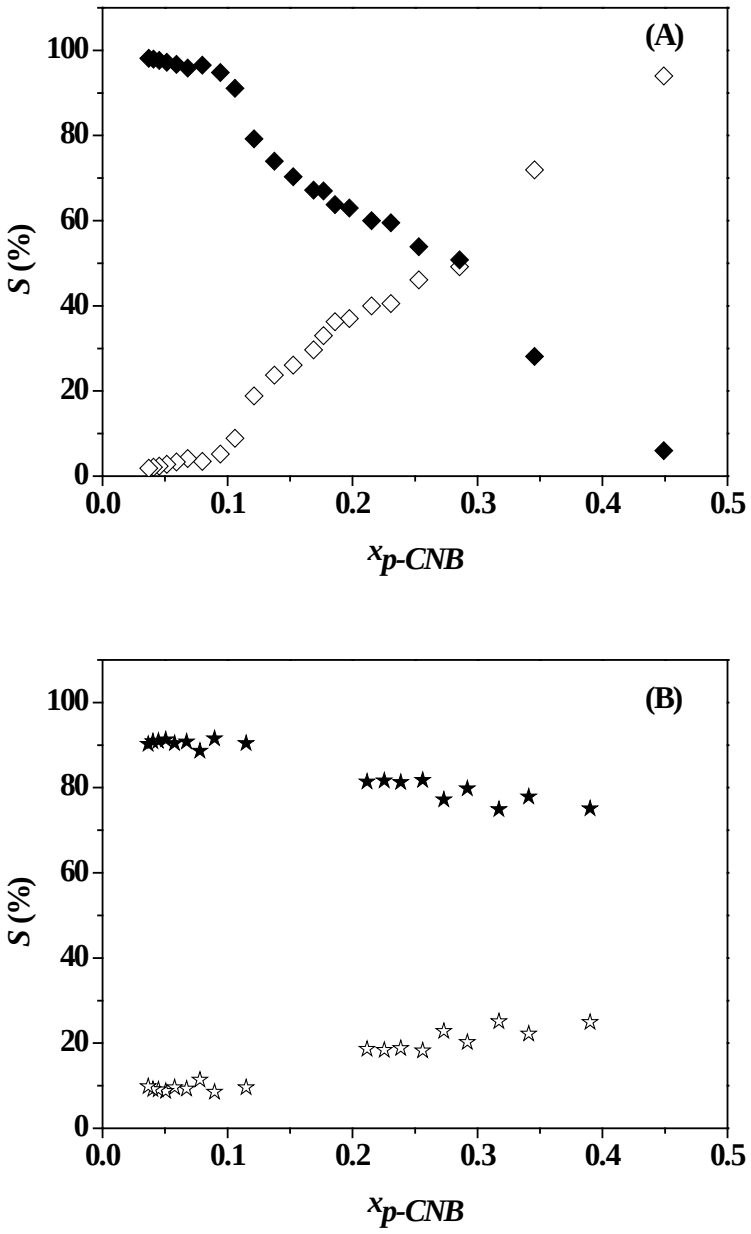

Figure 3.10: Variation of AN (solid symbols) and *p*-CAN (open symbols) selectivity (*S*) with *p*-CNB fractional conversion ($x_{p\text{-}CNB}$) for reaction over Au/CZ at 5-5: (A) activated at 473 K, *n/F* = 15.6-52×10^{-3} h; (B) activated at 673 K, *n/F* = 20.8-74.5×10^{-3} h.

(**Figure 3.9(A)**), *p*-CAN was the predominant product (S > 80%) over the range of $x_{p\text{-CNB}}$ values obtained by varying *n/F*. Taking dechlorination as the result of the action of support oxygen vacancies, the overall catalytic response is then governed by the supported Au phase and hydrogenation predominates. At 100-5 (see **Figure 3.9(B)**), AN was the major product at low $x_{p\text{-CNB}}$ (< 0.1) with a switch in selectivity to *p*-CAN at higher conversions: see selected selectivity values in **Table 3.3**. At the low H_2 content (5% v/v) in the feed, the available surface hydrogen is reduced with the result that the relative contribution due to dechlorination at oxygen vacancies is greater, resulting in high

selectivities to AN at low $x_{p\text{-CNB}}$. At higher *p*-CNB conversions ($x_{p\text{-CNB}} > 0.15$, achieved by varying *n/F*), the contribution of dechlorination must be limited by the availability of oxygen vacancies, which leads to a higher selectivity to *p*-CAN. As shown in **Figure 3.9(C)**, the behaviour of Au/CZ at 5-5 is similar to that at 100-5 in that AN is favoured at lower conversions with increasing preferential formation of *p*-CAN at higher $x_{p\text{-CNB}}$. This indicates that in terms of the catalytic response, support structure is not appreciably different for activation in 5% v/v and 100% H_2, which is consistent with the OSC data reported in **Figure 3.7** where the same degree of Ce^{4+} reduction (12%) was obtained. The results demonstrate that the extent of AN formation over Au/CZ is related to feed composition where, under H_2 lean conditions (5-5 and 100-5), the contribution from surface oxygen vacancies to dechlorination is more pronounced. The consequences of increasing Au/CZ activation temperature, taking the 5-5 condition, are illustrated in **Figure 3.10**. Post TPR at 473 K (**Figure 3.10(A)**), the selectivity response is very similar to that observed for the catalyst activated at 393 K with AN formation predominant at $x_{p\text{-CNB}} < 0.3$ and increasing preferential *p*-CAN production at higher conversions. In contrast, AN was the main product over Au/CZ activated 673 K irrespective of conversion, with a discernible increase in selectivity to *p*-CAN at higher $x_{p\text{-CNB}}$ (**Figure 3.10(B)**). Taking a general overview, AN production was preferred over a wider range of conversions with increasing activation temperature (from 393 to 673 K). This can be correlated to an inhibited Au activity allied to an increased participation of support oxygen vacancies.

The production of AN can proceed *via* a consecutive/parallel mechanism (**Figure 3.4(C)**). In this study, reaction *via* Path A was not a feature of catalysis as NB was not isolated as a reaction product. The possible consecutive/parallel steps can be represented by

$$p\text{-}CNB + 3H_2 \xrightarrow{k_2} p\text{-}CAN + 2H_2O \tag{3.3}$$

$$p\text{-}CAN + H_2 \xrightarrow{k_3} AN + HCl \tag{3.4}$$

$$p\text{-}CNB + 4H_2 \xrightarrow{k_1} AN + 2H_2O + HCl \tag{3.5}$$

and

$$\frac{dN_{p\text{-}CNB}}{d\left(n/F_{p\text{-}CNB}\right)} = -\left(k_1 + k_2\right) \times N_{p\text{-}CNB} \tag{3.6}$$

$$\frac{dN_{p\text{-}CAN}}{d\left(n/F_{p\text{-}CNB}\right)} = k_2 \times N_{p\text{-}CNB} - k_3 \times N_{p\text{-}CAN} \tag{3.7}$$

$$\frac{dN_{AN}}{d\left(n/F_{p\text{-}CNB}\right)} = k_3 \times N_{p\text{-}CAN} + k_1 \times N_{p\text{-}CNB} \tag{3.8}$$

where N_i represents the molar fraction of the *i*th compound and k_j is the pseudo-first order rate constant for step *j*. From a combination of Eqs (3.6) and (3.7)

$$\frac{dN_{p\text{-}CAN}}{dN_{p\text{-}CNB}} = -L + M \times \left(\frac{N_{p\text{-}CAN}}{N_{p\text{-}CNB}}\right) \tag{3.9}$$

with

$$L = \frac{k_2}{k_1 + k_2} \quad \therefore \quad M = \frac{k_3}{k_1 + k_2}$$

which, when integrated gives

$$N_{p\text{-}CAN} = \frac{L}{1-M} \times \left(N_{p\text{-}CNB}{}^{M} - N_{p\text{-}CNB}\right) + C \tag{3.10}$$

where *C* is a constant and the values of *L* and *M* can be determined by non-linear fitting. The applicability of this parallel/consecutive mechanism can be assessed from the representative cases presented in **Figure 3.11**, where it can be seen that the model provides a more than adequate fit to the experimental data. The rate constant ratios (k_1/k_2 and k_3/k_2) under different activation and reaction conditions, based on the values of *L* and *M*, are given in **Table 3.5**. A strictly consecutive reaction network should yield a value of *L* close to unity ($k_1 = 0$) where lower *L* values are consistent with an enhanced concerted conversion of *p*-CNB to AN. The CZ support alone (reduced at 393–673 K) did not exhibit any activity in the conversion of *p*-CNB. The presence of Au serves to activate *p*-CNB and/or provide a supply of reactive hydrogen for the hydrogenation and dechlorination steps. The production of AN requires a combined nitro group hydrogenation (action of Au) and dechlorination (action of oxygen vacancies). Moreover, there was no detectable conversion of *p*-CAN (as reactant) over CZ (or Au/Al_2O_3). Au/CZ promoted the conversion of *p*-CAN to AN (100% selective) with a rate constant (k_3 = 0.5 h^{-1} at 673 K, 5-5) that was an order of magnitude lower than the rate of AN production from *p*-CNB. A decrease in H_2 content in the feed resulted in an increase in

k_1/k_2 (see 100-100 *vs.* 100-5), which can be attributed to lesser surface hydrogen with a decrease in the degree of hydrogenation (on Au) relative to dechlorination (at the oxygen vacancies). Variation in the hydrogen content during activation (at 393 K, 100-5 *vs.* 5-5) did not have any appreciable influence on the kinetic parameters. An increase in activation temperature (from 393 to 673 K) was accompanied by a greater contribution from the concerted transformation of *p*-CNB to AN (higher k_1/k_2) resulting from increased oxygen vacancy formation that promotes dechlorination.

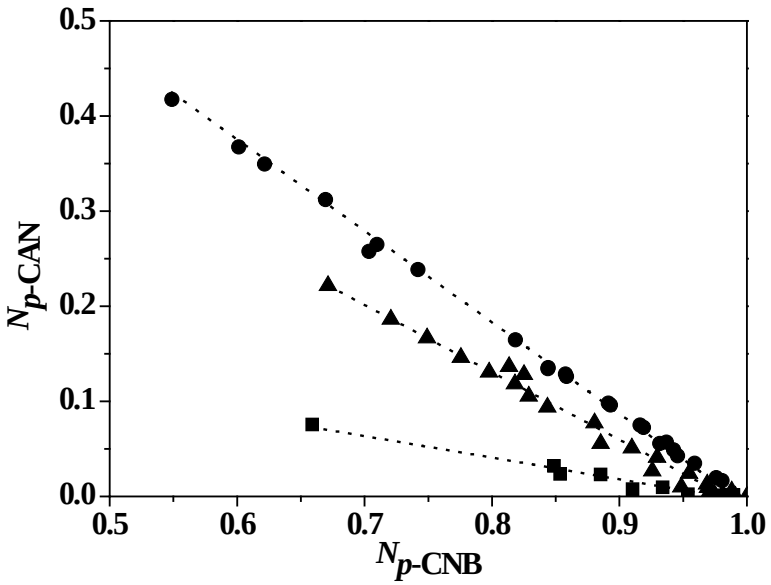

Figure 3.11: Dependence of *p*-CAN mole fraction ($N_{p\text{-CAN}}$) on *p*-CNB mole fraction ($N_{p\text{-CNB}}$) for reaction over Au/CZ at selected activation and reaction conditions: (●) 100-100, TPR to 393 K; (▲) 100-5, TPR to 393 K; (■) 5-5, TPR to 673 K; lines represent fit to the consecutive/parallel mechanism (see Eqs (3.6)-(3.10)).

Table 3.5: Values of the *L* and *M* parameters and rate constant ratios (k_1/k_2 and k_3/k_2, see Figure 4(C)) obtained from the fit (see Eqs (3.6)-(3.10)) of product composition generated over Au/CZ (see Figure 11) under different activation-reaction conditions.

TPR activation temperature (K)	Activation-reaction conditions	*L*	*M*	k_1/k_2	k_3/k_2
393	100-100	0.94	2.2×10^{-14}	0.06	2.4×10^{-14}
393	100-5	0.68	2.2×10^{-14}	0.46	3.3×10^{-14}
393	5-5	0.68	2.2×10^{-14}	0.48	3.3×10^{-14}
473	5-5	0.30	2.4×10^{-14}	2.29	7.5×10^{-14}
673	5-5	0.20	2.4×10^{-14}	3.97	1.2×10^{-13}

3.3.5 The Effect of Spillover Hydrogen

Hydrogen chemisorbed on reduced oxide supports can participate in hydrogenation [89] and dechlorination [90] steps. In order to probe the contribution of spillover hydrogen, a series of reactions were carried out using physical mixtures of Au/CZ+CZ and the results (for 5-5) in terms of *TOF*, selectivity and rate constant ratios are presented in **Table 3.6**. The occurrence of hydrogen spillover in catalyst+support physical combinations has been demonstrated where the two components are well mixed [91-93] or are present as discrete layers [91] with a reported [91,94] spillover transport across non-contiguous surfaces. A physical mixture of Au/CZ+CZ activated at 393 K delivered an equivalent *TOF* (**Table 3.6**) and product composition to that obtained over Au/CZ alone. There was, however, a substantial enhancement in *TOF* with increased selectivity to *p*-CAN for the physical mixture at the higher activation temperature (673 K). Hydrogen temperature programmed desorption (TPD) analysis revealed an equivalent H_2 release from Au/CZ+CZ (1.51 mol/mol$_{Au}$) and Au/CZ (1.43 mol/mol$_{Au}$) activated at 393 K, which is consistent with the common catalytic performance. In contrast, activation at 673 K resulted in appreciably greater H_2 TPD from Au/CZ+CZ (0.64 mol/mol$_{Au}$) relative to Au/CZ (0.39 mol/mol$_{Au}$). The additional hydrogen can undergo a "back spillover" to Au, contributing to increased formation of *p*-CAN and lower k_1/k_2. The samples reduced at 673 K accommodated less spillover hydrogen where a greater proportion of hydrogen consumed was used to reduce the CZ support. A representative H_2-TPD profile for Au/CZ is given in **Figure 3.12**, where the response for Au/Al_2O_3 is included for comparative purposes. Hydrogen release from Au/CZ is characterised by T_{max} at 833 K whereas desorption (10.5 mol/mol$_{Au}$) from Au/Al_2O_3, occurring over a wider temperature interval (from 730 to 1173 K), was an order of magnitude greater and must contribute to the higher recorded *TOF* (in **Table 3.3**). A physical mixture of Au/Al_2O_3 with Al_2O_3 generated an equivalent hydrogenation rate to that obtained with Au/Al_2O_3 alone.

3.3.6 Catalyst Deactivation

Both catalysts exhibited a time on-stream decline in *p*-CNB conversion (**Figure 3.4(A)**) for each set of activation/reaction conditions. Catalyst deactivation can be

Table 3.6: Turnover frequency (*TOF*) and reaction products (with selectivities (*S*)) at $x_{p\text{-CNB}}$ = 0.3) with corresponding values of the *L* and *M* parameters and rate constant ratios (k_1/k_2 and k_3/k_2 see Figure 4(C)) obtained from the fit (see Eqs (3.6)-(3.10)) of product composition over Au/CZ+CZ (Au/CZ: CZ = 1: 1.5) for catalyst activation at 393 and 673 K.

Activation temperature (K)	Activation-reaction conditions	*TOF* (h^{-1})[a] Au/CZ + CZ	$S_{0.3}$ (%)	*L*	*M*	k_1/k_2	k_3/k_2	$S_{0.3}$ (%)[b]
393	5-5	36	AN (32), *p*-CAN (68)	0.66	6.1×10^{-8}	0.52	9.0×10^{-8}	AN (28), *p*-CAN (72)
673	5-5	56	AN (30), *p*-CAN (70)	0.81	4.0×10^{-6}	0.24	4.9×10^{-6}	AN (78), *p*-CAN (22)

[a]Turnover frequency (*TOF*) values normalised with respect to Au dispersion, *i.e.* per Au surface atom
[b]*S* at $x_{p\text{-CNB}}$ = 0.3 over Au/CZ

Table 3.7: Initial conversion/selectivity (x_0/S_0) and conversion after 3 h on-stream (x_{3h}) for reaction over unused (Run 1) and regenerated (Run 2) Au/CZ: $n/F = 7.3\times10^{-3}$ - 2.6×10^{-2} h. Values of the *L* and *M* parameters and rate constant ratios (k_1/k_2 and k_3/k_2 see Figure 4(C)) were obtained from the fit (see Eqs (3.6)-(3.10)) of product composition data.

TPR activation temperature (K)	Activation-reaction conditions		x_0	x_{3h}	S_0 (%)	*L*	*M*	k_1/k_2	k_3/k_2
393	100-100	Run 1	0.90	0.29	*p*-CAN (98), AN (2)	refer to **Table 5**			
		Run 2	0.41	0.06	*p*-CAN (94), AN (6)	0.92	3.1×10^{-14}	0.08	3.4×10^{-14}
393	5-5	Run 1	0.07	0.01	*p*-CAN (20), AN (80)	refer to **Table 5**			
		Run 2	<0.01	<0.01	*p*-CAN (100), AN (0)	>0.99	2.2×10^{-14}	<0.01	2.2×10^{-14}
673	5-5	Run 1	0.11	0.05	*p*-CAN (15), AN (85)	refer to **Table 5**			
		Run 2	0.02	<0.01	*p*-CAN (86), AN (14)	0.54	4.4×10^{-14}	0.87	8.3×10^{-14}

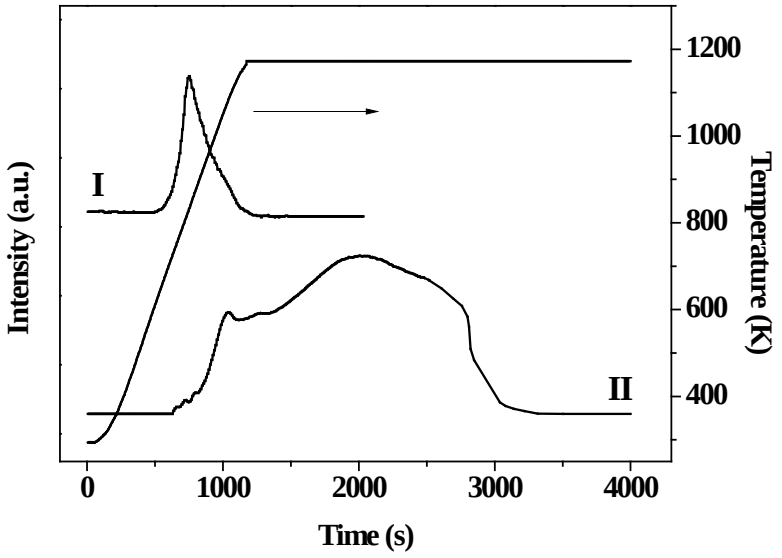

Figure 3.12: Hydrogen TPD profiles recorded for (I) Au/CZ (activated at 673 K) and (II) Au/Al_2O_3 (activated at 473 K).

attributed to coke formation [95] and, in the case of Au/CZ, poisoning by the Cl associated with AN production at the oxygen vacancy sites. In order to assess whether this temporal deactivation was reversible, catalyst regeneration was conducted (see section 2.3). Conversion/selectivity data pre- and post-regeneration are given in **Table 3.7**, taking the two activation/reaction extremes at 393 K (100-100 and 5-5) and activation temperature limits at 5-5 (393 K and 673 K). With regeneration, Au/CZ delivered (100-100 at 393 K) an initial conversion that was higher than that achieved at the end of the Run 1 (after 3 h on-stream) but a lower initial activity than that which characterised the unused catalyst, demonstrating that the temporal deactivation was not fully reversible. Nevertheless, product selectivity for the regenerated catalyst was essentially equivalent to that obtained in Run 1 and hydrogenation predominated to generate *p*-CAN as the principal product. In the case of 5-5, loss of activity during Run 1 was not recovered by regeneration. Moreover, *p*-CAN was the sole product in Run 2, representing a significant shift in selectivity from Run 1 where AN was the major product. Au/CZ activated at 673 K shows a similar response in that activity was not recoverable by regeneration and the catalyst in Run 2 exhibited preferential production of *p*-CAN. These observations suggest an irreversible deactivation of the oxygen vacancies by the Cl generated in Run 1 that

inhibits dechlorination. This is demonstrated by XPS analysis that has revealed a significant Cl content in the used Au/CZ samples (**Table 3.4**). It has been reported that Cl incorporation in Rh/CeO_2 occurs via the migration of chloride ions to support oxygen vacancies [85]. Furthermore, it has been proposed that CZ mixed oxides can strongly retain significant quantities of Cl [88]. It is significant that the residual Cl content exhibited by Au/Al_2O_3 (**Table 3.4**) was appreciably lower. We can discount Au sintering on CZ as a possible cause of deactivation as Au size distributions (and mean values) were equivalent pre- and post-reaction. We envisage Cl abstraction from *p*-CNB by the surface oxygen vacancies of the reduced CZ support. It has been demonstrated that H_2/reducing conditions (< 973 K) are ineffective in the removal of chloride ions from CeO_2 [73]. This is in keeping with our results where reductive regeneration did not recover the original catalyst activity. The catalytic data obtained post-regeneration were also fitted to the consecutive/parallel model and the results are included in **Table 3.7**. At 100-100, where the contribution from Au is predominant, the k_1/k_2 ratios were close in both Runs 1 and 2. However, under hydrogen lean conditions (5-5, 393 and 673 K), poisoning of oxygen vacancies was more severe with a significantly lower k_1/k_2 for the regenerated catalyst, particularly for Au/CZ activated at 393 K, which exhibited negligible dechlorination activity.

3.4 Conclusions

We have established a distinct catalytic response in the hydrogenation of *p*-CNB over nano-scale Au dispersed on non-reducible (Al_2O_3) and reducible ($Ce_{0.62}Zr_{0.38}O_2$, CZ) oxide supports. The results support the following:

(a) Au/Al_2O_3 promotes the exclusive production of *p*-CAN, *i.e.* 100% selectivity with respect to $–NO_2$ group reduction. Varying H_2 content in the activation gas stream does not affect catalyst performance but dilution of H_2 in the feed decreases rate. An increase in activation temperature (from 473 to 673 K) induces Au sintering with a consequent reduction in selective hydrogenation rate.

(b) Stronger Au interaction with CZ results in enhanced dispersion (relative to Au/Al_2O_3) and influences adsorptive and catalytic properties. The supported Au phase promotes reduction of CZ to generate oxygen vacancies, which is

facilitated at higher reduction temperatures.

(c) Kinetic analysis has revealed that *p*-CNB conversion over Au/CZ proceeds *via* parallel/consecutive steps involving combined hydrogenation and hydrodechlorination to give *p*-CAN and aniline. Dechlorination can be attributed to the action of support oxygen vacancies while spillover hydrogen contributes to *p*-CAN formation.

(d) An irreversible temporal loss of activity was observed for both catalysts with a decrease in the extent of dechlorination over Au/CZ, notably under hydrogen lean conditions. This is attributed to the incorporation of Cl in CZ (at oxygen vacancies), as demonstrated by XPS analysis of used catalysts. Regeneration in H_2 did not serve to recover the initial activity.

3.5 References

[3.1] M. Haruta, T. Kobayashi, H. Sano, N. Yamada, *Novel gold catalysts for the oxidation of carbon-monoxide at a temperature far below 0 ^oC,* Chem. Lett., 405-408 (1987)

[3.2] M. Haruta, S. Tsubota, T. Kobayashi, H. Kageyama, M.J. Genet, B. Delmon, *Low-temperature oxidation of Co over gold supported on TiO_2, α-Fe_2O_3, and Co_3O_4,* J. Catal., **144**, 175-192 (1993)

[3.3] B. Nkosi, N.J. Coville, G.J. Hutchings, *Reactivation of a supported gold catalyst for acetylene hydrochlorination*, Chem. Commun., 71-72 (1988)

[3.4] B. Hammer, J.K. Norskov, *Why gold is the noblest of all the metals*, Nature, **376**, 238-240 (1995)

[3.5] S. Carrettin, P. McMorn, P. Johnston, K. Griffin, G.J. Hutchings, *Selective oxidation of glycerol to glyceric acid using a gold catalyst in aqueous sodium hydroxide*, Chem. Commun., 696-697 (2002)

[3.6] A.A. Herzing, C.J. Kiely, A.F. Carley, P. Landon, G.J. Hutchings, *Identification of active gold nanoclusters on iron oxide supports for CO oxidation*, Science, **321**, 1331-1335 (2008)

[3.7] G.R. Bamwenda, A. Obuchi, A. Ogata, J. Oi, S. Kushiyama, K. Mizuno, *The role of the metal during NO_2 reduction by C_3H_6 over alumina and silica-supported*

catalysts, J. Mol. Catal. A: Chem., **126**, 151-159 (1997)

[3.8] D. Andreeva, V. Idakiev, T. Tabakova, A. Andreev, R. Giovanoli, *Low-temperature water-gas shift reaction on Au/α-Fe_2O_3 catalyst*, Appl. Catal. A: Gen., **134**, 275-283 (1996)

[3.9] G.J. Hutchings, J.K. Edwards, L.J. Roy, J.P. Wilcoxon, *Application of gold nanoparticles in catalysis*, Front. Nanosci., **3**, 249-293 (2012)

[3.10] P. Claus, *Heterogeneously catalysed hydrogenation using gold catalysts*, Appl. Catal. A: Gen., **291**, 222-229 (2005)

[3.11] A.S.K. Hashmi, *Gold-catalyzed organic reactions*, Chem. Rev., **107**, 3180-3211 (2007)

[3.12] L. McEwan, M. Julius, S. Roberts, J. Fletcher, *A review of the use of gold catalysts in selective hydrogenation reactions*, Gold. Bull., **43**, 298-306 (2010)

[3.13] A.S.K. Hashmi, G.J. Hutchings, *Gold catalysis*, Angew. Chem. Int. Ed., **45**, 7896-7936 (2006)

[3.14] G.C. Bond, D.T. Thompson, *Catalysis by gold*, Catal. Rev., **41**, 319-388 (1999)

[3.15] C. Mohr, H. Hofmeister, P. Claus, *The influence of real structure of gold catalysts in the partial hydrogenation of acrolein*, J. Catal., **213**, 86-94 (2003)

[3.16] C. Milone, C. Crisafulli, R. Ingoglia, L. Schipilliti, S. Galvagno, *A comparative study on the selective hydrogenation of α, β unsaturated aldehyde and ketone to unsaturated alcohols on Au supported catalysts*, Catal. Today, **122**, 341-351 (2007)

[3.17] X. Zhang, A. Corma, *Supported gold(III) catalysts for highly efficient three-component coupling reactions*, Angew. Chem. Int. Ed., **47**, 4358-4361 (2008)

[3.18] M. Boronat, P. Concepcion, A. Corma, S. Gonzalez, F. Illas, P. Serna, *A molecular mechanism for the chemoselective hydrogenation of substituted nitroaromatics with nanoparticles of gold on TiO_2 catalysts: A cooperative effect between gold and the support*, J. Am. Chem. Soc., **129**, 16230-16237 (2007)

[3.19] L.F. Liotta, *New frontiers in gold catalyzed reactions*, Catalysts, **2**, 299-302 (2012)

[3.20] M. Shekhar, J. Wang, W.-S. Lee, W.D. Williams, S.M. Kim, E.A. Stach, J.T. Miller, W.N. Delgass, F.H. Ribeiro, *Size and support effects for the water-gas shift catalysis over gold nanoparticles supported on model Al_2O_3 and TiO_2*, J. Am. Chem. Soc., **134**, 4700-4708 (2012)

[3.21] B.C. Campo, S. Ivanova, C. Gigola, C. Petit, M.A. Volpe, *Crotonaldehyde hydrogenation on supported gold catalysts*, Catal. Today, **133**, 661-666 (2008)

[3.22] R. Radnik, C. Mohr, P. Claus, *On the origin of binding energy shifts of core levels of supported gold nanoparticles and dependence of pretreatment and material synthesis*, Phys. Chem. Chem. Phys., **5**, 172-177 (2003)

[3.23] C. Binns, *Nanoclusters deposited on surfaces*, Surf. Sci. Rep., **44**, 1-49 (2001)

[3.24] D. Andreeva, V. Idakiev, T. Tabakova, L. Ilieva, P. Falaras, A. Bourlinos, A. Travlos, *Low-temperature water-gas shift reaction over Au/CeO_2 catalysts*, Catal. Today, **72**, 51-57 (2002)

[3.25] X.M. Song, A. Sayari, *Sulfated zirconia-based strong solid-acid catalysts: Recent progress*, Catal. Rev., **38**, 329-412 (1996)

[3.26] V. Idakiev, T. Tabakova, A. Naydenov, Z.Y. Yuan, B.L. Su, *Gold catalysts supported on mesoporous zirconia for low-temperature water-gas shift reaction*, Appl. Catal. B: Environ., **63**, 178-186 (2006)

[3.27] M. Comotti, W.C. Li, B. Spliethoff, F. Schuth, *Support effect in high activity gold catalysts for CO oxidation*, J. Am. Chem. Soc., **128**, 917-924 (2006)

[3.28] X. Zhang, H. Shi, B.Q. Xu, *Catalysis by gold: Isolated surface Au^{3+} ions are active sites for selective hydrogenation of 1,3-butadiene over Au/ZrO_2 catalysts*, Angew. Chem. Int. Ed., **44**, 7132-7135 (2005)

[3.29] S. Schimpf, M. Lucas, C. Mohr, U. Rodemerck, A. Bruckner, J. Radnik, H. Hofmeister, P. Claus, *Supported gold nanoparticles: in-depth catalyst characterization and application in hydrogenation and oxidation reactions*, Catal. Today, **72**, 63-78 (2002)

[3.30] D.P. He, H. Shi, Y. Wu, B.Q. Xu, *Synthesis of chloroanilines: selective hydrogenation of the nitro in chloronitrobenzenes over zirconia-supported gold catalyst*, Green Chem., **9**, 849-851 (2007)

[3.31] M. Manzoli, F. Boccuzzi, A. Chiorino, F. Vindigni, W.L. Deng, M.

Flytzani-Stephanopoulos, *Spectroscopic features and reactivity of CO adsorbed on different Au/CeO_2 catalysts*, J. Catal., **245**, 308-315 (2007)

[3.32] W.L. Deng, M. Flytzani-Stephanopoulos, *On the issue of the deactivation of Au-ceria and Pt-ceria water-gas shift catalysts in practical fuel-cell applications*, Angew. Chem. Int. Ed., **45**, 2285-2289 (2006)

[3.33] J. Guzman, S. Carrettin, A. Corma, *Spectroscopic evidence for the supply of reactive oxygen during CO oxidation catalyzed by gold supported on nanocrystalline CeO_2*, J. Am. Chem. Soc., **127**, 3286-3287 (2005)

[3.34] Q. Fu, W.L. Deng, H. Saltsburg, M. Flytzani-Stephanopoulos, *Activity and stability of low-content gold-cerium oxide catalysts for the water-gas shift reaction*, Appl. Catal. B: Environ., **56**, 57-68 (2005)

[3.35] M. Ozawa, *Role of cerium-zirconium mixed oxides as catalysts for car pollution: A short review*, J. Alloy. Compd., **275**, 886-890 (1998)

[3.36] E. Mamontov, T. Egami, R. Brezny, M. Koranne, S. Tyagi, *Lattice defects and oxygen storage capacity of nanocrystalline ceria and ceria-zirconia*, J. Phys. Chem. B, **104**, 11110-11116 (2000)

[3.37] G. Vlaic, R. Di Monte, P. Fornasiero, E. Fonda, J. Kaspar, M. Graziani, *The CeO_2-ZrO_2 system: Redox properties and structural relationships*, Stud. Surf. Sci. Catal., **116**, 185-195 (1998)

[3.38] D. Widmann, R. Leppelt, R.J. Behm, *Activation of a Au/CeO_2 catalyst for the CO oxidation reaction by surface oxygen removal/oxygen vacancy formation*, J. Catal., **251**, 437-442 (2007)

[3.39] J. Xiong, J.X. Chen, J.Y. Zhang, *Liquid-phase hydrogenation of o-chloronitrobenzene over supported nickel catalysts*, Catal. Commun., **8**, 345-350 (2007)

[3.40] F. Cardenas-Lizana, S. Gomez-Quero, N. Perret, M.A. Keane, *Support effects in the selective gas phase hydrogenation of p-chloronitrobenzene over gold*, Gold. Bull., **42**, 124-132 (2009)

[3.41] F. Cardenas-Lizana, S. Gomez-Quero, A. Hugon, L. Delannoy, C. Louis, M.A. Keane, *Pd-promoted selective gas phase hydrogenation of p-chloronitrobenzene over alumina supported Au*, J. Catal., **262**, 235-243 (2009)

[3.42] F. Cardenas-Lizana, S. Gomez-Quero, M.A. Keane, *Ultra-selective gas phase catalytic hydrogenation of aromatic nitro compounds over Au/Al_2O_3*, Catal. Commun., **9**, 475-481 (2008)

[3.43] F. Cardenas-Lizana, S. Gomez-Quero, M.A. Keane, *Exclusive production of chloroaniline from chloronitrobenzene over Au/TiO2 and Au/Al_2O_3*, Chemsuschem, **1**, 215-221 (2008)

[3.44] X. Wang, N. Perret, M.A. Keane, *The role of hydrogen partial pressure in the gas phase hydrogenation of p-Chloronitrobenzene over alumina supported Au and Pd: A consideration of reaction thermodynamics and kinetics*, Chem. Eng. J., **210**, 103-113 (2012)

[3.45] Y. Xie, N. Xiao, C. Yu, J. Qiu, *Magnetically recyclable Pt/C(Ni) nanocatalysts with improved selectivity for hydrogenation of o-chloronitrobenzene*, Catal. Commun., **28**, 69-72 (2012)

[3.46] G.-Y. Fan, L. Zhang, H.-Y. Fu, M.-L. Yuan, R.-X. Li, H. Chen, X.-J. Li, *Hydrous zirconia supported iridium nanoparticles: An excellent catalyst for the hydrogenation of haloaromatic nitro compounds*, Catal. Commun., **11**, 451-455 (2010)

[3.47] X. Meng, H. Cheng, S.-i. Fujita, Y. Hao, Y. Shang, Y. Yu, S. Cai, F. Zhao, M. Arai, *Selective hydrogenation of chloronitrobenzene to chloroaniline in supercritical carbon dioxide over Ni/TiO_2: Significance of molecular interactions*, J. Catal., **269**, 131-139 (2010)

[3.48] B. Zhao, Y.-W. Chen, *Hydrogenation of p-chloronitrobenzene on Mo, La, Fe, and W-modified NiCoB nanoalloy catalysts*, J. Non-Cryst. Solids, **356**, 839-847 (2010)

[3.49] R. Zanella, S. Giorgio, C.R. Henry, C. Louis, *Alternative methods for the preparation of gold nanoparticles supported on TiO_2*, J. Phys. Chem. B, **106**, 7634-7642 (2002)

[3.50] M. López-Haro, J.J. Delgado, J.M. Cies, E. del Rio, S. Bernal, R. Burch, M.A. Cauqui, S. Trasobares, J.A. Pérez-Omil, P. Bayle-Guillemaud, J.J. Calvino, *Bridging the gap between CO adsorption studies on gold model surfaces and supported nanoparticles*, Angew. Chem. Int. Ed., **49**, 1981-1985 (2010)

[3.51] M.P. Yeste, J.C. Hernández, S. Bernal, G. Blanco, J.J. Calvino, J.A. Pérez-Omil, J.M. Pintado, *Comparative study of the reducibility under H_2 and CO of two thermally aged $Ce_{0.62}Zr_{0.38}O_2$ mixed oxide samples*, Catal. Today, **141**, 409-414 (2009)

[3.52] G. Tavoularis, M.A. Keane, *The gas phase hydrodechlorination of chlorobenzene over nickel/silica*, J. Chem. Technol. Biotechnol., **74**, 60-70 (1999)

[3.53] M. Trueba, S.P. Trasatti, *γ-Alumina as a support for catalysts: a review of fundamental aspects*, Eur. J. Inorg. Chem., **2005**, 3393-3403 (2005)

[3.54] A.C. Gluhoi, X. Tang, P. Marginean, B.E. Nieuwenhuys, *Characterization and catalytic activity of unpromoted and alkali (earth)-promoted Au/Al_2O_3 catalysts for low-temperature CO oxidation*, Top. Catal., **39**, 101-110 (2006)

[3.55] C.K. Costello, J. Guzman, J.H. Yang, Y.M. Wang, M.C. Kung, B.C. Gates, H.H. Kung, *Activation of Au/γ-Al_2O_3 catalysts for CO oxidation: characterization by X-ray absorption near edge structure and temperature programmed reduction*, J. Phys. Chem. B, **108**, 12529-12536 (2004)

[3.56] M. Baron, O. Bondarchuk, D. Stacchiola, S. Shaikhutdinov, H.J. Freund, *Interaction of gold with cerium oxide supports: CeO_2 (111) thin films vs CeO_x nanoparticles*, J. Phys. Chem. C, **113**, 6042-6049 (2009)

[3.57] Q. Fu, H. Saltsburg, M. Flytzani-Stephanopoulos, *Active nonmetallic Au and Pt species on ceria-based water-gas shift catalysts*, Science, **301**, 935-938 (2003)

[3.58] Y. Zhou, J. Zhou, *Growth and sintering of Au-Pt nanoparticles on oxidized and reduced CeO_x (111) thin films by scanning tunneling microscopy*, J. Phys. Chem. Lett., **1**, 609-615 (2010)

[3.59] F. Cárdenas-Lizana, S. Gómez-Quero, G. Jacobs, Y. Ji, B.H. Davis, L. Kiwi-Minsker, M.A. Keane, *Alumina supported Au-Ni: surface synergism in the gas phase hydrogenation of nitro-compounds*, J. Phys. Chem. C, **116**, 11166-11180 (2012)

[3.60] N. Perret, X. Wang, L. Delannoy, C. Potvin, C. Louis, M.A. Keane, *Enhanced selective nitroarene hydrogenation over Au supported on β-Mo_2C and β-Mo_2C/Al_2O_3*, J. Catal., **286**, 172-183 (2012)

[3.61] R. Zanella, C. Louis, S. Giorgio, R. Touroude, *Crotonaldehyde hydrogenation by gold supported on TiO_2: structure sensitivity and mechanism*, J. Catal., **223**, 328-339 (2004)

[3.62] J.F. Jia, K. Haraki, J.N. Kondo, K. Domen, K. Tamaru, *Selective hydrogenation of acetylene over Au/Al_2O_3 catalyst*, J. Phys. Chem. B, **104**, 11153-11156 (2000)

[3.63] E. Bus, J.T. Miller, J.A. van Bokhoven, *Hydrogen chemisorption on Al_2O_3-supported gold catalysts*, J. Phys. Chem. B, **109**, 14581-14587 (2005)

[3.64] G.C. Bond, *Chemisorption and reactions of small molecules on small gold particles*, Molecules, **17**, 1716-1743 (2012)

[3.65] V.S. Narkhede, A.D. Toni, V.V. Narkhede, M. Guraya, J.W. Niemantsverdriet, M.W.E. van den Berg, W. Grunert, H. Gies, *Au/TiO_2 catalysts encapsulated in the mesopores of siliceous MCM-48 - Reproducible synthesis, structural characterization and activity for CO oxidation*, Micropor. Mesopor. Mater., **118**, 52-60 (2009)

[3.66] R. Kydd, J. Scott, W.Y. Teoh, K. Chiang, R. Amal, *Understanding photocatalytic metallization of preadsorbed ionic gold on titania, ceria, and zirconia*, Langmuir, **26**, 2099-2106 (2009)

[3.67] C.T. Campbell, C.H.F. Peden, *Chemistry-oxygen vacancies and catalysis on ceria surfaces*, Science, **309**, 713-714 (2005)

[3.68] H. Vidal, J. Kaspar, M. Pijolat, G. Colon, S. Bernal, A. Cordon, V. Perrichon, F. Fally, *Redox behavior of CeO_2-ZrO_2 mixed oxides: I. Influence of redox treatments on high surface area catalysts*, Appl. Catal. B: Environ., **27**, 49-63 (2000)

[3.69] S.E. Collins, J.M. Cies, E. del Rio, M. Lopez-Haro, S. Trasobares, J.J. Calvino, J.M. Pintado, S. Bernal, *Hydrogen interaction with a ceria-zirconia supported gold catalyst. Influence of CO co-adsorption and pretreatment conditions*, J. Phys. Chem. C, **111**, 14371-14379 (2007)

[3.70] S. Bernal, J.J. Calvino, G.A. Cifredo, J.M. Rodriguez-Izquierdo, V. Perrichon, A. Laachir, *Reversibility of hydrogen chemisorption on a ceria-supported rhodium catalyst*, J. Catal., **137**, 1-11 (1992)

[3.71] S. Bernal, J.J. Calvino, G.A. Cifredo, J.M. Rodriguez-Izquierdo, V. Perrichon, A.

Laachir, *The key role of highly dispersed rhodium in the chemistry of hydrogen ceria systems*, Chem. Commun., 460-462 (1992)

[3.72] S. Bernal, J.J. Calvino, G.A. Cifredo, J.M. Rodriguez-Izquierdo, *Comments on "Redox processes on pure ceria and Rb/CeO_2 catalyst monitored by X-ray-absorption (Fast Acquisition Mode)"*, J. Phys. Chem., **99**, 11794-11796 (1995)

[3.73] S. Bernal, J.J. Calvino, G.A. Cifredo, J.M. Gatica, J.A.P. Omil, A. Laachir, V. Perrichon, *Influence of the nature of the metal precursor salt on the redox behaviour of ceria in Rh/CeO_2 catalysts*, Stud. Surf. Sci. Catal., **96**, 419-429 (1995)

[3.74] T. Akita, M. Okumura, K. Tanaka, M. Kohyama, M. Haruta, *TEM observation of gold nanoparticles deposited on cerium oxide*, J. Mater. Sci., **40**, 3101-3106 (2005)

[3.75] T. Akita, M. Okumura, K. Tanaka, M. Kohyama, M. Haruta, *Analytical TEM observation of Au nano-particles on cerium oxide*, Catal. Today, **117**, 62-68 (2006)

[3.76] T. Akita, S. Tanaka, K. Tanaka, M. Haruta, M. Kohyama, *Sequential HAADF-STEM observation of structural changes in Au nanoparticles supported on CeO_2*, J. Mater. Sci., **46**, 4384-4391 (2011)

[3.77] J.M. Cíes, E. del Río, M. López-Haro, J.J. Delgado, G. Blanco, S. Collins, J.J. Calvino, S. Bernal, *Fully reversible metal deactivation effects in gold/ceria–zirconia catalysts: role of the redox state of the support*, Angew. Chem. Int. Ed., **49**, 9744-9748 (2010)

[3.78] C.J. Weststrate, R. Westerstrom, E. Lundgren, A. Mikkelsen, J.N. Andersen, A. Resta, *Influence of oxygen vacancies on the properties of ceria-supported gold*, J. Phys. Chem. C, **113**, 724-728 (2009)

[3.79] K. Okazaki, S. Ichikawa, Y. Maeda, M. Haruta, M. Kohyama, *Electronic structures of Au supported on TiO_2*, Appl. Catal. A: Gen., **291**, 45-54 (2005)

[3.80] P. Claus, A. Bruckner, C. Mohr, H. Hofmeister, *Supported gold nanoparticles from quantum dot to mesoscopic size scale: effect of electronic and structural properties on catalytic hydrogenation of conjugated functional groups*, J. Am.

Chem. Soc., **122**, 11430-11439 (2000)

[3.81] M. Pietrowski, M. Wojciechowska, *The origin of increased chemoselectivity of platinum supported on magnesium fluoride in the hydrogenation of chloronitrobenzene*, Catal. Today, **169**, 217-222 (2011)

[3.82] K.-i. Shimizu, T. Yamamoto, Y. Tai, A. Satsuma, *Selective hydrogenation of nitrocyclohexane to cyclohexanone oxime by alumina-supported gold cluster catalysts*, J. Mol. Catal. A: Chem., **345**, 54-59 (2011)

[3.83] K.-i. Shimizu, Y. Miyamoto, T. Kawasaki, T. Tanji, Y. Tai, A. Satsuma, *Chemoselective hydrogenation of nitroaromatics by supported gold catalysts: mechanistic reasons of size- and support-dependent activity and selectivity*, J. Phys. Chem. C, **113**, 17803-17810 (2009)

[3.84] R. Baltzly, A.P. Phillips, *The catalytic hydrogenolysis of halogen compounds*, J. Am. Chem. Soc., **68**, 261-265 (1946)

[3.85] F. Fajardie, J.F. Tempere, J.M. Manoli, G. Djega-Mariadassou, G. Blanchard, *Ceria lattice oxygen ion substitution by Cl- during the reduction of Rh(Cl)/CeO_2 catalysts. Formation and stability of CeOCl*, J. Chem. Soc.-Faraday Trans., **94**, 3727-3735 (1998)

[3.86] L. Kepinski, J. Okal, *Occurrence and mechanism of formation of CeOCl in Pd/CeO_2 catalysts*, J. Catal., **192**, 48-53 (2000)

[3.87] B. Aristizabal, C.A. Gonzalez, I. Barrio, M. Montes, C.M. de Correa, *Screening of Pd and Ni supported on sol-gel derived oxides for dichloromethane hydrodechlorination*, J. Mol. Catal. A: Chem., **222**, 189-198 (2004)

[3.88] P. Fornasiero, N. Hickey, J. Kaspar, C. Dossi, D. Gava, M. Graziani, *Redox and chemisorptive properties of ex-chloride and ex-nitrate Rh/$Ce_{0.6}Zr_{0.4}O_2$ catalysts - 1. Effect of low-temperature redox cycling*, J. Catal., **189**, 326-338 (2000)

[3.89] K.-D. Jung, A.T. Bell, *Role of hydrogen spillover in methanol synthesis over Cu/ZrO_2*, J. Catal., **193**, 207-223 (2000)

[3.90] M. Keane, G. Tavoularis, *The role of spillover hydrogen in gas phase catalytic aromatic hydrodechlorination and hydrogenation over nickel/silica*, React. Kinet. Catal. Lett., **78**, 11-18 (2003)

[3.91] W.C. Conner, J.L. Falconer, *Spillover in heterogeneous catalysis*, Chem. Rev.,

95, 759-788 (1995)

[3.92] J. Wang, L.M. Huang, Q.Z. Li, *Influence of different diluents in Pt/Al_2O_3 catalyst on the hydrogenation of benzene, toluene and o-xylene,* Appl. Catal. A: Gen., **175**, 191-199 (1998)

[3.93] A.D. Lueking, R.T. Yang, *Hydrogen spillover to enhance hydrogen storage - study of the effect of carbon physicochemical properties,* Appl. Catal. A: Gen., **265**, 259-268 (2004)

[3.94] P. Baeza, M.S. Ureta-Zanartu, N. Escalona, J. Ojeda, F.J. Gil-Llambias, B. Delmon, *Migration of surface species on supports: a proof of their role on the synergism between CoS_x or NiS_x and MoS_2 in HDS,* Appl. Catal. A: Gen., **274**, 303-309 (2004)

[3.95] E. Klemm, B. Amon, H. Redlingshofer, E. Dieterich, G. Emig, *Deactivation kinetics in the hydrogenation of nitrobenzene to aniline on the basis of a coke formation kinetics - investigations in an isothermal catalytic wall reactor,* Chem. Eng. Sci., **56**, 1347-1353 (2001)

CHAPTER 4

An Examination of Catalyst Deactivation in Nitroarene Hydrogenation over Supported Gold

In previous chapters, deactivation has been observed over Au catalysts in gas phase hydrogenation of *p*-chloronitrobenzene. In this chapter, source of Au catalyst deactivation and possible regeneration are studied, using Au/Al_2O_3 as a model catalyst. This chapter has been submitted to Chemical Engineering Journal for publication (see publication No. 1). Co-author M.L conducted part of the catalytic measurements and co-wrote the chapter. F.C.-L. and D.L. performed the STEM, XPS and chemical control calculations. L.K.-M. and M.A.K. directed the project and co-wrote the chapter.

4.1 Introduction

The chemical sector is experiencing a shift in emphasis from high reactant turnover to catalytic production routes that maximise selectivity to target high value products [1]. Selective production of functionalised anilines (extensively used in the manufacture of pharmaceuticals, agrochemicals and dyes [2]) from the corresponding nitro-compound is challenging. Conventional methodologies based on the Béchamp process have become obsolete due to the generation of large quantities (5-20 times greater than the target amine) of toxic waste in the form of iron hydroxide sludge, neutralisation salts and organic by-products [3]. Catalytic production has focused on batch liquid phase hydrogenation at elevated pressures (up to 40 atm [4,5]) and temperatures (up to 542 K [6]). In terms of process development, a switch to continuous gas phase operation at atmospheric pressure offers clear advantages in terms of energy efficiency for high throughput. We have previously reported the selective gas phase hydrogenation of a range of substituted nitroarenes over oxide supported Au [7-10]. Reaction exclusivity to the amine was achieved with enhanced selective hydrogenation rates for Au particles <5 nm. Targeted $–NO_2$ reduction in the presence of other reactive functionalities (*e.g.* –Cl,

–CH_3 or –OH) in continuous operation represents a significant advance over unselective batch processes using Pd [11-13], Pt [14-16], Ru [17] and Ni [18-20] catalysts. However, reaction over Au catalysts was typically accompanied by a temporal loss of activity [8,21], which must be addressed in the development of a sustainable hydrogenation process.

A search through the literature failed to unearth any published study that explicitly identifies the cause(s) of Au catalyst deactivation in nitroarene hydrogenation in standard liquid or gas phase operation. Deactivation has been a feature of gas phase nitroaromatic (nitrobenzene [22-26] and chloronitrobenzene (CNB) [27]) hydrogenation over hydrotalcite [22,23,28], Al_2O_3 [23,27], SiO_2 [25], MgO [23], activated carbon [26] and kieselguhr [24] supported Pd [22,23,27], Ni [26] and Cu [24,25]. This was ascribed to coke deposition [23-26] and/or the deleterious effects of water [22,23] generated as by-product. Vishwanathan *et al.* [27] reported increased resistance to coke formation during *o*-CNB hydrogenation due to alkali metal doping of Pd/Al_2O_3 but did not provide any clear reason for this effect. It should be noted that Pietrowski and Wojciechowska did not observe any deactivation (for up to 5 h on-stream) in *o*-CNB conversion over Ru/MgF_2 [29]. In this study, we have set out to identify the source of Au catalyst deactivation, taking the selective hydrogenation of *p*-CNB over Au/Al_2O_3 as a model system. To this end, we have evaluated the effect of inlet H_2/nitroarene, which has been proposed as a process variable that affects catalyst deactivation in hydrogenation [30].

4.2 Experimental

4.2.1 Catalyst Preparation and Activation

The γ-Al_2O_3 support (Puralox, Condea Vista Co.) was used as received. Au/Al_2O_3 (1% w/w) was prepared by deposition-precipitation (DP) using urea as basification agent. An aqueous mixture of urea (100-fold excess) and $HAuCl_4$ (4.4×10^{-5} mol cm^{-3}) was added to the support (30 g). The suspension was stirred and heated to 353 K (2 K min^{-1}) where the pH progressively increased to reach *ca.* 7 after 3 h as a result of thermally induced urea decomposition [31]. The solid was separated by centrifugation, washed at least ten

times with deionised water (with centrifugation between each washing until chlorine free) and dried in He (45 cm^3 min^{-1}) at 373 K (2 K min^{-1}) for 5 h. The catalyst was sieved (ATM fine test sieves) to a mean particle diameter (d_p) of 65 μm and stored at 277 K under He in the dark. Prior to use, the catalyst was activated in 60 cm^3 min^{-1} H_2 at 2 K min^{-1} to 603 K, which was maintained for 1 h.

4.2.2 Catalyst Characterisation

The Au content was measured by atomic absorption spectroscopy (Shimadzu AA-6650 spectrometer with an air-acetylene flame) from the diluted extract in aqua regia (25% v/v HNO_3/HCl). Temperature programmed reduction (TPR) and H_2 chemisorption were recorded using the commercial CHEM-BET 3000 (Quantachrome Instruments) unit with data acquisition/manipulation using the TPR Win™ software. The sample was loaded into a U-shaped Pyrex glass cell (3.76 mm i.d.) and heated in 17 cm^3 min^{-1} (Brooks mass flow controller) 5% v/v H_2/N_2 to 603 K at 2 K min^{-1}. The effluent gas passed through a liquid N_2 trap and H_2 consumption was monitored by a thermal conductivity detector (TCD). The activated sample was swept with a 65 cm^3 min^{-1} N_2 for 1.5 h, cooled to ambient or reaction (423 K) temperature and subjected to H_2 chemisorption using a pulse (10 μl) titration procedure. Hydrogen pulse introduction was repeated until the signal area was constant. In a blank test, chemisorption measurements for the (Al_2O_3) support alone did not result in any detectable uptake. Nitrogen adsorption-desorption isotherms were obtained at 77 K using the commercial automated Micromeritics Gemini 2390 system. Specific surface areas were calculated from the isotherms using the standard BET method. The mean pore size, cumulative pore volume and pore size distribution were obtained by BJH analysis [32] from the desorption isotherm; samples were outgassed at 423 K for 1 h prior to analysis. Thermogravimetric analysis (TGA) and differential scanning calorimetry (DSC) measurements were conducted using a SDT Q600 simultaneous TGA/DSC analyser (TA Instruments) that measured temporal mass and heat flow as a function of temperature. Samples (*ca.* 6 mg, *pre*- and *post*-reaction) were swept with air (100 cm^3 min^{-1}) and

ramped from ambient temperature to 603-1073 K at 10 K min^{-1}, followed by an isothermal hold (for up to 20 h). Elemental carbon analysis was determined using an Exeter CE-440 Elemental Analyser after sample combustion at *ca.* 1873 K.

Powder X-ray diffraction (XRD) was conducted on a Bruker/Siemens D500 incident X-ray diffractometer using Cu Kα radiation. The sample was scanned at 0.02º $step^{-1}$ over the range $20^{o} \leq 2\theta \leq 85^{o}$. The diffractogram pattern was identified using the JCPDS-ICDD reference standards, *i.e.* Au (04-0784) and γ-Al_2O_3 (10-0425). Gold particle size was determined by scanning transmission electron microscopy (STEM, JEOL 2200FS operated at an accelerating voltage of 200 kV with a nominal 0.5 nm probe size), employing Gatan DigitalMicrograph 1.82 for data acquisition/manipulation. Using an annular dark field detector with a minimum collection semi-angle of ~100 mrad, the recorded images have an intensity approximately proportional to $tZ^{1.7-2}$ (sample thickness *t,* average atomic number Z), facilitating good contrast between heavy and lighter element components. Samples for analysis were prepared by dispersion in acetone and deposited on a holey carbon/Cu grid (300 mesh). The number weighted mean Au diameter (d_{STEM}) was determined from a count of 300 particles

$$d_{STEM} = \frac{\sum_i n_i d_i}{\sum_i n_i} \qquad (4.1)$$

where n_i is the number of particles of diameter d_i. X-ray photoelectron spectroscopy (XPS) was conducted using an Axis Ultra instrument (Kratos Analytical) under ultra-high vacuum conditions (<10^{-8} Torr) with a monochromatic Al Kα X-ray source (1486.6 eV). The source power was maintained at 150 W and emitted photoelectrons sampled from a 750×350 μm^2 area at a take-off angle = 90°. The analyser pass energy was 80 eV for survey spectra (0–1000 eV) and 40 eV for high resolution spectra (Au $4f_{5/2}$ and Au $4f_{7/2}$). We define adventitious carbon as carbonaceous materials that deposit on all air exposed surfaces *via* physical adsorption [33]. The C (1*s*) profile for this adventitious carbon is characterised by a principal peak at 284.7±0.2 eV, indicative of alkyl type species (C-C, C-H) [34] and was used as an internal standard to compensate for charging effects [35]. Spectra curve fitting were performed using the CasaXPS

software.

4.2.3 Gas Phase Hydrogenation of p-Chloronitrobenzene (p-CNB)

The reactant (*p*-CNB, Sigma-Aldrich ≥98%) and solvent (ethanol, Fluka >98%) were used as supplied, without further purification. All the gases used (H_2, N_2, O_2 and He) were of ultra high purity (>99.99%, Carbagas/BOC).

Reactions were carried out under atmospheric pressure at 423 K, following *in situ* activation, in a continuous flow fixed bed (L = 0.4 cm) vertical glass reactor of internal diameter (d_r) = 12 mm. A layer of borosilicate glass beads (2 mm) served as preheating zone, ensuring that the *p*-CNB reactant was vaporised and reached reaction temperature before contacting the catalyst. Isothermal conditions (±1 K) were ensured by diluting the catalyst bed with ground glass (65 μm; catalyst bed length (L) = 0.4 cm); the ground glass was mixed thoroughly with catalyst before insertion into the reactor. Reaction temperature was continuously monitored by a thermocouple inserted in a thermowell within the catalyst bed. The *p*-CNB reactant was delivered as an ethanolic solution to the reactor *via* a glass/teflon air-tight syringe and teflon line using a microprocessor controlled infusion pump (Model 100 kd Scientific) at a fixed calibrated flow rate. A *co*-current flow of *p*-CNB and H_2 (or H_2/N_2) was maintained at $GHSV = 4\times10^3 - 22\times10^3$ h^{-1} with an inlet *p*-CNB molar flow (F) = 0.38 mmol h^{-1}. The ratio of catalyst mass (W) to the feed (W/F) spanned the range 13-131 g h mol^{-1}. Contact time (τ = 0.17–1 s) was adjusted by altering H_2 flow rate, maintaining a constant bed volume and inlet W/F. The reactor effluent was frozen in a liquid N_2 trap for subsequent capillary GC analysis. In a series of blank tests, passage of *p*-CNB (i) in a stream of H_2 through the empty reactor or over the support alone and (ii) in a flow of N_2 over Au/Al_2O_3, did not result in any detectable conversion. Catalyst regeneration *post*-reaction was carried out by thermal treatment (2 K min^{-1} from 423 K to 603 K) in air (60 cm^3 min^{-1}), maintaining the final temperature for 20 h. The catalyst was then contacted with (60 cm^3 min^{-1}) H_2 at 603 K for 1 h, temperature lowered to 423 K and catalytic activity/selectivity was subsequently measured as described above.

The composition of the reactor effluent (frozen in a liquid N_2 trap) was analyzed using a Perkin-Elmer Auto System XL chromatograph equipped with a programmed split/splitless injector and a flame ionization detector, employing a DB-1 50 m × 0.20 mm i.d. 0.33 μm film thickness capillary column (J&W Scientific). Data acquisition and manipulation were performed using the TotalChrom Workstation Version 6.3.2 (for Windows) chromatography data system. Fractional hydrogenation ($X_{p\text{-}CNB}$) was obtained from

$$X_{p\text{-CNB}} = \frac{[p\text{-CNB}]_{in} - [p\text{-CNB}]_{out}}{[p\text{-CNB}]_{in}} \tag{4.2}$$

where selectivity to *p*-chloroaniline (*p*-CAN) is given by

$$S_{p\text{-CAN}}(\%) = \frac{[p\text{-CAN}]_{out}}{[p\text{-CNB}]_{in} - [p\text{-CNB}]_{out}} \times 100 \tag{4.3}$$

Repeated reactions with different samples from the same batch of catalyst delivered conversion/selectivity values that were reproducible to within ±5%.

Table 4.1: Physico-chemical characteristics of Au/Al_2O_3 *pre*- and *post*- reaction.

Au loading (% w/w)		1.1
BET area ($m^2\ g^{-1}$)		191[a], 166[b], 169[c]
Total pore volume ($cm^3\ g^{-1}$)		0.45[a], 0.36[b], 0.33[c]
Mean pore radius (Å)		31[a], 29[b], 29[c]
TPR T_{max} (K)		450
H_2 chemisorption (μmol g_{Au}^{-1})		32[b,d], 396[b,e], 119[c,e]
Au size range (nm)		1-8[b,c]
d_{STEM} (nm)		3.6[b]; 3.2[c]
XPS Au binding energies (eV)	$4f_{5/2}$	83.4[b,c]
	$4f_{7/2}$	87.0[b,c]
Carbon content (% w/w)		0.9[b,f]; 6.3[c,f]

[a]Al_2O_3 support; [b]activated Au/Al_2O_3 *pre*-reaction; [c]Au/Al_2O_3 *post*-reaction; [d]at 298 K; [e]at 423 K; [f]from elemental analysis

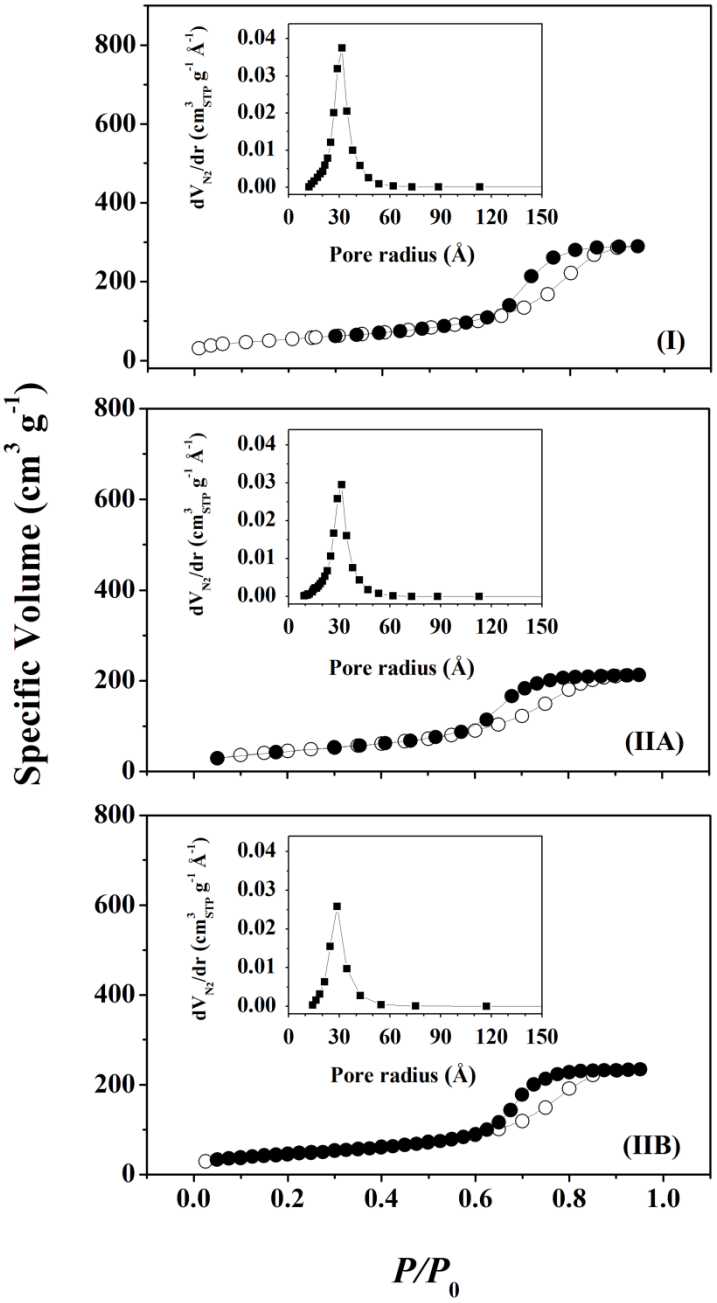

Figure 4.1: Nitrogen adsorption (solid symbols)/desorption (open symbols) isotherms for (I) Al_2O_3 and (II) Au/Al_2O_3 (A) *pre-* and (B) *post*-reaction. *Inset*: pore size distribution.

4.3 Results and Discussion

4.3.1 Catalyst Characterisation: Pre-reaction

Nitrogen adsorption/desorption isotherms for the Al_2O_3 support **(I)** can be compared with those generated for the activated (*post*-TPR) Au/Al_2O_3 **(IIA)** in **Figure 4.1**. The isotherms for Al_2O_3 show a hysteresis loop at $P/P_0 > 0.6$ that is characteristic of

mesoporous material (type IV IUPAC classification) [36]. The associated BET surface area (191 m^2 g^{-1}), pore volume (0.45 cm^3 g^{-1}) and mean radius (31 Å, see **Table 4.1**) agree with values (area <250 m^2 g^{-1} and pore volume <0.50 cm^3 g^{-1}) quoted in the literature [37] for γ-Al_2O_3. An increase in BET area (to 210 m^2 g^{-1}) was observed after Au deposition in the *as prepared* Au/Al_2O_3. Leerat and co-workers [38] and Wang *et al.* [39] also recorded a measurable increase in surface area (300→310 m^2 g^{-1}; 90→96 m^2 g^{-1}) for Au/Al_2O_3 and Au/TiO_2, respectively, prepared by deposition/precipitation. Postole *et al.* [40] reported a similar effect (233→249 m^2 g^{-1}) after the incorporation of Au on boron nitride, which they ascribed to the development of nano-pores during sample synthesis and drying. Catalyst activation by temperature programmed reduction (TPR) was monitored and the resultant profile (**Figure 4.2(I)**) is characterised by a single positive (H_2 consumption) peak with an associated maximum (T_{max}, **Table 4.1**) at 450 K. The amount of hydrogen consumed during TPR matches that required for Au^{3+} reduction to Au^0 [41]. Bus *et al.* [42], applying time-resolved *in situ* X-ray absorption spectroscopy (XAS), established the formation of oxidic or hydroxidic Au^{3+} species on Al_2O_3 that were reduced to zero valent Au after H_2 treatment at 440 K. The total (BET) surface area (166 m^2 g^{-1}) and pore volume (0.36 cm^3 g^{-1}) of Au/Al_2O_3 *post*-TPR were lower than those of the support (**Table 4.1**) but the pore size distribution (**Figure 4.1(IIA)**) was not significantly altered. Hydrogen chemisorption measurements are of practical importance in hydrogenation applications where the value recorded for Au/Al_2O_3 at ambient temperature (32 μmol g_{Au}^{-1}: **Table 4.1**) was far lower than the uptake determined for standard supported transition metal catalysts (*e.g.* Al_2O_3 supported Pd = 2450 μmol g_{Pd}^{-1} [43] and Pt = 3870 μmol g_{Pt}^{-1} [44]). This is consistent with the high activation energy barrier for dissociative adsorption on Au due to the filled d band [45]. Hydrogen chemisorption on Au/Al_2O_3 is an activated process with an increased uptake (by an order of magnitude) at the reaction temperature (423 K, **Table 4.1**). Bus *et al.* [46] have also reported a higher H_2 adsorption capacity for Au/Al_2O_3 with an increase in the temperature (298 K → 373 K).

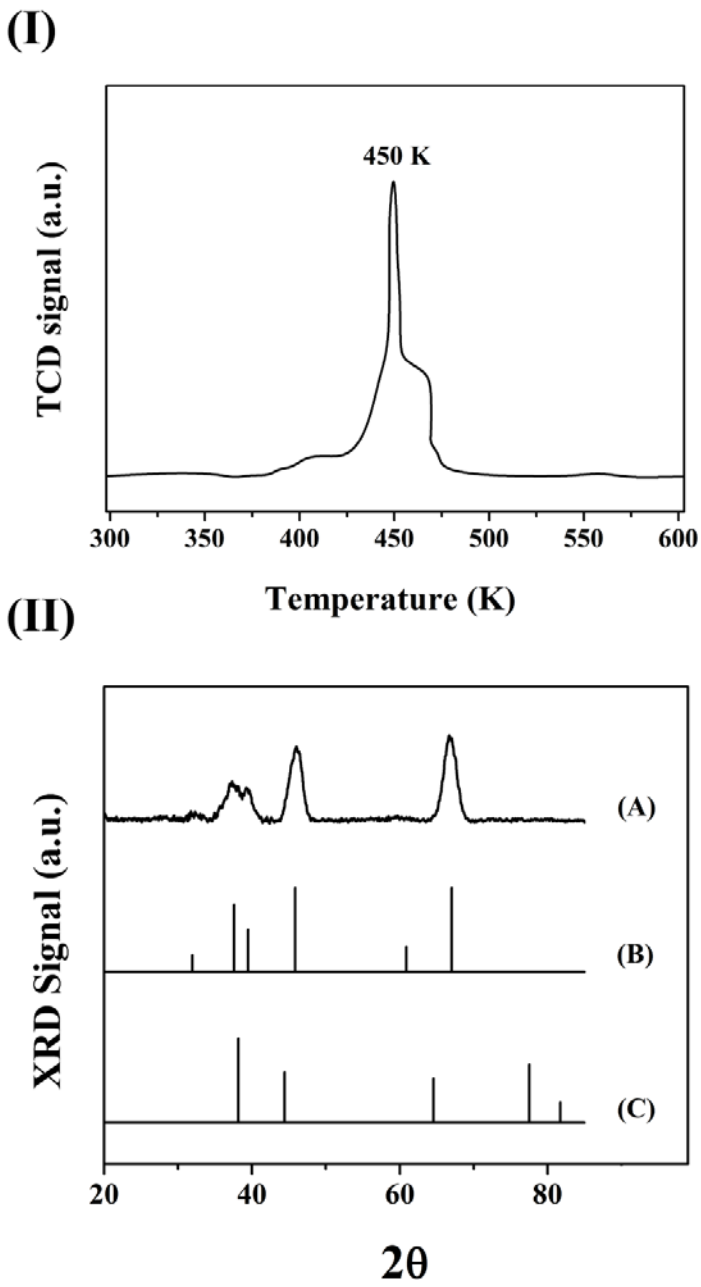

Figure 4.2: (I) Temperature programmed reduction (TPR) profile for Au/Al_2O_3; (II) XRD diffractogram of Au/Al_2O_3 *post*-TPR (A) with JCPDS-ICDD reference for (B) γ-Al_2O_3 (10-0425) and (C) Au (04-0784).

The XRD pattern for the activated catalyst showed four main peaks (**Figure 4.2(IIA)**) at 37.6°, 39.5°, 45.9° and 67.0° that correspond, respectively, to the (311), (222), (400) and (440) planes of γ-Al_2O_3 (**Figure 4.2(IIB)**, JCPDS-ICDD 10-0425). There was no detectable signal due to Au (**Figure 4.2(IIC)**, JCPDS-ICDD 04-0784), suggesting the occurrence of a well dispersed Au phase [47]. Indeed, the representative

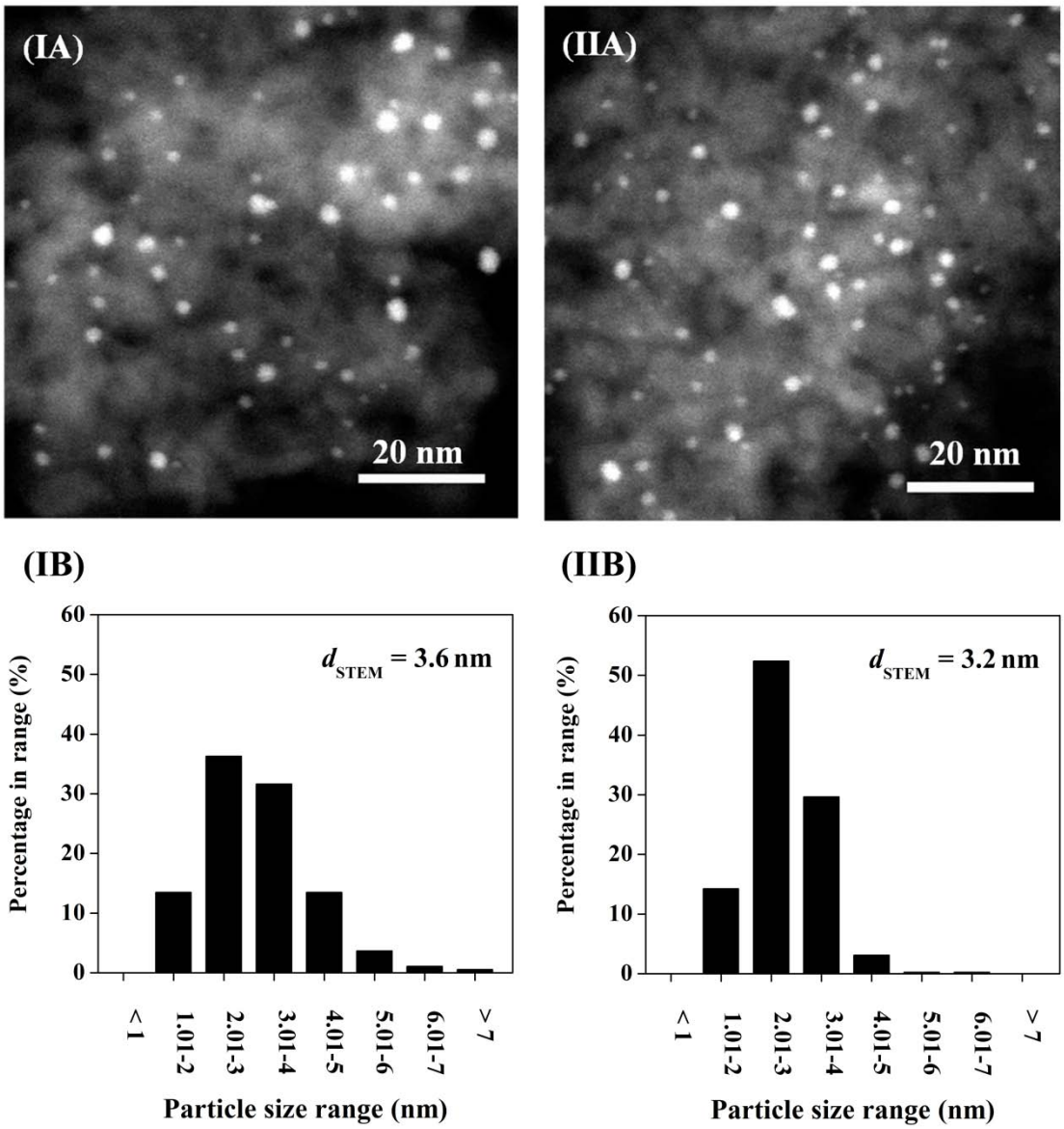

Figure 4.3: (A) Representative STEM images and (B) associated Au size distributions for Au/Al_2O_3 (I) *pre*- and (II) *post*-reaction.

STEM image shown in **Figure 4.3(IA)** confirms the presence of pseudo-spherical Au particles at the nanoscale (1-8 nm) that are homogeneously dispersed on the surface. The size distribution histogram in **Figure 4.3(IB)** gives a mean value of 3.6 nm with a predominant component (95%≤5 nm, the Au particle size range that has been identified as a crucial requirement for significant hydrogenation activity [48]. The XPS spectrum over the Au binding energy (BE) region, shown in **Figure 4.4(I)**, is characterised by two low intensity peaks with associated BE = 87.0 eV and 83.4 eV corresponding to $4f_{5/2}$ and $4f_{7/2}$ levels, respectively [49,50]. These BE values are

appreciably lower than those reported for oxidised (Au^{3+} $4f_{7/2}$ = 85.5-87.6 eV; Au^{+} $4f_{7/2}$ = 85.8-86.0 eV, [51]) and zero valent Au (Au $4f_{5/2}$ = 87.6 eV, Au $4f_{7/2}$ = 84.0 eV [49,50]), suggesting metal-support interaction that modifies Au electronic character [52]. Arrii *et al*. [53] have reported a similar downward shift in BE for Au on γ-Al_2O_3 (Au $4f_{7/2}$ = 83.1 eV) that they attributed to electron transfer from the support. This effect has also been observed for a range of alumina supported transition metals (Pd, Cu, Ni and Cr) [54]. The characterisation measurements demonstrate formation of nano-scale $Au^{\delta-}$ particles with a narrow size distribution.

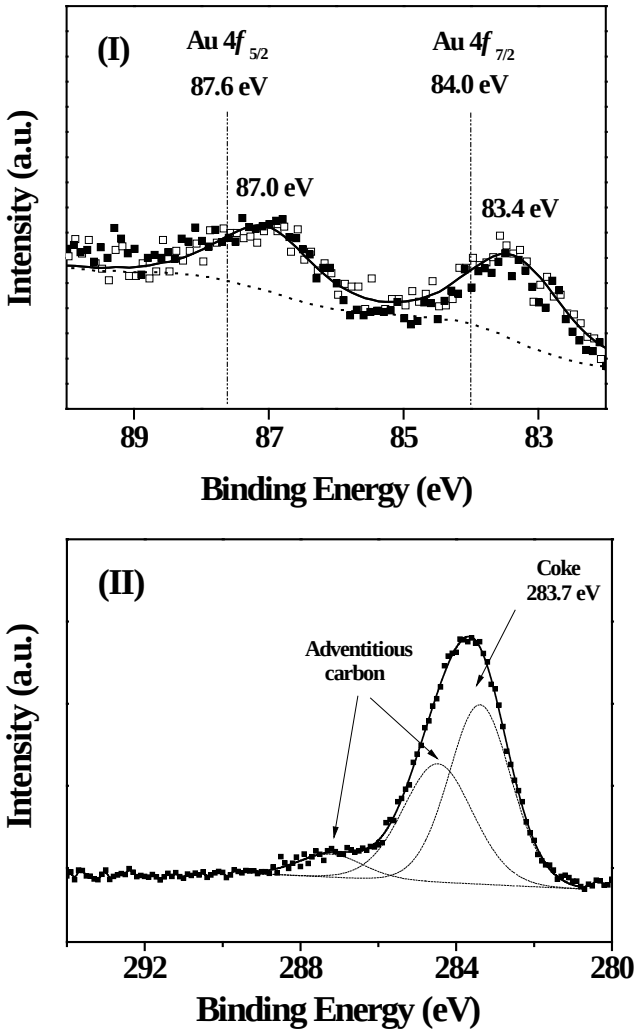

Figure 4.4: XPS spectrum over the (I) Au 4*f* and (II) C 1*s* region for Au/Al_2O_3 *pre*- (open symbols) and *post*- (solid symbols) reaction. *Note*: Dotted vertical lines in (I) identify position of the Au $4f_{5/2}$ and $4f_{7/2}$ peaks characteristic of Au^0 [49,50].

4.3.2 Catalyst Performance: Gas Phase Hydrogenation of p-Chloronitrobenzene (p-CNB)

We must stress from the outset that, under all reaction conditions, *p*-CNB was converted solely to the target *p*-CAN, a high value chemical with multiple applications in the fine chemical sector [55]. Reaction exclusivity results from a preferential $–NO_2$ activation on oxide supported Au that prevails even in the presence of other reactive (C=C, carbonyl, amide and ester) functions, as demonstrated by FTIR analysis [56].

4.3.2.1 Evaluation of Heat and Mass Transfer Limitations

A meaningful analysis of catalyst performance requires process operation under intrinsic kinetic control with negligible heat/mass transfer constraints. The application of plug-flow conditions ensures that bypass or axial dispersion effects are reduced while maintaining a radially well mixed flow where transport gradients are minimised [57,58]. The parameters and minimum values necessary to guarantee plug-flow are presented in **Table 4.2** [59-61]. The results confirm plug-flow operation.

Table 4.2: Requirements for plug-flow reactor operation [60].

Parameter	**Required**	**This work**
d_r/d_p	>10	185
L/d_p	>50	68
$\left(\frac{L}{d_p}\right)_{min} = (92.0)\cdot Re_p^{-0.23}\cdot n\cdot \ln\left(\frac{1}{1-X_{p-CNB}}\right)$ $Re_p = \frac{u\cdot d_p}{\nu_{H_2}}$	$L/d_p > (L/d_p)_{min}$	$(L/d_p)_{min} < 66$ $L/d_p = 68$

n (reaction order) = 1 [60]; $X_{p\text{-CNB}}$ = 0.15; u (superficial gas velocity) = 0.4-2.7 cm s^{-1}; ν_{H2} (kinematic viscosity of hydrogen) = 1.88 cm^2 s^{-1} [61]

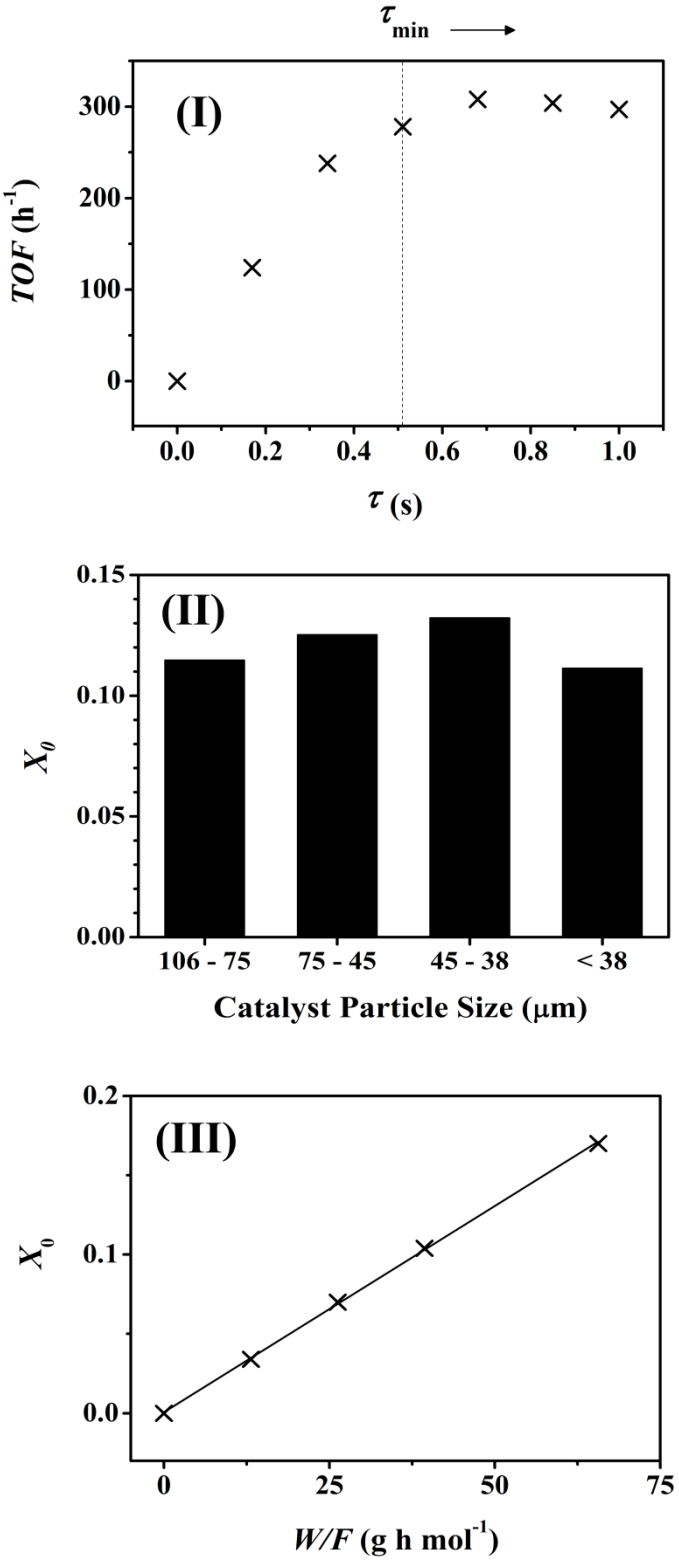

Figure 4.5: Variation of turnover frequency (*TOF*) and initial fractional conversion (X_0) with (I) contact time (τ), (II) catalyst particle size and (III) *W/F*.

Catalytic activity was assessed on the basis of initial fractional *p*-CNB conversion (X_0) obtained by fitting time on-stream $X_{p\text{-CNB}}$ data [10,28,43]. The resultant X_0 was

used to calculate initial turnover frequency (*TOF*) or rate per active site (based on Au dispersion from STEM analysis) as a measure of intrinsic catalyst performance. External mass/heat transfer constraints were evaluated using the well established criterion of varying contact time (τ) [57]. The results are presented in **Figure 4.5(I)** where it can be seen that *TOF* was largely insensitive to increasing τ from 0.5 to 1.0 s, indicative of minimal external mass and/or heat transport contributions to hydrogenation rate. At $\tau < 0.5$ s, the decline in *TOF* is the result of transport limitations that inhibit hydrogenation. Based on these results, τ was set at 0.5 s for subsequent tests.

The determination of isothermal conversion for particles with different size at constant space velocity is a robust test of intraphase concentration gradients [57]. Any variation in activity due to particle size is indicative of internal mass transfer limitations where invariance is consistent with chemical kinetic control. The results generated (see **Figure 4.5(II)**) indicate that internal mass transport effects do not contribute significantly to hydrogenation for catalyst particle size (d_p) ≤ 106 μm.

The parameters examined and results obtained in the evaluation of possible internal heat transfer constraints are given in **Table 4.3** [62-64]. The greatest temperature difference for a catalyst particle (ΔT_{max}) in the bed is determined by a combination/integration of microscopic mass and heat balances. This requires input due to reaction enthalpy (at 423 K) and the effective thermal conductivity of the bed (k_{eff}), which can be calculated using the approach of Woodside and Messmer [62]. The effective diffusivity (D_{eff}) is obtained from the molecular diffusivity of *p*-CNB in H_2 ($D_{p\text{-CNB},H_2}$) and tortuosity ($\tau_{Al_2O_3}$) of Al_2O_3 where the porosity ($\varepsilon_{Al_2O_3} = 0.52$) and $\tau_{Al_2O_3}$ (1.93) suggest low impedance with respect to reactant/product diffusion and the actual (or average) path traversed by the reacting species in the bulk is similar to that in the interstitial fluid [65]. The $D_{p\text{-CNB},H_2}$ parameter was obtained from the Satterfield correlation [63] (see **Table 4.3**) with contributions from component molecular weights (Mw_i), Lennard-Jones energy, binary pair (*p*-CNB and H_2) characteristic length ($\sigma_{p\text{-CNB},H_2}$) and the collision integral (Ω_D). The characteristic length (σ_{H_2}) and Lennard-Jones potential $(\varepsilon/k)_{H_2}$ for H_2 are taken from the literature [64]. The values for *p*-CNB were obtained from the critical properties (T_c, V_c, P_c and Z_c) and calculated

Table 4.3: Tests applied to assess internal heat transport limitations [62-64].

Parameter	Expression	Results
k_{eff}	$k_{\text{eff}} = k_{Al_2O_3}\left(\frac{k_{H_2}}{k_{Al_2O_3}}\right)^{\varepsilon_{Al_2O_3}}$	1.96 W m^{-1} K^{-1}
$\varepsilon_{Al_2O_3}$	$\varepsilon_{Al_2O_3} = \rho_{Al_2O_3} \times (\text{Pore Volume})$	0.52
$D_{\text{eff},p\text{-CNB}}$	$D_{\text{eff},p\text{-CNB}} = \left(\frac{\varepsilon_{Al_2O_3}}{\tau_{Al_2O_3}}\right) D_{p\text{-CNB},H_2}$	1.08 × 10^{-5} m^2 s^{-1}
$\tau_{Al_2O_3}$	$\tau_{Al_2O_3} = \frac{1}{\varepsilon_{Al_2O_3}}$	1.93
$D_{p\text{-CNB},H_2}$	$D_{p\text{-CNB},H_2} = 0.001858\left(\frac{\sqrt{T^3\left(\frac{Mw_{p\text{-CNB}} + Mw_{H_2}}{Mw_{p\text{-CNB}} \cdot Mw_{H_2}}\right)}}{P \cdot \sigma^2_{p\text{-CNB},H_2} \cdot \Omega_D}\right)$	3.99 × 10^{-5} m^2 s^{-1}
$\sigma_{p\text{-CNB},H2}$	$\sigma_{p\text{-CNB},H_2} = \frac{\sigma_{p\text{-CNB}} + \sigma_{H_2}}{2}$	5.72 Å
$(\varepsilon/k)_{p\text{-CNB}}$	$\left(\frac{\varepsilon}{k}\right)_{p\text{-CNB}} = 65.3 \cdot T_c \cdot Z_c^{18/5}$	186.1 K
$\sigma_{p\text{-CNB}}$	$\sigma_{p-\text{CNB}} = 0.1866 \cdot V_c^{1/3} \cdot Z_c^{-6/5}$	8.6 Å
$\Delta T_{\max}$	$\Delta T_{\max} = \frac{D_{\text{eff},p-\text{CNB}}(-\Delta H) C_{p-\text{CNB,bulk}}}{k_{\text{eff}}}$	0.5 K
β_e	$\beta_e = \frac{\Delta T_{\max}}{T}$	0.001

k_{Al2O3} = 23.0 W m^{-1} K^{-1} [61], k_{H2} = 0.2 W m^{-1} K^{-1} [61]; ρ_{Al2O3} = 1154 kg m^{-3};
σ_{H2} = 2.83 Å [64], $(\varepsilon/k)_{H2}$ = 59.7 K [64]; T_c = 730.25 K, V_c = 387 cm^3 g^{-1} mol^{-1},
P_c = 33.15 atm, Z_c = 0.21 [64]; Ω_D =0.88 [63]; $\Delta H_{423\,K}$ = 467.7 kJ mol^{-1} [43].

using Lydersen's method [64]; the extracted values are given in **Table 4.3**. The collision

integral (Ω_D =0.88) is available as a tabulated dependence on $kT/\varepsilon_{p\text{-CNB},H_2}$ [63]. The binary diffusivity of *p*-CNB in H_2 was estimated as 4×10^{-5} m^2 s^{-1}, which is of the same order of magnitude as experimental values obtained by gas chromatography for nitroarenes in H_2 or N_2 as carrier gas under similar reaction conditions (P = 1 atm, T = 488-493 K, $D_{\text{nitrobenzene},H_2} = 8 \times 10^{-5}$ m^2 s^{-1} [66]; P = 1 atm, T = 498 K, $D_{o\text{-nitrotoluene},N_2} = 2 \times 10^{-5}$ m^2 s^{-1} [67]). This yields a maximum temperature difference of 0.5 K for the catalyst particle, corresponding to an external Prater number (β_e) (at 423 K) of 0.001, which is sufficiently low to disregard internal heat profiles.

The above tests have established reaction conditions wherein concentration and temperature gradients in the catalyst bed are minimised and differential reactor conditions apply. This is further corroborated by the linear correlation (passing through the origin, **Figure 4.5(III)**) between X_0 and W/F, confirming chemical control where external or internal transport effects do not contribute to catalyst performance. Kinetic control prevails where τ = 0.5 s, particle size = 75 μm and $F = 3.8 \times 10^{-4}$ mol h^{-1}. These conditions were applied in further catalyst evaluation.

4.3.2.2 Effect of inlet H_2/p-CNB Ratio

Turnover of *p*-CNB over Au/Al_2O_3 was elevated with increasing inlet H_2/*p*-CNB (stoichiometry for *p*-CAN formation = 3) to attain a limiting value (**Figure 4.6(I)**). Vishwanathan *et al.* [68] reported a near first order (0.91) dependence of *o*-CNB hydrogenation rate on P_{H_2} over Pd/Al_2O_3 at 523 K with decreasing rate (and negative order (-0.23) in P_{H_2}) at higher temperatures (up to 583 K). Temporal catalyst stability (expressed as molar *p*-CAN production per mol Au) is presented in **Figure 4.6(II)**, taking reaction at H_2/*p*-CNB = 4 as representative. A decline in *p*-CAN output is evident, leading to a low residual conversion after 8 h on-stream. Hao *et al.* [52] proposed that the deactivation of Au/TiO_2 in *o*-CNB hydrogenation under supercritical CO_2 resulted from the formation of CO and carbonates with oxidation of surface Au^0 by CO_2 but this does not apply to our subcritical catalytic operation. The effect of H_2/*p*-CNB on the extent of catalyst deactivation, given as the ratio of rate obtained after 8 h on-stream (r_{8h})

to the initial value (r_0), is presented in **Figure 4.6(III)**. It can be seen that deactivation was more severe at H_2/*p*-CNB < 20 but was largely insensitive to H_2/*p*-CNB at higher values. The more pronounced catalyst deactivation at lower H_2/*p*-CNB suggests incomplete conversion of reaction intermediates. Indeed, a range of intermediates have been reported for *p*-CNB hydrogenation, including *p*-nitrosochlorobenzene [69,70], *p*-hydroxylamine [69,70] and *p*-(chorophenyl)- hydroxylamine [71]. Our results are in agreement with the work of Petrov *et al.* [24] who observed more severe deactivation of Cu/kieselguhr in gas phase nitrobenzene hydrogenation at lower P_{H_2}. The authors attributed this to coking linked to the generation of surface species ($C_6H_5NO_2$ and C_6H_5NHOH) at lower P_{H_2} where an increase in H_2/nitrobenzene served to convert these species to aniline. Klemm *et al.* [30] also noted a loss of activity in nitrobenzene hydrogenation over Pd/Al_2O_3, which they ascribed to carbon deposition that was more severe at lower P_{H_2}.

4.3.3 Catalyst Characterisation: Post-reaction

A spent Au/Al_2O_3 sample (after 8 h on-stream at H_2/*p*-CNB = 4) that exhibited low residual activity (see **Figure 4.6(II)**) was subjected to characterisation in order to identify the source of the loss of activity. The BET surface area, pore volume and mean radius of the used catalyst (**Table 4.1**) did not deviate significantly from that which characterised the unused activated sample. Indeed, the N_2 adsorption/desorption isotherms and associated pore size distribution largely coincided *pre*- (**Figure 4.1(IIA)**) and *post*- (**Figure 4.1(IIB)**) reaction. In contrast, there was a significant (more than 3-fold) decrease in H_2 chemisorption on the spent catalyst (**Table 4.1**). Lower H_2 uptake capacity can result from (i) decrease in Au dispersion (sintering), (ii) disruption to Au electronic properties and/or (iii) active site occlusion, possibly by carbon deposition. Hydrogen dissociative adsorption/activation occurs on low coordinated Au (corner and edge) sites, which are diminished by sintering resulting in an inhibition of hydrogenation activity [72].

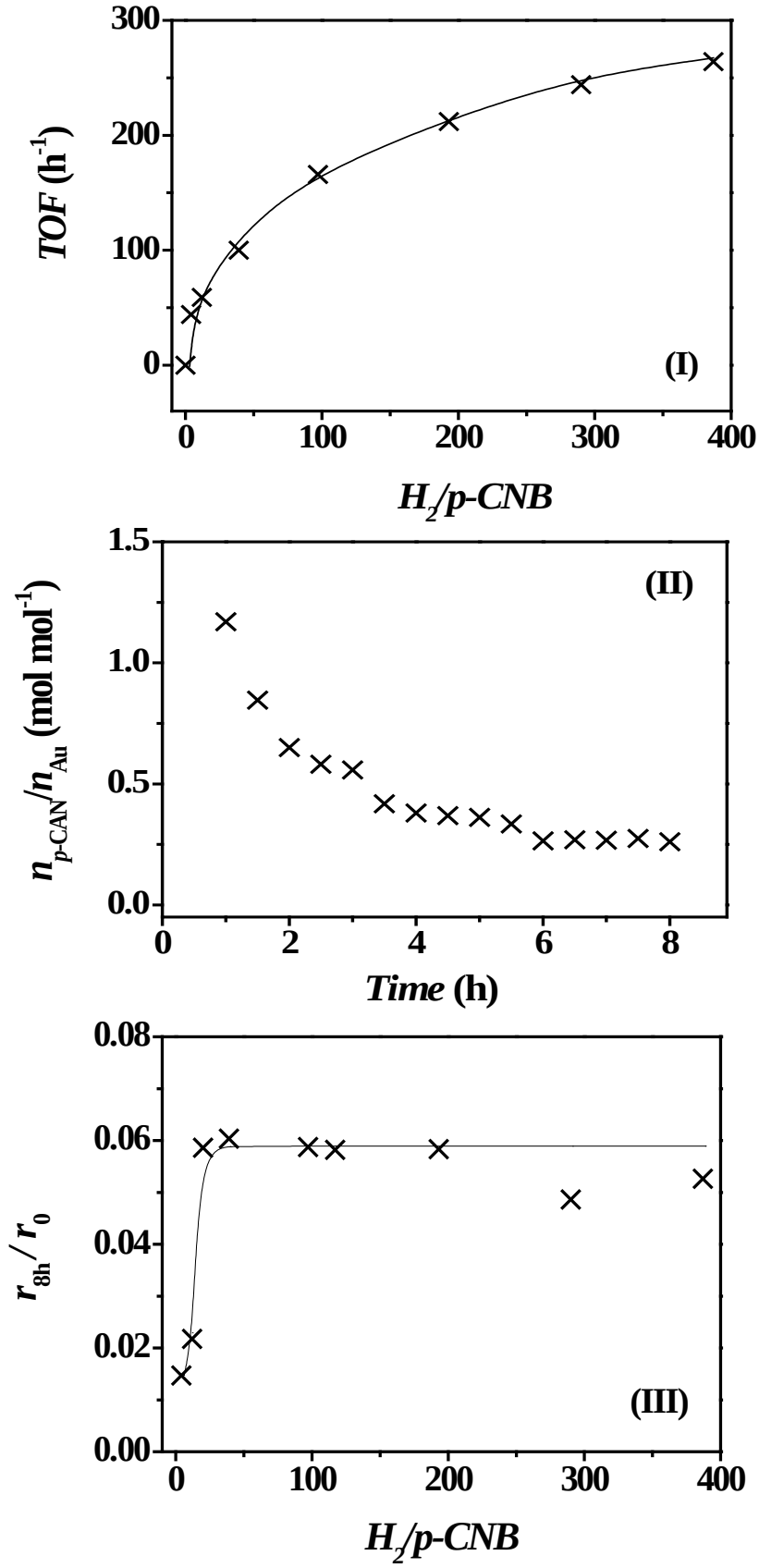

Figure 4.6: (I) *p*-CNB turnover frequency (*TOF*) as a function of inlet H_2/*p*-CNB; (II) variation of *p*-CAN production with time-on-stream at H_2/*p*-CNB = 4; (III) dependence of the degree of catalyst deactivation expressed as the ratio of the rate after 8 h on-stream relative to the initial value (r_{8h}/r_0) on inlet H_2/*p*-CNB.

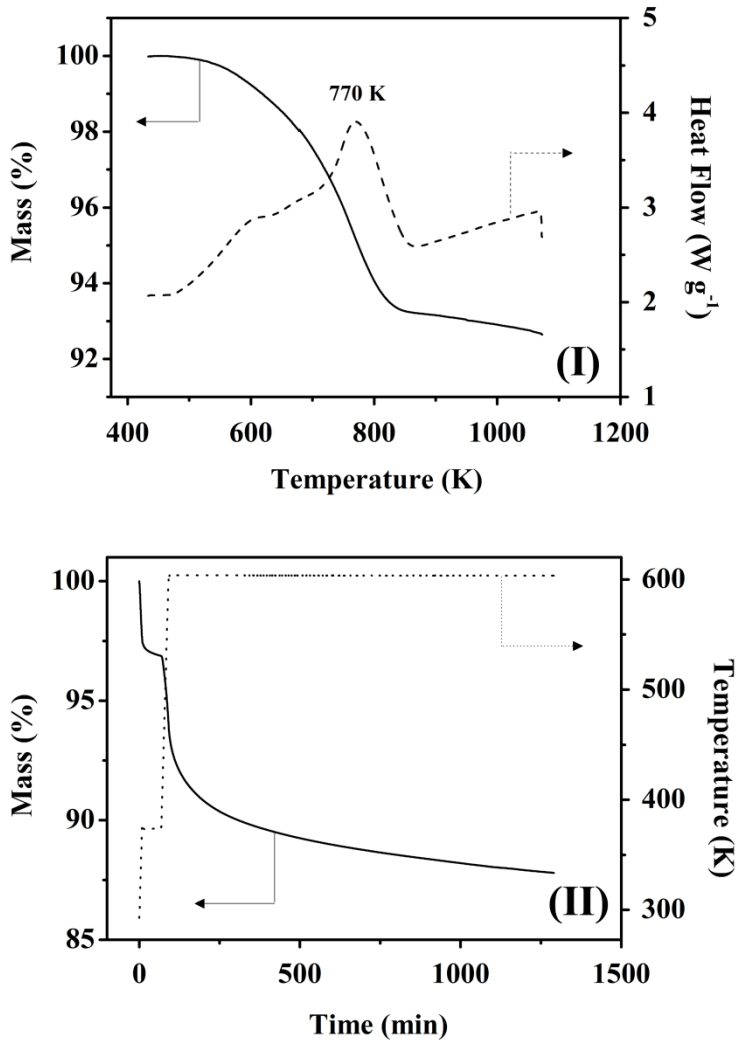

Figure 4.7: TGA (solid line) and DSC (dashed line) profiles generated in the oxidative treatment of spent Au/Al_2O_3 in (100 cm^3 min^{-1}) air at 10 K min^{-1} to (I) 1073 K and (II) 603 K (with a 20 h isothermal hold).

STEM analysis (see representative image in **Figure 4.3(IIA)**) did not revealed any major changes in Au size distribution (**Figure 4.3(IIB)**), 1-7 nm (mean = 3.2 nm) and we can rule out Au sintering during reaction. Moreover, the Au 4*f* XPS profile (**Figure 4.4(I)**) after reaction converges with that generated for the activated catalyst with equivalent BE values that are consistent with surface $Au^{\delta-}$.

Coke deposition during gas phase hydrogenation of acetylene over supported Au has been linked to loss of activity [73,74]. The C 1*s* XPS response of the unused activated Au/Al_2O_3 (not shown) presented two peaks characteristic of adventitious carbon as a result of sample contamination (see section 2.2.). In contrast, the spectrum

for the spent Au/Al_2O_3 (**Figure 4.4(II)**) exhibited an additional signal at lower BE (283.7 eV) that can be attributed to amorphous carbon or "coke" [75,76]. Bulk carbon analysis confirmed the XPS results with an appreciable content in the spent sample (6.3% w/w, **Table 4.1**), suggesting significant carbon deposition during reaction. The formation of a carbonaceous deposit was probed further by TG analysis, as shown in **Figure 4.7**. The unused catalyst was carried through as reference and the profiles presented refer solely to the carbon deposit. A mass loss in the temperature programmed oxidation is evident over the 400-1073 K range (**Figure 4.7(I)**), accompanied by a T_{max} = 770 K in the DSC profile. Castaño *et al.* [78] reported 1.4 % w/w coke formation (by TG oxidation from 300 to 800 K) on Au/HSM-5 during biphenyl hydrogenation. The total mass loss (*ca.* 7% w/w) determined in this study by TG is in reasonable agreement with the carbon content from elemental analysis. This surface carbon deposit can act to occlude/poison Au sites, resulting in suppressed H_2 chemisorption. However, carbon deposition did not result in any measurable change in BET area/porosity characteristics, suggesting that there was no significant pore blockage that could impose transport limitations and impact on hydrogenation rate.

4.3.4 Catalyst Regeneration

Regeneration of deactivated Au catalysts by oxidative treatment has been proposed in the literature for catalytic oxidation reactions [78] but this has yet to be applied in hydrogenation. We note the work of Diao *et al.* [25] who demonstrated carbon burn off from Cu/SiO_2 deactivated during gas phase nitrobenzene hydrogenation but the authors did not report catalytic data for the regenerated catalyst. The TG measurements have demonstrated carbon removal by oxidation (in air) up to 1073 K. However, such a high temperature exothermic treatment can result in significant catalyst structural modifications, notably Au sintering [79], with detrimental consequences for catalytic activity. Bond *et al.* [45] have highlighted the sensitivity of Au catalysts to thermal treatment where Au sintering is more pronounced in air relative to comparable treatment in H_2 or CO. Taking the full range TG profile given in **Figure 4.7(I)**, there is evidence

of significant mass loss at the original catalyst activation temperature (603 K). Applying the same oxidative treatment at 603 K, an isothermal hold for 20 h resulted in the profile shown in **Figure 4.7(II)**. The decrease in mass (by *ca.* 3% w/w) at 373 K can be attributed to loss of moisture and was also observed for the unused catalyst. Further ramping to 603 K resulted in a positive DSC response (not shown) associated with carbon burn-off and an ultimate mass loss that was close to that observed for TGA to 1073 K (**Figure 4.7(I)**). An equivalent oxidative + reductive (to 603 K in H_2) regeneration was applied in the catalyst test operated at H_2/*p*-CNB = 4. The initial rate (3.1 mol mol_{Au}^{-1} h^{-1}) following regeneration was close to that (3.3 mol mol_{Au}^{-1} h^{-1}) delivered by the catalyst in the first reaction cycle while full selectivity to *p*-CAN was retained for the regenerated catalyst, demonstrating the efficiency of the regeneration treatment.

4.4 Conclusions

We have established that carbon deposition is a cause of Au/Al_2O_3 temporal deactivation in the gas phase hydrogenation of *p*-CNB. Under explicit catalytic control, Au/Al_2O_3 promoted exclusive *p*-CAN formation where loss of activity with time on-stream was sensitive to the inlet H_2/*p*-CNB ratio with (4-390) with pronounced deactivation where H_2/*p*-CNB ≤ 390. Comprehensive characterisation of the activated unused and spent (after 8 h on-stream) Au/Al_2O_3 revealed no significant alteration to BET area (167±2 m^2 g^{-1}), porosity (volume = 0.34±0.02 cm^3 g^{-1}, mean radius = 29 Å), Au particle size (mean = 3.4±0.2 nm from STEM analysis) or electronic character ($Au^{\delta-}$ formation by XPS analysis) following reaction. Coke deposition is established by XPS and elemental analysis, which suppressed H_2 chemisorption under reaction conditions by occluding active sites, inhibiting hydrogenation. Oxidative regeneration (in air) followed by reactivation (in H_2) resulted in near complete recovery of the starting activity where full selectivity to *p*-CAN was retained.

4.5 References

[4.1] C. Jiménez-González, P. Poechlauer, Q. B. Broxterman, B.-S. Yang, D. A. Ende, J. Baird, C. Bertsch, R. E. Hannah, P. Dell'Orco, H. Noorrnan, S. Yee, R. Reintjens, A. Wells, V. Massonneau, J. Manley, *Key green engineering research areas for sustainable manufacturing: a perspective from pharmaceutical and fine chemicals manufacturers*, Org. Proc. Res. Dev., **15**, 900-911 (2011)

[4.2] H. U. Blaser, H. Steiner, M. Studer, *Selective catalytic hydrogenation of functionalized nitroarenes: an update*, ChemCatChem, **1**, 210-221 (2009)

[4.3] K. R. Westerterp, E. J. Molga, K. B. van Gelder, Catalytic hydrogenation reactors for the fine chemicals industries. Their design and operation, Stud. Surf. Sci. Catal., **108**, 47-57 (1997)

[4.4] M. Liu, W. Yu, H. Liu, *Selective hydrogenation of o-chloronitrobenzene over polymer-stabilized ruthenium colloidal catalysts*, J. Mol. Catal. A: Chem., **138**, 295-303 (1999)

[4.5] B. Zuo, Y. Wang, Q. Wang, J. Zhang, N. Wu, L. Peng, L. Gui, X. Wang, R. Wang, D. Yu, *An efficient ruthenium catalyst for selective hydrogenation of ortho-chloronitrobenzene prepared via assembling ruthenium and tin oxide nanoparticles*, J. Catal., **222**, 493-498 (2004)

[4.6] N. P. Sokolova, A. A. Balandin, N. P. Maksimova, Z. M. Skul'skaya, *Catalytic reduction of chloronitrobenzene to chloroanilines*, Russ. Chem. Bull., **15**, 1824-1829 (1966)

[4.7] F. Cárdenas-Lizana, S. Gómez-Quero, M. A. Keane, *Exclusive production of chloroaniline from chloronitrobenzene over Au/TiO_2 and Au/Al_2O_3*, ChemSusChem, **1**, 215-221 (2008)

[4.8] F. Cárdenas-Lizana, S. Gómez-Quero, N. Perret, M. A. Keane, *Support effects in the selective gas phase hydrogenation of p-chloronitrobenzene over gold*, Gold Bull., **42**, 124-132 (2009)

[4.9] F. Cárdenas-Lizana, S. Gómez-Quero, N. Perret, M. A. Keane, *Gold catalysis at*

the gas–solid interface: role of the support in determining activity and selectivity in the hydrogenation of m-dinitrobenzene, Catal. Sci. Technol., **1**, 652-661 (2011)

[4.10] F. Cárdenas-Lizana, S. Gómez-Quero, G. Jacobs, Y. Ji, B. H. Davis, L. Kiwi-Minsker, M. A. Keane, *Alumina supported Au–Ni: surface synergism in the gas phase hydrogenation of nitro-compounds*, J. Phys. Chem. C, **116**, 11166-11180 (2012)

[4.11] Q. Xu, X.-M. Liu, J.-R. Chen, R.-X. Li, X.-J. Li, *Modification mechanism of Sn^{4+} for hydrogenation of p-chloronitrobenzene over PVP-Pd/γ-Al_2O_3*, J. Mol. Catal. A: Chem., **260**, 299-305 (2006)

[4.12] G. Zhang, L. Wang, K. Shen, D. Zhao, H. S. Freeman, *Hydrogenation of o-chloronitrobenzene on a Pd/C catalyst doped with metal oxide nanoparticles*, Chem. Eng. J., **141**, 368-374 (2008)

[4.13] L. Jiang, H. Gu, X. Xu, X. Yan, *Selective hydrogenation of o-chloronitrobenzene (o-CNB) over supported Pt and Pd catalysts obtained by laser vaporization deposition of bulk metals*, J. Mol. Catal. A: Chem., **310**, 144-149 (2009)

[4.14] B. Coq, A. Tijani, F. Figuéras, *Immobilization of rhodium complexes of amine-functionalized BDPP and chiraphos on a soluble form of the strongly acidic Nafion-H cation exchange resin*, J. Mol. Catal., **71**, 317-333 (1992)

[4.15] X. Yang, H. Liu, *Influence of metal ions on hydrogenation of o-chloronitrobenzene over platinum colloidal clusters*, Appl. Catal. A: Gen., **164**, 197-203 (1997)

[4.16] X.-X. Han, R.-X. Zhou, G.-H. Lai, B.-H. Yue, X.-M. Zheng, *Effect of transition metal (Cr, Mn, Fe, Co, Ni and Cu) on the hydrogenation properties of chloronitrobenzene over Pt/TiO_2 catalysts*, J. Mol. Catal. A: Chem., **209**, 83-87 (2004)

[4.17] M. Liu, J. Zhang, J. Liu, W. W. Yu, *Synthesis of PVP-stabilized Pt/Ru colloidal nanoparticles by ethanol reduction and their catalytic properties for selective hydrogenation of ortho-chloronitrobenzene*, J. Catal., **278**, 1-7 (2011)

[4.18] X. Yan, J. Sun, Y. Wang, J. Yang, *A Fe-promoted Ni–P amorphous alloy catalyst*

(Ni–Fe–P) for liquid phase hydrogenation of m- and p-chloronitrobenzene, J. Mol. Catal. A: Chem., **252**, 17-22 (2006)

[4.19] N. Yao, J. Chen, J. Zhang, J. Zhang, *Influence of support calcination temperature on properties of Ni/TiO_2 for catalytic hydrogenation of o-chloronitrobenzene to o-chloroaniline*, Catal. Commun., **9**, 1510-1516 (2008)

[4.20] J. X. Chen, N. Yao, R. J. Wang, J. Y. Zhang, *Hydrogenation of chloronitrobenzene to chloroaniline over Ni/TiO_2 catalysts prepared by sol–gel method*, Chem. Eng. J., **148**, 164-172 (2009)

[4.21] F. Cárdenas-Lizana, S. Gómez-Quero, A. Hugon, L. Delannoy, C. Louis, M. A. Keane, *Pd-promoted selective gas phase hydrogenation of p-chloronitrobenzene over alumina supported Au*, J. Catal., **262**, 235-243 (2009)

[4.22] P. Sangeetha, P. Seetharamulu, K. Shanthi, S. Narayanan, K.S. Rama Raob, *Studies on Mg-Al oxide hydrotalcite supported Pd catalysts for vapor phase hydrogenation of nitrobenzene*, J. Mol. Catal. A: Chem., **273**, 244-249 (2007)

[4.23] P. Sangeetha, K. Shanthi, K. S. R. Rao, B. Viswanathan, P. Selvam, *Hydrogenation of nitrobenzene over palladium-supported catalysts-effect of support*, Appl. Catal. A: Gen., **353**, 160-165 (2009)

[4.24] L. Petrov, K. Kumbilieva, N. Kirkov, *Kinetic model of nitrobenzene hydrogenation to aniline over industrial copper catalyst considering the effects of mass transfer and deactivation*, Appl. Catal., **59**, 31-43 (1990)

[4.25] S. Diao, W. Qian, G. Luo, F. Wei, Y. Wang, *Gaseous catalytic hydrogenation of nitrobenzene to aniline in a two-stage fluidized bed reactor*, Appl. Catal. A: Gen., **286**, 30-35 (2005)

[4.26] A. Nieto-Márquez, S. Gil, A. Romero, J. L. Valverde, S. Gómez-Quero, M. A. Keane, *Gas phase hydrogenation of nitrobenzene over acid treated structured and amorphous carbon supported Ni catalysts*, Appl. Catal. A: Gen., **363**, 188-198 (2009)

[4.27] V. Vishwanathan, V. Jayasri, P. M. Basha, N. Mahata, L. M. Sikhwivhilu, N. J. Coville, *Gas phase hydrogenation of ortho-chloronitrobenzene (o-CNB) to ortho-chloroaniline (o-CAN) over unpromoted and alkali metal*

promoted-alumina supported palladium catalysts, Catal. Commun., **9**, 453-458 (2008)

[4.28] F. Cárdenas-Lizana, B. Bridier, C. C. K. Shin, J. Pérez-Ramírez, L. Kiwi-Minsker, *Promotional effect of Ni in the selective gas-phase hydrogenation of chloronitrobenzene over Cu-based catalysts*, ChemCatChem, **4**, 668-673 (2012)

[4.29] M. Pietrowski, M. Wojciechowska, *An efficient ruthenium-vanadium catalyst for selective hydrogenation of ortho-chloronitrobenzene*, Catal. Today, **142**, 211-214 (2009)

[4.30] E. Klemm, B. Amon, H. Redlingshöfer, E. Dieterich, G. Emig, *Deactivation kinetics in the hydrogenation of nitrobenzene to aniline on the basis of a coke formation kinetics - investigations in an isothermal catalytic wall reactor*, Chem. Eng. Sci., **56**, 1347-1353 (2001)

[4.31] M. Khoudiakov, M. C. Gupta, S. Deevi, *Au/Fe_2O_3 nanocatalysts for CO oxidation: A comparative study of deposition–precipitation and coprecipitation techniques*, Appl. Catal. A: Gen., **291**, 151-161 (2005)

[4.32] E. P. Barrett, L. G. Joyner, P. P. Halenda, *The determination of pore volume and area distributions in porous substances. i. computations from nitrogen isotherms*, J. Am. Chem. Soc., **73**, 373-380 (1951)

[4.33] T. L. Barr, S. Seal, *Nature of the use of adventitious carbon as a bindingenergy standard*, J. Vac. Sci. Technol. A, **13**, 1239-1246 (1995)

[4.34] C. D. Wagner, *Studies of the charging of insulators in ESCA*, J. Electron Spectrosc. Relat. Phenom., **18**, 345-349 (1980)

[4.35] M. C. Biesinger, L. W. M. Lau, A. R. Gerson, R. St. C. Smart, *Resolving surface chemical states in XPS analysis of first row transition metals, oxides and hydroxides: Sc, Ti, V, Cu and Zn*, Appl. Surf. Sci., **257**, 887-898 (2010)

[4.36] I. Chorkendorff, J. W. Niemantsverdriet, Conceps of Modern Catalysis and Kinetics, Wiley-VCH, Weinheim, 2003

[4.37] M. Trueba, S. P. Trasatti, γ-Alumina as a Support for catalysts, Eur. J. Inorg. Chem., **17**, 3393-3403 (2005)

[4.38] J. Leerat, S. Osuwan, E. Gulari, *Lean-burn nox reduction by propene over gold supported on alumina catalysts derived from the sol–gel method*, Catal. Lett., **141**, 62-67 (2011)

[4.39] H. Wang, J. L. Faria, S. J. Dong, Y. Chang, *Mesoporous Au/TiO_2 composites preparation, characterization, and photocatalytic properties*, Mater. Sci. Eng. B-Adv. Funct. Solid-State Mater., **177**, 913-919 (2012)

[4.40] G. Postole, A. Gervasini, C. Guimon, A. Auroux, B. Bonnetot, *Influence of the preparation method on the surface characteristics and activity of boron-nitride-supported noble metal catalysts*, J. Phys. Chem. B, **110**, 12572-12580 (2006)

[4.41] A. C. Gluhoi, X. Tang, P. Marginean, B. E. Nieuwenhuys, *Characterization and catalytic activity of unpromoted and alkali (earth)-promoted Au/Al_2O_3 catalysts for low-temperature CO oxidation*, Top. Catal., **39**, 101-110 (2006)

[4.42] E. Bus, R. Prins, J. A. van Bokhoven, *Time-resolved in situ XAS study of the preparation of supported gold clusters*, Phys.Chem.Chem.Phys., **9**, 3312-3320 (2007)

[4.43] X. Wang, N. Perret, M. A. Keane, *The role of hydrogen partial pressure in the gas phase hydrogenation of p-chloronitrobenzene over alumina supported Au and Pd: A consideration of reaction thermodynamics and kinetics*, Chem. Eng. J., **210**, 103-113 (2012)

[4.44] E. Bus, J. A. van Bokhoven, *Hydrogen chemisorption on supported platinum, gold, and platinum-gold-alloy catalysts*, Phys.Chem.Chem.Phys., **9**, 2894-2902 (2007)

[4.45] G. C. Bond, C. Louis, D. T. Thompson, Catalysis by Gold, Imperial College Press, London, 2006

[4.46] E. Bus, J. T. Miller, J. A. van Bokhoven, *Hydrogen chemisorption on Al_2O_3-supported gold catalysts*, J. Phys. Chem. B, **109**, 14581-14587 (2005)

[4.47] S. Díaz-Moreno, D. C. Koningsberger, A. Muñoz-Páez, *The "invisible" metal particles in catalysis*, Nucl. Instrum. Methods Phys. Res., Sect. B, **133**, 15-23 (1997)

[4.48] P. Claus, *Heterogeneously catalysed hydrogenation using gold catalysts*, Appl. Catal. A: Gen., **291**, 222-229 (2005)

[4.49] A. Yu. Vasil'kov, S. A. Nikolaev, V. V. Smirnov, A. V. Naumkin, I. O. Volkov, V. L. Podshibikhin, *An XPS study of the synergetic effect of gold and nickel supported on SiO_2 in the catalytic isomerization of allylbenzene*, Mendeleev Commun., **17**, 268-270 (2007)

[4.50] A. V. Naumkin, A. Yu. Vasil'kov, I. O. Volkov, V. V. Smirnov, S. A. Nikolaev, *X-ray photoelectron spectra and structure of composites prepared via deposition of Au, Ni, and Au + Ni nanoparticles on SiO_2 from colloidal solutions in triethylamine*, Inorg. Mater., **43**, 381-385 (2007)

[4.51] A. M. Visco, F. Neri, G. Neri, A. Donato, C. Milone, S. Galvagno, *X-ray photoelectron spectroscopy of Au/Fe_2O_3 catalysts*, Phys.Chem.Chem.Phys., **1**, 2869-2873 (1999)

[4.52] Y. Hao, R. Liu, X. Meng, H. Cheng, F. Zhao, *Deactivation of Au/TiO_2 catalyst in the hydrogenation of o-chloronitrobenzene in the presence of CO_2*, J. Mol. Catal. A: Chem., **335**, 183-188 (2011)

[4.53] S. Arrii, F. Morfin, A. J. Renouprez, J. L. Rousset, *Oxidation of co on gold supported catalysts prepared by laser vaporization: direct evidence of support contribution*, J. Am. Chem. Soc., **126**, 1199-1205 (2004)

[4.54] B. Ealet, E. Gillet, *Metal-alumina interface: influence of the metal electronegativity and of the substrates stoichiometry*, Surf. Sci., **367**, 221-230 (1996)

[4.55] C. Xiao, X. D. Wang, C. Lian, H. Q. Liu, M. H. Liang, Y. Wang, Selective *hydrogenation of halonitrobenzenes*, Curr. Org. Chem., **16**, 280-296 (2012)

[4.56] K. Shimizu, Y. Miyamoto, T. Kawasaki, T. Tanji, Y. Tai, A. Satsuma, *Chemoselective hydrogenation of nitroaromatics by supported gold catalysts: mechanistic reasons of size- and support-dependent activity and selectivity*, J. Phys. Chem. C, **113**, 17803-17810 (2009)

[4.57] C. Perego, S. Peratello, *Experimental methods in catalytic kinetics*, Catal. Today, **52**, 133-145 (1999)

[4.58] E. López, S. Ordóñez, H. Sastre, F. V. Díez, *Kinetic study of the gas-phase hydrogenation of aromatic and aliphatic organochlorinated compounds using a Pd/Al_2O_3 catalyst*, J. Hazard. Mater., **97**, 281-294 (2003)

[4.59] A. Renken, L. Kiwi-Minsker, Catalytic Reaction: Engineering Principles, Willey-VCH, Weinhem, 2012

[4.60] F. Cárdenas-Lizana, S. Gómez-Quero, M. A. Keane, *Ultra-selective gas phase catalytic hydrogenation of aromatic nitro compounds over Au/Al_2O_3*, Catal. Commun., **9**, 475-481 (2008)

[4.61] D. R. Lide, Handbook of Chemistry and Physical Properties, 88th ed., Taylor Francis, Boca Raton, 2007-2008

[4.62] W. Woodside, J. H. *Messmer, Thermal conductivity of porous media. ii. consolidated rocks*, J. Appl. Phys., **32**, 1688-1699 (1961)

[4.63] C. N. Satterfield, Mass Transfer in Heterogeneous Catalysis, M.I.T. Press, Cambridge, 1970

[4.64] R. C. Reid, J. M. Prausnitz, B. E. Poling, The Properties of Gases and Liquids, 4^{th} ed., McGraw-Hill, New York, 1987

[4.65] L. Shen, Z. Chen, *Critical review of the impact of tortuosity on diffusion*, Chem. Eng. Sci., **62**, 3748-3755 (2007)

[4.66] V. R. Choudhary, M. G. Parande, *Gas chromatographic study of binary diffusion of nitrobenzene and aniline in hydrogen*, J. Chromatogr., **132**, 344-348 (1977)

[4.67] S. M. Ashraf, R. Srivastava, A. Hussain, *Determination of binary gas-phase diffusion coefficients using chromatography*, J. Chem. Eng. Data, **31**, 100-102 (1986)

[4.68] V. Vishwanathan, V. Jayasri, P. M. Basha, *Vapor phase hydrogenation of o-chloronitrobenzene (o-CNB) over alumina supported palladium catalyst — a kinetic study*, React. Kinet. Catal. Lett., **91**, 291-298 (2007)

[4.69] V. I. Savchenko, T. V. Denisenko, S. Y. Sklyar, V. D. Simonov, Russ. J. Inorg. Chem., **11**, 2149-2153 (1975)

[4.70] B. Coq, A. Tijani, F. Figuéras, *Particle size effect on the kinetics of p-chloronitrobenzene hydrogenation over platinum/alumina catalysts*, J. Mol.

Catal., **68**, 331-345 (1991)

[4.71] I. A. Ilchenko, A. V. Bulatov, I. E. Uflyand, V. N. Sheinker, *Hydrogenation of chloronitrobenzenes on heterogenized Pd(II) chelates*, Kinet. Catal., **32**, 691-693 (1991)

[4.72] C. Kartusch, J. A. van Bokhoven, *Hydrogenation over gold catalysts: The interaction of gold with hydrogen*, Gold Bull., **42**, 343-348 (2009)

[4.73] Y. Azizi, C. Petit, V. Pitchon, *Formation of polymer-grade ethylene by selective hydrogenation of acetylene over Au/CeO_2 catalyst*, J. Catal., **256**, 338-344 (2008)

[4.74] A. C. Gluhoi, J. W. Bakker, B. E. Nieuwenhuys, *Gold, still a surprising catalyst: Selective hydrogenation of acetylene to ethylene over Au nanoparticles*, Catal. Today, **154**, 13-20 (2010)

[4.75] B. M. Weckhuysen, M. P. Rosynek, J. H. Lunsford, *Characterization of surface carbon formed during the conversion of methane to benzene over Mo/H-ZSM-5 catalysts*, Catal. Lett., **52**, 31-36 (1998)

[4.76] B. A. Sexton, A. E. Hughes, D. M. Bibby, *An XPS study of coke distribution on ZSM-5*, J. Catal., **109**, 126-131 (1988)

[4.77] P. Castaño, T. A. Zepeda, B. Pawelec, M. Makkee, J. L. G. Fierro, *Enhancement of biphenyl hydrogenation over gold catalysts supported on Fe-, Ce- and Ti-modified mesoporous silica (HMS)*, J. Catal., **267**, 30-39 (2009)

[4.78] P. Konova, A. Naydenov, T. Tabakova, D. Mehandjiev, *Deactivation of nanosize gold supported on zirconia in CO oxidation*, Catal. Commun., **5**, 537-542 (2004)

[4.79] Y. Zhou, J. Zhou, *Growth and sintering of Au-Pt nanoparticles on oxidized and reduced ceox(111) thin films by scanning tunneling microscopy*, J. Phys. Chem. Lett., **1**, 609-615 (2010)

CHAPTER 5

Towards Sustainable Chemoselective Nitroarene Hydrogenation using Supported Gold

Targeting at process sustainability, in this chapter, we have compared Au and Pd catalysts in the hydrogenation of *o*-chloronitrobenzene, where batch liquid and gas phase continuous operations are both investigated. Catalyst stability, E (Environmental)-Factor, effects of hydrogen partial pressure and solvent (as a carrier) are also studied. This chapter is in preparation for publication (see publication No. 14). Co-author F.C.-L. conducted the reactions in batch liquid phase reactor and co-wrote the chapter. M.A.K. directed the project and co-wrote the chapter.

5.1 Introduction

Sustainability is now widely recognised as a crucial issue facing the chemical sector, where the application of catalysis to reduce energy requirements and achieve high selectivity to target products is key to the application of "green chemistry" [1]. Aromatic amines, in general, and *o*-chloroaniline (*o*-CAN), in particular, are widely used in the manufacture of a range of agrochemicals, pharmaceuticals, dyes, and pigments [2]. The conventional route to haloamines *via* reduction of the corresponding nitro-compound by Fe promoted reaction in acid media (the Béchamp process) suffers from major drawbacks, notably low product yields and the generation of significant quantities of toxic (polluting) Fe/FeO sludge waste [3]. Catalytic hydrogenation employing transition metals can serve as a cleaner alternative but the economic benefits depend critically on catalyst performance. Catalytic hydrogenation of chloronitrobenzenes (CNBs) has employed Ni-, Pt-, Ru- and Pd-based catalysts but unwanted dechlorination has proved unavoidable at high conversions [4,5]. Indeed, the appreciable waste associated with the conversion of substituted nitroarenes led Sheldon [6] to introduce the concept of the E (Environmental)-Factor ($kg_{waste}\ kg_{product}^{-1}$), which

highlighted the severe environmental impact of amine production.

Chemoselectivity, the ability to selectively react one functional group while preserving other, often more reactive, functionalities is a major challenge in the hydrogenation of halo-nitroarenes. To date, chloro-nitroarene hydrogenation has focused on batch liquid phase operation [2,5,7-10] where, in order to enhance amine yield, high operating temperatures (up to 542 K [8]) and pressures (up to 40 atm [9,10]) have been employed, resulting in energy intensive processes [11,12]. The catalytic systems have typically involved coupled batch reactors, one in use while a second is recharged with catalyst/reactant; if only one vessel is employed, “down time” results. Incomplete mixing in batch reactors results in significant mass/heat transfer gradients, which extend reaction time, leading to by-product formation with the requirement for subsequent separation/purification stages to extract the target product. Operation at high H_2 pressure is a safety concern [13] and the use of alternative hydrogen donors (ammonium chloride [14], ammonium formate [15], hydrazine [16], sodium hydrogen sulphide [17], sodium borohydride [18] and acetic acid [19]) has been considered. In any case, the requirement for additional separation stages, often under reflux conditions [19] impacts on sustainability. Batch liquid *o*-CNB hydrogenation has involved the use of a range of volatile solvents, including methanol [10,20], ethanol [21], butanol [8], diethyl ether [20], acetonitrile [22], and toluene [23] with serious implications in terms of safety (flammability) and environmental impact (toxic emissions).

From the above, it is clear that there is a sustainability gap in conventional batch liquid hydrogenation of functionalised nitroarenes. In this study, drawing on established green chemistry principles [24,25], we have set out to develop a low energy, atom efficient selective *o*-CNB hydrogenation operated in continuous gas flow mode, employing laboratory synthesised titania supported Au (Au/TiO_2) as catalyst and water as solvent/carrier. A move from batch liquid to continuous gas flow operation circumvents down time and the use of additional chemicals as hydrogen donors/derivatisation agents while facilitating high throughput. In this work, activated carbon supported palladium (Pd/C), widely applied in the hydrogenation of CNBs [26,27], is adopted as a benchmark catalyst.

5.2 Experimental

5.2.1 Catalyst Preparation and Activation

The TiO_2 support (P25, Degussa) was used as received. A 0.1 % w/w Au/TiO_2 was prepared by deposition-precipitation. Urea, used as basification agent, was added (*ca.* 100-fold excess) to a $HAuCl_4$ solution (5×10^{-4} M) containing the TiO_2 support and the suspension stirred and heated to 353 K for 3 h. The pH of the suspension progressively increased to reach *ca.* 7 as a result of the thermally-induced urea decomposition

$$NH_2\text{-}CO\text{-}NH_2 + 3H_2O \xrightarrow{T=353K} 2NH_4^+ + 2OH^- + CO_2 \qquad (5.1)$$

The solid obtained was separated by centrifugation, washed ten times with deionised water (with centrifugation between each washing) and dried under He (45 cm^3 min^{-1}) at 373 K (2 K min^{-1}) for 5 h. Prior to use in catalysis, the sample (sieved into a batch of 75 μm average diameter) was activated in 60 cm^3 min^{-1} H_2 at 2 K min^{-1} to 473 K, which was maintained for 1 h. For comparison purposes, a commercial 10 w/w % Pd/C catalyst (Aldrich) activated at 573 K (10 K min^{-1}) in H_2 was used as benchmark.

5.2.2 Catalyst Characterisation

The Au loading was determined by inductively coupled plasma-optical emission spectrometry (ICP-OES, Vista-PRO, Varian Inc.) from the diluted extract of aqua regia. Nitrogen adsorption-desorption isotherms were obtained at 77 K using the commercial automated Micromeritics Gemini 2390 system. Specific surface areas were calculated from the isotherms using the standard BET method. Mean pore size, cumulative pore volume and pore size distributions were obtained from BJH analysis of the desorption isotherm; samples were outgassed at 423 K for 1 h prior to analysis. Temperature programmed reduction (TPR) and H_2 chemisorption were determined using the commercial CHEM-BET 3000 (Quantachrome) unit. The samples were loaded into a U-shaped Quartz cell (3.76 mm i.d.) and heated in 17 cm^3 min^{-1} (Brooks mass flow controlled) 5% v/v H_2/N_2 at 2 K min^{-1} to 473 K (Au/TiO_2) or 10 K min^{-1} to 573 K (Pd/C). The effluent gas passed through a liquid N_2 trap and changes in H_2 consumption were monitored by TCD with data acquisition/manipulation using the TPR Win™

software. The reduced samples were maintained at the final temperature in a flow of H_2 until the signal returned to baseline, swept with 65 cm^3 min^{-1} N_2 for 1.5 h, cooled to reaction (423 K) or ambient temperature and subjected to H_2 chemisorption using a pulse (10-50 µl) titration procedure. BET surface area and H_2 chemisorption values were reproducible to within ±5 %; the values quoted represent the mean. Powder X-ray diffractograms were recorded on a Bruker/Siemens D500 incident X-ray diffractometer using Cu Kα radiation. The samples were scanned (0.02º $step^{-1}$) over the range $5º \leq 2\theta \leq 85º$. The diffractograms were identified using the JCPDS-ICDD reference standards, *i.e.* TiO_2-anatase (21-1272), TiO_2-rutile (21-1276), Au (4-0784) and Pd (05-0681). Metal particle morphology and size were determined by transmission electron microscopy analysis; JEOL JEM 2011 HRTEM unit with a UTW energy dispersive X-ray detector (Oxford Instruments), operated at an accelerating voltage of 200 kV using Gatan DigitalMicrograph 3.4 for data acquisition/manipulation. The specimens were prepared by dispersion in acetone and deposited on a holey carbon/Cu grid (300 Mesh). Up to 200 individual metal particles were counted and the surface area-weighted metal diameter (d_{TEM}) was calculated from

$$d_{TEM} = \frac{\sum_i n_i d_i^3}{\sum_i n_i d_i^2} \tag{5.2}$$

where n_i is the number of particles of diameter d_i.

5.2.3 Catalytic Procedures

5.2.3.1 Liquid Phase Operation

Liquid phase hydrogenation (T = 423 K; P_{H_2} = 5-12 atm (P_{total} = 13-20 atm)) was carried out in a commercial semi-batch stirred stainless steel reactor (100 cm^3 autoclave, Büchi AG, Uster, Switzerland) equipped with a pressure controlled H_2 supply system. Hydrogen consumption in the reactor vessel was monitored on-line with a press flow gas controller (BPC-6002, Büchi, Switzerland) and a stainless steel 6-blade disk turbine impeller (equipped with a self-gassing hollow shaft) provided effective agitation (1800 rpm) that served to minimise mass transport constraints. A recirculator (HAAKE B-N3)

was used to stabilise the reaction temperature to within ±1 K using oil (Shell Thermia: thermal conductivity = 0.45 kJ m^{-1} h^{-1} K^{-1}; specific heat = 2.4 kJ kg^{-1} K^{-1}) as the thermal medium. At the beginning of each run, a 80 cm^3 ethanolic solution (0.3×10^{-2}–6.4×10^{-2} mol dm^{-3}) of *o*-CNB was charged and flushed three times with N_2 under constant agitation. The catalyst was activated *ex-situ* in a quartz reactor (300 mm (length) × 10 mm (*i.d.*); 60 cm^3 min^{-1} H_2; *GHSV* = 200 h^{-1}) to 473 K (Au/TiO_2, 2 K min^{-1}) or 573 K (Pd/C, 10 K min^{-1}), cooled to ambient temperature and kept in an inert (N_2) atmosphere. The catalyst was then fluidised in a flow of N_2, transferred to the reactor and the temperature stabilised (*ca.* 45 min) under gentle stirring (*ca.* 300 rpm). Hydrogen was introduced, the system was pressurised to the final reaction pressure and full agitation was engaged (time t = 0 for reaction). In a series of blank tests, reaction in the absence of catalyst did not result in any measurable conversion. The initial $-NO_2$/metal (Au or Pd) molar ratio spanned the range 251-3333. A *non*-invasive liquid sampling system *via* a syringe with in-line filters allowed a controlled removal of aliquots ($\leq$ 0.5 cm^3) from the reactor for analysis.

5.2.3.2 Gas Phase Operation

Gas phase reactions were carried out under atmospheric pressure, *in situ* immediately after activation, in a fixed bed vertical continuous flow glass reactor (*i.d.* = 15 mm) at T = 423 K under conditions of negligible heat/mass transport limitations. A preheating zone (layer of borosilicate glass beads) ensured that the inlet *o*-CNB was vaporised and reached the reaction temperature before contacting the catalyst. Isothermal conditions (±1 K) were maintained by thoroughly mixing the catalyst with ground glass (75 μm). The temperature was continuously monitored by a thermocouple inserted in a thermowell within the catalyst bed. An ethanolic and/or aqueous solution of *o*-CNB was delivered, in a co-current flow of H_2 (or H_2/He mixture), *via* a glass/teflon air-tight syringe and a teflon line using a microprocessor controlled infusion pump (Model 100 kd Scientific) at a fixed calibrated flow rate. The inlet *o*-CNB molar flow (F) was in the range 5.5×10^{-3}–0.76 mmol h^{-1} where the molar metal to inlet *o*-CNB spanned a 2.5×10^{-4}–0.34 h interval. Hydrogen content in the feed was varied from P_{H_2} =

4.4×10^{-2} to 0.88 atm, the flow rate of which was controlled by a mass flow controller and the total flow rate (H_2 + He) monitored using a Humonics (Model 520) digital flowmeter; $GHSV = 2\times10^4$ h^{-1}. In a series of blank tests, passage of *o*-CNB reactant in a stream of H_2 through the empty reactor did not result in any detectable conversion.

The composition of the product mixture from both reactors was determined by capillary gas chromatography, employing a Perkin-Elmer Auto System XL gas chromatograph equipped with a programmed split/splitless injector and a flame ionization detector, using a DB-1 50 m × 0.20 mm i.d., 0.33 μm film thickness capillary column (J&W Scientific). Reactant (*o*-CNB, Sigma-Aldrich, ≥98 %) and solvent (ethanol, Sigma Aldrich, ≥99 %) were used as received without further purification and the gases (H_2, He and N_2) employed were of ultra high purity (99.999%). Repeated reactions delivered conversion/selectivity values that were reproducible to better than ± 5 %. Fractional hydrogenation ($x_{o\text{-}CNB}$) was obtained from

$$x_{o-CNB} = \frac{[o-CNB]_{in} - [o-CNB]_{out}}{[o-CNB]_{in}} \tag{5.3}$$

where selectivity with respect to *o*-CAN is given by

$$S_{o-CAN}(\%) = \frac{[o-CAN]_{out}}{[o-CNB]_{in} - [o-CNB]_{out}} \times 100 \tag{5.4}$$

Table 5.1: Physicochemical characteristics of Au/TiO_2 and Pd/C.

	Au/TiO_2	Pd/C
TPR T_{max} (K)	373[a]	373[b]
BET area (m^2 g^{-1})	48[a] (49)[c]	826
Pore volume (cm^3 g^{-1})	0.13[a] (0.07) [c]	-
Mean pore radius (Å)	55[a] (51) [c]	-
H_2 chemisorption (μmol g_{metal}^{-1})	20[d] /183[e]	1691[d] /637[e]
Metal particle size range (nm)	1-8	1-9
Mean size (d_{TEM}, nm)	4.0	5.4

[a]values refer to Au/TiO_2; [b]negative peak due to the decomposition of β-Pd hydride;
[c]values refer to TiO_2 (support)
[d]measurements conducted at 298 K
[e]measurements conducted at 423 K

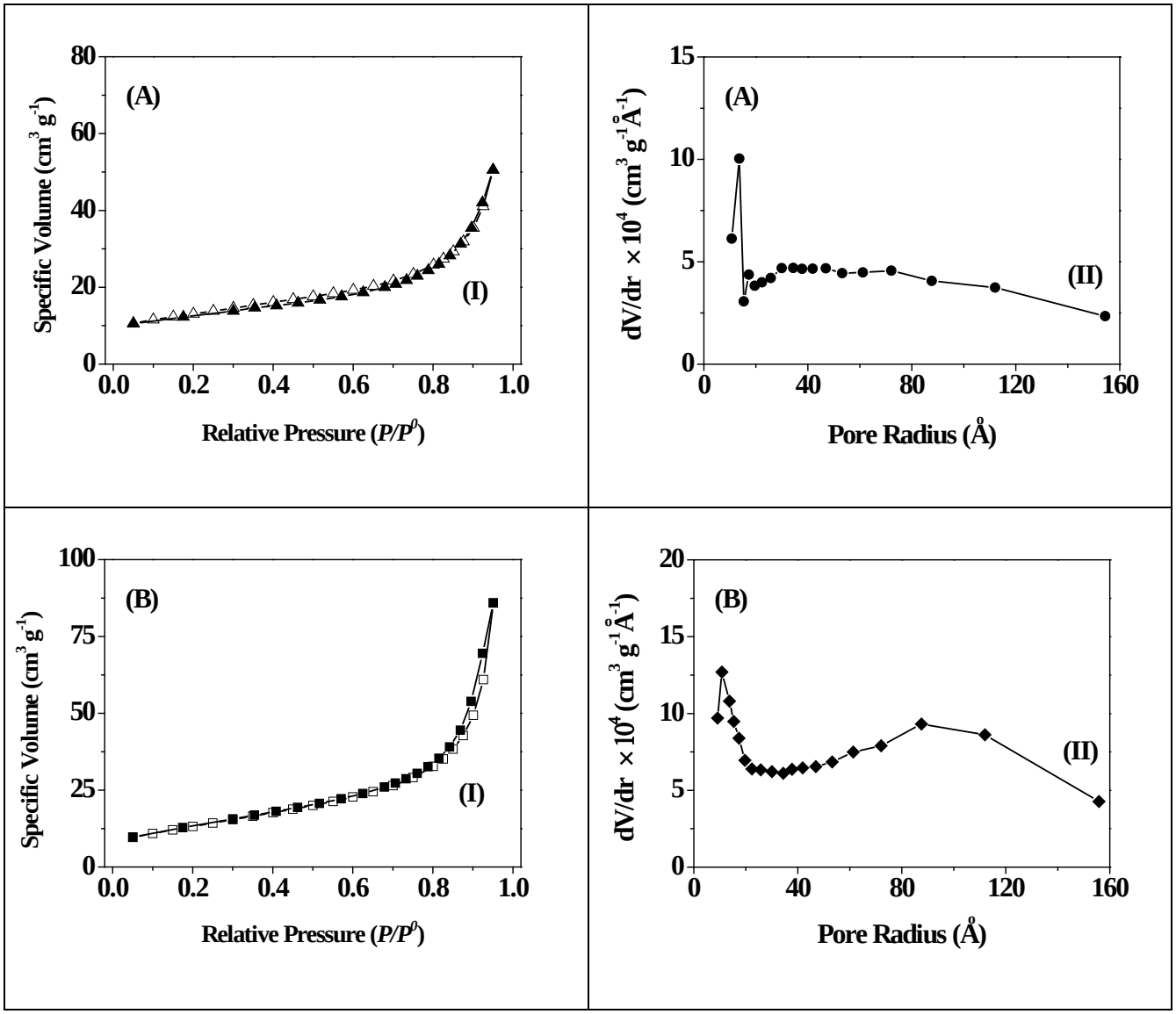

Figure 5.1: (I) Nitrogen adsorption (open symbols) and desorption (solid symbols) isotherms with (II) associated pore size distributions for (A) TiO_2 and (B) Au/TiO_2.

5.3 Results and Discussion

5.3.1 Catalyst Characteristics

The specific surface area and porosity of the TiO_2 support (A) and Au/TiO_2 catalyst (B) are recorded in **Table 5.1**. The N_2 adsorption/desorption isotherms are given in **Figure 5.1** with pore radii distribution over the 10-160 Å range, which is characteristic of mesoporous materials. The surface area of Au/TiO_2 coincided with that of the starting TiO_2 but there was a measurable increase in pore volume and mean radius that has been observed previously [28]. Temperature programmed reduction (TPR) of the TiO_2

support (to 473 K) did not result in any measurable H_2 consumption, which is consistent with the literature [29]. Titania reduction is observed at elevated temperatures (> 850 K) where the incorporation of Au serves to decrease the reduction temperature by up to 480 K [30]. Hydrogen consumption with an associated temperature maximum (T_{max}) at 373 K was observed in the TPR of Au/TiO_2 (**Figure 5.2(A)**). A single TPR peak has been reported elsewhere for Au/TiO_2 with T_{max} at 378 K [31] and 383 K [32] and evidence of concomitant support reduction [33]. Indeed, H_2 consumption during TPR (9.2 mmol g_{Au}^{-1}) was measurably higher than that (7.6 mmol g_{Au}^{-1}) required from Au^{3+} to Au^0,

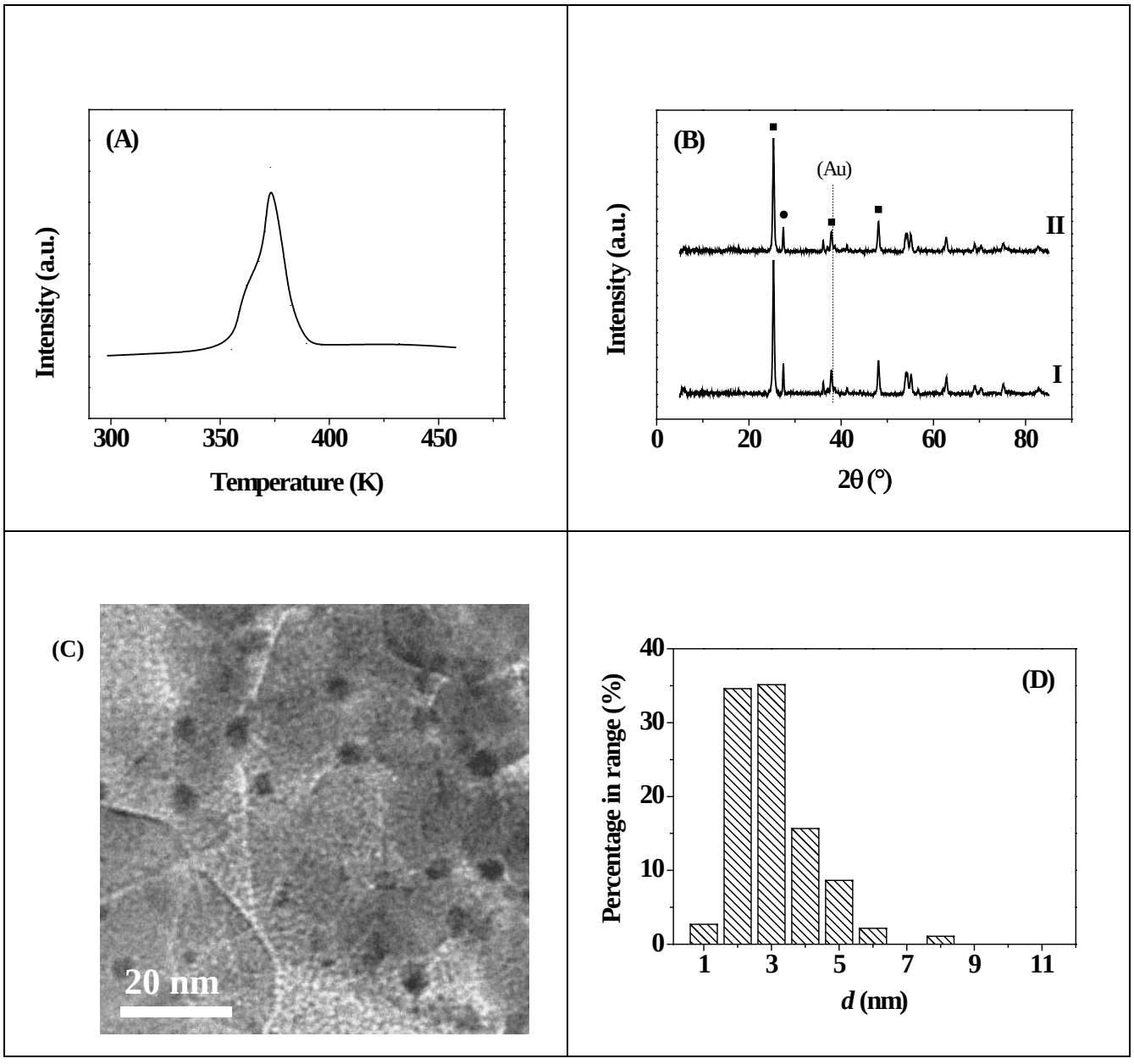

Figure 5.2: Au/TiO_2 characterisation: (A) TPR profile; (B) XRD patterns for (I) TiO_2 and (II) Au/TiO_2 (■, anatase;●, rutile); (C) representative TEM image with associated (D) Au particle size distribution histogram.

suggesting partial reduction of TiO_2. This can be significant in nitro group hydrogenation as the oxygen vacancies formed during carrier reduction (eg. Ni/TiO_2) can activate the reactant with N=O polarisation [34]. We accordingly adopted a reduction temperature of 473 K in Au/TiO_2 activation.

The XRD patterns (**Figure 5.2(B)**) coincide for the TiO_2 support (I) and Au/TiO_2 (II) and are characterised by signals at 2θ = 25.3°, 37.8° and 48.1° corresponding to the (101), (004) and (200) planes of tetragonal anatase (JCPDS-ICDD 21-1272). The peak at 27.4° is diagnostic of tetragonal rutile (JCPDS-ICDD 21-1276). The anatase content (80% volume fraction) from XRD analysis matches the reported Degussa P25 composition [35]. There was no detectable signals for Au metal (principal peak at 38.1°), suggesting a well dispersed Au phase (<5 nm) [36]. Gold particle size was determined by TEM analysis, which revealed pseudo-spherical Au particles in the size range 1-8 (**Figure 5.2(C)**). The Au particle size distribution histogram presented in **Figure 5.2(D)** was used to generate a surface area-weighted mean diameter (4.0 nm). The formation of supported Au particles at the nanoscale (<10 nm) is critical in hydrogenation reactions [5]. It is widely accepted that Au exhibits a higher barrier than other transition metals (Pt, Pd and Ni) for H_2 dissociation due to the filled *d*-band and chemisorption proceeds at edge and corner sites. A decrease in particle size increases the preponderance of such sites, enhancing H_2 activation and associated hydrogenation activity [37,38]. We have demonstrated previously that the specific rate of nitro-compound reduction (nitrocyclohexane [33], *p*-CNB [39] and *m*-dinitrobenzene (*m*-DNB) [40]) increased with decreasing mean Au particle size (from 9 to 3 nm). Ambient temperature H_2 chemisorption following TPR delivered an uptake (20 µmol g_{Au}^{-1}) that is close to instrument detection limits. Uptake was appreciably increased (to 183 µmol g_{Au}^{-1}) for pulse titration at the reaction temperature (423 K) indicating that H_2 dissociation on supported Au is an activated process, in line with observations by Bus *et al.* [37] and Lin *et al.* [41].

Critical characteristics of the benchmark Pd/C catalyst are presented in **Table 5.1** and **Figure 5.3**. The BET surface area (826 $m^2\ g^{-1}$) is within the range of values (90-1300 $m^2\ g^{-1}$) reported elsewhere [42,43] for carbon supported Pd catalysts. TPR analysis (to 573 K) generated a single negative peak with T_{max} = 373 K (**Figure 5.3(A)**)

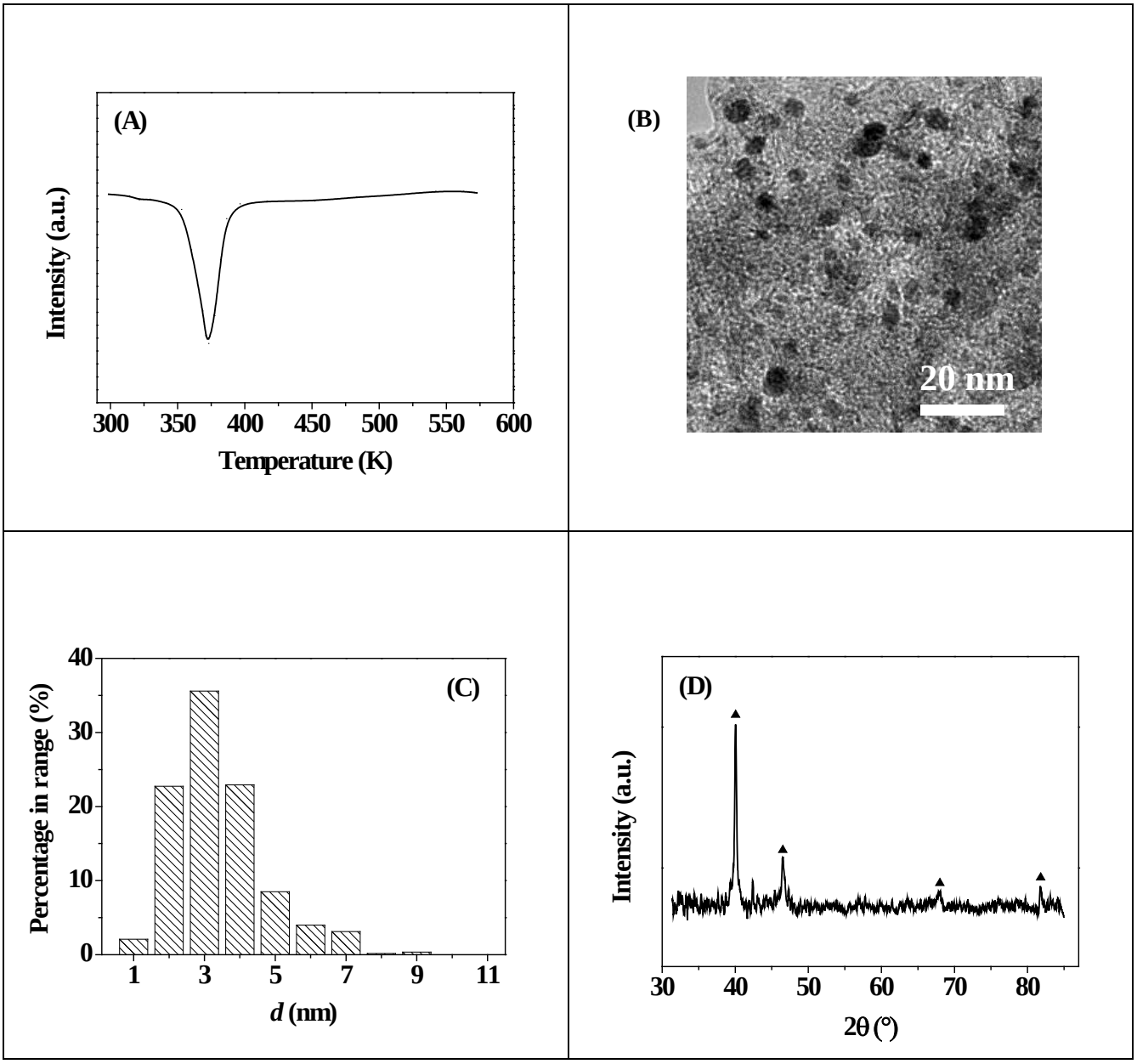

Figure 5.3: Pd/C characterisation: (A) TPR profile; (B) representative TEM image with (C) Pd particle size distribution histogram and (D) XRD pattern (▲, Pd).

that can be attributed to H_2 generated during the thermal decomposition of β–Pd hydride. It is well established that zero valent Pd can absorb H_2 at ambient temperature [44] to form a hydride phase where the H_2 partial pressure exceeds 0.02 atm [45]; a pressure of 0.05 atm was used in this study. This hydride is unstable and decomposes at 340-390 K with subsequent H_2 release [46,47]. The H_2 that results from hydride decomposition is dependent on Pd size with an upper limit of 0.66 $mol_H\ mol_{Pd}^{-1}$ for bulk Pd [48] decreasing to *ca.* 0.1 $mol_H\ mol_{Pd}^{-1}$ for a mean Pd size of *ca.* 2 nm [4]. The value recorded in this study (0.16 $mol_H\ mol_{Pd}^{-1}$) suggests the formation of well dispersed Pd at

the nano-scale. This is confirmed by TEM analysis (**Figure 5.3(B)**) with Pd particles in the 1-9 nm range **Figure 5.3(C)** and a surface area weighted mean of 5.4 nm. Ambient temperature H_2 chemisorption (1691 μmol g_{Pd}^{-1}) far exceeded that measured for Au//TiO_2 (**Table 5.1**). Indeed, H_2 chemisorption on supported Pd is a valid means of estimating Pd particle size [49] where the value (4.7 nm) obtained (adopting a Pd/H adsorption stoichiometry = 1) is in good agreement with the TEM measurement. The associated XRD pattern (**Figure 5.3(D)**) exhibits signals at 40.7°, 46.1°, 68.1° and 82.1° that can be assigned to Pd (111), (200), (220) and (311) planes respectively. A crystal size of 6.1 nm was obtained by applying standard line broadening analysis [50]. In contrast to supported Au, (exothermic) H_2 chemisorption on Pd/C decreased (to 637 μmol g_{Pd}^{-1}) at the reaction temperature but this still exceeded the value recorded for Au/TiO_2.

5.3.2 Catalytic Response

5.3.2.1 Pd/C vs. Au/TiO_2: Batch Liquid Phase Operation

The reaction network and associated CNB hydrogenation products that have been reported and recently reviewed in [3] are presented (for *o*-CNB as reactant) in **Figure 5.4**. In addition to the target *o*-CAN, nitrobenzene (NB) and aniline (AN) are produced *via* hydrodechlorination of *o*-CNB with further hydrogenation, as observed for Pd/Al_2O_3 [4,8], NiCoB [51], Au/$Ce_xZr_{1-x}O_2$ [52] and bimetallic Pd-Rh and Pd-Fe catalysts [53]. Hydrodeamination to chlorobenzene has been reported for reaction over Pt/Al_2O_3 [54]. Benzene formation has been noted by Xiao *et al.* [3]. Chloronitroso- and chlorohydroxylamine- intermediates can undergo side (condensation/hydrogenation) reactions with *o*-CAN to generate toxic by-products (*e.g.* dichloroazoxybenzene, dichloroazobenzene and dichlorohydrazobenzene), which have been observed over Pt powders [55]. Moreover, Zhang *et al.* [23] have reported formation of 2,2′-dichlorohydrazobenzene in the hydrogenation of *o*-CNB over Pd/C. Exclusive production of *o*-CAN is challenging but process sustainability requires minimisation of unwanted (and toxic) by-products, enhancing atom efficiency and circumventing the need for separation/purification steps.

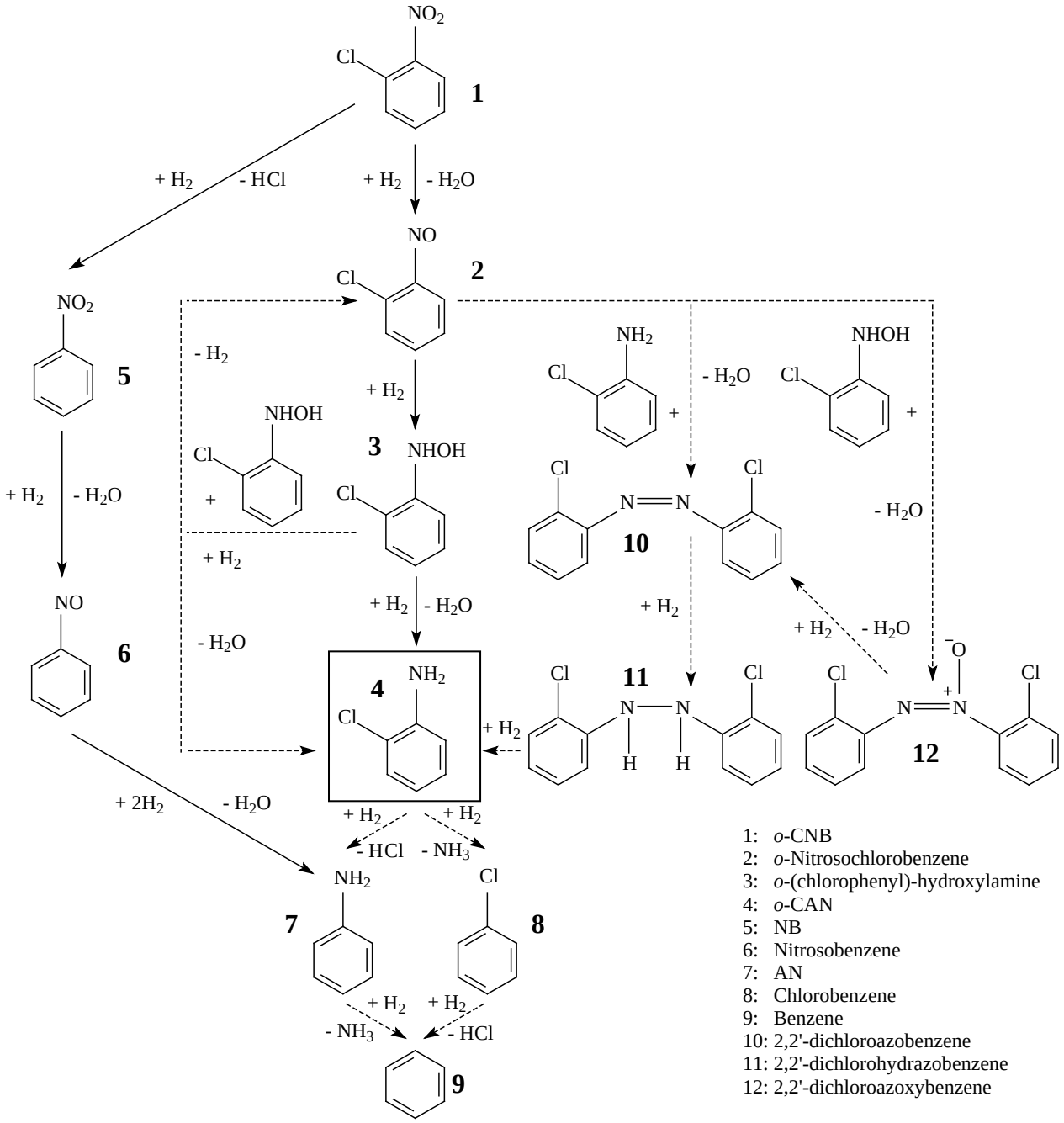

Figure 5.4: Reaction pathways associated with the hydrogenation of *o*-CNB (1): solid arrows (routes observed in this work); dotted arrows (possible steps reported in the literature); target *o*-CAN product (4) has been framed.

Taking batch liquid phase reaction as the standard mode of operation, we first assess the catalytic performance of Au/TiO_2 against the benchmark Pd/C. A representative (P_{H_2} = 5 atm) *o*-CNB concentration profile for reaction over Pd/C is shown in **Figure 5.5(A)** where complete conversion was achieved after 1 h. Selectivity (S_i) was time invariant with the generation of *o*-CAN as principal product (S = 79%)

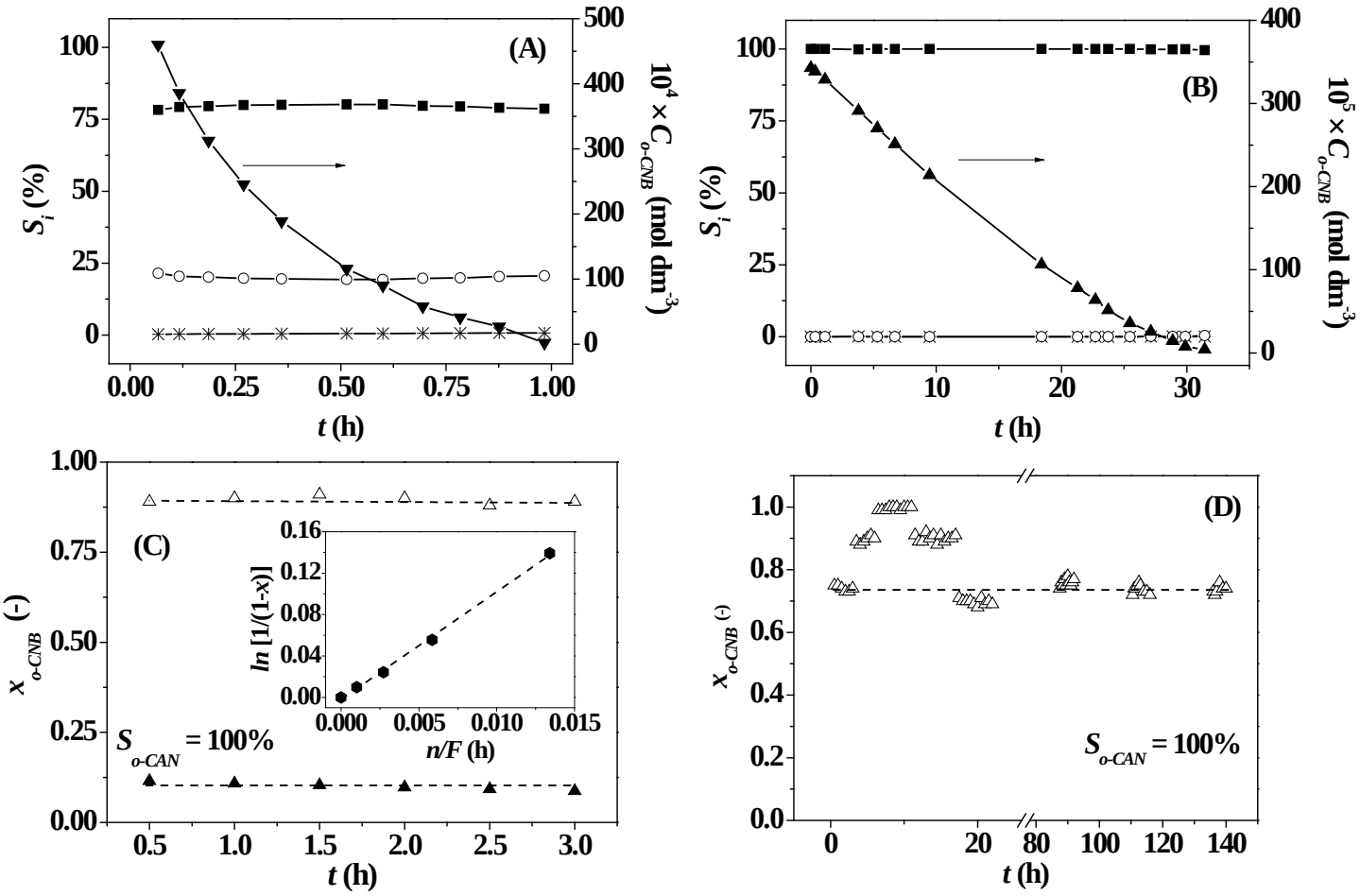

Figure 5.5: Liquid phase batch reaction: temporal variation of *o*-CNB concentration ($C_{o\text{-}CNB}$) and product selectivity for reaction over (A) Pd/C (initial *o*-CNB/Pd molar ratio = 3333) and (B) Au/TiO_2 (initial *o*-CNB/Au = 251) at P_{H2} = 5 atm in batch liquid phase operation (■: *o*-CAN; ○: AN; ✳: NB). Gas phase continuous reaction: (C) representative variation of *o*-CNB fractional conversion ($x_{o\text{-}CNB}$) with time on-stream for reaction over Au/TiO_2; $n/F = 12 \times 10^{-3}$ h (▲) and 16×10^{-2} (△); inset shows pseudo-first order kinetic plot (n/F = 1.0-13.4 × 10^{-3} h); (D) variation of fractional conversion over Au/TiO_2 for up to 140 h on-stream: $x_{o\text{-}CNB}$ variations between 3-17 h are due to a switch in n/F from 0.08 to 0.34 h.

with AN as by-product (S = 20%) and trace NB formation (S = 1%). An increase in pressure (to P_{H2} = 12 atm) served to elevate the rate of *o*-CNB consumption with a measurable increase in *o*-CAN selectivity at the expense of AN, as shown in **Table 5.2**. As an equivalent product distribution was obtained at all conversions, AN and *o*-CAN must be generated in a parallel conversion of *o*-CNB (as shown in **Figure 5.4**) rather than stepwise coupled hydrogenation/hydrodechlorination. There is evidence in the literature suggesting that selectivity in CNB hydrogenation is sensitive to P_{H2}, where an increase in pressure (0.5-4.0 MPa) favoured CAN formation over Pt-Au/TiO_2 [56]. The increase in activity and selectivity translates into a higher *o*-CAN production rate but

Table 5.2: Effect of P_{H2} on the (batch) liquid phase catalytic hydrogenation of *o*-CNB over Pd/C and Au/TiO_2.

	P_{H2} = 5 atm		P_{H2} = 8 atm		P_{H2} = 10 atm		P_{H2} = 12 atm	
Catalyst	r[a]	S_i % (Product)	r[a]	S_i % (Product)	r[a]	S_i % (Product)	r[a]	S_i % (Product)
Pd/C	2290	79 (*o*-CAN) 20 (AN) 1 (NB)	2470	79 (*o*-CAN) 20 (AN) 1 (NB)	2650	81(*o*-CAN) 18 (AN) 1 (NB)	2910	86 (*o*-CAN) 13 (AN) 1 (NB)
Au/TiO_2	10	100 (*o*-CAN)	40	100 (*o*-CAN)	58	100 (*o*-CAN)	167	100 (*o*-CAN)

[a]$mol_{o\text{-CNB}}\ mol_{metal}^{-1}\ h^{-1}$

Table 5.3: Comparison of (batch) liquid *vs.* (continuous) gas phase operation in the hydrogenation of *o*-CNB over Au/TiO_2.

Operation mode	P_{total} (atm)	r ($mol_{o\text{-CNB}}\ mol_{Au}^{-1}\ h^{-1}$)	Down time[a] Steps (h)	Production capacity (tonne $mol_{Au}^{-1}\ year^{-1}$)	E-Factor[b]
Batch (liquid)	13	10	$t_1+t_2+t_3+t_4+t_5$ (10)	8.4	8
Continuous (gas)	1	12	$t_1+t_2+t_3$ (3)	13.4	0.3[c]/0.7[d]

[a]time required for: reactor loading (t_1); catalyst activation (t_2); temperature/pressure stabilization (t_3); unload/reload of product/reactant solution (t_4); catalyst filtration-washing-reloading (t_5)

[b]based on 90% recovery of ethanol (solvent)

[c]unreacted H_2 is recycled

[d]no H_2 recycle

this is offset by the energy required to operate the reactor at elevated (12 atm) pressure, notwithstanding the safety concerns associated with handling pressurised H_2, particularly at a commercial scale. In any case, formation of AN and NB as significant by-products necessitates subsequent separation operations.

The critical role of catalysis in 21st century chemical processing is to achieve maximum selectivity to a high value product, rather than reactant turnover [57]. This is embedded in the green chemistry ethos in terms of "atom economy" where synthetic methods should be designed to maximise the incorporation of all raw materials used in the process into the final product [58]. This objective is not achieved in *o*-CNB hydrogenation using the commercial Pd/C catalyst. It has been demonstrated that hydrogenation over Au delivers lower rates than "conventional" catalytic metals (*e.g.* Ni, Pd and Pt) [59,60]. This can be attributed to a lesser capacity of supported Au to adsorb/dissociate H_2, as demonstrated by the chemisorption measurements given in **Table 5.1**. The performance of Au/TiO_2 was tested in the batch reactor under the same conditions employed for Pd/C; the results are presented in **Figure 5.5(B)** and **Table 5.2**. Complete conversion of the starting *o*-CNB concentration over Au/TiO_2 required extended reaction times where the rates obtained were appreciably lower (by a factor of up to 200) than those recorded for Pd/C. We should note that Ide *et al.* have also reported lower (100-400 fold) hydrogenation rates for Au/C relative to Pd/C in the liquid phase conversion of crotonaldehyde and methyl vinyl ketone [61]. Reaction over Au/TiO_2 was 100% selective to *o*-CAN where an increase in H_2 pressure elevated the (selective) hydrogenation rate to a greater extent than observed for Pd/C. We can attribute this to a pressure driven increased availability of surface hydrogen on Au/TiO_2 that serves to enhance the degree of hydrogenation. Sheldon's E-Factor is a useful index with which to evaluate process sustainability and the application of green chemistry [6,62]. Taking a 90% recovery of ethanol (solvent), the measured E-factor for the batch processing of *o*-CNB was lower using Au/TiO_2 (8) relative to Pd/C (10) and both were at the lower end of the range (5-50) that prevails in the fine chemical sector [62]. We could not find any E-factors associated specifically with halo-aniline production for comparison purposes. The chemoselective performance of Au/TiO_2 satisfies four of the twelve green chemistry principles [24,25,63]: (i) waste prevention, avoiding treatment

and clean up steps; (ii) atom economy, in maximising conversion of reactant (*o*-CNB) to product (*o*-CAN); (iii) circumvented use of derivatives to enhance selectivity; (iv) effective application of catalysis. Based on these results, Au/TiO_2 was employed as catalyst for further process optimisation.

5.3.2.2 Au/TiO_2: Batch Liquid-Phase vs. Continuous Gas-Phase Operation

A brainstorming exercise [64] involving the American Chemical Society (ACS), Green Chemistry Institute (GCI) and global pharmaceutical corporations has highlighted the switch from batch to continuous processing as crucial for the sustainable manufacture of fine chemicals. Adopting this imperative, we have examined *o*-CNB hydrogenation in continuous gas phase operation where the feed is vaporised and carried through a fixed catalyst bed. This has the advantage of simultaneous reactant delivery and product removal where the process is operated at a steady state. Catalyst-reactant contact time is a critical process parameter that can influence activity/selectivity [65,66] and can be tuned in continuous operation but this is not possible in batch mode. Batch liquid phase systems can be subject to appreciable transport limitations that are removed in continuous gas phase mode [67] with improvements in safety/energy usage [68] and cost [69] when operated at atmospheric pressure. Continuous operation overcomes the drawback of down time that is a decided drawback of batch processes. Moreover, economies of scale favour continuous processes for high throughput.

We must note from the outset that continuous gas phase hydrogenation over Au/TiO_2 resulted in the exclusive formation of *o*-CAN under all the conditions considered in this work. The representative temporal conversion profiles presented in **Figure 5.5(C)** establish invariant activity for up to 3 h on-stream and steady state conversions values were accordingly used in our kinetic analysis. We have previously shown [52] the applicability of pseudo-first order kinetics according to the reactor/kinetic expression

$$\ln\left[\frac{1}{(1-x_{o\text{-}CNB})}\right] = k\left(\frac{n}{F}\right) \tag{5.5}$$

where *n/F* (molar Au to inlet hourly *o*-CNB feed rate) has the physical significance of

contact time. The linear relationship (between $\ln(1- x_{o\text{-}CNB})^{-1}$ and n/F) shown in the inset to **Figure 5.5(C)** confirms adherence to first order behaviour, which allows determination of the hydrogenation rate constant (k). Catalyst lifetime is a crucial consideration in chemical processing where overall process efficiency is governed by both selectivity and catalyst stability [70]. Catalyst deactivation in $-NO_2$ group reduction has been a feature of a number of studies and ascribed to carbon deposition [71], deleterious effects due to water formation (as by-product) [72], chlorine poisoning [52] and metal sintering [52]. Catalyst testing was extended over a prolonged (up to 140 h) time on-stream where the results presented in **Figure 5.5(D)** demonstrate maintenance of the initial level of activity. As a further test, contact time was increased (0.08-0.34 h) during the stability measurements with a corresponding increase in activity and a return to the initial level of activity on switching back to the starting conditions. We must stress that the increase in contact time resulted in full conversion of *o*-CNB to *o*-CAN, i.e. 100% continuous yield of the target amine.

Both batch liquid and continuous gas phase catalytic operations were conducted at the same reaction temperature (423 K) but at different pressures, *i.e.* 1 atm (gas phase) and up to 13 atm (liquid phase). This represents significant differences in energy demands with potential safety hazards for liquid phase operation and is a decided sustainability gap. Application of green chemistry should be directed at ambient conditions to ensure energy efficiency [58]. A direct comparison of both modes of operation at a common pressure was not possible as Au/TiO_2 did not exhibit any measurable liquid phase activity at 1 atm. Any meaningful comparison should normalise the *o*-CAN generated with respect to total process time to generate a measure of production capacity [73]. The liquid phase reaction was run in time-sequential steps with appreciable periods between batches associated with reactor loading (t_1), catalyst activation (t_2), temperature/pressure stabilisation (t_3), extraction and recharge of the product and new reactant solution (t_4) and catalyst filtration-washing-reloading (t_5) (**Table 5.3**). Any down time ($t_1+t_2+t.$) in gas phase operation is limited due to the combined (a) catalyst stability, (b) continuous reactant supply and product removal and (c) facile separation of catalyst from reactants/product. Taking reaction conditions that deliver an equivalent rate of selective *o*-CNB hydrogenation in both modes of operation,

the down time involved between batches is significantly greater than that required for the start-up of the continuous reactor. Given prolonged catalyst stability with time on-stream (**Figure 5.5(D)**), any down time in gas phase operation is negligible relative to total process time. The estimated production capacity (projected on an annual basis in **Table 5.3**) is appreciably greater for continuous *o*-CAN production. We should note that productivities were calculated on 24 h working day, which will entail significant labour costs associated with operating the system. We should flag the decrease in E-Factor (to below 1, **Table 5.3**) that accompanies the shift from batch to continuous operation.

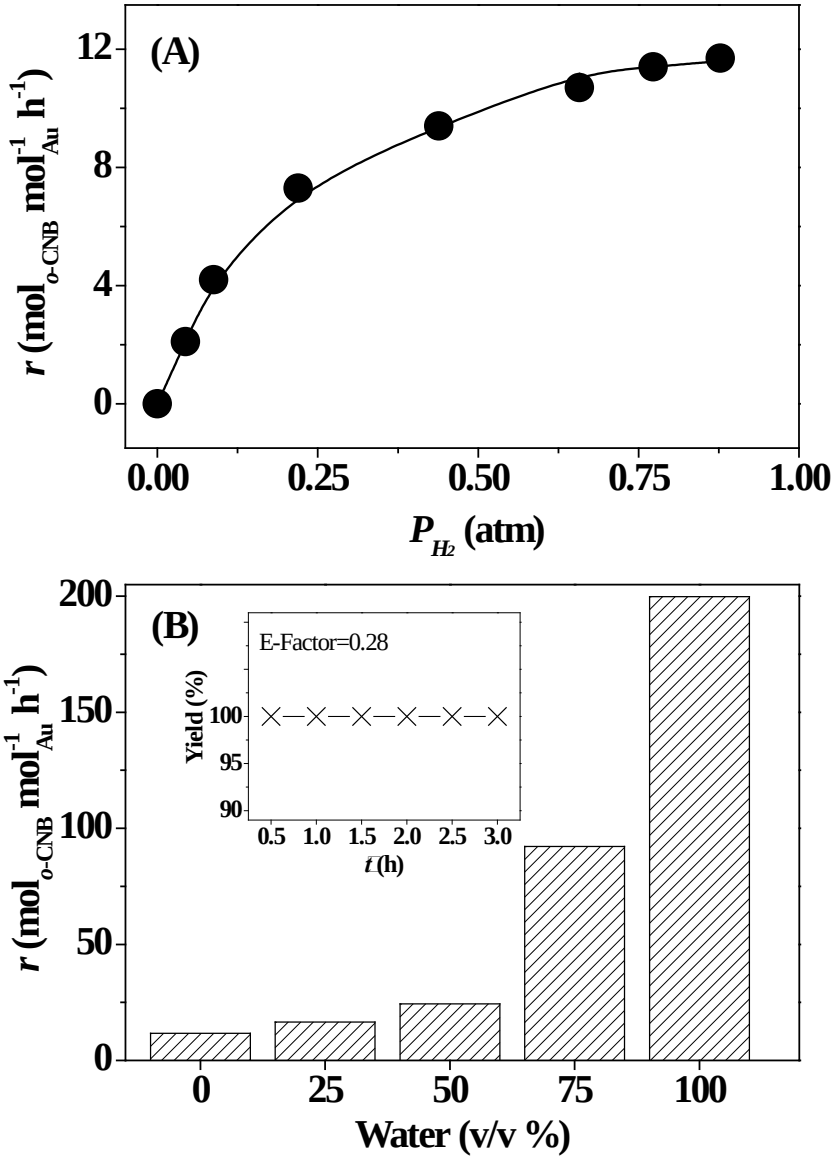

Figure 5.6: (A) Rate of hydrogenation (*r*) of *o*-CNB (in ethanol) over Au/TiO_2 as a function of H_2 partial pressure; (B) Dependence of rate on water content (% volume) in the carrier (water and water+ethanol mixtures); inset: *o*-CAN yield (%) with time on-stream in gas phase continuous operation using water carrier at P_{H2} = 0.66 atm.

Recycle of unreacted H_2 to the reactor results in an even lower E-factor. This further closes the sustainability gap, facilitating cleaner continuous synthesis that can remove a possible bottleneck in the production of amines "on demand". Further process optimisation that addresses H_2 usage and the nature of the solvent is the focus of the following section.

5.3.2.3 Gas Phase Continuous Operation over Au/TiO_2: H_2 Usage and Solvent

Gas phase nitroarene hydrogenation is typically conducted where the inlet H_2 is far in excess of the stoichiometric requirement [4,30,52]. Operation under H_2 lean conditions is an important sustainability consideration in terms of atom efficiency, energy utilisation and safety [74]. We addressed this by examining the effect of varying H_2 partial pressure (from 0.9 to 0.04 atm) on reaction rate and the results are presented in **Figure 5.6(A)**. Full selectivity to the target *o*-CAN was achieved at each P_{H_2}, albeit with a decrease in selective hydrogenation rate at lower P_{H_2} to residual activity under stoichiometric conditions (inlet H_2/*o*-CNB = 3). The rate dependence was most pronounced at P_{H_2} < 0.50 atm and reached a limiting value at higher P_{H_2}. We can identify P_{H_2} = 0.66 atm as a lower limit that achieves near maximum reaction rate. Use of a diluted H_2 stream while maintaining rate/productivity serves to enhance process safety, satisfying another critical green chemistry principle [24,25,63].

The catalytic data presented to this point refer to reaction using ethanolic *o*-CNB solutions. Green chemistry principles recommend, if possible, the use of "safer" solvents in tandem with milder reaction conditions. Water, as an environmentally benign solvent, represents a cleaner and inexpensive alternative. Indeed, the feasibility of conducting reactions in water rather than organic solvents has been a long-standing goal for synthetic chemists [16]. Although it has been demonstrated [21,75] that the polar properties of water can impact on hydrogenation activity/selectivity in liquid phase reactions, the effect in gas phase operation where water serves as a carrier has not been evaluated. It is, however, known that catalyst performance in gas phase hydrogenation reactions can be influenced by the solvent (or carrier) due to competitive adsorption [76]. The use of water and water/ethanol mixtures as *o*-CNB carrier was examined and

the results are shown in **Figure 5.6(B)** where it can be seen that rate increased markedly with increasing water content; full selectivity to *o*-CAN was again achieved for each reaction. This promotional effect is not entirely without precedent [77] as Ning *et al.* [21] have reported enhanced *p*-CNB reduction over Ru/SiO_2 using water as solvent (in comparison with organic alcohols (from methanol to pentanol)) in liquid phase batch reaction, which they attributed to more favourable desorption of the halo-amine product. Maity *et al.* observed increased activity over Pt/polymer in water relative to methanol and toluene again in batch operation [75]. Activity in gas phase hydrogenation over supported Au is limited by the available surface reactive hydrogen [4] and any additional supply of hydrogen should improve rate. Dissociative chemisorption of water on supported Au has been proposed under conditions similar to those applied in this study, which served to increase activity in the water-gas shift reaction (WGSR) [78-80]. Moreover, Shekhar *et al*. have demonstrated that TiO_2 as Au support contributes directly to WGSR by activating water in the feed to generate a high surface coverage of reactive species [79]. Enhanced selective hydrogenation of the aqueous *o*-CNB feed can then be ascribed to surface activation/dissociation of water, generating reactive hydrogen that contributes to $–NO_2$ reduction. Under these process conditions, time invariant 100% yield of *o*-CAN was achieved (inset to **Figure 5.6(B)**) with an E-Factor (0.28) that was appreciably below unity.

5.4 Conclusions

Current production of functionalised aromatic amines via hydrogenation of the corresponding nitroarene exhibits a sustainability gap in terms of energy, atom efficiency and the requirement for separation/purification to extract the target product. Taking *o*-CNB hydrogenation as a model reaction, we have systematically evaluated catalyst and process variables to arrive at a sustainable route to *o*-CAN. Reaction over a commercial (10% w/w) Pd/C (Pd particles in the size range 1-9 nm, mean = 5.4 nm) in liquid phase batch operation was non-selective, generating AN and NB as by-products. An increase in P_{H2} (from 5 to 12 atm) increased rate and *o*-CAN selectivity but failed to achieve target *o*-CAN exclusivity. A laboratory synthesised (0.1% w/w) Au/TiO_2 (1-8

nm Au particles, mean = 4.0 nm) exhibited full selectivity to *o*-CAN in batch liquid phase but with lower activity than Pd/C. A switch to gas phase continuous processing facilitated 100% selectivity to *o*-CAN at 1 atm, minimising down time with stable conversion for up to 140 h on-stream. This translates into increased product capacity (13.4 tonne mol_{Au}^{-1} $year^{-1}$) relative to batch operation (8.4 tonne mol_{Au}^{-1} $year^{-1}$). This was accompanied by a substantial decrease in the E-factor (kg_{waste} $kg_{product}^{-1}$) from 8 to 0.3. Reaction rate exhibited a dependence on P_{H_2} < 0.50 atm but attained a limiting value at higher P_{H_2}; efficient H_2 usage requires operation at P_{H_2} = 0.66 atm. Use of water as carrier delivered a substantially higher selective hydrogenation rate (200 $mol_{o\text{-CNB}}$ mol_{Au}^{-1} h^{-1}) relative to ethanol (12 $mol_{o\text{-CNB}}$ mol_{Au}^{-1} h^{-1}), which can be attributed to the generation of reactive hydrogen *via* water dissociation on Au/TiO_2. The results establish sustainable catalytic haloaniline production that is based on green chemistry principles.

5.5 References

[5.1] P.T. Anastas, M.M. Kirchhoff, T.C. Williamson, *Catalysis as a foundational pillar of green chemistry*, Appl. Catal. A: Gen., **221**, 3-13 (2001)

[5.2] H.-U. Blaser, H. Steiner, M. Studer, *Selective catalytic hydrogenation of functionalized nitroarenes: an update*, ChemCatChem, **1**, 210-221 (2009)

[5.3] C. Xiao, X. Wang, C. Lian, H. Liu, M. Liang, Y. Wang, *Selective hydrogenation of halonitrobenzenes*, Curr. Org. Chem., **16**, 280-296 (2012)

[5.4] X. Wang, N. Perret, M.A. Keane, *The role of hydrogen partial pressure in the gas phase hydrogenation of p-Chloronitrobenzene over alumina supported Au and Pd: a consideration of reaction thermodynamics and kinetics*, Chem. Eng. J., **210**, 103-113 (2012)

[5.5] F. Cárdenas-Lizana, M. Keane, *The development of gold catalysts for use in hydrogenation reactions*, J. Mater. Sci., **48**, 543-564 (2013)

[5.6] R.A. Sheldon, *Atom efficiency and catalysis in organic synthesis*, Pure Appl. Chem., **72**, 1233-1246 (2000)

[5.7] C. Xi, H. Cheng, J. Hao, S. Cai, F. Zhao, *Hydrogenation of o-chloronitrobenzene*

to o-chloroaniline over Pd/C in supercritical carbon dioxide, J. Mol. Catal. A: Chem., **282**, 80-84 (2008)

[5.8] F. Cárdenas-Lizana, S. Gómez-Quero, M.A. Keane, *Clean production of chloroanilines by selective gas phase hydrogenation over supported Ni catalysts*, Appl. Catal. A: Gen., **334**, 199-206 (2008)

[5.9] B. Zuo, Y. Wang, Q. Wang, J. Zhang, N. Wu, L. Peng, L. Gui, X. Wang, R. Wang, D. Yu, *An efficient ruthenium catalyst for selective hydrogenation of ortho-chloronitrobenzene prepared via assembling ruthenium and tin oxide nanoparticles*, J. Catal., **222**, 493-498 (2004)

[5.10] M. Liu, W. Yu, H. Liu, *Selective hydrogenation of o-chloronitrobenzene over polymer-stabilized ruthenium colloidal catalysts*, J. Mol. Catal. A: Chem., **138**, 295-303 (1999)

[5.11] B. Coq, A. Tijani, F. Figuéras, *Influence of alloying platinum for the hydrogenation of p-chloronitrobenzene over PtM/Al_2O_3 catalysts with Mn, Pb, Ge, Al, Zn*, J. Mol. Catal., **71**, 317-333 (1992)

[5.12] Y.-C. Liu, Y.-W. Chen, *Hydrogenation of p-chloronitrobenzene on lanthanum-promoted NiB nanometal catalysts*, Ind. Eng. Chem. Res., **45**, 2973-2980 (2006)

[5.13] L.C. Shirvill, T.A. Roberts, M. Royle, D.B. Willoughby, T. Gautier, *Safety studies on high-pressure hydrogen vehicle refuelling stations: Releases into a simulated high-pressure dispensing area*, Int. J. Hydrogen Energy, **37**, 6949-6964 (2012)

[5.14] T. Tsukinoki, H. Tsuzuki, *Organic reaction in water. Part 5. Novel synthesis of anilines by zinc metal-mediated chemoselective reduction of nitroarenes*, Green Chem., **3**, 37-38 (2001)

[5.15] D.C. Gowda, B. Mahesh, *Catalytic transfer hydrogenation of aromatic nitro compounds by employing ammonium formate and 5% platinum on carbon*, Synth. Commun., **30**, 3639-3644 (2000)

[5.16] U. Sharma, P.K. Verma, N. Kumar, V. Kumar, M. Bala, B. Singh, *Phosphane-free green protocol for selective nitro reduction with an iron-based catalyst*, Chem. Eur. J., **17**, 5903-5907 (2011)

[5.17] S. Ravi Kanth, G. Venkat Reddy, V.V.V.N.S. Rama Rao, D. Maitraie, B. Narsaiah, P. Shanthan Rao, *A simple and convenient method for the reduction of nitroarenes*, Synth. Commun., **32**, 2849-2853 (2002)

[5.18] Y.K. Park, S.B. Choi, H.J. Nam, D.-Y. Jung, H.C. Ahn, K. Choi, H. Furukawa, J. Kim, *Catalytic nickel nanoparticles embedded in a mesoporous metal-organic framework*, Chem. Commun., **46**, 3086-3088 (2010)

[5.19] P. Barman, T. Bhattacharjee, *Solvent-free reduction of aromatic nitro compounds with alumina supported iron powder and acetic acid under microwave irradiation*, Can. J. Chem. Eng. Tech., **1**, 16-20 (2010)

[5.20] M. Pietrowski, M. Wojciechowska, *An efficient ruthenium-vanadium catalyst for selective hydrogenation of ortho-chloronitrobenzene*, Catal. Today, **142**, 211-214 (2009)

[5.21] J. Ning, J. Xu, J. Liu, H. Miao, H. Ma, C. Chen, X. Li, L. Zhou, W. Yu, *A remarkable promoting effect of water addition on selective hydrogenation of p-chloronitrobenzene in ethanol*, Catal. Commun., **8**, 1763-1766 (2007)

[5.22] V. Vishwanathan, V. Jayasri, P. Mahaboob Basha, N. Mahata, L. Sikhwivhilu, N.J. Coville, *Gas phase hydrogenation of ortho-chloronitrobenzene (o-CNB) to ortho-chloroaniline (o-CAN) over unpromoted and alkali metal promoted-alumina supported palladium catalysts*, Catal. Commun., **9**, 453-458 (2008)

[5.23] G. Zhang, L. Wang, K. Shen, D. Zhao, H.S. Freeman, *Hydrogenation of o-chloronitrobenzene on a Pd/C catalyst doped with metal oxide nanoparticles*, Chem. Eng. J., **141**, 368-374 (2008)

[5.24] P. Anastas, N. Eghbali, *Green chemistry: principles and practice*, Chem. Soc. Rev., **39**, 301-312 (2010)

[5.25] U.B. Demirci, P. Miele, *Overview of the relative greenness of the main hydrogen production processes*, J. Clean. Prod., **52**, 1-10 (2013)

[5.26] H. Liu, M. Liang, C. Xiao, N. Zheng, X. Feng, Y. Liu, J. Xie, Y. Wang, *An excellent Pd-based nanocomposite catalyst for the selective hydrogenation of para-chloronitrobenzene*, J. Mol. Catal. A: Chem., **308**, 79-86 (2009)

[5.27] J. Li, X.-Y. Shi, Y.-Y. Bi, J.-F. Wei, Z.-G. Chen, *Pd nanoparticles in ionic liquid*

brush: a highly active and reusable heterogeneous catalytic assembly for solvent-free or on-water hydrogenation of nitroarene under mild conditions, ACS Catal., **1**, 657-664 (2011)

[5.28] J. Yu, H. Yu, B. Cheng, M. Zhou, X. Zhao, *Enhanced photocatalytic activity of TiO_2 powder (P25) by hydrothermal treatment*, J. Mol. Catal. A: Chem., **253**, 112-118 (2006)

[5.29] P.R. Ettireddy, N. Ettireddy, S. Mamedov, P. Boolchand, P.G. Smirniotis, *Surface characterization studies of TiO_2 supported manganese oxide catalysts for low temperature SCR of NO with NH_3*, Appl. Catal. B: Environ., **76**, 123-134 (2007)

[5.30] F. Cárdenas-Lizana, S. Gómez-Quero, N. Perret, M.A. Keane, *Gold catalysis at the gas-solid interface: role of the support in determining activity and selectivity in the hydrogenation of m-dinitrobenzene*, Catal. Sci. Tech., **1**, 652-661 (2011)

[5.31] S.Y. Liu, S.M. Yang, *Complete oxidation of 2-propanol over gold-based catalysts supported on metal oxides*, Appl. Catal. A: Gen., **334**, 92-99 (2008)

[5.32] A. Hugon, L. Delannoy, C. Louis, *Supported gold catalysts for selective hydrogenation of 1,3-butadiene in the presence of an excess of alkenes*, Gold Bull., **41**, 127-138 (2008)

[5.33] X. Wang, N. Perret, M.A. Keane, *Gas phase hydrogenation of nitrocyclohexane over supported gold catalysts*, Appl. Catal. A: Gen., **467**, 575-584 (2013)

[5.34] J. Xiong, J. Chen, J. Zhang, *Liquid-phase hydrogenation of o-chloronitrobenzene over supported nickel catalysts*, Catal. Commun., **8**, 345-350 (2007)

[5.35] R.I. Bickley, T. Gonzalez-Carreno, J.S. Lees, L. Palmisano, R.J.D. Tilley, *A structural investigation of titanium dioxide photocatalysts*, J. Solid State Chem., **92**, 178-190 (1991)

[5.36] D.H. Kim, Y.-H. Chin, G.G. Muntean, A. Yezeretz, N.W. Currier, W.S. Epling, H.-Y. Chen, H. Hess, C.H.F. Peden, *Relationship of Pt particle size to the NOx storage performance of thermally aged $Pt/BaO/Al_2O_3$ lean NO_x trap catalysts*, Ind. Eng. Chem. Res., **45**, 8815-8821 (2006)

[5.37] E. Bus, J.T. Miller, J.A. van Bokhoven, *Hydrogen chemisorption on Al_2O_3-supported gold catalysts*, J. Phys. Chem. B, **109**, 14581-14587 (2005)

[5.38] A. Corma, M. Boronat, S. Gonzalez, F. Illas, *On the activation of molecular hydrogen by gold: a theoretical approximation to the nature of potential active sites*, Chem. Commun., 3371-3373 (2007)

[5.39] F. Cárdenas-Lizana, S. Gómez-Quero, N. Perret, M.A. Keane, *Support effects in the selective gas phase hydrogenation of p-chloronitrobenzene over gold*, Gold Bull., **42**, 124-132 (2009)

[5.40] F. Cárdenas-Lizana, S. Gómez-Quero, H. Idriss, M.A. Keane, *Gold particle size effects in the gas-phase hydrogenation of m-dinitrobenzene over Au/TiO_2*, J. Catal., **268**, 223-234 (2009)

[5.41] S. Lin, M.A. Vannice, *Gold dispersed on TiO_2 and SiO_2: adsorption properties and catalytic behavior in hydrogenation reactions*, Catal. Lett., **10**, 47-61 (1991)

[5.42] J. Choi, S. Noh, S. Han, S. Yoon, C.-S. Lee, T.-S. Hwang, Y. Rhee, *Formic acid oxidation by carbon-supported palladium catalysts in direct formic acid fuel cell*, Korean J. Chem. Eng., **25**, 1026-1030 (2008)

[5.43] P. Luo, K. Xu, R. Zhang, L. Huang, J. Wang, W. Xing, J. Huang, *Highly efficient and selective reduction of nitroarenes with hydrazine over supported rhodium nanoparticles*, Catal. Sci. Tech., **2**, 301-304 (2012)

[5.44] C. Shi, B.W.L. Jang, *Nonthermal RF plasma modifications on Pd/gamma-Al_2O_3 for selective hydrogenation of acetylene in the presence of ethylene*, Ind. Eng. Chem. Res., **45**, 5879-5884 (2006)

[5.45] V. Ferrer, A. Moronta, J. Sanchez, R. Solano, S. Bernal, D. Finol, *Effect of the reduction temperature on the catalytic activity of Pd-supported catalysts*, Catal. Today, **107-108**, 487-492 (2005)

[5.46] S. Gómez-Quero, F. Cárdenas-Lizana, M.A. Keane, *Effect of metal dispersion on the liquid-phase hydrodechlorination of 2,4-dichlorophenol over Pd/Al_2O_3*, Ind. Eng. Chem. Res., **47**, 6841-6853 (2008)

[5.47] C.M. Mendez, H. Olivero, D.E. Damiani, M.A. Volpe, *On the role of Pd [beta]-hydride in the reduction of nitrate over Pd based catalyst*, Appl. Catal. B: Environ., **84**, 156-161 (2008)

[5.48] W. Palczewska, *Catalytic reactivity of hydrogen on palladium and nickel hydride phases*, Adv. Catal., **24**, 245-291 (1975)

[5.49] G. Prelazzi, M. Cerboni, G. Leofanti, *Comparison of H_2 adsorption, O_2 adsorption, H_2 titration, and O_2 titration on supported palladium catalysts*, J. Catal., **181**, 73-79 (1999)

[5.50] G. Li, L. Jiang, Q. Jiang, S. Wang, G. Sun, *Preparation and characterization of Pd_xAg_y/C electrocatalysts for ethanol electrooxidation reaction in alkaline media*, Electrochim. Acta, **56**, 7703-7711 (2011)

[5.51] B. Zhao, Y.-W. Chen, *The effect of poly-N-vinylpyrrolidone modification on NiCoB catalysts for hydrogenation of p-chloronitrobenzene*, Mater. Chem. Phys., **125**, 763-768 (2011)

[5.52] X. Wang, N. Perret, J.J. Delgado, G. Blanco, X. Chen, C.M. Olmos, S. Bernal, M.A. Keane, *Reducible support effects in the gas phase hydrogenation of p-chloronitrobenzene over gold*, J. Phys. Chem. C, **117**, 994-1005 (2013)

[5.53] Z. Yu, S. Liao, Y. Xu, B. Yang, D. Yu, *Hydrogenation of nitroaromatics by polymer-anchored bimetallic palladium-ruthenium and palladium-platinum catalysts under mild conditions*, J. Mol. Catal. A: Chem., **120**, 247-255 (1997)

[5.54] B. Coq, A. Tijani, R. Dutartre, F. Figuéras, *Influence of support and metallic precursor on the hydrogenation of p-chloronitrobenzene over supported platinum catalysts*, J. Mol. Catal., **79**, 253-264 (1993)

[5.55] X. Wang, M. Liang, J. Zhang, Y. Wang, *Selective hydrogenation of aromatic chloronitro compounds*, Curr. Org. Chem., **11**, 299-314 (2007)

[5.56] D. He, X. Jiao, P. Jiang, J. Wang, B.-Q. Xu, *An exceptionally active and selective Pt-Au/TiO_2 catalyst for hydrogenation of the nitro group in chloronitrobenzene*, Green Chem., **14**, 111-116 (2012)

[5.57] G. Somorjai, C. Kliewer, *Reaction selectivity in heterogeneous catalysis*, React. Kinet. Catal. Lett., **96**, 191-208 (2009)

[5.58] P.T. Anastas, J.C. Warner, Green Chemistry: Theory and Practice, Oxford University Press: New York, 1998

[5.59] P. Claus, *Heterogeneously catalysed hydrogenation using gold catalysts*, Appl. Catal. A: Gen., **291**, 222-229 (2005)

[5.60] G.C. Bond, C. Louis, D.T. Thompson, *Catalysis by Gold*, Imperial College Press, London, 2006

[5.61] M.S. Ide, B. Hao, M. Neurock, R.J. Davis, *Mechanistic insights on the hydrogenation of α,β-unsaturated ketones and aldehydes to unsaturated alcohols over metal catalysts*, ACS Catal., **2**, 671-683 (2012)

[5.62] R.A. Sheldon, *The E Factor: fifteen years on*, Green Chem., **9**, 1273-1283 (2007)

[5.63] D. Jiri George, Ionizing Radiation and Polymers, William Andrew Publishing, Oxford, 2013

[5.64] C. Jiménez-González, P. Poechlauer, Q.B. Broxterman, B.-S. Yang, D. am Ende, J. Baird, C. Bertsch, R.E. Hannah, P. Dell'Orco, H. Noorman, S. Yee, R. Reintjens, A. Wells, V. Massonneau, J. Manley, *Key green engineering research areas for sustainable manufacturing: a perspective from pharmaceutical and fine chemicals manufacturers*, Org. Process. Res. Dev., **15**, 900-911 (2011)

[5.65] P. Serna, M. Lopez-Haro, J.J. Calvino, A. Corma, *Selective hydrogenation of nitrocyclohexane to cyclohexanone oxime with H_2 on decorated Pt nanoparticles*, J. Catal., **263**, 328-334 (2009)

[5.66] X. Chen, A. Zhao, Z. Shao, C. Li, C.T. Williams, C. Liang, *Synthesis and catalytic properties for phenylacetylene hydrogenation of silicide modified nickel catalysts*, J. Phys. Chem. C, **114**, 16525-16533 (2012)

[5.67] J.F. Jenck, F. Agterberg, M.J. Droescher, *Products and processes for a sustainable chemical industry: a review of achievements and prospects*, Green Chem., **6**, 544-556 (2004)

[5.68] N. Yoswathananont, K. Nitta, Y. Nishiuchi, M. Sato, *Continuous hydrogenation reactions in a tube reactor packed with Pd/C*, Chem. Commun., 40-42 (2005)

[5.69] G. Centi, S. Perathoner, *Catalysis and sustainable (green) chemistry*, Catal. Today, **77**, 287-297 (2003)

[5.70] J.A. Moulijn, A.E. van Diepen, F. Kapteijn, *Catalyst deactivation: is it predictable?: What to do?*, Appl. Catal. A: Gen., **212**, 3-16 (2001)

[5.71] F. Cárdenas-Lizana, X. Wang, D. Lamey, M. Li, L. Kiwi-Minsker, M.A. Keane, *An examination of catalyst deactivation in hydrogenation over supported gold*, manuscript in preparation

[5.72] P. Sangeetha, P. Seetharamulu, K. Shanthi, S. Narayanan, K.S. Rama Rao, *Studies on Mg-Al oxide hydrotalcite supported Pd catalysts for vapor phase*

hydrogenation of nitrobenzene, J. Mol. Catal. A: Chem., **273**, 244-249 (2007)

[5.73] A. Goršek, P. Glavič, *Design of batch versus continuous processes: part I: single-purpose equipment*, Chem. Eng. Res. Des., **75**, 709-717 (1997)

[5.74] F. Stoessel, *Experimental study of thermal hazards during the hydrogenation of aromatic nitro compounds*, J. Loss Prevent. Proc., **6**, 79-85 (1993)

[5.75] P. Maity, S. Basu, S. Bhaduri, G.K. Lahiri, *Superior performance of a nanostructured platinum catalyst in water: hydrogenations of alkenes, aldehydes and nitroaromatics*, Adv. Synth. Catal., **349**, 1955-1962 (2007)

[5.76] R.L. Augustine, R.W. Warner, M.J. Melnick, *Heterogeneous catalysis in organic chemistry. 3. Competitive adsorption of solvents during alkene hydrogenations*, J. Org. Chem., **49**, 4853-4856 (1984)

[5.77] X. Wu, J. Xiao, Metal-catalyzed reactions in water, Wiley-VCH, Weinheim, 2013

[5.78] J. Gong, *Structure and surface chemistry of gold-based model catalysts*, Chem. Rev., **112**, 2987-3054 (2012)

[5.79] M. Shekhar, J. Wang, W.-S. Lee, W.D. Williams, S.M. Kim, E.A. Stach, J.T. Miller, W.N. Delgass, F.H. Ribeiro, *Size and support effects for the water-gas shift catalysis over gold nanoparticles supported on model Al_2O_3 and TiO_2*, J. Am. Chem. Soc., **134**, 4700-4708 (2012)

[5.80] R. Burch, *Gold catalysts for pure hydrogen production in the water-gas shift reaction: activity, structure and reaction mechanism*, Phys. Chem. Chem. Phys., **8**, 5483-5500 (2006)

CHAPTER 6

Selective Gas Phase Hydrogenation of p-Nitrobenzonitrile to *p*-Aminobenzonitrile over Zirconia Supported Gold

In this chapter, ZrO_2 has been synthesised, characterised and employed as gold support. The catalytic action of Au/ZrO_2 has been examined in the gas phase hydrogenation of *p*-nitrobenzonitrile to *p*-aminobenzonitrile, compared with Au/Al_2O_3, Ni/Al_2O_3 and Pd/Al_2O_3. This chapter is in preparation for publication (see publication No. 11). Co-author Y.H. conducted part of the catalytic reactions and co-wrote the chapter. M.A.K. directed the project and co-wrote the chapter.

6.1 Introduction

Zirconia (ZrO_2) was found to have widespread application in catalysis, structural engineering, electrolysis, biomedicine and clinical trials [1-3]. This study focuses on ZrO_2 as a metal (Au) catalyst support [4]. We should also note the use of ZrO_2 alone to promote transesterification [5], acylation [6], bromination [7], carbomagnetisation [8] and the multi-step reaction of hydrazines with alkynes [9]. Nonetheless, ZrO_2 has principally been employed as a support due to its adjustable (*via* variations in synthesis, precursor and use of dopants) textural, structural and chemical properties [10]. Notable examples include Fe- [11] and Co-based [12] Fischer-Tropsch synthesis, steam reforming over Pt group metals [13] and Ni [14] and the use of Cu to treat vehicular exhaust gas [15]. The development of supported Au in chemoselective catalysis is now the subject of appreciable research, as evaluated in a number of critical reviews [16-19]. Zirconia supported Au is a relatively unexplored catalyst formulation that has been applied in low temperature water gas shift reaction [20], CO oxidation [21] and the hydrogenation of 1,3-butadiene, acrolein and crotonaldehyde [22]. Koeppel *et al*. [23] demonstrated activity for Au/ZrO_2 in the hydrogenation of CO_2 in the early 1990s,

where it was found that crystalline (relative to amorphous) ZrO_2 delivered enhanced performance. Zhang *et al*. [21] have reported that Au/ZrO_2 with comparably sized Au (4−5 nm) and ZrO_2 (5−15 nm) outperformed systems with a similar Au size on larger ZrO_2 (40−200 nm) particles in CO oxidation. Of particular relevance to this study, the same group achieved high selectivities (up to 99.6%) in the liquid phase hydrogenation of *p*- and *o*-chloronitrobenzene and 2,5-dichloronitrobenzene, limiting the degree of C–Cl bond scission [24].

Drawing on this literature, we have prepared a crystalline ZrO_2 supported Au catalyst for use in the gas phase hydrogenation of *p*-nitrobenzonitrile (*p*-NBN). The target amine product (*p*-aminobenzonitrile (*p*-ABN)) is commercially important in the production of a diversity of agrochemicals, pharmaceuticals, dyestuffs, urethanes and fine chemicals [25]. The literature [25-32] dealing with *p*-NBN hydrogenation is quite limited and has focused on batch liquid phase reactions at elevated pressures (up to 6 MPa [30]) where high selectivity to *p*-ABN is challenging. We can flag selectivities up to 97% achieved using Au/TiO_2 and Au/Fe_2O_3 at near complete *p*-NBN conversion [26]. We provide here the first reported gas phase hydrogenation of *p*-NBN over supported Au where the low operating pressure (1 atm) in continuous mode translates into reduced energy consumption at higher throughput. We have also examined the catalytic action of Au/Al_2O_3 for comparison purposes as this system has been applied in (aromatic [33] and aliphatic [34]) nitro group, carbonyl group [35] and C–C triple/double bond [36] hydrogenation. Moreover, supported Ni [30] and Pd [37] used to promote *p*-NBN hydrogenation serve as benchmark catalysts in this work. Purity of the target amine is an important consideration given the difficult separation (by distillation) of hydrogenation products with similar boiling points [30]. Consequently, we have set out, as an explicit goal of this study, to achieve exclusive selectivity to *p*-ABN.

6.2 Experimental

6.2.1 Chemicals

Zirconium (IV) oxychloride octahydrate ($ZrOCl_2 \cdot 8H_2O$, ≥ 99.5%) and gold (III)

chloride hydrate (99.999%) were obtained from Sigma-Aldrich and the ammonia solution (35% w/w NH_3) was supplied by Fisher Scientific. All the gases used were of high purity (99.9%, BOC gases). The reactant (*p*-nitrobenzonitrile, Aldrich (≥ 98%)), solvent (1-butanol, Riedel-de Haen (≥ 99.5%)), urea (Riedel-de Häen (≥ 99%)) and γ-Al_2O_3 support (Puralox, Condea Vista Co.) were used as received without further treatment.

6.2.2 Catalyst Preparation

The zirconia support precursor was prepared by precipitation with dropwise addition of $ZrOCl_2 \cdot 8H_2O$ (0.1 M) to aqueous NH_3 (2.5 M) under vigorous stirring. Temporal pH changes were measured with a crystal-body electrode coupled to a data logging and collection system (Pico Technology), calibrated with standard buffer solutions (pH 7 and 10). The resultant hydrogel was washed thoroughly with deionised water until free of chloride ions ($AgNO_3$ test), dried at 373 K for 24 h and calcined (1 K min^{-1}) in flowing air (60 cm^3 min^{-1}) at 673-973 K for 5 h. Gold (nominal 1% w/w loading) was incorporated on ZrO_2 (calcined at 673 K) by deposition-precipitation. Urea, used as basification agent, was added (*ca.* 100-fold excess) to a solution of $HAuCl_4$ (5.1×10^{-3} M), ZrO_2 added and the suspension stirred (300 rpm) and heated to 353 K (2 K min^{-1}) for 4 h. The pH of the suspension progressively increased to *ca.* 6.5 after 4 h as a result of thermal urea decomposition

$$NH_2\text{-}CO\text{-}NH_2 + 3H_2O \xrightarrow{T=353K} 2NH_4^+ + 2OH^- + CO_2 \qquad (6.1)$$

The solid obtained was separated by centrifugation, washed with deionised water (with centrifugation between each washing) and dried in He (60 cm^3 min^{-1}) at 373 K (2 K min^{-1}) for 5 h. For comparison purposes, Au/Al_2O_3 (1 w/w %) was prepared by standard impregnation of Al_2O_3 with aqueous $HAuCl_4$ (7.3×10^{-3} M) where the slurry was heated at 2 K min^{-1} to 353 K and agitated (600 rpm) in a He purge. In addition, Pd/Al_2O_3 and Ni/Al_2O_3 prepared by impregnation with $Pd(NO_3)_2$ and $Ni(NO_3)_2$ as described elsewhere [38] were employed as benchmark catalysts. The samples were sieved to 75 μm average particle diameter (ATM fine test sieves) and metal loading determined by inductively

coupled plasma-optical emission spectrometry (ICP-OES, Vista-PRO, Varian Inc.) from the diluted extract of aqua regia.

6.2.3 Catalyst Characterisation

The pH associated with the point of zero charge (pH_{PZC}) of the ZrO_2 support was determined using the potentiometric mass titration technique [39]. Three different masses of ZrO_2 (0.025, 0.050 and 0.075 g) were immersed in 50 cm^3 0.1 M NaCl to which a known amount of NaOH (0.1 M) had been added to adjust the pH to *ca.* 11. After pH stabilisation (*ca.* 1 h), sample titration was performed under continuous agitation in He with HCl (0.1 M) as titrant; temporal changes to pH were measured as described above. Nitrogen adsorption-desorption isotherms were obtained at 77 K using the commercial Micromeritics Gemini 2390 automated system. Specific surface area was obtained using the standard BET method and the average pore size, cumulative pore volume and pore size distribution obtained from BJH analysis of the desorption isotherm; samples were outgased at 423 K for 1 h prior to analysis. Temperature programmed reduction (TPR) and H_2 chemisorption were recorded using the commercial CHEMBET 3000 (Quantachrome Instrument) unit; data acquisition/manipulation employed the TPR Win^{TM} software. The sample was loaded into a U-shaped quartz cell (100 mm × 3.76 mm i.d.) and heated in 17 cm^3 min^{-1} (Brooks mass flow controlled) 5% v/v H_2/N_2 at 2-10 K min^{-1} to 473-1073 K. Following TPR (to 473 K), the samples were swept with 65 cm^3 min^{-1} N_2 for 1.5 h, cooled to ambient or reaction (423 K) temperature and subjected to H_2 chemisorption using a pulse (10 µl) titration procedure. Hydrogen pulse introduction was repeated until the signal area was constant, indicating surface saturation. Powder X-ray diffractograms (XRD) were recorded on a Bruker/Siemens D500 incident X-ray diffractometer using Cu Kα radiation. The sample was scanned at a rate of 0.02º $step^{-1}$ over the range $5º \leq 2\theta \leq 85º$. The diffractograms were identified using the JCPDS-ICDD reference standards, *i.e.* Au (Card No. 04-0784), ZrO_2 (tetragonal (50-1089) and monoclinic (37-1487)) and γ-Al_2O_3 (10-0425). The monoclinic fraction was calculated, based on the work of Toraya *et al*. [40], using the integrated intensities (I) of the (111) and (-111) monoclinic

(m-ZrO_2) and (011) tetragonal (t-ZrO_2) signals,

$$X_m = \frac{I_m(-111)+I_m(111)}{I_m(-111)+I_m(111)+I_t(011)}; \qquad V_m = \frac{1.31 \times X_m}{1+0.31 \times X_m} \tag{6.2}$$

where X_m represents the intensity ratio and V_m the fraction of monoclinic ZrO_2. Transmission electron microscopy was conducted on a JEOL JEM 2011 HRTEM unit with a UTW energy dispersive X-ray (EDX) detector (Oxford Instruments) operated at an accelerating voltage of 200 kV with Gatan Digital Micrograph 3.4 for data acquisition/manipulation. Samples were dispersed in acetone and deposited on a holey carbon/Cu grid (300 Mesh). The metal particle size is given as a surface area-weighted mean (d_{TEM}) according to

$$d_{TEM} = \frac{\sum_i n_i d_i^3}{\sum_i n_i d_i^2} \tag{6.3}$$

where n_i is the number of particles of diameter d_i and $\Sigma\ n_i = 250$. XPS spectra were collected on a SPECS (Phoibos MCD 150) X-ray photoelectron spectrometer, using an Al Kα (hv = 1486.6 eV) x-ray source. Binding energies were calibrated with respect to the C-C/C-H components of the C 1s peak (binding energy = 284.7 eV); spectra processing employed the Casa XPS software package.

6.2.4 Catalytic Procedure

Reactions were carried out *in situ,* immediately after activation (at 2 K min^{-1} to 473 K in 60 cm^3 min^{-1} H_2 for 1h) in a continuous flow fixed bed vertical glass reactor (i.d. = 15 mm, l = 600 mm) at 423 K and 1 atm. The catalytic reactor and operating conditions to ensure negligible heat/mass transport limitations have been fully described elsewhere [41,42] but some features, pertinent to this study, are given below. A layer of borosilicate glass beads served as a preheating zone, ensuring that the organic reactants were vaporised and reached reaction temperature before contacting the catalyst. Isothermal conditions (± 1 K) were ensured by diluting the catalyst bed with ground glass (75 μm); the ground glass was mixed thoroughly with catalyst before insertion

into the reactor. Reaction temperature was continuously monitored by a thermocouple inserted in a thermowell within the catalyst bed. The *p*-NBN reactant was delivered *via* a glass/teflon air-tight syringe and teflon line using a microprocessor controlled infusion pump (Model 100 kd Scientific) at a fixed calibrated flow rate. A co-current flow of *p*-NBN and H_2 was maintained at a $GHSV = 2 \times 10^4$ h^{-1} with an inlet *p*-NBN molar flow (F) in the range 4.0×10^{-5}–7.2×10^{-5} mol h^{-1}; the molar Au (n_{Au}) to F content spanned the range 1.6×10^{-3}–14×10^{-2} h. In a series of blank tests, passage of *p*-NBN in a stream of H_2 through the empty reactor or over the support(s) alone did not result in any detectable conversion. The reactor effluent was frozen in a liquid nitrogen trap for subsequent analysis, which was made using a Perkin-Elmer Auto System XL gas chromatograph equipped with a programmed split/splitless injector and a flame ionization detector, employing a DB-1 50 m × 0.20 mm i.d. 0.33 μm film thickness capillary column (J&W Scientific). Repeated reactions with different samples from the same batch of catalyst delivered raw data that were reproducible to within ± 7 %.

6.3 Results and discussion

6.3.1 Catalyst Characteristics

6.3.1.1 ZrO_2 Synthesis and Characterisation

Solution pH during ZrO_2 synthesis exhibited a temporal decrease from 11.8 to 9.3, at which point [43] precipitation was complete (see **Figure 6.1(A)**). Synthesis was conducted under basic conditions as this generates a hydrous precursor that can be converted to ZrO_2 with higher surface area than achieved at low pH [43]. The as prepared ZrO_2 (after drying) exhibited a surface area (280 m^2 g^{-1}, **Table 6.1**) close to that reported for similar preparation conditions [44,45]. The XRD pattern (not shown) for this sample did not exhibit any diffraction peaks due to crystalline ZrO_2, indicating an amorphous state. It has, however, been observed elsewhere that sample calcination is required at temperatures in excess of 573 K to generate a crystalline phase [48]. Moreover, it has been demonstrated that support crystallinity is critical for Au/ZrO_2

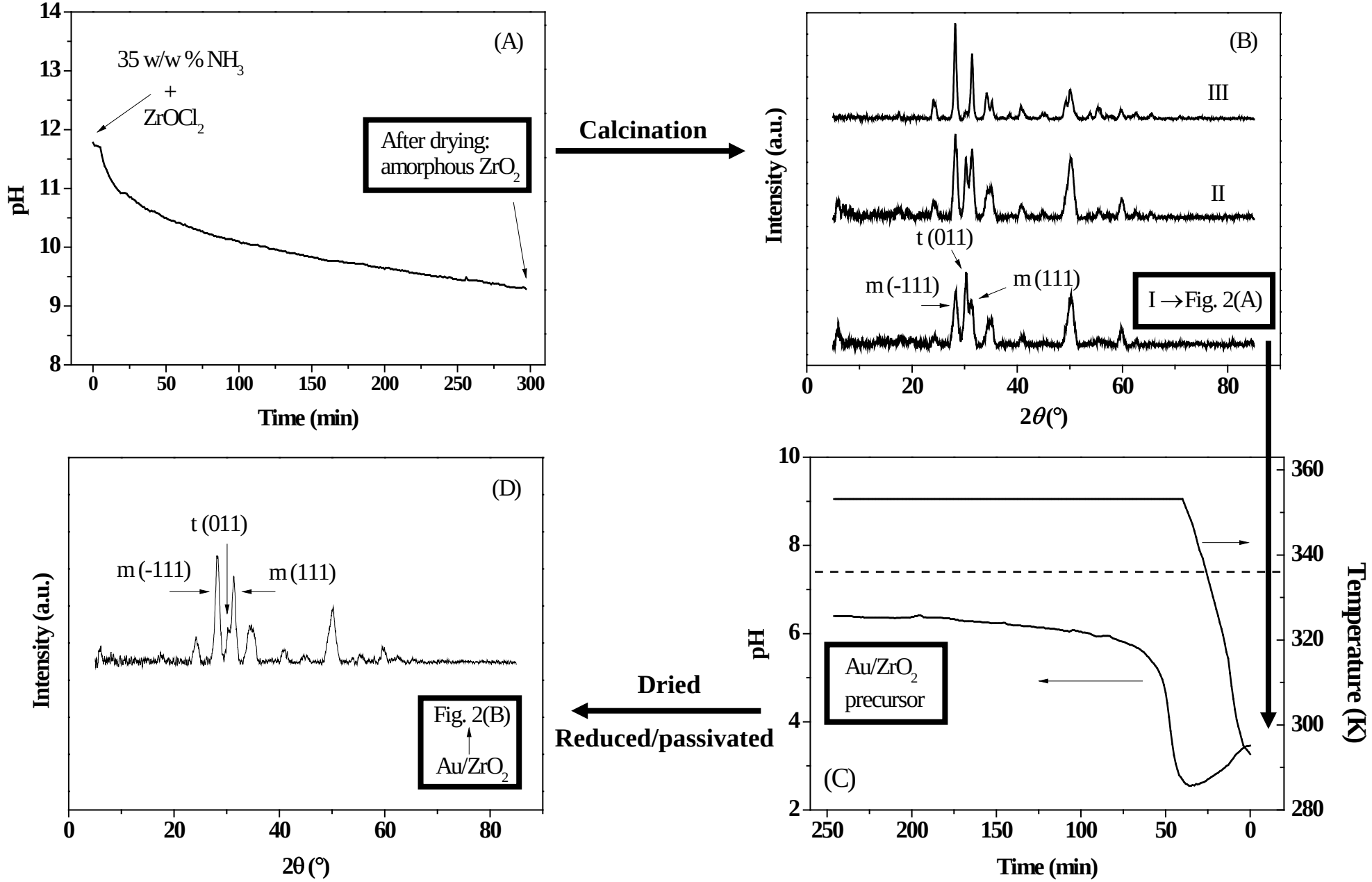

Figure 6.1: (A) Temporal pH variation in the preparation of ZrO_2; (B) XRD patterns of ZrO_2 calcined at (I) 673 K, (II) 723 K and (III) 973 K; (C) Temporal pH and temperature variation in the preparation of Au/ZrO_2. *Note*: dashed line identifies pH_{PZC} of the ZrO_2 support; (D) XRD patterns of reduced/passivated Au/ZrO_2.

Table 6.1: BET surface area, porosity and crystallinity characteristics of ZrO_2 and Au/ZrO_2.

Sample (calcination temperature)	BET surface area ($m^2\ g^{-1}$)[a]	Total pore volume ($cm^3\ g^{-1}$)[b]	Mean pore radius (Å)[c]	Monoclinic phase (%)	Crystallite size (nm)[d]
ZrO_2[e]	280 (289 [44,45])	0.19 (0.19 [44])	14 (15 [49])	-	-
ZrO_2 (673 K)	104 (120 [46],123 [24],110 [4])	0.14 (0.16 [46])	19	58	10.7
ZrO_2 (723 K)	89	0.09	15	72	11.8
ZrO_2 (973 K)	25 (22 [4],40 [47],13 [48])	0.07	31	97 (96 [50])	16.2
Au/ZrO_2[f]	93	0.13	19	88	11.6

[a]values quoted in the literature are given in parentheses

[b]cumulative volume of pores with radii in range 8-1500 Å from BJH analysis

[c]from BJH analysis of desorption isotherm (2V/A)

[d]calculated using Scherrer formula from (-111) and (111) peaks for monoclinic ZrO_2 and (011) peak for tetragonal ZrO

[e]sample as prepared (and dried at 373 K)

[f]ZrO_2 calcined at 673 K

catalytic activity in hydrogenation reactions [23]. It is immediately evident from the entries in **Table 6.1** that increasing calcination temperature served to lower surface area and total pore volume. Zhao *et al.* [49] reported a surface area decrease from 349 (as prepared) to 15 m^2 g^{-1} (calcined at 1073 K). Mercera *et al.* [44] noted that the initial high specific surface area fell drastically (by 97%) for calcination up to 1123 K and attributed this to crystallite growth with an accompanying phase transformation and/or thermally induced sintering. The XRD patterns for calcined ZrO_2 samples, presented in **Figure 6.1(B)**, exhibited the three main characteristic peaks [47,48] for monoclinic ((-111), (111)) and tetragonal (011) crystalline phases based on the JCPDS references (37-1484 and 50-1089). It can be seen that the intensity of the tetragonal (011) peak relative to the monoclinic (-111) and (111) signals was lower at higher temperatures, indicating a thermal dependence of phase composition. The monoclinic content was obtained by applying eq. (6.2) and is given in **Table 6.1**; a near pure monoclinic phase was obtained at 973 K. Xu and co-workers recorded a 96% monoclinic content after treatment at 973 K [50]. Chuah *et al.* [43] have shown that ZrO_2 phase composition is sensitive to precipitation temperature, pH and thermal treatment. A mixed phase that was predominantly monoclinic (50-78%) was formed at synthesis temperatures in the range 303-353 K in basic media with subsequent calcination at 773 K. We observed (see **Table 6.1**) an increase in crystallite size (from 10.7 to 16.2 nm) at higher temperatures, which agrees with the findings of Stichert *et al*. [51].

Use of a high surface area support on which to anchor Au particles can ensure a well dispersed metal phase at the *nano*-scale, which is critical for appreciable hydrogenation activity [52,53]. As ZrO_2 crystallinity is a requirement for enhanced hydrogenation performance, the sample resulting from calcination at 673 K (BET area = 104 m^2 g^{-1}) was chosen as the Au carrier. The N_2 adsorption isotherms for this sample are shown in **Figure 6.2(A)**, where the observed hysteresis is typical of (type IV) mesoporous materials. The resultant pore size distribution (10–29 Å) and mean pore radius (19 Å) are diagnostic of a well-developed mesopore framework [44,54]. Metal/support interactions are crucial in determining ultimate metal loading and size distribution. In catalyst preparation by deposition-precipitation, the pH associated with

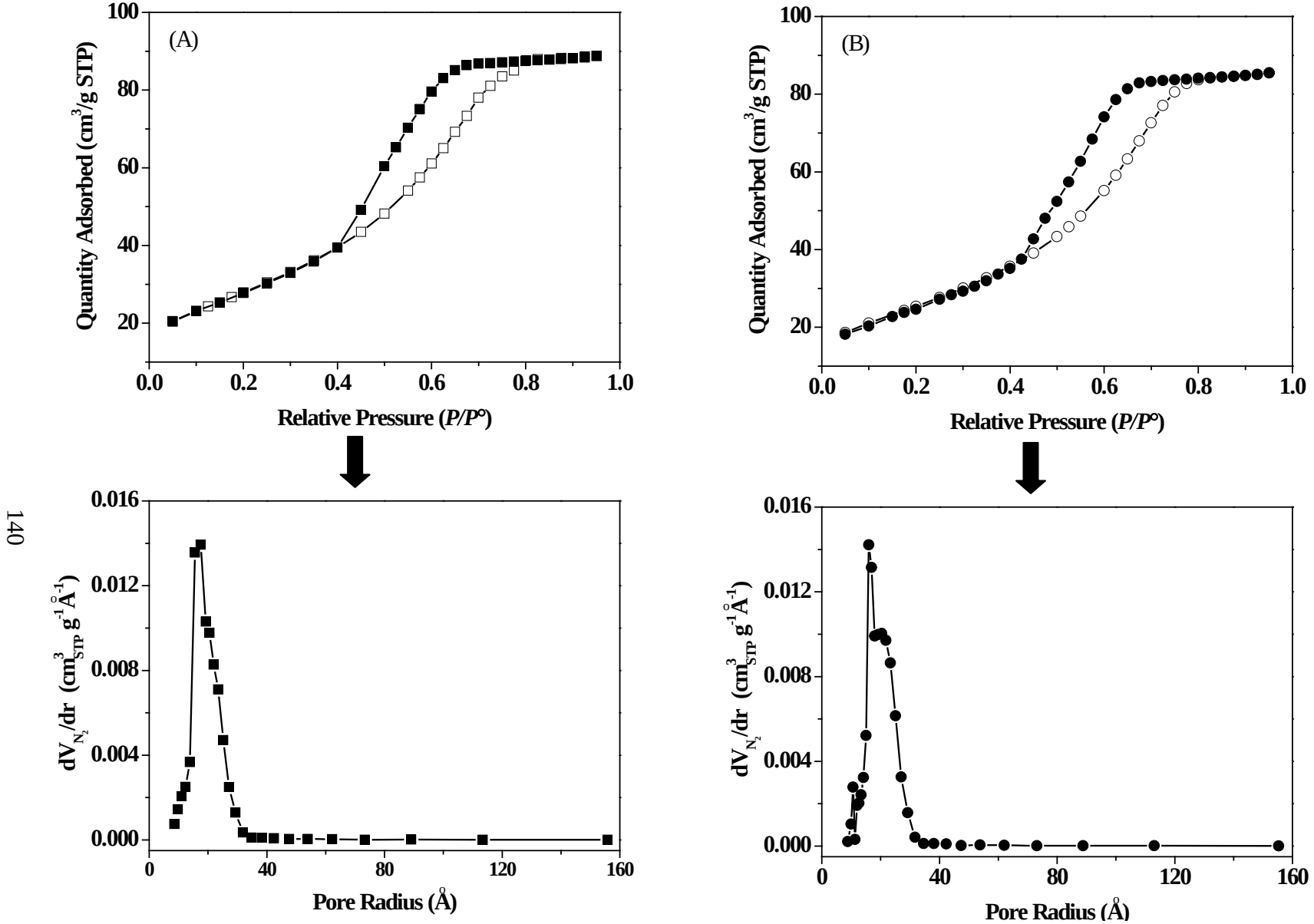

Figure 6.2: Nitrogen adsorption (open symbols) and desorption (solid symbols) isotherms with associated pore size distributions for (A) ZrO_2 (post calcination at 673 K) and (B) Au/ZrO_2 (post TPR at 473 K).

Table 6.2: Physicochemical characteristics of Au/ZrO_2 and Au/Al_2O_3: gold loading, BET surface area, total pore volume and mean radius, temperature programmed reduction (TPR) T_{max} with associated H_2 consumption, H_2 chemisorbed/desorbed (TPD), surface area weighted mean Au diameter (d_{TEM}), dispersion (D) and Au $4f_{7/2}$ binding energy (BE).

Catalyst		Au/ZrO_2	Au/Al_2O_3
Au loading (% w/w)		0.8	1.1
BET surface area ($m^2\ g^{-1}$)		93	161
Total pore volume ($cm^3\ g^{-1}$)		0.13	0.36
Mean pore radius (Å)		19	30
TPR	T_{max} (K)	452	417
	H_2 consumed (mmol g_{Au}^{-1})	7.0	7.1
H_2 chemisorption (µmol g_{Au}^{-1})[a]		56	19
H_2 chemisorption (µmol g_{Au}^{-1})[b]		154	61
H_2 desorbed (mmol g_{Au}^{-1})		28	24
d_{TEM} (nm)		7.0	7.8
D (%)		18	16
XPS BE (Au $4f_{7/2}$)		83.5	83.2

[a]at ambient temperature
[b]at reaction temperature (423 K)

the point of zero charge (pH_{PZC}) is a critical property of the support that determines the extent of precursor-support interaction as a function of solution pH [39]. A pH_{PZC} of 7.4 was determined experimentally for the ZrO_2 support, which is within the range of values (6.2-8.5) reported elsewhere [55,56]. The pH_{PZC} is dependent on ZrO_2 preparation and composition where a higher value (8.5) is associated with the pure monoclinic phase relative to the tetragonal form (6.2) [55].

6.3.1.2 Au/ZrO_2 and Au/Al_2O_3 Synthesis and Characterisation

The temporal pH variation in Au/ZrO_2 preparation is shown in **Figure 6.1(C)** where the pH_{PZC} of ZrO_2 (7.4) is identified by the horizontal dashed line. The initial pH drop can be linked to temperature induced $HAuCl_4$ hydrolysis [57]. A further increase

in temperature (to 353 K) led to a progressive decomposition of urea accompanied by an increase in pH. As the solution pH remained below the pH_{PZC}, the support retained a net positive charge favouring interaction with anionic gold species ($AuCl_4^-$ and/or $Au(OH)Cl_3^-$) in solution [58] and the surface sites served as nucleation centres for Au deposition [59]. The incorporation of Au on ZrO_2 resulted in a measurable decrease in surface area and pore volume (**Table 6.1**). The associated N_2 isotherms (**Figure 6.2(B)**) exhibited type IV hysteresis of mesopore materials with pore radii in the 10-29 Å range and mean = 19 Å.

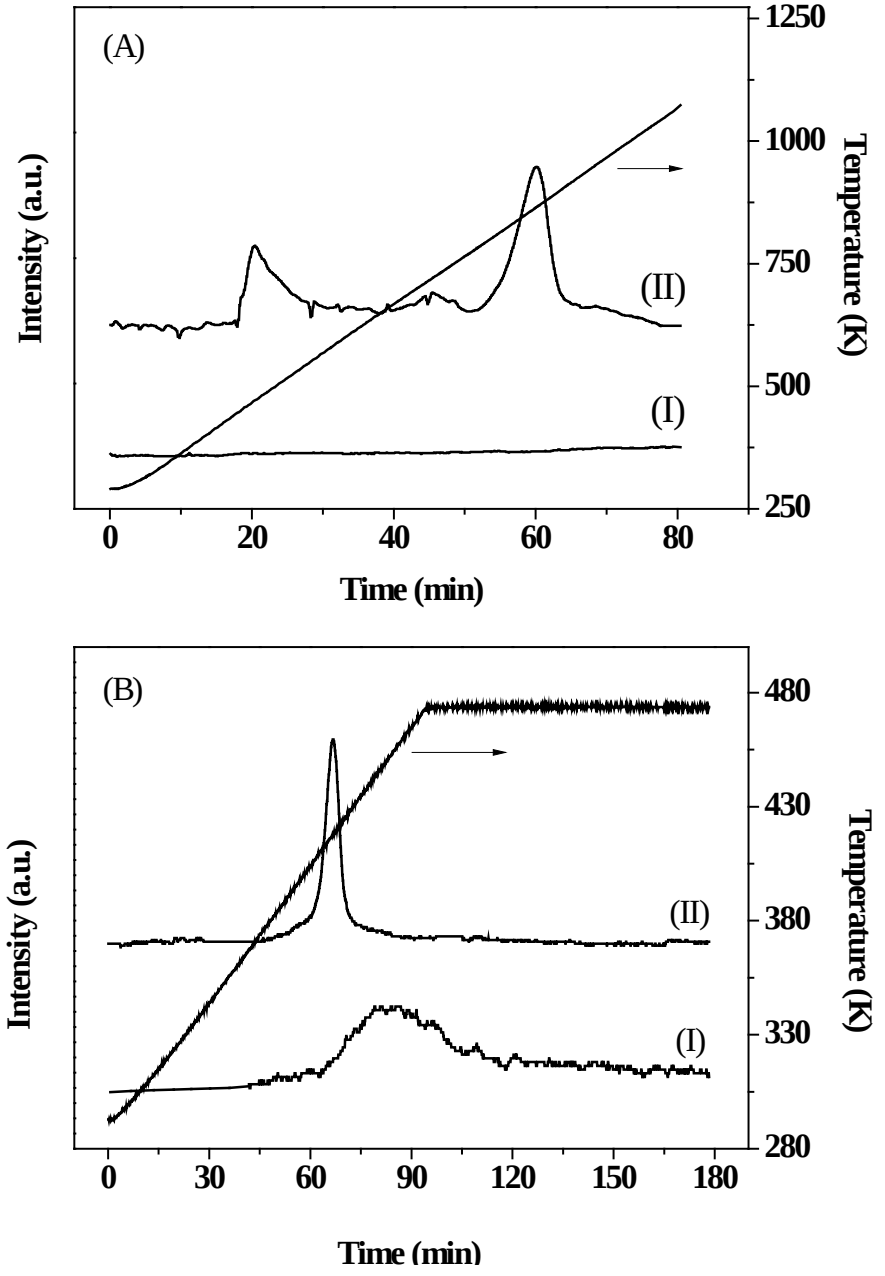

Figure 6.3: (A) Temperature programmed reduction (TPR) profiles (10 K min^{-1} to 1073 K) for (A) (I) ZrO_2 and (II) Au/ZrO_2; (B) TPR profiles (2 K min^{-1} to 473 K) for (I) Au/ZrO_2 and (II) Au/Al_2O_3.

Alumina supported Au, carried through in this study for comparative purposes was characterised by a surface area (161 m^2 g^{-1}, **Table 6.2**), total pore volume (0.36 cm^3 g^{-1}) and average pore size (30 Å) that is in line with a related Au/Al_2O_3 system [33].

Temperature programmed reduction (TPR) screening (to 1073 K) was conducted to assess reducibility of ZrO_2 and Au/ZrO_2; the resultant profiles are presented in **Figure 6.3(A)**. There was no detectable H_2 consumption or release in the TPR of the ZrO_2 support, which agrees with earlier reports [60,61]. The TPR profile of Au/ZrO_2 exhibited two positive peaks (H_2 consumption), where the lower temperature signal can be assigned to the reduction of the supported Au^{3+} phase. The peak at 865 K is then attributable to a partial reduction of (surface) Zr^{4+} (to Zr^{3+}) associated with the support. Xu *et al.* have observed two reduction peaks (at 483–503 and 823–853 K) for Au/ZrO_2 precalcined at 573 K [62]. This suggests that the incorporation of Au facilitates support reduction during TPR as has been proposed for Au/CeO_2 [34], $Au/Ce_xZr_{1-x}O_2$ [63] and Au/TiO_2 [64]. Grau-Crespo and co-workers [65], applying density functional theory, have demonstrated that the presence of Au in the ZrO_2 lattice can impact on surface redox properties under reducing conditions. A final reduction temperature of 473 K was accordingly employed to reduce the supported Au precursor without modifying the ZrO_2 support. The associated TPR profile (**Figure 6.2(B)**) exhibits a single peak with T_{max} = 452 K where the H_2 consumed (**Table 6.2**) corresponds to that required (to within 10%) for the reduction of supported Au^{3+} to Au^0. Reduction of Au/Al_2O_3 generated a single peak at a lower temperature (417 K) where H_2 consumption coincides with that required for Au precursor reduction and there was no contribution from the "non-reducible" Al_2O_3 carrier [34]. The requisite reduction temperature is determined by Au-support interactions [64], where the higher TPR T_{max} for Au/ZrO_2 (452 K) suggests stronger interaction than in the case of Au/Al_2O_3 (417 K). This can be significant in that Lopez-Sanchez and Lennon have related catalytic performance for Au/TiO_2 and Au/Fe_2O_3 (in propyne hydrogenation) to the interaction of Au (at an equivalent particle size) with the support [66]. Moreover, Liu and Yang proposed that weaker Au support-interactions (low T_{max} in TPR) led to inferior activity [67].

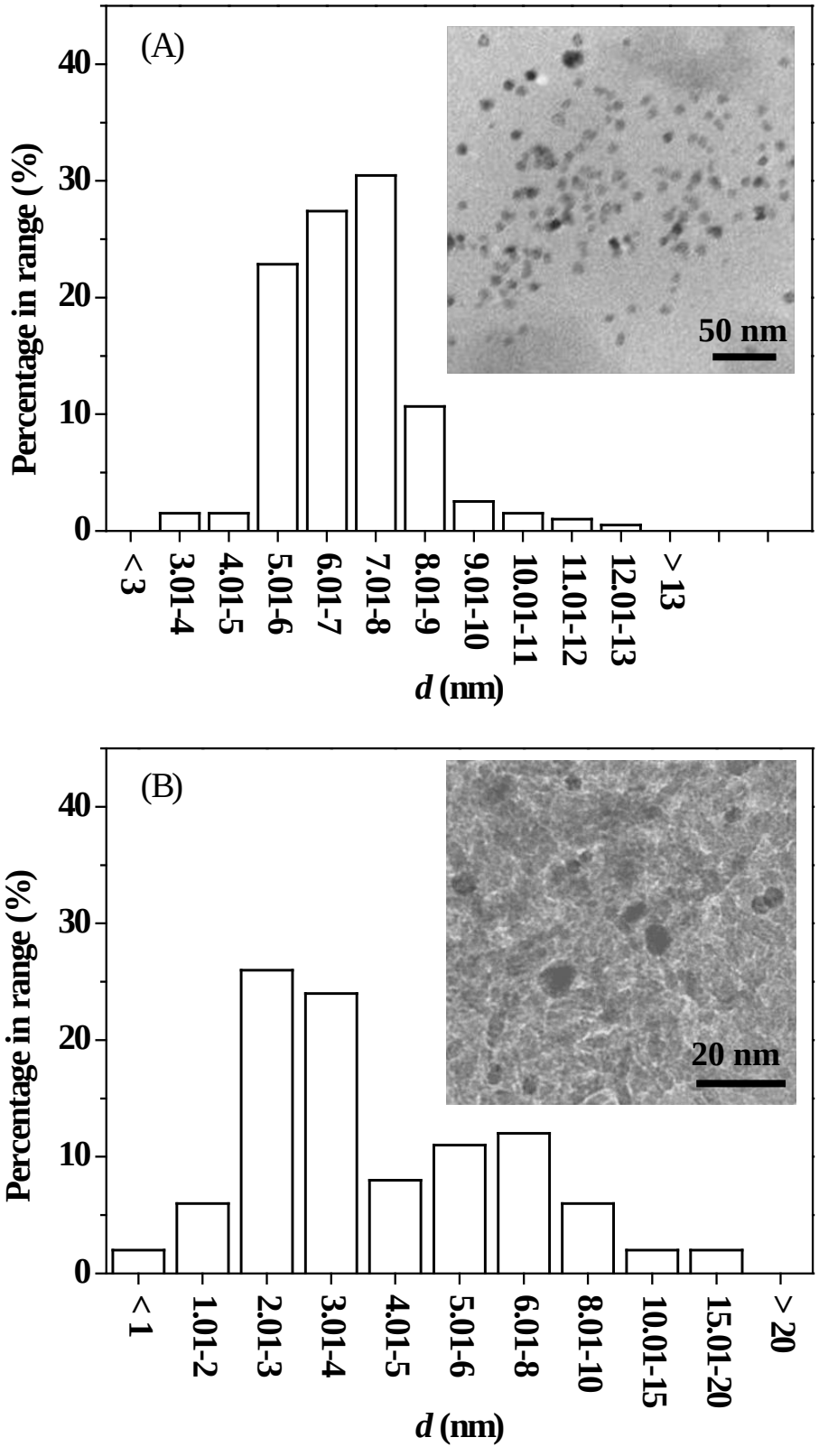

Figure 6.4: Gold particle size distribution histograms with representative TEM images (inset) for (A) Au/ZrO_2 and (B) Au/Al_2O_3.

The XRD pattern of activated Au/ZrO_2 (**Figure 6.1(D)**) coincides with the starting ZrO_2 support (Profile I, **Figure 6.1(B)**) in terms of peak position. However, the intensity of

the tetragonal (011) signal (at 2θ = 30.3°) was markedly lower with a consequent increase in monoclinic character (from 58 to 88%) due to the incorporation of Au. Such a phase change in the support alone would require elevated calcination temperature, accompanied by a significantly lower BET surface area (see **Table 6.1**). The XRD pattern for Au/ZrO_2 as prepared matched that obtained for the activated catalyst and the support phase change was not the result of the TPR step. Xie and co-workers [47] have reported that exposure of tetragonal ZrO_2 to 3 kPa H_2O or immersion in water at 298 K resulted in extensive (*ca.* 80%) transformation to the monoclinic form without loss of surface area, an effect that they attributed to differences in surface free energy between the two phases after water adsorption. In our Au/ZrO_2 preparation, the support was contacted with an aqueous Au salt solution with pH and temperature variations for up to 4 h that must contribute to the observed phase change. Representative TEM images and associated Au particle size distributions for Au/ZrO_2 (A) and Au/Al_2O_3 (B) are provided in **Figure 6.4**. The micrographs reveal discrete Au particles at the nano-scale that exhibit a quasi-spherical morphology with comparable surface area weighted mean diameters (7-8 nm, **Table 6.2**).

While the nature of H_2-Au interactions in supported Au systems has yet to be well established, the consensus that emerges suggests a high activation energy barrier for dissociative adsorption [53]. Dissociative chemisorption has been associated with low coordination Au sites and shows a dependence on Au size [52,68]. The ambient temperature H_2 chemisorption on Au/ZrO_2 was significantly greater (by a factor of 3) than that recorded for Au/Al_2O_3 (**Table 6.2**). Moreover, H_2 adsorption is an activated process that was enhanced at higher temperature (to 423 K, **Table 6.2**). Bus *et al*. have also recorded an increase in H_2 chemisorption with increasing temperature (from 298 to 373 K) [69]. Given the equivalence in Au size, the differences in H_2 uptake on Au/ZrO_2 and Au/Al_2O_3 may be linked to Au electronic structure. Boronat *et al*. [70] have proposed, from density functional calculations, that Au atoms (on TiO_2) active for H_2 dissociation must be neutral or with a net charge close to zero and located at corner or edge positions, not directly bonded to the support. In earlier work, we have established that Au electronic structure [33,64] is an important property that determines

hydrogenation activity and selectivity. XPS analysis was conducted to probe Au electronic state and the profiles over the Au 4*f* binding energy (BE) region are presented in **Figure 6.5**. The response for Au/ZrO_2 is characterised by peaks at 83.5 eV and 87.3 eV that agree with Au $4f_{7/2}$ (83.6 eV [71], 83.8 eV [72]) and $4f_{5/2}$ (87.6 eV [71]) BE values reported elsewhere. The Au/Al_2O_3 profile exhibited signals at 83.2 eV and 87.0 eV that also match the literature [73,74]. Both catalysts exhibited a shift to lower BE relative to the reference metallic Au $4f_{7/2}$ (84.0 eV), indicating electron transfer from the support to the nano-scale Au [75]. An electron-rich ($Au^{\delta-}$) phase is accordingly generated on both supports with a greater degree of electron transfer (on the basis of BE values) from Al_2O_3. Indeed, it has been demonstrated by Ealet and Gillet that electronegative Au acts as an electron acceptor with respect to Al, inducing electron transfer [76]. The lower degree of charge associated with Au on ZrO_2 relative to Al_2O_3 may account for enhanced H_2 chemisorption on Au/ZrO_2. Shimizu *et al*. [77-79] have proposed that dissociation of H_2 at the Au [77,78] (or Ag [79]) support interface generates $H^{\delta-}$ on Au (or Ag) and $H^{\delta+}$ stabilized by the support oxygen.

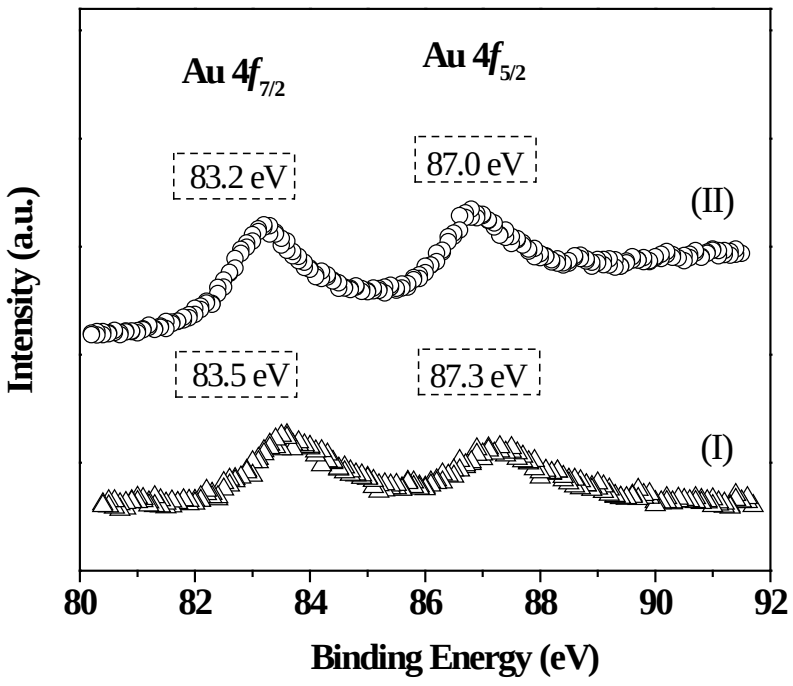

Figure 6.5: XPS spectra over the Au 4*f* region for (I) Au/ZrO_2 and (II) Au/Al_2O_3.

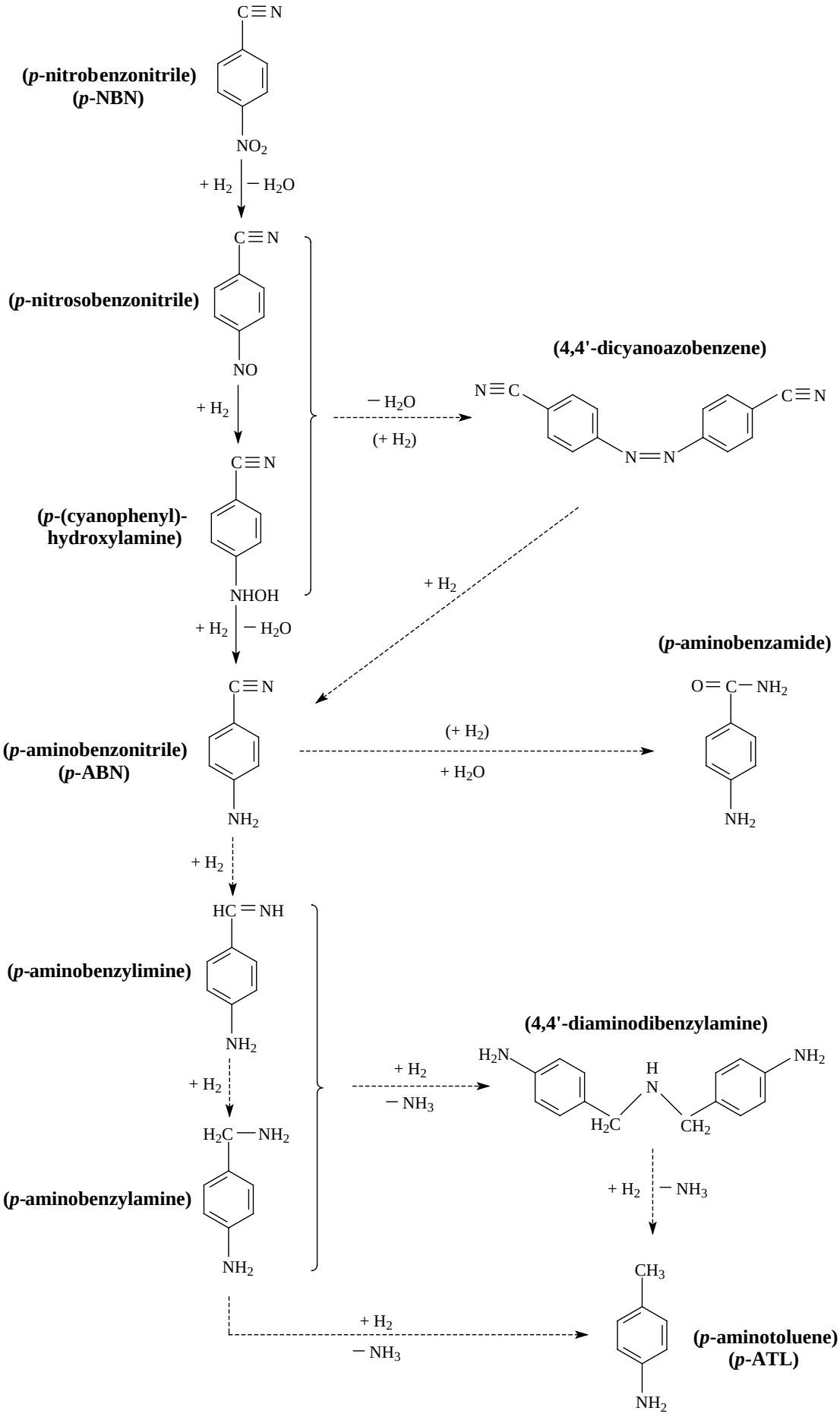

Figure 6.6: Reaction pathways associated with the hydrogenation of *p*-NBN, identifying steps observed in this study (solid arrows) and additional steps reported in the literature [27,30-32] (dashed arrows).

The generation of electron rich $Au^{\delta-}$ on Al_2O_3 may inhibit this process due to repulsion between $Au^{\delta-}$ and $H^{\delta-}$, leading to lower overall uptake. Hydrogen release during TPD from both catalysts is similar but far exceeded that recorded in the chemisorption measurements (**Table 6.2**), suggesting the occurrence of spillover hydrogen during TPR. The spillover phenomenon is well established for supported metals [80], including Au [33,34,63], where H_2 dissociates at metal sites, generating H atoms that diffuse or "spillover" onto the support. This is significant as we have demonstrated previously that spillover hydrogen contributes to nitroarene reduction [33].

6.3.2 Catalytic Response

The hydrogenation of *p*-NBN presents enormous selectivity challenges, generating up to 15 intermediates and products as established by Koprivova and Cerveny [30]. While an overall reaction scheme can involve disproportionation, reduction, condensation, hydrodenitrogenation and hydrodecarbonation, a simplified pathway is presented in **Figure 6.6** that applies to the published (liquid phase) catalytic studies [30,31]. Conversion of *p*-NBN to the target *p*-ABN generates partially hydrogenated *p*-nitrosobenzonitrile and *p*-(cyanophenyl)-hydroxylamine [27] as intermediates that can undergo condensation to give 4,4´-dicyanoazobenzene [30]. The *p*-ABN formed can be further hydrogenated to primary amines (*p*-aminobenzylamine and *p*-aminobenzamide) [30] with subsequent hydrogenolysis to give *p*-aminotoluene (*p*-ATL) [30,31]. Furthermore, primary amine condensation results in secondary amine (4,4'-diaminodibenzylamine) formation that can also be converted to *p*-ATL. Fractional *p*-NBN conversion ($x_{p\text{-NBN}}$) is illustrated as a function of time on-stream in **Figure 6.7(A)**. The temporal activity response can be expressed in terms of the empirical relationship [33,39]

$$\frac{(x_{p-NBN} - x_0)}{(x_{3h} - x_0)} = \frac{\Delta t}{(\beta + \Delta t)} \tag{6.4}$$

where x_{3h} represents conversion after 3 h on-stream and β is a time scale fitting parameter. Fit convergence yields x_0 (initial conversion) used to derive the rate constant

(*k*) according to

$$\ln(1-x_0)^{-1} = k\left(\frac{n}{F}\right) \tag{6.5}$$

where n/F has the physical significance of contact time. The linear relationship between $\ln(1\text{-}x_0)^{-1}$ and n/F for both catalysts is shown in **Figure 6.7(B)**.

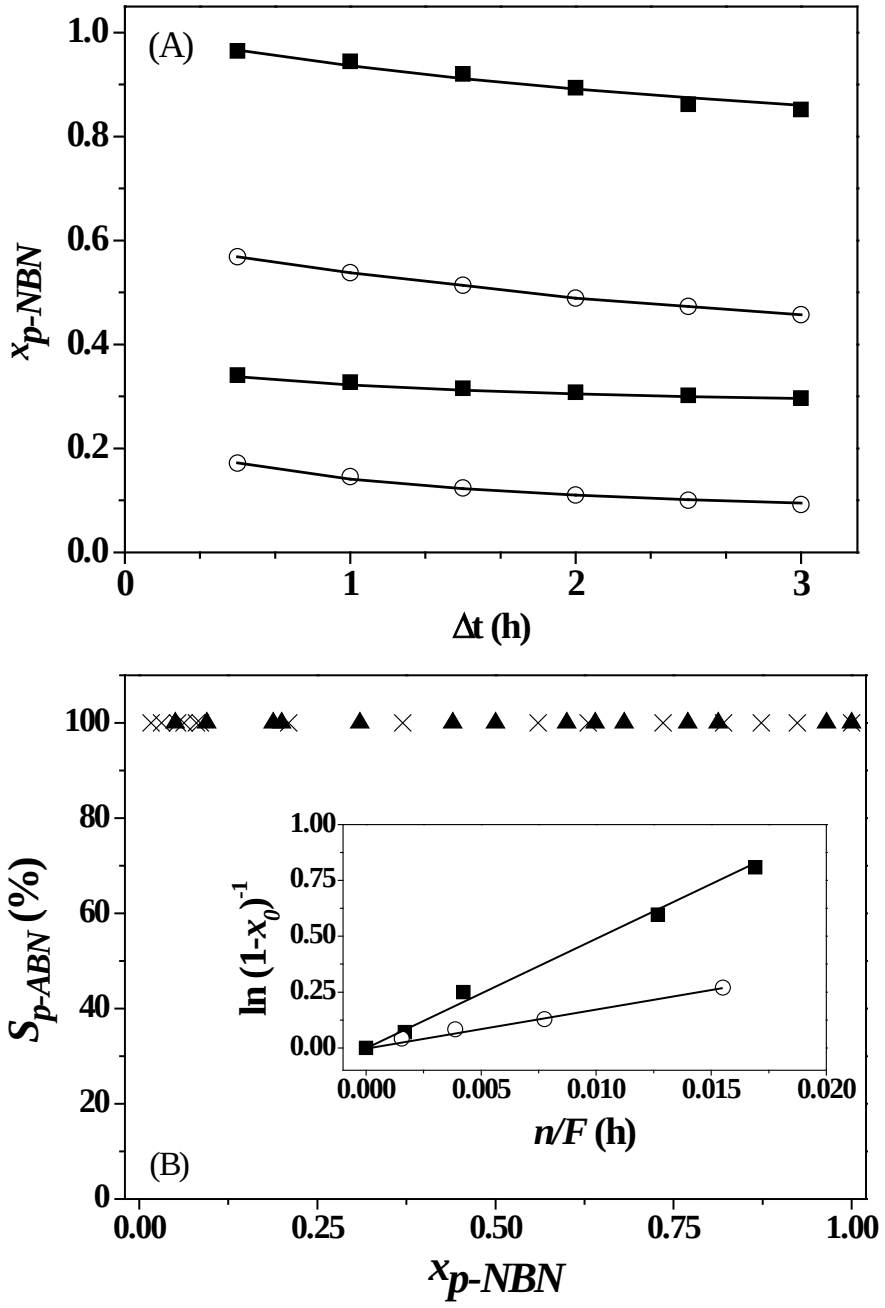

Figure 6.7: (A) Time on-stream variation of *p*-NBN fractional conversion ($x_{p\text{-}NBN}$) over Au/ZrO_2 (■) and Au/Al_2O_3 (○): n/F: 1.6-5.4 × 10^{-2} h; lines represent fit to eq. (6.4). (B) *p*-ABN selectivity ($S_{p\text{-}ABN}$) as a function of $x_{p\text{-}NBN}$ over Au/ZrO_2 (▲) and Au/Al_2O_3 (×); inset: pseudo-first order kinetic plots for reaction over Au/ZrO_2 (■) and Au/Al_2O_3 (○).

The experimentally determined rate constants were normalised with respect to Au dispersion to give *p*-NBN turnover frequencies (*TOF*, h^{-1}). The catalytic results are presented in **Table 6.3**, where it can be seen that Au/ZrO_2 delivered a significantly higher *TOF* relative to Au/Al_2O_3. The activity of Au catalysts in nitro group reduction (chloronitrobenzene [81], dinitrobenzene [64] and nitrocyclohexane [34]) has been demonstrated to show a dependence on Au size, where smaller Au particles (at the nano-scale) deliver higher specific rates. Given the equivalent mean Au diameters for Au/ZrO_2 and Au/Al_2O_3, the difference in rate can be attributed to Au electronic structure, *i.e.* increased relative electron transfer from Al_2O_3 (to generate $Au^{\delta-}$) that serves to suppress H_2 uptake under reaction conditions with a resultant higher *TOF* delivered by Au/ZrO_2. Moreover, increased electron density at Au sites on Al_2O_3 can result in strong repulsive effects with respect to electron rich $–NO_2$ (as an electron withdrawing group), leading to unfavourable nitro-group activation that inhibits activity, as discussed elsewhere [33].

Table 6.3: Catalytic performance of Au/ZrO_2, Au/Al_2O_3, Pd/Al_2O_3 and Ni/Al_2O_3 in terms of *p*-NBN turnover frequency (*TOF*) and *p*-ABN selectivity ($S_{p\text{-}ABN}$) at partial (x = 0.1) and complete (x = 1) *p*-NBN conversion.

Catalyst	*TOF* (h^{-1})	$S_{p\text{-}ABN}$ (%) at $x_{p\text{-NBN}}$ = 0.1	$S_{p\text{-}ABN}$ (%) at $x_{p\text{-NBN}}$ = 1
Au/ZrO_2	267	100	100
Au/Al_2O_3	109	100	100
Pd/Al_2O_3[a]	1717	100	0[b]
Ni/Al_2O_3[a]	123	0[b]	0[b]

[a] $x_{p\text{-NBN}}$ = 0.1 obtained using 10% v/v H_2 in He as carrier gas
[b] *p*-aminotoluene (*p*-ABT) was the sole product

Both Au catalysts promoted the exclusive production of *p*-ABN at every level of conversion ($x_{p\text{-}NBN}$ from 0 to 1) as shown in **Figure 6.7(B)**, *i.e.* a 100% yield of the target amine. This is a significant finding as reaction exclusivity to *p*-ABN has not been reported previously. The only gas phase study with which we can compare our results

dates from the 1950s where Hata and Watanabe [31] investigated the hydrogenation of various aromatic nitriles (including the three NBN isomers) over a Ni–Cu catalyst at 523-573 K and reported, as principal products, aniline, toluidine and ABN (< 32% yield). Reaction of benzonitrile over Au/ZrO_2 or Au/Al_2O_3 did not result in any conversion. In contrast, use of nitrobenzene as feed generated aniline where Au/ZrO_2 delivered a higher *TOF* (238 h^{-1}) than Au/Al_2O_3 (67 h^{-1}) under identical reaction conditions. This is consistent with the reaction selectivity for *p*-NBN where the nitrile function remains unreacted and Au/ZrO_2 is intrinsically more active. Recently, Corma *et al*. have employed both homogeneous [25] and heterogeneous [26] catalysts to convert NBN to ABN, where Au/TiO_2 exhibited the highest selectivity (99%) for reaction at 25 atm and 413 K [25]. Unfortunately, these studies did not include any *TOF* values that we can relate to our measurements. The move from batch liquid to gas phase continuous operation is, however, an important process development in terms of increased throughput and energy efficiency where 100% yield at ambient pressure represents enhanced sustainability.

In order to further probe reaction selectivity in gas phase operation, we employed Pd/Al_2O_3 and Ni/Al_2O_3 as benchmark catalysts (characterisation details provided elsewhere [38]) that have shown appreciable activity in nitro- [38] and carbonyl-group [35] reduction; results are presented in **Table 6.3**. Drawing on published work, application of Pd(II) acetate in liquid phase hydrogenation of *p*-NBN gave a 77% *p*-ABN yield [27], whereas Raney Ni was non-selective, generating (from *o*-NBN) a range of intermediates and by-products including *o*-aminobenzylamine, *o*-aminobenzamide, o-ATL, 3,3'-dicyanoazobenzene and 3,3'-diaminodibenzylamine etc. (see **Figure 6.6**) [30]. Gas phase reaction over Pd/Al_2O_3 exhibited a significantly higher *TOF* relative to the two supported Au systems with full selectivity to *p*-ABN at low fractional *p*-NBN conversion ($x_{p\text{-NBN}}$ = 0.1). Higher conversion was accompanied by hydrogenolysis to *p*-ATL as the sole product, possibly *via* consecutive *p*-NBN→*p*-ABN→*p*-ATL. There was no detectable *p*-ABN for reaction over Ni/Al_2O_3 at all levels of conversion with exclusive production of *p*-ATL at *TOF* close to that recorded for Au/Al_2O_3. These results establish superior performance for supported Au

(notably Au/ZrO_2) and viable application in the clean continuous production of high value functionalised amines.

6.4 Conclusions

We have synthesised crystalline ZrO_2 used to support Au and employed in the gas phase continuous hydrogenation of *p*-nitrobenzonitrile (*p*-NBN) to *p*-aminobenzonitrile (*p*-ABN), comparing the catalytic response with Au/Al_2O_3. The results support the following:

(a) Precipitation of $ZrOCl_2 \cdot 8H_2O$ with aqueous NH_3 generated amorphous ZrO_2 that was transformed to crystalline monoclinic and tetragonal phases following calcination (in air at 673-1073 K). Higher calcination temperatures increased the monoclinic content with a concomitant decrease in surface area/pore volume and increase in crystallite size. Introduction of Au to (calcined) ZrO_2 by deposition-precipitation facilitated tetragonal→monoclinic phase transformation.

(b) Temperature programmed reduction of Au/ZrO_2 to 473 K served to reduce the supported Au precursor to zero valent metal where higher temperatures resulted in a partial (Au promoted) reduction of the support. TEM analysis established quasi-spherical supported Au particles at the nano-scale (3-13 nm); XPS analysis has revealed electron transfer from the support to generate $Au^{\delta-}$.

(c) Conversion of *p*-NBN over Au/ZrO_2 and Au/Al_2O_3 was fully selective to the target *p*-ABN product. Au/ZrO_2 generated higher *TOF* that is linked to greater H_2 uptake under reaction conditions and a more effective $–NO_2$ activation that is related to differences in Au electronic character on both supports.

(d) Au/ZrO_2 outperformed Pd/Al_2O_3 and Ni/Al_2O_3 where the former only delivered selectivity to *p*-ABN at low conversions with a switch in preference to *p*-aminotoluene (*p*-ATL) whereas Ni/Al_2O_3 was non-selective, promoting *p*-ATL at all levels of conversion.

6.5 References

[6.1] A.V. Chadwick, G. Mountjoy, V.M. Nield, I.J.F. Poplett, M.E. Smith, J.H. Strange, M.G. Tucker, *solid-state NMR and x-ray studies of the structural evolution of nanocrystalline zirconia*, Chem. Mater., **13**, 1219-1229 (2001)

[6.2] B. Al-Amleh, K. Lyons, M. Swain, *Clinical trials in zirconia: a systematic review*, J. Oral Rehabil., **37**, 641-652 (2010)

[6.3] S. Agathopoulos, S. Pina, R.N. Correia, *A review of recent investigations on zirconia joining for biomedical applications*, Adv. Joining Ceram., **138**, 133-147 (2012)

[6.4] T. Yamaguchi, *Application of ZrO_2 as a catalyst and a catalyst support*, Catal. Today, **20**, 199-217 (1994)

[6.5] J. D' Souza, N. Nagaraju, *Vapour phase transesterification over solid acids for the synthesis of isoamyl salicylate*, Indian J. Chem. Technol., **11**, 401-409 (2004)

[6.6] K.J. Ratnam, R.S. Reddy, N.S. Sekhar, M.L. Kantam, F. Figueras, *Sulphated zirconia catalyzed acylation of phenols, alcohols and amines under solvent free conditions*, J. Mol. Catal. A: Chem., **276**, 230-234 (2007)

[6.7] S.-T. Wong, C.-C. Hwang, C.-Y. Mou, *Tungstated zirconia catalyzed bromination of phenol red under nearly neutral solution*, Appl. Catal. B: Environ., **63**, 1-8 (2006)

[6.8] A.H. Hoveyda, J.P. Morken, A.F. Houri, Z. Xu, *The mechanism of the zirconium-catalyzed carbomagnesiation reaction. efficient and selective catalytic carbomagnesiation with higher alkyls of magnesium*, J. Am. Chem. Soc., **114**, 6692-6697 (1992)

[6.9] T. Gehrmann, J. Lloret Fillol, S.A. Scholl, H. Wadepohl, L.H. Gade, *Zirconium-catalyzed multistep reaction of hydrazines with alkynes: a non-Fischer-type pathway to indoles*, Angew. Chem. Int. Ed., **50**, 5757-5761 (2011)

[6.10] X.M. Song, A. Sayari, *Sulfated zirconia-based strong solid-acid catalysts: recent progress*, Catal. Rev., **38**, 329-412 (1996)

[6.11] F.R. van den Berg, M.W.J. Craje, A.M. van der Kraan, J.W. Geus, *Reduction behaviour of Fe/ZrO_2 and Fe/K/ZrO_2 Fischer-Tropsch catalysts*, Appl. Catal. A: Gen., **242**, 403-416 (2003)

[6.12] Y. Liu, K. Fang, J. Chen, Y. Sun, *Effect of pore size on the performance of mesoporous zirconia-supported cobalt Fischer-Tropsch catalysts*, Green Chem., **9**, 611-615 (2007)

[6.13] J.-L. Bi, Y.-Y. Hong, C.-C. Lee, C.-T. Yeh, C.-B. Wang, *Novel zirconia-supported catalysts for low-temperature oxidative steam reforming of ethanol*, Catal. Today, **129**, 322-329 (2007)

[6.14] S. Li, C. Zhang, P. Zhang, G. Wu, X. Ma, J. Gong, *On the origin of reactivity of steam reforming of ethylene glycol on supported Ni catalysts*, Phys. Chem. Chem. Phys., **14**, 4066-4069 (2012)

[6.15] A. Sharma, *Zirconia-supported copper oxide: catalyst for removal of vehicular exhaust gas pollutants*, J. Environ. Eng., **132**, 956-959 (2006)

[6.16] A.S.K. Hashmi, G.J. Hutchings, *Gold catalysis*, Angew. Chem. Int. Ed., **45**, 7896-7936 (2006)

[6.17] A. Corma, H. Garcia, *Supported gold nanoparticles as catalysts for organic reactions*, Chem. Soc. Rev., **37**, 2096-2126 (2008)

[6.18] J. Gong, *Structure and surface chemistry of gold-based model catalysts*, Chem. Rev., **112**, 2987-3054 (2012)

[6.19] F. Cárdenas-Lizana, M. Keane, *The development of gold catalysts for use in hydrogenation reactions*, J. Mater. Sci., **48**, 543-564 (2013)

[6.20] V. Idakiev, T. Tabakova, A. Naydenov, Z.Y. Yuan, B.L. Su, *Gold catalysts supported on mesoporous zirconia for low-temperature water-gas shift reaction*, Appl. Catal. B: Environ., **63**, 178-186 (2006)

[6.21] X. Zhang, H. Wang, B.-Q. Xu, *Remarkable nanosize effect of zirconia in Au/ZrO_2 catalyst for CO oxidation*, J. Phys. Chem. B, **109**, 9678-9683 (2005)

[6.22] Y. Zhang, X. Cui, F. Shi, Y. Deng, *Nano-gold catalysis in fine chemical synthesis*, Chem. Rev., **112**, 2467-2505 (2012)

[6.23] R.A. Koeppel, A. Baiker, C. Schild, A. Wokaun, *Carbon dioxide hydrogenation*

over Au/ZrO_2 catalysts from amorphous precursors: catalytic reaction mechanism, J. Chem. Soc.-Faraday Trans., **87**, 2821-2828 (1991)

[6.24] D.P. He, H. Shi, Y. Wu, B.Q. Xu, *Synthesis of chloroanilines: selective hydrogenation of the nitro in chloronitrobenzenes over zirconia-supported gold catalyst*, Green Chem., **9**, 849-851 (2007)

[6.25] A. Corma, C. González-Arellano, M. Iglesias, F. Sánchez, *Gold complexes as catalysts: chemoselective hydrogenation of nitroarenes*, Appl. Catal. A: Gen., **356**, 99-102 (2009)

[6.26] A. Corma, P. Serna, *Chemoselective hydrogenation of nitro compounds with supported gold catalysts*, Science, **313**, 332-334 (2006)

[6.27] R.J. Rahaim, R.E. Maleczka, *Pd-catalyzed silicon hydride reductions of aromatic and aliphatic nitro groups*, Org. Lett., **7**, 5087-5090 (2005)

[6.28] U. Sharma, P.K. Verma, N. Kumar, V. Kumar, M. Bala, B. Singh, *Phosphane-free green protocol for selective nitro reduction with an iron-based catalyst*, Chem.-Eur. J., **17**, 5903-5907 (2011)

[6.29] U. Sharma, P. Kumar, N. Kumar, V. Kumar, B. Singh, *Highly chemo- and regioselective reduction of aromatic nitro compounds catalyzed by recyclable copper(II) as well as cobalt(II) phthalocyanines*, Adv. Synth. Catal., **352**, 1834-1840 (2010)

[6.30] K. Koprivova, L. Cerveny, *Hydrogenation of nitrobenzonitriles using Raney nickel catalyst*, Res. Chem. Intermediat., **34**, 93-101 (2008)

[6.31] K. Hata, K.-I. Watanabe, *Catalytic hydrogenation of aromatic nitrites*, B. Chem. Soc. Jpn., **32**, 861-867 (1959)

[6.32] L. Pehlivan, E. Metay, S. Laval, W. Dayoub, P. Demonchaux, G. Mignani, M. Lemaire, *Iron-catalyzed selective reduction of nitro compounds to amines*, Tetrahedron Lett., **51**, 1939-1941 (2010)

[6.33] X. Wang, N. Perret, M.A. Keane, *The role of hydrogen partial pressure in the gas phase hydrogenation of p-chloronitrobenzene over alumina supported Au and Pd: a consideration of reaction thermodynamics and kinetics*, Chem. Eng. J., **210**, 103-113 (2012)

[6.34] X. Wang, N. Perret, M.A. Keane, *Gas phase hydrogenation of nitrocyclohexane over supported gold catalysts*, Appl. Catal. A: Gen., **467**, 575-584 (2013)

[6.35] N. Perret, F. Cárdenas-Lizana, M.A. Keane, *Selective hydrogenation of benzaldehyde to benzyl alcohol over Au/Al_2O_3*, Catal. Commun., **16**, 159-164 (2011)

[6.36] J. Jia, K. Haraki, J.N. Kondo, K. Domen, K. Tamaru, *Selective hydrogenation of acetylene over Au/Al_2O_3 catalyst*, J. Phys. Chem. B, **104**, 11153-11156 (2000)

[6.37] H. Moll, H. Musso, H. Schröder, *Hydrogenation of o-nitrobenzonitrile to anthranilamide*, Angew. Chem. Int. Ed., **2**, 212-212 (1963)

[6.38] F. Cárdenas-Lizana, S. Gómez-Quero, M.A. Keane, *Clean production of chloroanilines by selective gas phase hydrogenation over supported Ni catalysts*, Appl. Catal. A: Gen., **334**, 199-206 (2008)

[6.39] N. Perret, X. Wang, L. Delannoy, C. Potvin, C. Louis, M.A. Keane, *Enhanced selective nitroarene hydrogenation over Au supported on β-Mo_2C and β-Mo_2C/Al_2O_3*, J. Catal., **286**, 172-183 (2012)

[6.40] H. Toraya, M. Yoshimura, S. Somiya, *Calibration curve for quantitative analysis of the monoclinic-tetragonal ZrO_2 system by x-ray diffraction*, J. Am. Ceram. Soc., **67**, C-119-C-121 (1984)

[6.41] G. Tavoularis, M.A. Keane, *The gas phase hydrodechlorination of chlorobenzene over nickel/silica*, J. Chem. Technol. Biotechnol., **74**, 60-70 (1999)

[6.42] M.A. Keane, *Gas phase hydrogenation/hydrogenolysis of benzaldehyde and o-tolualdehyde over Ni/SiO_2*, J. Mol. Catal. A: Chem., **118**, 261-269 (1997)

[6.43] G.K. Chuah, S. Jaenicke, S.A. Cheong, K.S. Chan, *The influence of preparation conditions on the surface area of zirconia*, Appl. Catal. A: Gen., **145**, 267-284 (1996)

[6.44] P.D.L. Mercera, J.G. Van Ommen, E.B.M. Doesburg, A.J. Burggraaf, J.R.H. Ross, *Zirconia as a support for catalysts: evolution of the texture and structure on calcination in air*, Appl. Catal., **57**, 127-148 (1990)

[6.45] S.-F. Yin, B.-Q. Xu, *On the preparation of high-surface-area nano-zirconia by reflux-digestion of hydrous zirconia gel in basic solution*, Chem. Phys. Chem., **4**,

277-281 (2003)

[6.46] X. Zhang, H. Shi, B.-Q. Xu, *Comparative study of Au/ZrO_2 catalysts in CO oxidation and 1,3-butadiene hydrogenation*, Catal. Today, **122**, 330-337 (2007)

[6.47] S. Xie, E. Iglesia, A.T. Bell, *Water-assisted tetragonal-to-monoclinic phase transformation of ZrO_2 at low temperatures*, Chem. Mater., **12**, 2442-2447 (2000)

[6.48] C. Su, D. He, J. Li, Z. Chen, Q. Zhu, *Influences of preparation parameters on the structural and catalytic performance of zirconia in isosynthesis*, J. Mol. Catal. A: Chem., **153**, 139-146 (2000)

[6.49] H.X. Zhao, J.G. Chen, Y.H. Sun, *Effect of calcination temperature on the performance of Co/ZrO_2 catalysts for Fischer-Tropsch synthesis*, Prepr. Pap.-Am. Chem. Soc., Div. Fuel Chem. , **48**, 734-735 (2003)

[6.50] Z. Xu, L. Chen, Y. Shao, D. Yin, S. Zheng, *Catalytic hydrogenation of aqueous nitrate over Pd-Cu/ZrO_2 catalysts*, Ind. Eng. Chem. Res., **48**, 8356-8363 (2009)

[6.51] W. Stichert, F. Schuth, *Influence of crystallite size on the properties of zirconia*, Chem. Mater., **10**, 2020-2026 (1998)

[6.52] G.C. Bond, C. Louis, D.T. Thompson, *Catalysis by Gold*, Imperial College Press, London, 2006

[6.53] G.C. Bond, *Chemisorption and reactions of small molecules on small gold particles*, Molecules, **17**, 1716-1743 (2012)

[6.54] S. Li, M. Li, C. Zhang, S. Wang, X. Ma, J. Gong, *Steam reforming of ethanol over Ni/ZrO_2 catalysts: effect of support on product distribution*, Int. J. Hydrogen Energy, **37**, 2940-2949 (2012)

[6.55] S. Ardizzone, C.L. Bianchi, *Electrochemical features of zirconia polymorphs. The interplay between structure and surface OH species*, J. Electroanal. Chem., **465**, 136-141 (1999)

[6.56] S. Ardizzone, M.G. Cattania, P. Lugo, *Interfacial electrostatic behaviour of oxides: correlations with structural and surface parameters of the phase*, Electrochim. Acta, **39**, 1509-1517 (1994)

[6.57] F. Moreau, G.C. Bond, *Gold on titania catalysts, influence of some*

physicochemical parameters on the activity and stability for the oxidation of carbon monoxide, Appl. Catal. A: Gen., **302**, 110-117 (2006)

[6.58] R. Zanella, C. Louis, *Influence of the conditions of thermal treatments and of storage on the size of the gold particles in Au/TiO_2 samples*, Catal. Today, **107-108**, 768-777 (2005)

[6.59] F. Moreau, G.C. Bond, A.O. Taylor, *Gold on titania catalysts for the oxidation of carbon monoxide: control of pH during preparation with various gold contents*, J. Catal., **231**, 105-114 (2005)

[6.60] D.L. Hoang, H. Lieske, *Effect of hydrogen treatments on ZrO_2 and Pt/ZrO_2 catalysts*, Catal. Lett., **27**, 33-42 (1994)

[6.61] F.B. Noronha, E.C. Fendley, R.R. Soares, W.E. Alvarez, D.E. Resasco, *Correlation between catalytic activity and support reducibility in the CO_2 reforming of methane over Pt/$Ce_xZr_{1-x}O_2$ catalysts*, Chem. Eng. J., **82**, 21-31 (2001)

[6.62] X. Zhang, H. Shi, B.-Q. Xu, *Catalysis by gold: isolated surface Au^{3+} ions are active sites for selective hydrogenation of 1,3-butadiene over Au/ZrO_2 catalysts*, Angew. Chem. Int. Ed., **44**, 7132-7135 (2005)

[6.63] X. Wang, N. Perret, J.J. Delgado, G. Blanco, X. Chen, C.M. Olmos, S. Bernal, M.A. Keane, *Reducible support effects in the gas phase hydrogenation of p-chloronitrobenzene over gold*, J. Phys. Chem. C, **117**, 994-1005 (2013)

[6.64] F. Cárdenas-Lizana, S. Gómez-Quero, N. Perret, M.A. Keane, *Gold catalysis at the gas-solid interface: role of the support in determining activity and selectivity in the hydrogenation of m-dinitrobenzene*, Catal. Sci. Tech., **1**, 652-661 (2011)

[6.65] R. Grau-Crespo, N.C. Hernandez, J.F. Sanz, N.H. de Leeuw, *Redox properties of gold-substituted zirconia surfaces*, J. Mater. Chem., **19**, 710-717 (2009)

[6.66] J.A. Lopez-Sanchez, D. Lennon, *The use of titania- and iron oxide-supported gold catalysts for the hydrogenation of propyne*, Appl. Catal. A: Gen., **291**, 230-237 (2005)

[6.67] S.Y. Liu, S.M. Yang, *Complete oxidation of 2-propanol over gold-based catalysts supported on metal oxides*, Appl. Catal. A: Gen., **334**, 92-99 (2008)

[6.68] C. Kartusch, J.A. van Bokhoven, *Hydrogenation over gold catalysts: The interaction of gold with hydrogen*, Gold Bull., **42**, 343-348 (2009)

[6.69] E. Bus, J.T. Miller, J.A. van Bokhoven, *Hydrogen chemisorption on Al_2O_3-supported gold catalysts*, J. Phys. Chem. B, **109**, 14581-14587 (2005)

[6.70] M. Boronat, F. Illas, A. Corma, *Active sites for H_2 adsorption and activation in Au/TiO_2 and the role of the support*, J. Phys. Chem. A, **113**, 3750-3757 (2009)

[6.71] A. Alshammari, A. Köckritz, V.N. Kalevaru, A. Bagabas, A. Martin, *Direct oxidation of cyclohexane to adipic acid using nano-gold catalysts*, Appl. Petrochem. Res., **2**, 61-67 (2012)

[6.72] R. Radnik, C. Mohr, P. Claus, *On the origin of binding energy shifts of core levels of supported gold nanoparticles and dependence of pretreatment and material synthesis*, Phys. Chem. Chem. Phys., **5**, 172-177 (2003)

[6.73] S. Arrii, F. Morfin, A.J. Renouprez, J.L. Rousset, *Oxidation of CO on gold supported catalysts prepared by laser vaporization: direct evidence of support contribution*, J. Am. Chem. Soc., **126**, 1199-1205 (2004)

[6.74] Q. Deng, X.-M. Li, Z.-S. Peng, Y.-F. Long, L.-M. Xiang, T.-J. Cai, *Catalytic performance and kinetics of Au/γ-Al_2O_3 catalysts for low-temperature combustion of light alcohols*, Trans. Nonferr. Metal Soc., **20**, 437-442 (2010)

[6.75] N. Kruse, S. Chenakin, *XPS characterization of Au/TiO_2 catalysts: Binding energy assessment and irradiation effects*, Appl. Catal. A: Gen., **391**, 367-376 (2011)

[6.76] B. Ealet, E. Gillet, *Metal-alumina interface: influence of the metal electronegativity and of the substrates stoichiometry*, Surf. Sci., **367**, 221-230 (1996)

[6.77] K.-i. Shimizu, Y. Miyamoto, T. Kawasaki, T. Tanji, Y. Tai, A. Satsuma, *Chemoselective hydrogenation of nitroaromatics by supported gold catalysts: mechanistic reasons of size- and support-dependent activity and selectivity*, J. Phys. Chem. C, **113**, 17803-17810 (2009)

[6.78] K.-i. Shimizu, T. Yamamoto, Y. Tai, A. Satsuma, *Selective hydrogenation of nitrocyclohexane to cyclohexanone oxime by alumina-supported gold cluster*

catalysts, J. Mol. Catal. A: Chem., **345**, 54-59 (2011)

[6.79] K.-i. Shimizu, Y. Miyamoto, A. Satsuma, *Size- and support-dependent silver cluster catalysis for chemoselective hydrogenation of nitroaromatics*, J. Catal., **270**, 86-94 (2010)

[6.80] W.C. Conner, J.L. Falconer, *Spillover in heterogeneous catalysis*, Chem. Rev., **95**, 759-788 (1995)

[6.81] F. Cardenas-Lizana, S. Gomez-Quero, N. Perret, M.A. Keane, *Support effects in the selective gas phase hydrogenation of p-chloronitrobenzene over gold*, Gold Bull., **42**, 124-132 (2009)

CHAPTER 7

Selective Gas Phase Hydrogenation of Nitroarenes over Mo_2C Supported Au-Pd

In this chapter, synthesis of Mo_2C supported Au and Au-Pd (nominal Au/Pd = 10 and 30) from colloidal nanoparticles stabilised by polyvinyl alcohol is reported. Equivalent Au/Al_2O_3 and $Au\text{-}Pd/Al_2O_3$ are prepared as benchmark. Those catalysts are examined in gas phase hydrogenation of nitroarenes including nitrobenzene, *p*-chloronitrobenzene and *p*-nitrobenzonitrile. This chapter is in preparation for publication (see publication No. 13). Co-author N.P. prepared the catalysts; L.D. conducted the TEM and XPS measurements and co-wrote the chapter. C.L. and M.A.K. directed the project and co-wrote the chapter.

7.1 Introduction

The use of bimetallic catalysts is experiencing increased research interest [1] due to enhanced activity [2,3], selectivity [4] and resistance to poisoning [5] when compared with corresponding mono-metallic systems. This has been exploited in commercial applications, notably Pd-Zn in hydrogen production [6], Pd-Au in vinyl acetate synthesis [7], Cu-Zn in methanol production [8] and Fe-Cr in the water gas shift reaction [9]. This study focuses on Au-Pd formulations, which to date have been used in the synthesis of hydrogen peroxide from H_2 and O_2 [10,11], NO_2 decomposition [12], hydrodesulphurisation (of thiophene and dibenzothiophene [13]), hydrodechlorination (of trichloroethene [14]), oxidation (of glycerol [15], CO [16,17], benzyl alcohol, cinnamyl alcohol, 2-octen-1-ol and *n*-octanol [18]) and hydrogenation (of 1,3-butadiene [19], benzaldehyde [5], naphthalene and toluene [20,21], acetylene [22], allyl alcohol [2] and cinnamaldehyde [23]). Improved performance relative to monometallic Pd and Au catalysts has been attributed to ensemble, ligand or geometric effects [24-26]. Prior studies have established chemoselectivity in targeted $–NO_2$ reduction in functionalised nitrocompounds [27-29] over supported Au. Reaction exclusivity is important in minimising waste and can close the sustainability gap associated with non-selective processes using standard (Pd [28], Ru [30] or Ni [31]) transition metal catalysts. However, the hydrogenation rates delivered by supported Au fall below that achieved

with non-selective metal catalysts [32]. It is now crucial to increase selective hydrogenation rate to address the key commercial consideration of productivity, *i.e.* combination of activity and selectivity. Gold activation of H_2 is the limiting step due to the high energy barrier for dissociative adsorption [33]. We have explored the use of Mo_2C as a support that can chemisorb H_2 and increase surface concentration, leading to higher hydrogenation rates [34]. We demonstrated that Au/Mo_2C delivered higher selective hydrogenation rates relative to Au/Al_2O_3 but further improvements are required in Au/Mo_2C synthesis, particularly with respect to Au particle size as H_2 activation is dependent on Au coordination and dispersion [35,36]. Preliminary data [3] established that the addition of Pd to Au on Al_2O_3 (prepared by deposition/precipitation) increased hydrogenation activity but lower selectivities were recorded at higher Pd loading. We have now examined the viability of Mo_2C supported Au-Pd to elevate rate while retaining selectivity in the hydrogenation of nitroarenes.

The challenge in supported bimetallic catalyst synthesis is to exert control over surface composition and size/dispersion [37]. To date, supported Au-Pd catalysts have principally been prepared by impregnation (incipient [20,38,39] and wet [3,5,19,40]) and (co)-deposition [3,10,11,19,41] methods. Synthesis procedure can influence ultimate metal loading, morphology and structure [11,22] where, despite the miscibility of Au and Pd, surface segregation and the formation of isolated single metal particles can occur [3]. Use of Au-Pd catalysts have largely focused on Au addition to modify Pd catalytic properties, where Au/Pd ratio < 1 [22,42,43]. This study takes the opposite approach where Pd inclusion is directed at promoting selective hydrogenation rate. A range of oxides, including Fe_2O_3 [41], TiO_2 [44], ZrO_2 [11] and MgO [14] have been used as Au-Pd support with the predominance of Al_2O_3 [3,14,19-21,41] and SiO_2 [10,14,21,22,39,45-47] as carriers. In this study, we report the first preparation of Au-Pd/Mo_2C (Au/Pd ratio $\geq$ 10) using colloidal polyvinyl alcohol (PVA), which provides a protective layer around the metal nanoparticles that prevents agglomeration in solution and generates smaller supported metal particles [48]. Use of "protecting" agents (*e.g.* polyvinyl pyrrolidone (PVP) [13] and PVA [15,18]) to minimise nanoparticles aggregation has been applied in the preparation of carbon supported Au [49], Pd [50] and Au-Pd [15,18]. The catalytic action of Au-Pd/Mo_2C is examined here in the hydrogenation of nitrobenzene (NB), *p*-chloronitrobenzene (*p*-CNB) and *p*-nitrobenzonitrile (*p*-NBN), where Au-Pd/Al_2O_3 served as benchmark.

7.2 Experimental

7.2.1 Chemicals

Gold (III) chloride hydrate ($HAuCl_4.xH_2O$, 99.999%), palladium tetraamine dinitrate ($Pd(NH_3)_4(NO_3)_2$, 99.99%) and polyvinyl alcohol (PVA, 87-89%) were obtained from Aldrich, molybdic acid (H_2MoO_4, 99%) from Merck and $NaBH_4$ (>99%) from Fluka. All the gases used were of high purity (99.9%) and supplied by BOC or Air Liquide. The nitro-reactants (nitrobenzene (NB), *p*-chloronitrobenzene (*p*-CNB) and *p*-nitrobenzonitrile (*p*-NBN) supplied by Aldrich (≥ 98%)) and solvent (1-butanol, Riedel-de Haen, 99.8%) were used as received without further purification.

7.2.2 Catalyst Preparation

β-Mo_2C was synthesised *via* temperature programmed carburisation of H_2MoO_4 (2 g) in 20 % v/v CH_4 in H_2 (340 cm^3 min^{-1}). The temperature was ramped at 1 K min^{-1} to 973 K, maintained for 1 h and cooled to ambient temperature under H_2 with sample passivation in 1 % v/v O_2/He (30 cm^3 min^{-1}) for 1 h. The passivation step was necessary to circumvent autothermal oxidation upon contact with air [51]. Gold was then incorporated using an Au sol that was deposited on the Mo_2C (or Al_2O_3) support with a nominal loading of 1 % w/w. Aqueous solutions of $HAuCl_4$ (6 cm^3, 2.5×10^{-2} M) and PVA (1.5 cm^3, 2.3×10^{-6} M; Au/PVA = 50) were added to 200 cm^3 distilled water with vigorous agitation for 3 min, a freshly prepared solution of $NaBH_4$ (4.5 cm^3, 0.1 M) then added ($NaBH_4$/Au = 3) with a resultant colour change from light yellow to red, indicating reduction of Au^{3+} to Au^0. The sol was acidified to pH = 2 with H_2SO_4 (0.1 M), 3 g support added to the mixture, which was maintained under vigorous stirring at ambient temperature for 2 h and the water removed on a rotary evaporator. Bimetallic synthesis followed an equivalent protocol where 1 % w/w Au/Mo_2C (or Au/Al_2O_3) was suspended in 200 cm^3 distilled water to which a known amount of PVA solution (2.3×10^{-6} M; Pd/PVA = 80) was added under vigorous stirring with subsequent addition of $Pd(NH_3)_4(NO_3)_2$ (4.7×10^{-3} M; nominal Au/Pd = 10 or 30). The solution was sparged with H_2 (50 cm^3 min^{-1}) for 2 h, the mixture stirred for a further 16 h and water removed by rotary evaporation. The samples as prepared were heated (2 K min^{-1}) in 600 cm^3 min^{-1} N_2 to 773 K for 1 h, cooled to ambient temperature and subjected to thermal reduction in 100 cm^3 min^{-1} H_2 to 773 K (at 2 K min^{-1}). Upon cooling, the samples were

passivated as above for off-line analysis. The bimetallic catalysts are labelled as Au-Pd/Mo_2C(or Al_2O_3)-X, where X represents the nominal Au/Pd molar ratio (= 10 or 30).

7.2.3 Catalyst Characterisation

The Au, Mo, Cl and Al contents of the samples as prepared were measured by inductively coupled plasma (ICP) atom emission spectroscopy (CNRS Centre of Chemical Analysis, Vernaison). Carbon content was determined using an Exeter CE-440 Elemental Analyser after sample combustion at *ca.* 1873 K. Temperature programmed reduction (TPR), BET surface area and H_2 chemisorption were measured using the commercial CHEM-BET 3000 (Quantachrome) unit. The passivated samples were loaded into a U-shaped Quartz cell (10 cm × 3.76 mm i.d.) and heated in 17 cm^3 min^{-1} (Brooks mass flow controlled) 5% v/v H_2/N_2 at 2 K min^{-1} to 523±1 K, which was held for 1 h. The effluent gas passed through a liquid N_2 trap and H_2 consumption was monitored by TCD with data acquisition/manipulation using the TPR Win^{TM} software. The samples were swept with 65 cm^3 min^{-1} N_2 for 1.5 h, cooled to ambient temperature and subjected to H_2 chemisorption using a pulse (10 µl) titration procedure. Hydrogen pulse introduction was repeated until the signal area was constant, indicating surface saturation. BET surface area was determined (post TPR) in 30% v/v N_2/He using pure N_2 (99.9%) as internal standard. At least three cycles of N_2 adsorption-desorption in the flow mode were employed to determine total surface area using the standard single point method. BET area and H_2 chemisorption measurements were reproducible to within ±3% and the values quoted represent the mean.

Powder X-ray diffractograms (XRD) were recorded on a Bruker/Siemens D500 incident X-ray diffractometer using Cu Kα radiation. The samples were scanned at 0.02º $step^{-1}$ over the range $20º \leq 2\theta \leq 80º$ and the diffractograms identified using JCPDS-ICDD reference standards, *i.e.* Au (Card No. 04-0784), Pd (05-0681), β-Mo_2C (11-0680) and δ-Al_2O_3 (16-394). Thermogravimetric analysis (TGA) and differential scanning calorimetry (DSC) measurements were conducted using a SDT Q600 simultaneous TGA/DSC analyser (TA Instruments) that measured temporal mass and heat flow as a function of temperature. Samples were swept with air/N_2 (100 cm^3 min^{-1}) and ramped (10 K min^{-1}) from ambient temperature to 373 K with an isothermal hold (for 1 h) and subsequent heating to 773 K. Transmission electron microscopy (TEM) was performed using a JEOL 2010 electron microscope operating at 200 kV. Samples for analysis were crushed and homogenously dispersed in ethanol by ultrasonication and

a drop of the suspension was deposited on a carbon-coated copper grid and evaporated. Up to 200 individual Au particles were counted for each catalyst and the mean metal particle sizes are given as the surface area-weighted average (d) according to [52]

$$d = \frac{\sum_i n_i d_i^3}{\sum_i n_i d_i^2} \tag{7.1}$$

where n_i is the number of particles of diameter d_i. XPS spectra were collected on a SPECS (Phoibos MCD 150) x-ray photoelectron spectrometer using an Al Kα (hv = 1486.6 eV) x-ray source. The binding energies (BE) were calibrated with respect to the C-C/C-H components of the C 1*s* peak (BE = 284.7 eV). Spectra processing applied the Casa XPS software package.

7.2.4 Catalytic Procedure

Reactions were carried out under *in situ*, immediately after activation (at 2 K min^{-1} to 523 K in 60 cm^3 min^{-1} H_2) in a continuous flow fixed bed vertical glass reactor (i.d. = 15 mm, l = 600 mm) at 493 K and 1 atm. The catalytic reactor and operating conditions to ensure negligible heat/mass transport limitations have been fully described elsewhere [53,54]. A layer of borosilicate glass beads served as a preheating zone, ensuring that the organic reactants were vaporised and reached reaction temperature before contacting the catalyst. Isothermal conditions (± 1 K) were ensured by diluting the catalyst bed with ground glass (75 μm); the ground glass was mixed thoroughly with catalyst before insertion into the reactor. Reaction temperature was continuously monitored by a thermocouple inserted in a thermowell within the catalyst bed. The reactant (NB, *p*-CNB or *p*-NBN) was delivered *via* a glass/teflon air-tight syringe and teflon line using a microprocessor controlled infusion pump (Model 100 kd Scientific) at a fixed calibrated flow rate. A co-current flow of organic and H_2 was maintained at a *GHSV* = 2×10^4 h^{-1} with an inlet organic flow (F) in the range 0.06–0.38 mmol h^{-1}; the molar Au (n_{Au}) to F content spanned the range 2×10^{-3} – 6×10^{-2} h. In a series of blank tests, passage of each reactant in a stream of H_2 through the empty reactor did not result in any detectable conversion. The reactor effluent was frozen in a liquid nitrogen trap for subsequent analysis, which was made using a Perkin-Elmer Auto System XL gas chromatograph equipped with a programmed split/splitless injector and flame ionization detector, employing a DB-1 50 m × 0.20 mm i.d. 0.33 μm film thickness capillary column (J&W Scientific). Repeated reactions with different samples from the same batch of

catalyst delivered raw data that were reproducible to within ±6 %. Taking *p*-NBN as an example, fractional hydrogenation (x_i) was obtained from

$$x_i = \frac{[p-NBN]_{in} - [p-NBN]_{out}}{[p-NBN]_{in}} \tag{7.2}$$

where selectivity with respect to *p*-aminobenzonitrile (*p*-ABN) is given by

$$S_i(\%) = \frac{[p-ABN]_{out}}{[p-NBN]_{in} - [p-NBN]_{out}} \times 100 \tag{7.3}$$

7.3 Results and Discussion

7.3.1 Catalyst Characterisation

The Al_2O_3 and Mo_2C supported Au and Au-Pd samples exhibited Au loading close to the nominal 1 % w/w with Au/Pd ratios approaching the target values (30 and 10) for the bimetallic catalysts, as demonstrated by the entries in **Table 7.1**. Moreover, Mo/C (for the carbide systems) was very close to 2, confirming synthesis of an Mo_2C phase with no significant free carbon, which can occlude Mo active sites and lower activity, as reported elsewhere [55]. In order to remove residual PVA, thermal treatment of the samples (as prepared) was necessary. It has been shown that calcination in air at 773 K with subsequent reduction in H_2 was effective in PVA removal [56]. While calcination can be applied to the alumina based samples, oxidative treatment is not applicable in the case of Mo_2C as the support can undergo deep oxidation with irreversible structural modifications at high temperature treatment in air. We examined the feasibility of thermal treatment in N_2, taking Au-Pd/Al_2O_3-10 and Au-Pd/Mo_2C-10 as representative samples. TGA-DSC analysis of Au-Pd/Al_2O_3-10 generated the profiles shown in **Figure 7.1** where treatment in air (A) and N_2 (B) resulted in equivalent profiles. The endothermic response at 328 K (from DSC) can be attributed to loss of physisorbed water while the exothermic mass loss at higher temperature (T > 400 K) can be attributed to the removal of PVA. The overall change in mass converged (at *ca.* 6 % w/w) in both cases, suggesting equivalence of the treatment in air and N_2. Thermal treatment of Au-Pd/Mo_2C-10 in N_2 showed comparable behaviour (**Figure 7.1(C)**) with a low temperature endothermic release and greater mass loss at higher temperature. We accordingly applied the same thermal treatment (to 773 K) in N_2 for both alumina and carbide samples.

The temperature programmed reduction (TPR) profiles for Au-Pd/Al_2O_3-10 and Au-Pd/Mo_2C-10 are presented in **Figure 7.2**. As the Au component was reduced by

Table 7.1: Au content (% w/w), Au/Pd and Mo/C ratios, BET surface area, temperature programmed reduction (TPR) T_{max}, metal particle size range and surface area weighted mean diameter (d), H_2 chemisorption and XPS binding energies (BE) for Au $4f_{7/2}$, Pd $3d_{3/2}$ and Mo $3d_{5/2}$.

	Au (% w/w)	Molar ratio		BET (m^2 g^{-1})	TPR T_{max} (K)	Particle size (nm)		H_2 chemisorption (μmol g^{-1})	BE XPS (eV)	
		Au/Pd	Mo/C			range	mean (d)		Au $4f_{7/2}$	Mo $3d_{5/2}$
Au/Al_2O_3	0.94	-	-	104	-	1-8	5.4	0.4	83.0	-
$Au\text{-}Pd/Al_2O_3$-30	0.97	27	-	100	-	1-8	4.6	0.7	-	-
$Au\text{-}Pd/Al_2O_3$-10	0.95	9	-	101	-	1-7	4.5	1.2	83.0	-
Mo_2C	-	-	1.95	57	500	1-7	-	0.4	-	228.4
Au/Mo_2C	0.81	-	1.95	42	493	1-7	4.3	1.0	84.2	228.4
$Au\text{-}Pd/Mo_2C$-30	0.87	32	2.00	38	476	1-7	4.2	1.5	-	-
$Au\text{-}Pd/Mo_2C$-10	0.84	14	1.96	34	437	1-7	4.3	2.1	84.2 (340.8[a])	228.4

[a]Pd $3d_{3/2}$

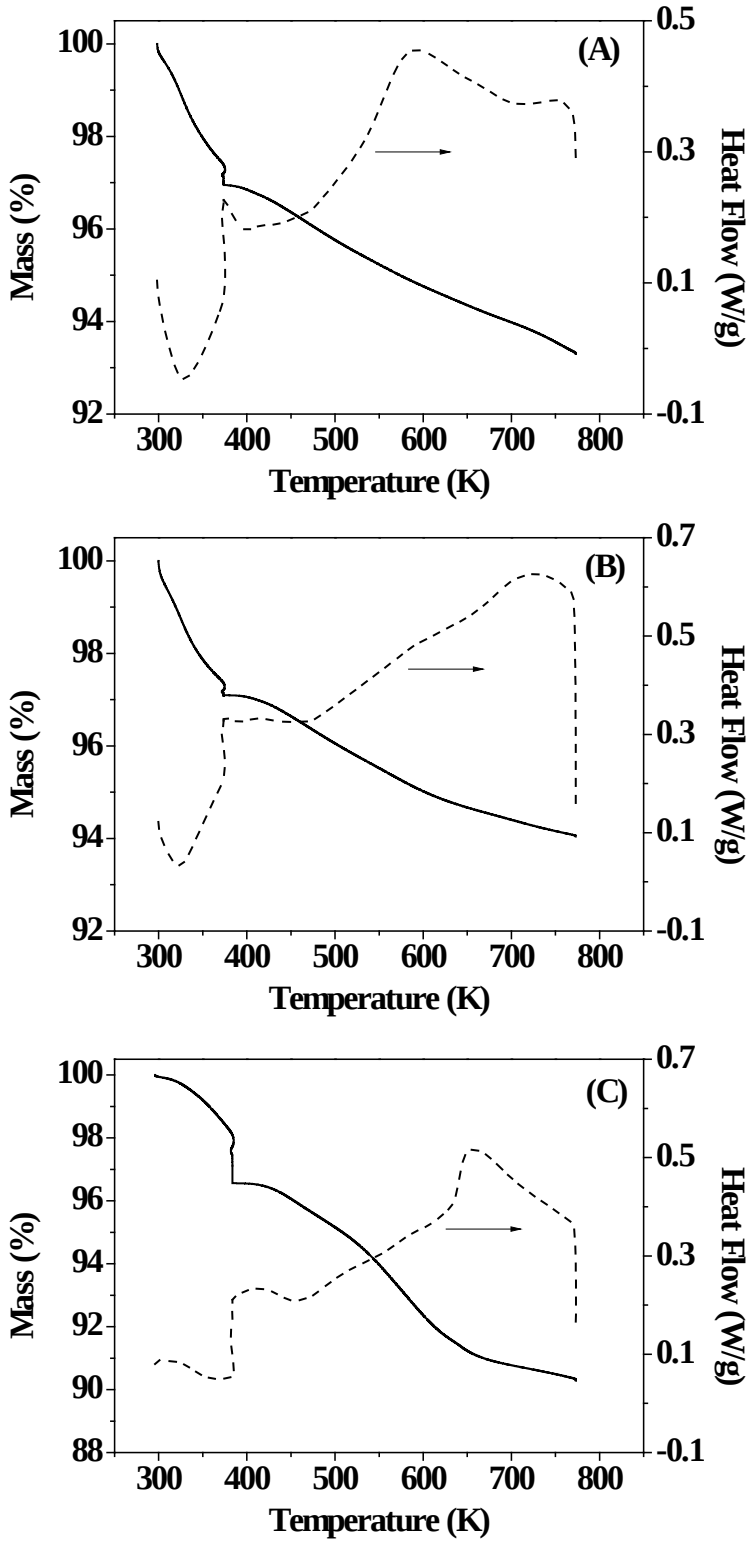

Figure 7.1: TGA (solid line) and DSC (dashed line) profiles generated in the pre-treatment of (A) Au-Pd/Al_2O_3-10 in air, (B) Au-Pd/Al_2O_3-10 in N_2 and (C) Au-Pd/Mo_2C-10 in N_2; 100 cm^3 min^{-1} gas flow at 10 K min^{-1} to 373 K (held for 1 h) and then to 773 K.

$NaBH_4$ during preparation, there was no detectable TPR response for Au-Pd/Al_2O_3-10 (**Figure 7.2(I)**). The TPR signal recorded for Au-Pd/Mo_2C-10 (II) can be ascribed to the removal of the passivation layer from the carbide support. A single reduction peak

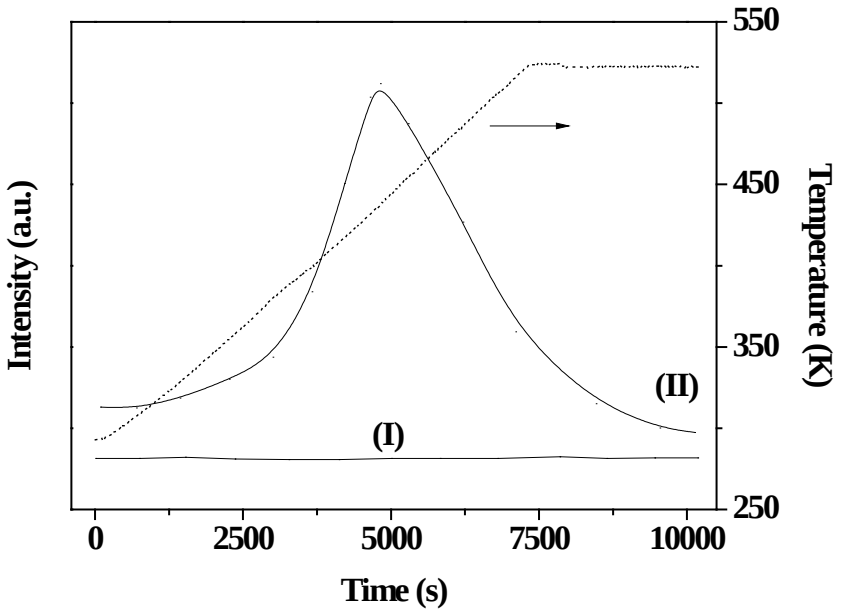

Figure 7.2: Temperature programmed reduction (TPR) profiles for Au-Pd/Al_2O_3-10 (I) and Au-Pd/Mo_2C-10 (II).

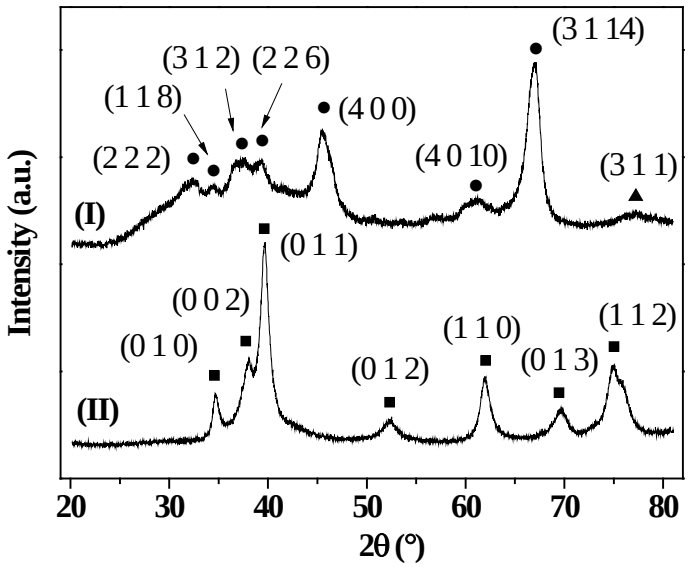

Figure 7.3: XRD patterns for Au-Pd/Al_2O_3-10 (I) and Au-Pd/Mo_2C-10 (II). XRD peak assignments are based on JCPDS-ICDD reference standards: δ-Al_2O_3 (●, 16-394); β-Mo_2C (■, 11-0680); Au (▲, 04-0784).

during TPR of Mo_2C (at 493 K) and Au/Mo_2C (at 430 K) has been recorded elsewhere [34]. The temperature corresponding to maximum H_2 consumption (T_{max}, **Table 7.1**) indicates that the inclusion of Au promoted the removal of the passivation layer lowering the requisite temperature, which was further facilitated with the addition of Pd. The BET surface area of the carbide systems showed a decrease with metal loading, suggesting partial pore filling by the metal component that was not evident for the

alumina samples (BET area = 100-104 m^2 g^{-1}). The XRD profile of the Al_2O_3 supported catalysts (taking Au-Pd/Al_2O_3-10 as representative (**Figure 7.3(I)**) presented peaks that are characteristic of the δ-Al_2O_3 support [57]. The signal at 2θ = 77.5° can be assigned to Au (3 1 1) but the intensity is too weak to allow any meaningful calculation of Au size from standard line broadening. The XRD pattern for Au-Pd/Mo_2C-10 (**Figure 7.3(II)**) is consistent with hexagonal β-Mo_2C, showing characteristic (0 1 0), (0 0 2), (0 1 1), (0 1 2), (1 1 0), (0 1 3) and (1 1 2) carbide peaks. There was no detectable signal due to bulk oxide (MoO_3 or MoO_2), indicating that the oxide precursor had been fully converted to the carbide and that the passivation step resulted in superficial (rather than bulk) oxidation. Gold detection is hampered by overlap with XRD peaks due to the carbide but the absence of an Au (2 0 0) peak at 44°5 suggests the occurrence of nano-sized Au particles There was no detectable diffraction peaks due to Pd (notably at 40.1° (1 1 1)) in the bimetallic samples but this can be attributed to the low associated loading, which rendered any response below instrument detection limits.

Gold particle size is critical in hydrogenation application [33,58]. We have shown that Au particles < 5 nm are intrinsically more active in the gas phase hydrogenation of *p*-CNB and *m*-dinitrobenzene (*m*-DNB) [32]. Transmission electron microscopy was employed to determined Au size distribution and representative TEM images (of Au-Pd/Al_2O_3-10 (A) and Au-Pd/Mo_2C-10 (B)) are presented in **Figure 7.4(I)**, where well dispersed pseudo-spherical particles in the 1–8 nm size range (**Figure 7.4(II)**) are in evidence. A similar size distribution applies to all the catalysts prepared in this study where the values recorded in **Table 7.1** for the bimetallic catalysts are composites and apply to both Au and Pd. An essentially equivalent mean size (4-5 nm) was obtained for both Al_2O_3 and Mo_2C systems. This is particularly significant in the latter case as previous Au/Mo_2C synthesis by standard deposition-precipitation (with urea) generated an appreciably wider (4-20 nm) distribution with a mean of 13.4 nm [34]. We provide here the first report of Mo_2C supported Au preparation using PVA as a stabilising agent, which has generated homogenously dispersed Au nanoparticles in monometallic and (Au-Pd) bimetallic catalyst preparation. Hydrogen dissociation on supported Au is accompanied by a higher activation energy barrier than standard catalytic transition metals (Pd, Pt and Ni) [33]. Adsorption is dependent on Au coordination where dissociation is facilitated at edge and corner sites and favoured by higher Au dispersion (particles < 10 nm) with a greater preponderance of low coordination sites [35,36]. Ambient temperature H_2 chemisorption on Au/Al_2O_3 was low (0.4 μmol g^{-1}, see **Table 7.1**) and is in agreement with previous reports [28,59].

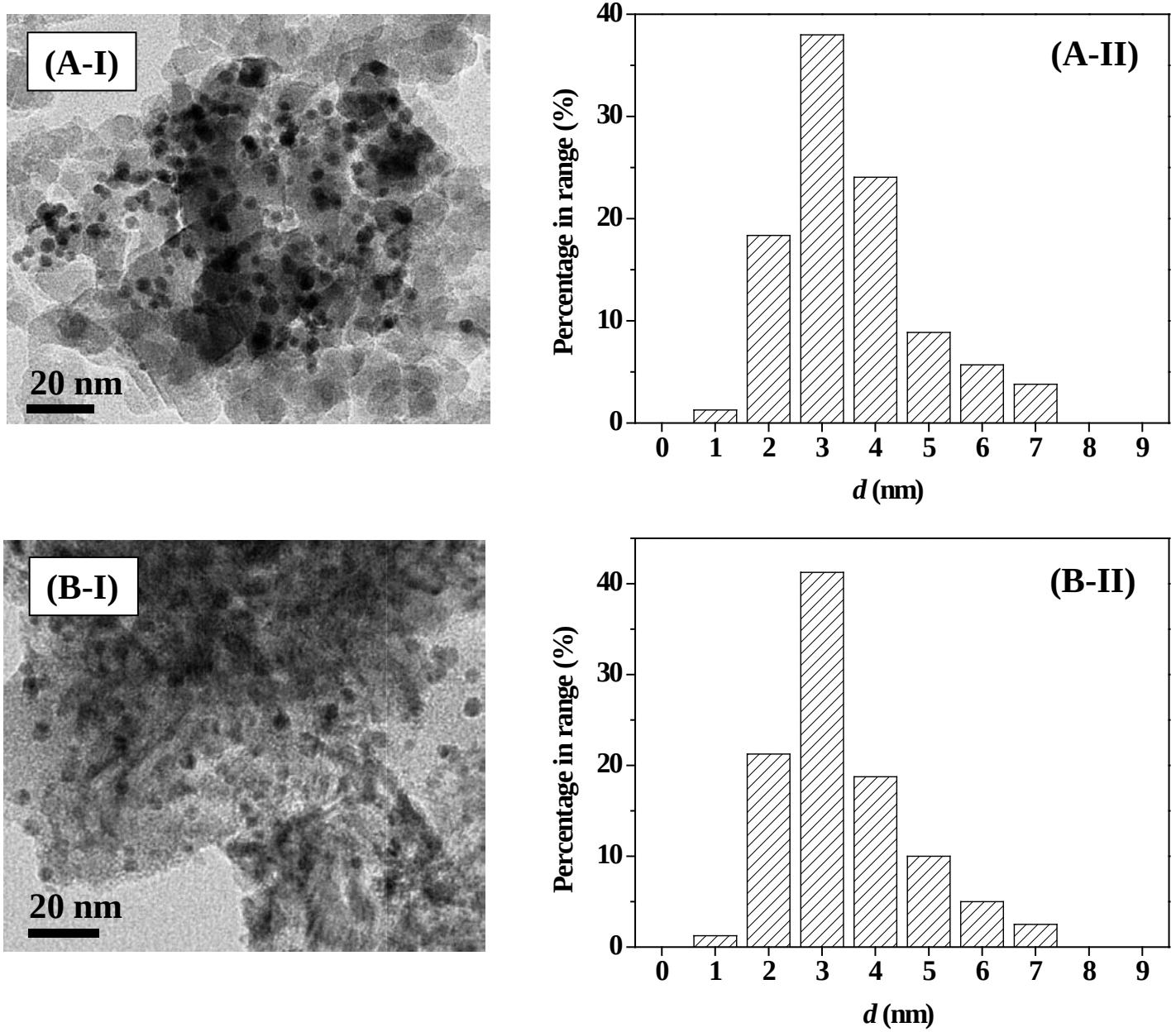

Figure 7.4: Representative TEM images (I) with associated particle size distribution (II) for Au-Pd/Al_2O_3-10 (A) and Au-Pd/Mo_2C-10 (B).

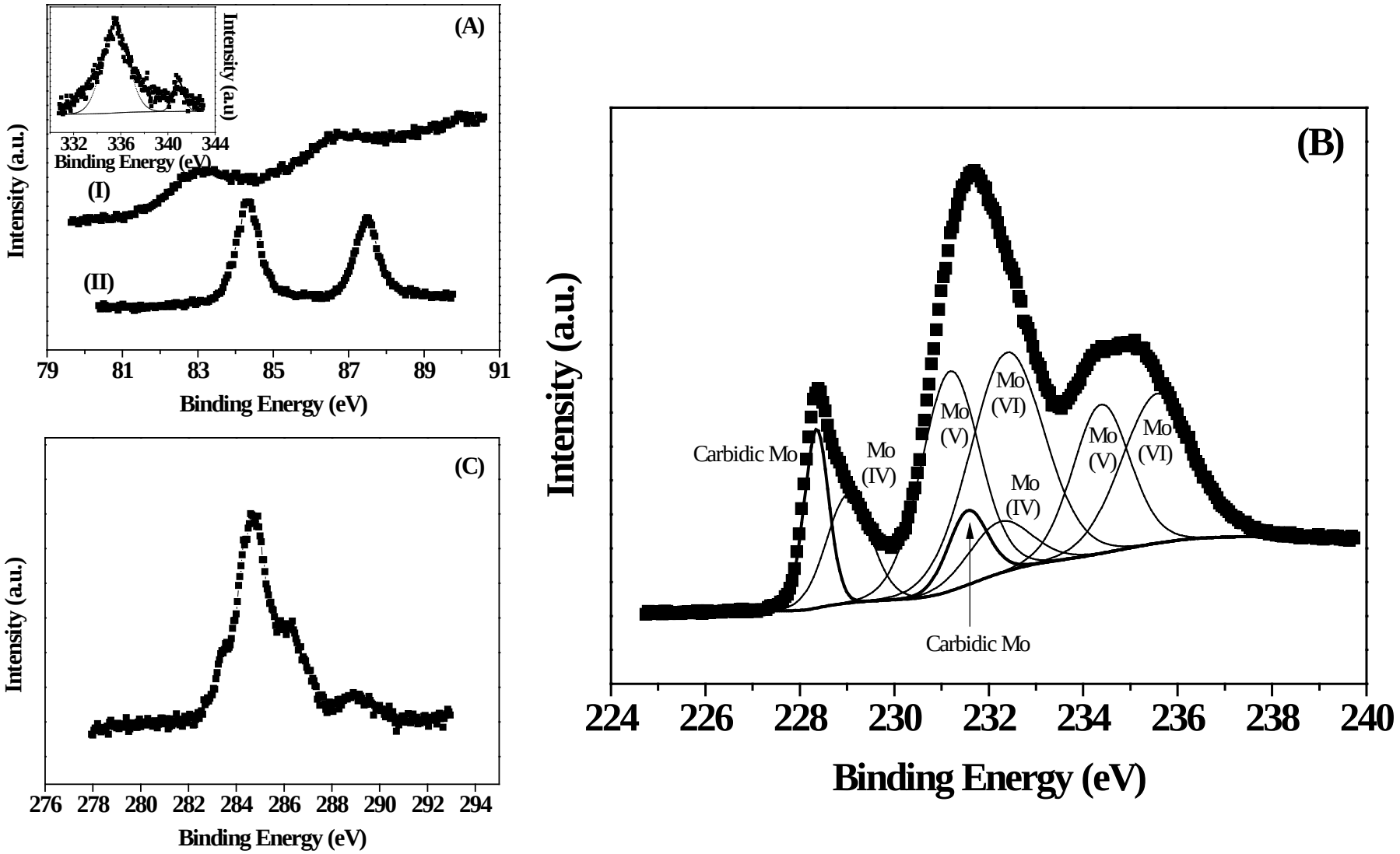

Figure 7.5: XPS spectra (A) over the Au 4*f* region for Au-Pd/Al_2O_3-10 (I) and Au-Pd/Mo_2C-10 (II); inset: XPS spectrum over the Pd 3*d* region for Au-Pd/Mo_2C-10. (B) XPS spectrum for Au-Pd/Mo_2C-10 over the Mo 3*d* region where lines represent peaks after deconvolution; carbidic Mo (solid line), Mo (IV) (dashed line), Mo (V) (dotted line) and Mo (VI) (dashed-dotted line). (C) XPS spectrum over C 1*s* region for Au-Pd/Mo_2C-10.

Inclusion of Pd resulted in a significant increase in H_2 uptake that was enhanced at lower Au/Pd, as was also observed for catalysts prepared by deposition/precipitation [34]. The greater chemisorption capacity exhibited by the carbide samples cannot be attributed to metal particle size, which essentially coincided for all the samples. The observed response must be due to additional chemisorption on Mo_2C where uptake again showed an increase with increasing Pd content.

The electronic structure of the supported metal can impact on hydrogenation performance [27,28,60,61], where $–NO_2$ adsorption/activation is favoured on electron-deficient sites [28,62]. Electronic character was probed by XPS analysis and the resultant spectra are presented in **Figure 7.5**. The Au 4*f* binding energy (BE) showed a dependence on the support but was unaffected by Pd inclusion (**Table 7.1**). The Au $4f_{7/2}$ signal for the Al_2O_3 supported samples exhibited a BE at 83.0 eV that is appreciably lower than the value (84.2 eV) recorded for the carbide systems (**Figure 7.5(A)**). Given that the BE for metallic Au is 84.0 eV [63,64], the XPS response suggests electron transfer from Al_2O_3 to Au to generate an electron-rich ($Au^{\delta-}$) phase. Indeed, it has been reported that electronegative Au can act as an electron acceptor with respect to Al, resulting in electron transfer [65]. In contrast, the Au $4f_{7/2}$ BE associated with the carbide systems is close to the metallic reference. Overlap of the Pd $3d_{5/2}$ signal with Au $4d_{5/2}$ as noted by Yang *et al.* [66] prevented an explicit assignment but peak deconvolution revealed a signal at 340.8 eV for Au-Pd/Mo_2C-10 (**Table 7.1** and **Figure 7.5(A)** inset), which is close to the characteristic signal for metallic Pd (at 340.5±0.1 eV [28,62]. Wang *et al.* have observed a similar response (Pd $3d_{3/2}$ at 340.9 eV) in the case of Pd-Mo_2C/graphitic carbon [67]. The XPS spectrum over the Mo 3*d* region is given in **Figure 7.5(B)** where peaks at 228.4 and 234.9 eV are consistent with Mo_2C [67,68]. In addition to the carbidic Mo contribution, signals at higher BE can be attributed to oxidised states of Mo that arise from the passivation treatment, *i.e.* Mo(IV) (229.0 eV) [69], Mo(V) (231.2 eV) [70] and Mo(VI) (232.4 eV) [71]. The C 1*s* profile is shown in **Figure 7.5(C)** where the signal at 283.4 eV can be attributed to carbidic carbon [72], the peak at 284.6 eV is due to graphitic carbon [67] and the higher BE response (at 286.3 and 288.6 eV) can be ascribed to contributions from C-O [69] and C=O [73], respectively.

7.3.2 Catalytic Response

This is the first reported application of Mo_2C supported bimetallic (Au-Pd)

catalysts in (gas phase) hydrogenation where we examine the conversion of a series of nitroarenes (NB, *p*-CNB, *p*-NBN), carrying Al_2O_3 supported Au and Au-Pd through as benchmark. The target amine products are commercially important in the production of a diversity of agrochemicals, pharmaceuticals, dyestuffs, urethanes and fine chemicals [74,75]. The hydrogenation of nitrobenzene (NB) to aniline (AN) is first examined to establish differences in hydrogenation activity. Fractional NB conversion (x_i) is illustrated as a function of time on-stream over Au/Mo_2C (as a representative catalyst) in **Figure 7.6(A)**. The temporal variation in activity can be expressed in terms of the empirical relationship [29,76]

$$\frac{(x - x_0)}{(x_{3h} - x_0)} = \frac{\Delta t}{(\beta + \Delta t)} \tag{7.4}$$

where x_{3h} represents conversion after 3 h on-stream and β is a time scale fitting parameter. Fit convergence yielded x_0 (initial conversion), which was used to obtain the reaction rate (normalised with respect to mol Au), given in **Figure 7.6(B)**. Reaction over all the catalysts employed in this work resulted in exclusive AN production where Au/Mo_2C outperformed Au/Al_2O_3, delivering a greater than three-fold higher rate. This can be ascribed, at least in part, to the greater available surface hydrogen determined in the pulse chemisorption measurements (**Table 7.1**). The enhanced activity extends to the supported bimetallics where the inclusion of Pd increased rate for both systems with the highest values recorded for Au/Pd = 10. In previous work [77-79], we established Au particle size effects in $–NO_2$ group hydrogenation with an increase in intrinsic activity with decreasing size (from 10 to 3 nm). However, this should not be a consideration here, given the equivalent size distribution and mean size (4-5 nm, **Table 7.1**) in all the catalysts. Supported Au electronic character is critical where repulsive effects must prevail in the interaction of the electron rich $–NO_2$ group with $Au^{\delta-}$ sites on Al_2O_3, which serve to limit activation leading to lower hydrogenation rates relative to the carbide catalysts.

Clean synthesis of target high value product(s) is the imperative for 21st century chemical processes where chemoselective catalysis can ensure atom efficiency, avoiding by-product formation and waste treatment [32]. Selectivity is problematic in the hydrogenation of *p*-CNB [80,81] where a range of intermediates and by-products, including nitrobenzene (NB) and AN have been reported for reaction over Pd and Ni catalysts in both liquid and gas phase operations [28,62,82,83]. A simplified reaction pathway is presented in **Figure 7.7(A)**, where the target *p*-CAN formed *via* $–NO_2$ reduction (step I) can undergo hydrodechlorination to AN (step II) or alternatively NB

is first generated by hydrodechlorination (step III) with subsequent hydrogenation to AN (step IV). In published studies, reaction over Pd/Al_2O_3 promoted production of NB and AN [28] whereas Pd/C [62] and $Au/Ce_xZr_{1-x}O_2$ [29] generated *p*-CAN and AN. This was explained on the basis of metal/support interactions that governed metal particle size and electronic structure. Fractional *p*-CNB conversion also declined with time on-stream, as shown in **Figure 7.6(A)** for Au-Pd/Mo_2C-30, where application of Eq. (7.4) again provided an adequate fit to the experimental data. Hydrogenation of *p*-CNB over all the catalysts considered in this study resulted in exclusive *p*-CAN formation. As in the case of NB, the carbide catalysts delivered appreciable higher rates than the equivalent alumina samples (**Figure 7.6(B)**). The inclusion of Pd again served to elevate *p*-CNB hydrogenation activity. This is consistent with earlier work using Au-Pd/Al_2O_3 prepared by deposition/precipitation but increased Pd content (to Au/Pd = 8) in that study resulted in NB formation as a result of Pd promoted hydrodechlorination [3]. We should stress that 100% *p*-CAN yield was achieved over Au-Pd/Mo_2C-10 and Au-Pd/Mo_2C-30, i.e. full selectivity to *p*-CAN at 100% conversion of the inlet *p*-CNB feed. This represents a significant advance in the sustainable production of a target amine where reaction exclusivity at full reactant conversion removes the requirement for down-stream separation/purification unit operations.

Catalyst performance was further assessed in the gas phase hydrogenation of *p*-nitrobenzonitrile (*p*-NBN), where the limited available literature [74,84-86] refers to batch liquid phase reactions at elevated pressures (up to 6 MPa) and high selectivity to *p*-aminobenzonitrile (*p*-ABN) has proven to be challenging. Koprivova and Cerveny [85] have identified 15 possible intermediates and products in liquid phase operation. While an overall reaction scheme can involve disproportionation, reduction, condensation, hydrodenitrogenation and hydrodecarbonation, a simplified pathway is presented in **Figure 7.7(B)** that applies to liquid phase studies employing Raney Ni and Ni–Cu catalysts [85,86]. Conversion of *p*-NBN to the target *p*-ABN (step I) can be accompanied by further hydrogenation to *p*-aminobenzamide (step II) or *p*-aminobenzylamine (step III) [85] with subsequent hydrogenolysis to *p*-aminotoluene (step IV) [85,86]. A representative temporal *p*-NBN conversion (over Au-Pd/Mo_2C-10) is given in **Figure 7.6(A)**, where initial conversion was obtained from the fit to Eq. (7.4). Full selectivity to the target *p*-ABN product was recorded over all the catalysts with 100% yield achieved with Au-Pd/Mo_2C-10 and Au-Pd/Mo_2C-30. This exceeds the highest yields (*ca.* 99% over Au/TiO_2 [74] and *ca.* 97% over Au/Fe_2O_3) [84] reported for batch liquid systems. We must stress that economies of scale favour continuous processes for

high throughput while circumventing multistage separation and treatment steps that are required in discontinuous batch processes. The only reported gas phase catalysis study dates from the 1950s where Hata and Watanabe [86] investigated the hydrogenation of various aromatic nitriles (including the three NBN isomers) over a Ni–Cu catalyst at 523-573 K and reported, as principal products, AN, toluidine and ABN (< 32% yield).

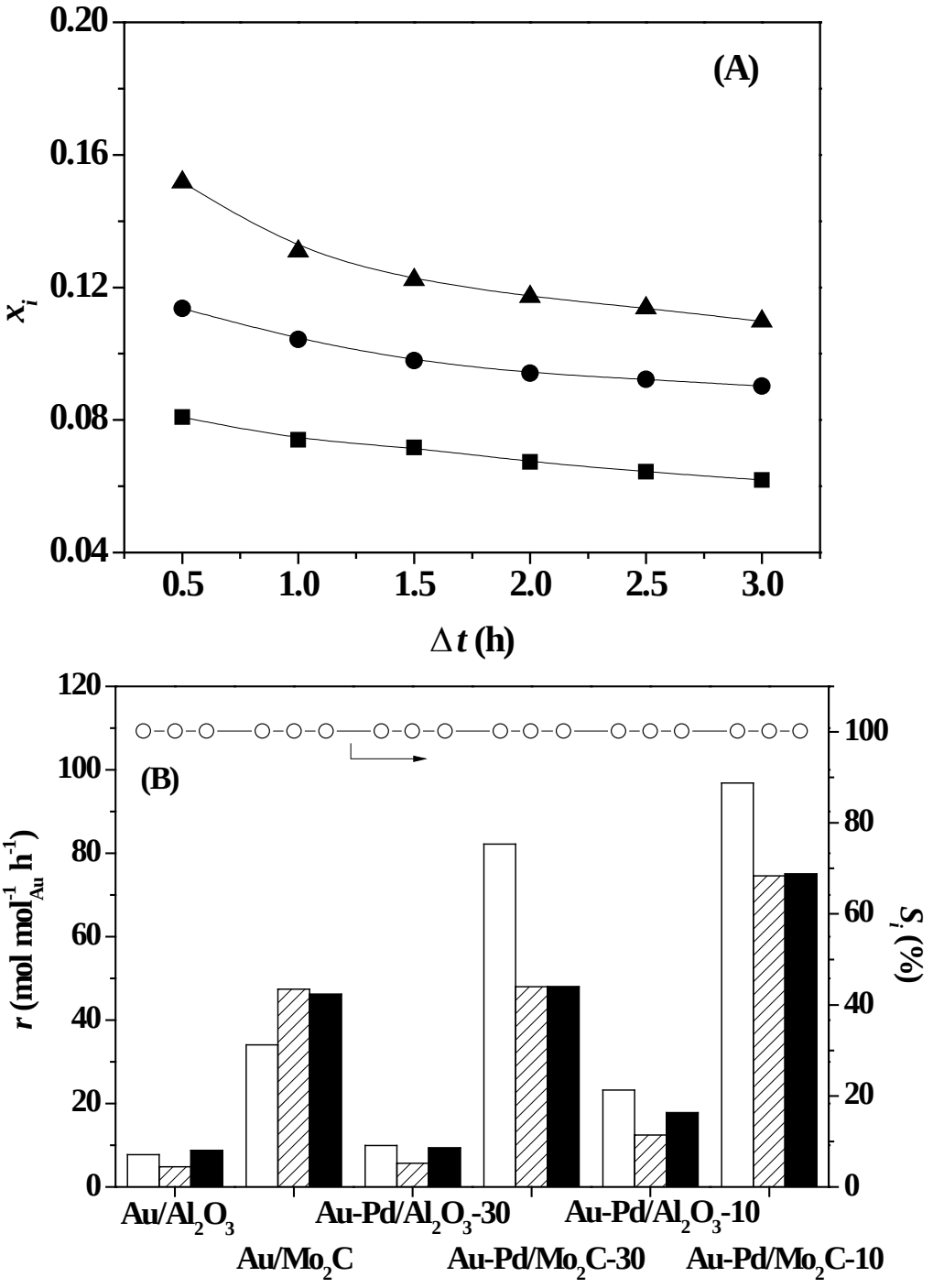

Figure 7.6: (A) Representative variation of NB (■), *p*-CNB (●) and *p*-NBN (▲) fractional conversion (x_i) with time on-stream over Au/Mo$_2$C (■), Au-Pd/Mo$_2$C-30 (●) and Au-Pd/Mo$_2$C-10 (▲). (B) Reaction rate with associated selectivity to the target amines (AN, *p*-CAN and *p*-ABN): NB (open bars); *p*-CNB (hatched bars); *p*-NBN (solid bars).

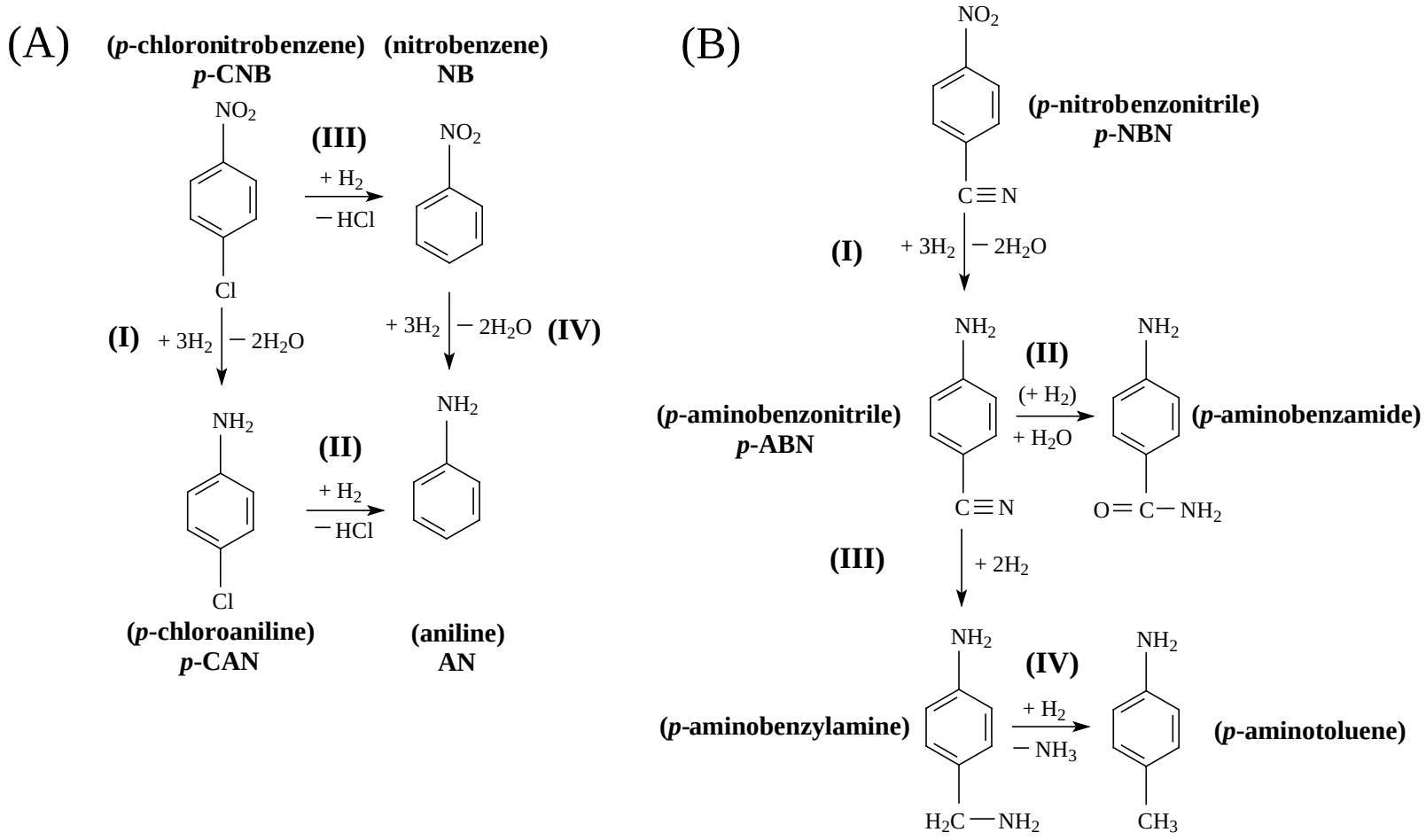

Figure 7.7: Reaction pathways for (A) *p*-CNB and (B) *p*-NBN hydrogenation.

As in the case of NB and *p*-CNB reactants, selective *p*-NBN hydrogenation reaction rate was elevated with Pd inclusion, where the carbide catalysts delivered enhanced activity relative to the alumina counterparts.

7.4 Conclusions

We provide the first reported synthesis of Mo_2C supported (Au-Pd) bimetallic catalysts that have been used to promote the gas phase hydrogenation of nitroarenes (NB, *p*-CNB and *p*-NBN) where Al_2O_3 supported Au and Au-Pd served as benchmark. The carbide was synthesised by the temperature programmed carburisation (of H_2MoO_4 in CH_4/H_2) and confirmed by XRD analysis. Bimetallic catalyst synthesis using Au and Pd colloids employed polyvinyl alcohol (PVA) as stabiliser to avoid agglomeration and resulted in a well dispersed supported metal phase with particles in the 1-8 nm size range (mean = 4-5 nm). The bimetallics exhibited increased H_2 chemisorption capacity with higher uptake on Au-Pd/Mo_2C relative to Au-Pd/Al_2O_3. XPS analysis has established the formation of electron rich species ($Au^{\delta-}$) on Al_2O_3 where the binding energy for Au on Mo_2C (both monometallic and Au-Pd bimetallics) was close to the metallic Au reference. All the (carbide and alumina based) catalysts were 100% selective in promoting $-NO_2$ hydrogenation to the target amine. The carbide systems exhibited (greater than 3-fold) higher selective hydrogenation rates that were enhanced with increasing Pd content (Au/Pd from 30 to 10), which can be attributed to increased reactive surface hydrogen and more effective $-NO_2$ activation. We achieved 100% yield of the target amine for reaction over Au-Pd/Mo_2C-10 and Au-Pd/Mo_2C-30 in continuous operation. The results have established controlled preparation of well dispersed Au-Pd on Mo_2C and application in the clean synthesis of high value amines.

7.5 References

[7.1] F. Tao, *Synthesis, catalysis, surface chemistry and structure of bimetallic nanocatalysts*, Chem. Soc. Rev., **41**, 7977-7979 (2012)

[7.2] R.W.J. Scott, O.M. Wilson, S.-K. Oh, E.A. Kenik, R.M. Crooks, *Bimetallic palladium-gold dendrimer-encapsulated catalysts*, J. Am. Chem. Soc., **126**, 15583-15591 (2004)

[7.3] F. Cárdenas-Lizana, S. Gómez-Quero, A. Hugon, L. Delannoy, C. Louis, M.A. Keane, *Pd-promoted selective gas phase hydrogenation of p-chloronitrobenzene over alumina supported Au*, J. Catal., **262**, 235-243 (2009)

[7.4] S. Chandra Shekar, J. Krishna Murthy, P. Kanta Rao, K.S. Rama Rao, E. Kemnitz, *Selective hydrogenolysis of dichlorodifluoromethane (CCl_2F_2) over CCA supported palladium bimetallic catalysts*, Appl. Catal. A: Gen., **244**, 39-48 (2003)

[7.5] F. Menegazzo, P. Canton, F. Pinna, N. Pernicone, *Bimetallic Pd-Au catalysts for benzaldehyde hydrogenation: effects of preparation and of sulfur poisoning*, Catal. Commun., **9**, 2353-2356 (2008)

[7.6] V. Dal Santo, A. Gallo, A. Naldoni, M. Guidotti, R. Psaro, *Bimetallic heterogeneous catalysts for hydrogen production*, Catal. Today, **197**, 190-205 (2012)

[7.7] F. Gao, D.W. Goodman, *Pd-Au bimetallic catalysts: understanding alloy effects from planar models and (supported) nanoparticles*, Chem. Soc. Rev., **41**, 8009-8020 (2012)

[7.8] P. Gao, F. Li, F. Xiao, N. Zhao, N. Sun, W. Wei, L. Zhong, Y. Sun, *Preparation and activity of Cu/Zn/Al/Zr catalysts via hydrotalcite-containing precursors for methanol synthesis from CO_2 hydrogenation*, Catal. Sci. Technol., **2**, 1447-1454 (2012)

[7.9] D.-W. Lee, M.S. Lee, J.Y. Lee, S. Kim, H.-J. Eom, D.J. Moon, K.-Y. Lee, *The review of Cr-free Fe-based catalysts for high-temperature water-gas shift reactions*, Catal. Today, **210**, 2-9 (2013)

[7.10] J.K. Edwards, A. Thomas, A.F. Carley, A.A. Herzing, C.J. Kiely, G.J. Hutchings, *Au-Pd supported nanocrystals as catalysts for the direct synthesis of hydrogen peroxide from H_2 and O_2*, Green Chem., **10**, 388-394 (2008)

[7.11] F. Menegazzo, M. Signoretto, M. Manzoli, F. Boccuzzi, G. Cruciani, F. Pinna, G. Strukul, *Influence of the preparation method on the morphological and composition properties of Pd-Au/ZrO2 catalysts and their effect on the direct synthesis of hydrogen peroxide from hydrogen and oxygen*, J. Catal., **268**, 122-130 (2009)

[7.12] X. Wei, X.-F. Yang, A.-Q. Wang, L. Li, X.-Y. Liu, T. Zhang, C.-Y. Mou, J. Li, *Bimetallic Au-Pd alloy catalysts for N_2O decomposition: effects of surface structures on catalytic activity*, J. Phys. Chem. C, **116**, 6222-6232 (2010)

[7.13] M.L. Guzmán-Castillo, E. López-Salinas, J.J. Fripiat, J. Sánchez-Valente, F. Hernández-Beltrán, A. Rodríguez-Hernández, J. Navarrete-Bolaños, *Active sulfated alumina catalysts obtained by hydrothermal treatment*, J. Catal., **220**, 317-325 (2003)

[7.14] M.O. Nutt, K.N. Heck, P. Alvarez, M.S. Wong, *Improved Pd-on-Au bimetallic nanoparticle catalysts for aqueous-phase trichloroethene hydrodechlorination*, Appl. Catal. B: Environ., **69**, 115-125 (2006)

[7.15] C.L. Bianchi, P. Canton, N. Dimitratos, F. Porta, L. Prati, *Selective oxidation of glycerol with oxygen using mono and bimetallic catalysts based on Au, Pd and Pt metals*, Catal. Today, **102-103**, 203-212 (2005)

[7.16] F. Gao, Y. Wang, D.W. Goodman, *CO oxidation over AuPd(100) from ultrahigh vacuum to near-atmospheric pressures: the critical role of contiguous Pd atoms*, J. Am. Chem. Soc., **131**, 5734-5735 (2009)

[7.17] F. Gao, Y. Wang, D.W. Goodman, *CO oxidation over AuPd(100) from ultrahigh vacuum to near-atmospheric pressures: CO adsorption-induced surface segregation and reaction kinetics*, J. Phys. Chem. C, **113**, 14993-15000 (2009)

[7.18] A. Villa, N. Janjic, P. Spontoni, D. Wang, D.S. Su, L. Prati, *Au-Pd/AC as catalysts for alcohol oxidation: effect of reaction parameters on catalytic activity and selectivity*, Appl. Catal. A: Gen., **364**, 221-228 (2009)

[7.19] A. Hugon, L. Delannoy, J.-M. Krafft, C. Louis, *Selective hydrogenation of 1,3-butadiene in the presence of an excess of alkenes over supported bimetallic gold-palladium catalysts*, J. Phys. Chem. C, **114**, 10823-10835 (2010)

[7.20] B. Pawelec, A.M. Venezia, V. La Parola, E. Cano-Serrano, J.M. Campos-Martin, J.L.G. Fierro, *AuPd alloy formation in Au-Pd/Al_2O_3 catalysts and its role on aromatics hydrogenation*, Appl. Surf. Sci., **242**, 380-391 (2005)

[7.21] A.M. Venezia, V.L. Parola, B. Pawelec, J.L.G. Fierro, *Hydrogenation of aromatics over Au-Pd/SiO_2-Al_2O_3 catalysts; support acidity effect*, Appl. Catal. A: Gen., **264**, 43-51 (2004)

[7.22] A. Sárkány, O. Geszti, G. Sáfrán, *Preparation of Pd_{shell}-Au_{core}/SiO_2 catalyst and catalytic activity for acetylene hydrogenation*, Appl. Catal. A: Gen., **350**, 157-163 (2008)

[7.23] X. Yang, D. Chen, S. Liao, H. Song, Y. Li, Z. Fu, Y. Su, *High-performance Pd-Au bimetallic catalyst with mesoporous silica nanoparticles as support and its catalysis of cinnamaldehyde hydrogenation*, J. Catal., **291**, 36-43 (2012)

[7.24] P. Weinberger, L. Szunyogh, B.I. Bennett, *Theoretical band-structure spectroscopy of Au_xPd_{1-x} alloys*, Phys. Rev. B, **47**, 10154-10157 (1993)

[7.25] A. Groß, *Reactivity of bimetallic systems studied from first principles*, Top. Catal., **37**, 29-39 (2006)

[7.26] Z. Abbasi, M. Haghighi, E. Fatehifar, S. Saedy, *Synthesis and physicochemical characterization of nanostructured Pt/CeO_2 catalyst used for total oxidation of toluene*, Int. J. Chem. React. Eng., **9**, A45(41-19) (2011)

[7.27] F. Cardenas-Lizana, S. Gomez-Quero, N. Perret, M.A. Keane, *Gold catalysis at the gas-solid interface: role of the support in determining activity and selectivity in the hydrogenation of m-dinitrobenzene*, Catal. Sci. Technol., **1**, 652-661 (2011)

[7.28] X. Wang, N. Perret, M.A. Keane, *The role of hydrogen partial pressure in the gas phase hydrogenation of p-chloronitrobenzene over alumina supported Au and Pd: a consideration of reaction thermodynamics and kinetics*, Chem. Eng. J., **210**, 103-113 (2012)

[7.29] X. Wang, N. Perret, J.J. Delgado, G. Blanco, X. Chen, C.M. Olmos, S. Bernal, M.A. Keane, *Reducible support effects in the gas phase hydrogenation of p-chloronitrobenzene over gold*, J. Phys. Chem. C, **117**, 994-1005 (2013)

[7.30] M. Pietrowski, M. Wojciechowska, *An efficient ruthenium-vanadium catalyst for selective hydrogenation of ortho-chloronitrobenzene*, Catal. Today, **142**, 211-214 (2009)

[7.31] N. Perret, F. Cárdenas-Lizana, M.A. Keane, *Selective hydrogenation of benzaldehyde to benzyl alcohol over Au/Al_2O_3*, Catal. Commun., **16**, 159-164 (2011)

[7.32] F. Cárdenas-Lizana, M.A. Keane, *The development of gold catalysts for use in hydrogenation reactions*, J. Mater. Sci., **48**, 543-564 (2013)

[7.33] G.C. Bond, C. Louis, D.T. Thompson, Catalysis by Gold, Imperial College Press, London, 2006

[7.34] N. Perret, X. Wang, L. Delannoy, C. Potvin, C. Louis, M.A. Keane, *Enhanced selective nitroarene hydrogenation over Au supported on β-Mo_2C and β-Mo_2C/Al_2O_3*, J. Catal., **286**, 172-183 (2012)

[7.35] E. Bus, J.T. Miller, J.A. van Bokhoven, *Hydrogen chemisorption on Al_2O_3-supported gold catalysts*, J. Phys. Chem. B, **109**, 14581-14587 (2005)

[7.36] A. Corma, M. Boronat, S. Gonzalez, F. Illas, *On the activation of molecular hydrogen by gold: a theoretical approximation to the nature of potential active sites*, Chem. Commun., 3371-3373 (2007)

[7.37] D. Wang, Y. Li, *Bimetallic nanocrystals: liquid-phase synthesis and catalytic applications*, Adv. Mater., **23**, 1044-1060 (2011)

[7.38] Y.-F. Han, Z. Zhong, K. Ramesh, F. Chen, L. Chen, T. White, Q. Tay, S.N. Yaakub, Z. Wang, *Au promotional effects on the synthesis of H_2O_2 directly from*

H_2 and O_2 on supported Pd-Au alloy catalysts, J. Phys. Chem. C, **111**, 8410-8413 (2007)

[7.39] J. Xu, T. White, P. Li, C. He, J. Yu, W. Yuan, Y.-F. Han, *Biphasic Pd-Au alloy catalyst for low-temperature CO oxidation*, J. Am. Chem. Soc., **132**, 10398-10406 (2010)

[7.40] M. Hasbi Ab Rahim, Q. He, J.A. Lopez-Sanchez, C. Hammond, N. Dimitratos, M. Sankar, A.F. Carley, C.J. Kiely, D.W. Knight, G.J. Hutchings, *Gold, palladium and gold-palladium supported nanoparticles for the synthesis of glycerol carbonate from glycerol and urea*, Catal. Sci. Technol., **2**, 1914-1924 (2012)

[7.41] J.K. Edwards, B. Solsona, P. Landon, A.F. Carley, A. Herzing, M. Watanabe, C.J. Kiely, G.J. Hutchings, *Direct synthesis of hydrogen peroxide from H_2 and O_2 using Au-Pd/Fe_2O_3 catalysts*, J. Mater. Chem., **15**, 4595-4600 (2005)

[7.42] G.C. Bond, A.F. Rawle, *Catalytic hydrogenation in the liquid phase. Part 1. Hydrogenation of isoprene catalysed by palladium, palladium-gold and palladium-silver catalysts*, J. Mol. Catal. A: Chem., **109**, 261-271 (1996)

[7.43] A. Sarkany, P. Hargittai, A. Horvath, *Controlled synthesis of PDDA stabilized Au-Pd bimetallic nanostructures and their activity in hydrogenation of acetylene*, Top. Catal., **46**, 121-128 (2007)

[7.44] J.K. Edwards, B.E. Solsona, P. Landon, A.F. Carley, A. Herzing, C.J. Kiely, G.J. Hutchings, *Direct synthesis of hydrogen peroxide from H_2 and O_2 using TiO_2-supported Au-Pd catalysts*, J. Catal., **236**, 69-79 (2005)

[7.45] Y.F. Han, J.H. Wang, D. Kumar, Z. Yan, D.W. Goodman, *A kinetic study of vinyl acetate synthesis over Pd-based catalysts: kinetics of vinyl acetate synthesis over Pd-Au/SiO_2 and Pd/SiO_2 catalysts*, J. Catal., **232**, 467-475 (2005)

[7.46] D. Kumar, M.S. Chen, D.W. Goodman, *Synthesis of vinyl acetate on Pd-based catalysts*, Catal. Today, **123**, 77-85 (2007)

[7.47] A.M. Venezia, V. La Parola, G. Deganello, B. Pawelec, J.L.G. Fierro, *Synergetic effect of gold in Au/Pd catalysts during hydrodesulfurization reactions of model compounds*, J. Catal., **215**, 317-325 (2003)

[7.48] P. Zhao, N. Li, D. Astruc, *State of the art in gold nanoparticle synthesis*, Coordin. Chem. Rev., **257**, 638-665 (2013)

[7.49] S. Yongprapat, A. Therdthianwong, S. Therdthianwong, *Au/C catalyst prepared by polyvinyl alcohol protection method for direct alcohol alkaline exchange membrane fuel cell application*, J. Appl. Electrochem., **42**, 483-490 (2012)

[7.50] J.M. Nadgeri, M.M. Telkar, C.V. Rode, *Hydrogenation activity and selectivity behavior of supported palladium nanoparticles*, Catal. Commun., **9**, 441-446 (2008)

[7.51] Y.S. Kwon, A.A. Gromov, A.P. Ilyin, A.A. Ditts, J.S. Kim, S.H. Park, M.H. Hong, *Features of passivation, oxidation and combustion of tungsten nanopowders by air*, Int. J. Refract. Met. Hard Mater., **22**, 235-241 (2004)

[7.52] F. Cárdenas-Lizana, S. Gómez-Quero, M.A. Keane, *Exclusive production of chloroaniline from chloronitrobenzene over Au/TiO_2 and Au/Al_2O_3*, ChemSusChem, **1**, 215-221 (2008)

[7.53] M.A. Keane, *Gas phase hydrogenation/hydrogenolysis of benzaldehyde and o-tolualdehyde over Ni/SiO_2*, J. Mol. Catal. A: Chem., **118**, 261-269 (1997)

[7.54] G. Tavoularis, M.A. Keane, *The gas phase hydrodechlorination of chlorobenzene over nickel/silica*, J. Chem. Technol. Biotechnol., **74**, 60-70 (1999)

[7.55] J.-S. Choi, G. Bugli, G. Djéga-Mariadassou, *Influence of the degree of carburization on the density of sites and hydrogenating activity of molybdenum carbides*, J. Catal., **193**, 238-247 (2000)

[7.56] N.E. Kolli, L. Delannoy, C. Louis, *Bimetallic Au-Pd catalysts for selective hydrogenation of butadiene: Influence of the preparation method on catalytic properties*, J. Catal., **297**, 79-92 (2013)

[7.57] I. Pettiti, S. Colonna, S. De Rossi, M. Faticanti, G. Minelli, P. Porta, *XAS characterization and CO oxidation on δ-alumina supported La, Mn, Co and Fe oxides*, Phys. Chem. Chem. Phys., **6**, 1350-1358 (2004)

[7.58] G.C. Bond, *Chemisorption and reactions of small molecules on small gold particles*, Molecules, **17**, 1716-1743 (2012)

[7.59] P. Claus, *Heterogeneously catalysed hydrogenation using gold catalysts*, Appl. Catal. A: Gen., **291**, 222-229 (2005)

[7.60] S. Nikolaev, V. Smirnov, *Selective hydrogenation of phenylacetylene on gold nanoparticles*, Gold Bull., **42**, 182-189 (2009)

[7.61] S.A. Nikolaev, V.V. Smirnov, *Synergistic and size effects in selective hydrogenation of alkynes on gold nanocomposites*, Catal. Today, **147**, S336-S341 (2009)

[7.62] F. Cardenas-Lizana, Y. Hao, M. Crespo-Quesada, I. Yuranov, X. Wang, M.A. Keane, L. Kiwi-Minsker, *Selective gas phase hydrogenation of p-chloronitrobenzene over Pd catalysts: role of the support*, ACS Catal., **3**, 1386-1394 (2013)

[7.63] M. Baron, O. Bondarchuk, D. Stacchiola, S. Shaikhutdinov, H.J. Freund, *Interaction of gold with cerium oxide supports: CeO_2(111) thin films vs CeO_x nanoparticles*, J. Phys. Chem. C, **113**, 6042-6049 (2009)

[7.64] H. Cho, H. Park, T.P. Russell, S. Park, *Precise placements of metal nanoparticles from reversible block copolymer nanostructures*, J. Mater. Chem., **20**, 5047-5051 (2010)

[7.65] B. Ealet, E. Gillet, *Metal-alumina interface: influence of the metal electronegativity and of the substrates stoichiometry*, Surf. Sci., **367**, 221-230 (1996)

[7.66] C. Yang, A.K. Manocchi, B. Lee, H. Yi, *Viral-templated palladium nanocatalysts for Suzuki coupling reaction*, J. Mater. Chem., **21**, 187-194 (2011)

[7.67] R. Wang, J. Yang, K. Shi, B. Wang, L. Wang, G. Tian, B. Bateer, C. Tian, P. Shen, H. Fu, *Single-step pyrolytic preparation of Mo_2C/graphitic carbon nanocomposite as catalyst carrier for the direct liquid-feed fuel cells*, RSC Adv., **3**, 4771-4777 (2013)

[7.68] R. Barthos, A. Szechenyi, F. Solymosi, *Efficient H_2 production from ethanol over Mo_2C/C nanotube catalyst*, Catal. Lett., **120**, 161-165 (2008)

[7.69] A.C. Lausche, J.A. Schaidle, L.T. Thompson, *Understanding the effects of sulfur on Mo_2C and Pt/Mo_2C catalysts: methanol steam reforming*, Appl. Catal. A: Gen., **401**, 29-36 (2011)

[7.70] M. Shimoda, T. Hirata, K. Yagisawa, M. Okochi, A. Yoshikawa, *Deconvolution of Mo 3d X-ray photoemission spectra γ-Mo_4O_{11}: agreement with prediction from bond length-bond strength relationships*, J. Mater. Sci. Lett., **8**, 1089-1091 (1989)

[7.71] Z.B.Z. Wei, P. Grange, B. Delmon, *XPS and XRD studies of fresh and sulfided Mo_2N*, Appl. Surf. Sci., **135**, 107-114 (1998)

[7.72] T.P. St. Clair, S.T. Oyama, D.F. Cox, S. Otani, Y. Ishizawa, R.-L. Lo, K.-i. Fukui, Y. Iwasawa, *Surface characterization of α-Mo_2C (0001)*, Surf. Sci., **426**, 187-198 (1999)

[7.73] S.J. Ardakani, X. Liu, K.J. Smith, *Hydrogenation and ring opening of naphthalene on bulk and supported Mo_2C catalysts*, Appl. Catal. A: Gen., **324**, 9-19 (2007)

[7.74] A. Corma, C. González-Arellano, M. Iglesias, F. Sánchez, *Gold complexes as catalysts: chemoselective hydrogenation of nitroarenes*, Appl. Catal. A: Gen., **356**, 99-102 (2009)

[7.75] H.-U. Blaser, H. Steiner, M. Studer, *Selective catalytic hydrogenation of functionalized nitroarenes: an update*, ChemCatChem, **1**, 210-221 (2009)

[7.76] F. Cárdenas-Lizana, S. Gómez-Quero, G. Jacobs, Y. Ji, B.H. Davis, L. Kiwi-Minsker, M.A. Keane, *Alumina supported Au-Ni: surface synergism in the gas phase hydrogenation of nitro-compounds*, J. Phys. Chem. C, **116**, 11166-11180 (2012)

[7.77] F. Cárdenas-Lizana, S. Gómez-Quero, H. Idriss, M.A. Keane, *Gold particle size effects in the gas-phase hydrogenation of m-dinitrobenzene over Au/TiO_2*, J. Catal., **268**, 223-234 (2009)

[7.78] F. Cárdenas-Lizana, S. Gómez-Quero, N. Perret, M.A. Keane, *Support effects in the selective gas phase hydrogenation of p-chloronitrobenzene over gold*, Gold Bull., **42**, 124-132 (2009)

[7.79] X. Wang, N. Perret, M.A. Keane, *Gas phase hydrogenation of nitrocyclohexane over supported gold catalysts*, Appl. Catal. A: Gen., **467**, 575-584 (2013)

[7.80] F. Cárdenas-Lizana, S. Gómez-Quero, M.A. Keane, *Clean production of chloroanilines by selective gas phase hydrogenation over supported Ni catalysts*, Appl. Catal. A: Gen., **334**, 199-206 (2008)

[7.81] C. Xiao, X. Wang, C. Lian, H. Liu, M. Liang, Y. Wang, *Selective hydrogenation of halonitrobenzenes*, Curr. Org. Chem., **16**, 280-296 (2012)

[7.82] J.-F. Su, B. Zhao, Y.-W. Chen, *Hydrogenation of p-chloronitrobenzene on Mo-doped NiB cluster catalysts*, Ind. Eng. Chem. Res., **50**, 1580-1587 (2011)

[7.83] B. Zhao, Y.-W. Chen, *Hydrogenation of p-chloronitrobenzene on Mo, La, Fe, and W-modified NiCoB nanoalloy catalysts*, J. Non-Cryst. Solids, **356**, 839-847 (2010)

[7.84] A. Corma, P. Serna, *Chemoselective hydrogenation of nitro compounds with supported gold catalysts*, Science, **313**, 332-334 (2006)

[7.85] K. Koprivova, L. Cerveny, *Hydrogenation of nitrobenzonitriles using Raney nickel catalyst*, Res. Chem. Intermed., **34**, 93-101 (2008)

[7.86] K. Hata, K.-I. Watanabe, *Catalytic hydrogenation of aromatic nitrites*, Bull. Chem. Soc. Jpn., **32**, 861-867 (1959)

CHAPTER 8

Gas Phase Hydrogenation of Nitrocyclohexane over Supported Gold Catalysts

In previous chapters, the hydrogenation of aromatic nitro-compounds has been investigated over various supported gold catalysts. In this chapter, the chemoselectivity of gold in gas phase hydrogenation has been extended to aliphatic (cyclic) nitro compound, *i.e.* nitrocyclohexane, where different Au supports (Al_2O_3, ZrO_2, CeO_2 and TiO_2) have been considered. This chapter has been published in Applied Catalysis A: General (see publication No. 5). Co-author N.P. participated in the discussion and co-wrote the chapter. M.A.K. directed the project and co-wrote the chapter.

8.1 Introduction

Cyclohexanone oxime is commercially important as an intermediate in the production of nylon-6, which is widely used in polymer synthesis. Standard cyclohexanone oxime production from cyclohexanone is inefficient due to the low cyclohexanone yields (3-10% [1-3]) obtained in the industrial oxidation of cyclohexane. Moreover, oxime formation from cyclohexanone employs a hydroxylamine salt (usually the sulphate) where the equilibrium must be displaced with addition of ammonia to maintain pH = 7 [4], generating significant quantities of ammonium sulphate waste [5]. A controlled oxidation of cyclohexylamine (obtained from nitrobenzene hydrogenation) can produce the oxime but this necessitates extended reaction times (up to 10 days) to arrive at a 60% yield [6] with the involvement of environmentally toxic chemicals (oleum, halides and nitrogen oxides) and associated waste production [7]. Direct hydrogenation of nitrocyclohexane (NC) to the oxime represents a possible alternative [7,8]. Selectivity in NC hydrogenation is challenging as the oxime can undergo further hydrogenation to an amine (cyclohexylamine) and ketone (cyclohexanone), where the latter requires the participation of water, as shown in **Figure 8.1**. Moreover, condensation involving

cyclohexylamine and cyclohexanone can generate cyclohexyl-cyclohexylidene amine (CCA) with subsequent hydrogenation to dicyclohexylamine (DCA) [8].

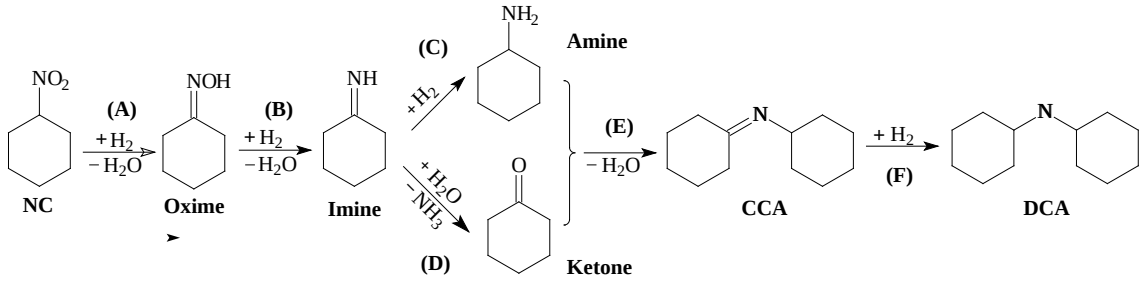

Figure 8.1: Reaction pathway associated with the hydrogenation of nitrocyclohexane (NC).

A comprehensive search through the literature only unearthed eight reports dealing with NC hydrogenation to oxime [5,7-13]. The earliest work dates from the 1960s where a one step NC hydrogenation was reported by DuPont [9,10] in a liquid phase process operated at 413 K and elevated pressure (35 bar) using a Pd catalyst to give an oxime yield of *ca.* 70%. This work was taken further by Knifton, employing homogenous Cu(I, II) and Ag(I) catalysts with CO as reducing agent to give 89% oxime yield, where efficiency increased in the order: Ag(I) < Cu(II) ≈ Cu(I) [11,13]. There followed a 30 year period of apparent inactivity until Corma *et al.* [12] reported the use of Au/TiO_2 to promote the reaction in the liquid phase, achieving 91% selectivity at nearly complete NC conversion. The same group subsequently recorded 85% selectivity to the oxime over Na promoted Pt/TiO_2 [8]. A similar level of performance has also been recorded for Pd on carbon nanotubes [5]. In the sequential reaction pathway (**Figure 8.1**), the critical challenge is to circumvent conversion of the reactive imine intermediate *via* steps C and D. The high activation energy barrier for dissociative H_2 adsorption on supported Au can be significant in this reaction system and has been used to good effect in selective hydrogenation [14], notably in the conversion of nitroarenes [15], aldehydes [16,17], ketones [18] and 1,3-butadiene [16,19]. Shimizu and co-workers [7] have compared the performance of oxide (Al_2O_3, SiO_2, MgO and TiO_2) supported Au in NC hydrogenation where Au/Al_2O_3 exhibited the highest oxime yield (86%). The limited applications of Au catalysts in NC hydrogenation have been conducted in batch liquid phase at high pressures (up to 15 bar) where all the products presented in **Figure 8.1** were obtained with

additional unidentified by-products [7] and ε-caprolactam [20].

In this study, we provide the first report of NC hydrogenation in continuous gas phase (at 1 atm) operation. We can flag a recent “white paper” [21], which identified a switch from batch to continuous processing as #1 priority for sustainable manufacture in the fine chemical sector. We first examine possible thermodynamic constraints and then focus on the use of Au/Al_2O_3 to probe the effect of critical process parameters, *i.e.* space velocity, temperature and H_2 partial pressure. In addition, we have studied the role of the support (Au on Al_2O_3, TiO_2, CeO_2 and ZrO_2) and identify the surface interactions that determine catalyst performance.

8.2 Thermodynamic Analysis

Chemical thermodynamics provide a useful guide to the maximum conversion (and selectivity response) that is possible under given reaction conditions and is an essential initial consideration in the design of a catalytic process [22]. Each organic intermediate and product presented in **Figure 8.1** in addition to H_2, H_2O and NH_3 were considered in the thermodynamic calculations. Setting the inlet NC at 1 mol, product distribution at equilibrium was determined with varying reaction temperature (353-473 K) at a total pressure of 1 atm, where the H_2/NC molar ratio was kept constant at 2500 (a representative value that was typically employed in catalyst testing). The equilibrium calculations were carried out using CHEMCAD (Version 6) where the Gibbs reactor facility was applied to obtain product composition under conditions of minimised Gibbs free energy (non-stoichiometric approach) [23]. For thermodynamic equilibrium calculations, there are in general two approaches: non-stoichiometry and stoichiometry. In the non-stoichiometric method, the equilibrium composition of the system is found by the direct minimisation of the Gibbs free energy for a given set of species without any specification of the possible reactions that might take place in the system. In the stoichiometric approach, the system is described by a group of stoichiometrically independent reactions, which, however, are typically chosen arbitrarily from a set of possible reactions. Efforts to study the system's response in terms of the arbitrarily chosen chemical reactions may lead to erroneous conclusions. The equation of state for fugacity employed the Soave–Redlich–Kwong approach [22]. The total Gibbs function is given by

$$G^t = \sum_{i=1}^{N} n_i \bar{G}_i = \sum_{i=1}^{N} n_i \bar{\mu}_i = \sum n_i G_i^0 + RT \sum n_i \ln \frac{\hat{f}_i}{f_i^0} \quad (8.1)$$

For gas phase reaction equilibrium, $\hat{f}_i = \hat{\phi}_i y_i P$, $f_i^0 = P^0$ and $\Delta G^0 = \Delta G_{f_i}^0$ and the minimum Gibbs free energy of each gaseous species and total for the system can be expressed by

$$\Delta G_{f_i}^0 + RT \ln \frac{\hat{\phi}_i y_i P}{P^0} + \sum_k \lambda_k a_{ik} = 0 \quad (8.2)$$

$$\sum_{i=1}^{N} n_i (\Delta G_{f_i}^0 + RT \ln \frac{\hat{\phi}_i y_i P}{P^0} + \sum_k \lambda_k a_{ik}) = 0 \quad (8.3)$$

according to the Lagrange undetermined multiplier method [24] with the elemental balance constraint

$$\sum_{i=1}^{N} n_i a_{ik} = A_k \quad (8.4)$$

8.3 Experimental Procedures

8.3.1 Catalyst Preparation

The commercial supports (Al_2O_3 (Puralox, Condea Vista Co.), CeO_2 (Grace Davison) and TiO_2 (P25, Degussa)) were used as received. Zirconia (ZrO_2) was synthesised by the precipitation of $ZrOCl_2$ (0.1 M) with aqueous NH_3 (2.5 M) under vigorous stirring (600 rpm) at pH 9.4-11.8. The resultant hydrogel was washed thoroughly with deionised water and dried at 373 K for 24 h with subsequent calcination (1 K min^{-1}) in flowing air (60 cm^3 min^{-1}) at 673 K for 5 h. The supported Au catalysts were prepared by deposition-precipitation. Urea, used as basification agent, was added (100-fold excess) to a solution of $HAuCl_4$, the support introduced and the suspension stirred and heated to 353 K (2 K min^{-1}) for 3 h. The pH progressively increased to reach *ca.* 7 after 3 h as a result of thermally induced urea decomposition

$$NH_2\text{-}CO\text{-}NH_2 + 3H_2O \xrightarrow{T=353K} 2NH_4^+ + 2OH^- + CO_2 \quad (8.5)$$

The resultant solid was separated by centrifugation, washed repeatedly with deionised water until the wash water was Cl-free (based on the $AgNO_3$ test) and dried in He (45 cm^3

min^{-1}) at 373 K (2 K min^{-1}) for 5 h. The catalysts were sieved to 75 μm average particle diameter (ATM fine test sieves) and the Au loadings determined by inductively coupled plasma-optical emission spectrometry (ICP-OES, Vista-PRO, Varian Inc.).

8.3.2 Catalyst Characterisation

Temperature programmed reduction (TPR), BET surface area, H_2 chemisorption and temperature programmed desorption (TPD) measurements were recorded on the commercial CHEM-BET 3000 (Quantachrome Instrument) unit with data acquisition/manipulation using the TPR Win^{TM} software. The samples were loaded into a U-shaped Pyrex glass cell (100 mm × 3.76 mm i.d.) and heated in 17 cm^3 min^{-1} (Brooks mass flow controlled) 5% v/v H_2/N_2 at 2 K min^{-1} to 473 K. The effluent gas passed through a liquid N_2 trap and changes in H_2 consumption were monitored by TCD (thermal conductivity detector). The reduced samples were swept with 65 cm^3 min^{-1} N_2 for 1.5 h, cooled to 298-423 K and subjected to H_2 chemisorption using a pulse (10 μl) titration procedure; H_2 pulses were repeated until the signal area was constant, indicating surface saturation. Hydrogen TPD in N_2 (65 cm^3 min^{-1}) was conducted at 50 K min^{-1} to 1173 K with a final isothermal hold until the signal returned to baseline. BET areas were recorded in a 30% v/v N_2/He flow with pure N_2 (99.9%) as internal standard. At least two cycles of N_2 adsorption-desorption were used to obtain total surface area using the standard single point method. Pore volume measurements were performed using the commercial automated Micromeritics Gemini 2390 system. Samples were outgassed at 423 K under N_2 for 1 h prior to analysis. Total pore volume was obtained at a relative N_2 pressure of P/P_0 = 0.95. The degree of support reduction was determined from O_2 titration measurements. Samples reduced (in 60 cm^3 min^{-1} H_2, 2 K min^{-1}) at 473 K for 1 h were swept with 65 cm^3 min^{-1} He for 1.5 h and subjected to a pulse (50 μl) O_2 titration. It has been demonstrated previously that there is a negligible contribution from Au to the total O_2 adsorbed [25] and support reduction can be related to O_2 uptake. Powder X-ray diffractograms (XRD) were recorded on a Bruker/Siemens D500 incident X-ray diffractometer using Cu $K\alpha$ radiation. The samples were scanned at a rate of 0.02º $step^{-1}$ over the $5^o \leq 2\theta \leq 85^o$ range and the diffractograms compared with JCPDS-ICDD reference

standards. Gold particle morphology and size were determined by transmission (TEM, JEOL JEM 2011) and scanning transmission electron microscopy (STEM, JEOL 2200FS) electron microscopy, employing Gatan DigitalMicrograph 1.82 for data acquisition/manipulation. Samples for analysis were prepared by dispersion in acetone and deposited on a holey carbon/Cu grid (300 Mesh). The surface area weighted mean metal particle size (d_{TEM}) was obtained from

$$d_{TEM} = \frac{\sum_i n_i d_i^3}{\sum_i n_i d_i^2} \tag{8.6}$$

where n_i is the number of particles of diameter d_i and $\Sigma\, n_i > 200$.

8.3.3 Catalytic Procedure

Reactions were carried out (1 atm, 353-473 K), following *in situ* catalyst activation at 473 K (2 K min^{-1}) for 1 h, in a continuous flow fixed bed vertical glass reactor (i.d. = 15 mm, l = 600 mm). The reactor and operating conditions for negligible heat/mass transport limitations have been fully described elsewhere [26,27] but features pertinent to this study are given below. A layer of borosilicate glass beads served as preheating zone, ensuring that the NC reactant was vaporised and reached reaction temperature before contacting the catalyst. Isothermal conditions (± 1 K) were achieved by diluting the catalyst bed with ground glass (75 μm). Reaction temperature was continuously monitored by a thermocouple inserted in a thermowell within the catalyst bed. The organic reactant was delivered *via* a glass/teflon air-tight syringe and teflon line using a microprocessor controlled infusion pump (Model 100 kd Scientific) at a fixed calibrated flow rate. A co-current flow of NC (or oxime) and H_2 (or H_2/He, 0.8×10^{-3} atm $\leq P_{H2} \leq$ 0.93 atm) was maintained at $GHSV$= 2–6×10^4 h^{-1} with an NC (or oxime) molar flow (F) of 4.8×10^{-5}–2.4×10^{-4} mol h^{-1}, inlet molar H_2/NC (or H_2/oxime) up to 7400 and molar Au (n) to F ratio in the 4.7×10^{-3}–11×10^{-2} h range. At the low partial pressures of NC ($\leq 0.8\times10^{-3}$ atm) in the feed, thermochemical calculations have confirmed that the reactant is in the gas phase over the temperature range applied. In a series of blank tests, passage of NC (or oxime) in a stream of H_2 through the empty reactor or over the support alone did not result in any detectable conversion. The reactor effluent was trapped in liquid nitrogen for analysis

on a Perkin-Elmer Auto System XL GC equipped with programmed split/splitless injector and flame ionisation detector, employing a DB-1 50 m×0.20 mm i.d. 0.33 μm film thickness capillary column (J&W Scientific). NC (Sigma-Aldrich, ≥ 9 7% w/w purity), cyclohexanone oxime (≥ 99.5%) and cyclohexane (≥ 99.5%) as carrier were used without further purification. Repeated reactions with different samples from the same batch of catalyst delivered raw conversion and selectivity data that were reproducible to within ± 5%.

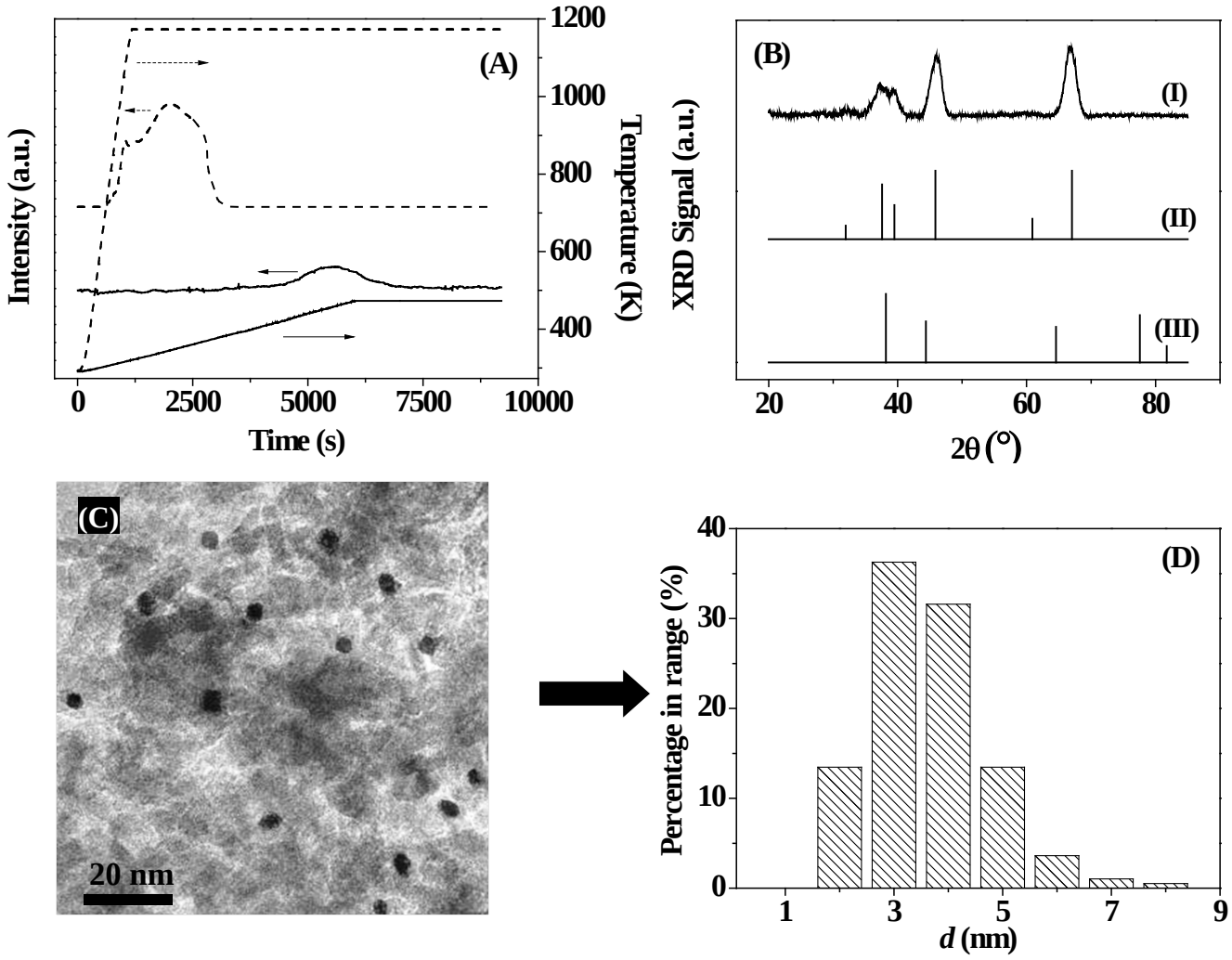

Figure 8.2: Characterisation of Au/Al_2O_3 in terms of (A) TPR (solid lines) and TPD (dashed lines) profiles; (B) XRD diffractograms of (I) activated Au/Al_2O_3 with JCPDS-ICDD reference for (II) γ-Al_2O_3 (10-0425) and (III) Au (04-0784); (C) Representative TEM image and (D) Au particle size (*d*) distribution.

8.4 Results and Discussion

Au catalysts have been employed in this work because it has been established chemoselective in the hydrogenation of various nitrocompounds [12,28-30]. Au/Al_2O_3

was selected as benchmark catalyst as it has been shown to exhibit the highest oxime selectivity in liquid phase operation [7]. The support Lewis acid sites can serve to activate the nitro group [7,31-33] and enhance hydrogen dissociation on Au [7,32], possibly contributing to greater efficiency.

Table 8.1: Physico-chemical characteristics of the supported Au catalysts.

	Au/Al_2O_3	Au/TiO_2	Au/CeO_2	Au/ZrO_2
Au loading (% w/w)	1.1	1.2	3.0	0.8
BET ($m^2\ g^{-1}$)	166 (191) [a]	47 (52)	108 (113)	93 (104)
Total pore volume ($cm^3\ g^{-1}$)	0.36	0.12	0.15	0.13
TPR T_{max} (K)	461	365	420	453
Theoretical TPR H_2 consumption[b] (µmol g^{-1})	84	91	198	61
Measured TPR H_2 consumption (µmol g^{-1})	87	126	544	56
H_2 chemisorption (µmol g_{Au}^{-1}) at 298 K	37	25	16	57
H_2 chemisorption (µmol g_{Au}^{-1}) at 423 K	379	244	73	154
H_2 released during TPD (µmol g^{-1})	564	109	156	223
O_2 titration (mmol $mol_{support}^{-1}$) at 473 K	0.8	1.7	4.0	1.0
Au size range (nm)	2-8	2-9	1-5	3-12
d_{TEM} (nm)	4.3	4.7	3.0	7.0

[a]values in parenthesis refer to BET surface area of the support
[b]amount of hydrogen required to fully reduce the Au precursor

8.4.1 Au/Al_2O_3 Characteristics

The reducibility of Au/Al_2O_3 was assessed by temperature programmed reduction (TPR) and the resultant profile is presented in **Figure 8.2(A)**. The temperature associated with maximum hydrogen consumption (T_{max}) is recorded in **Table 8.1**. The bare γ-Al_2O_3 support did not show any detectable H_2 consumption (or release) as noted elsewhere [34]. The TPR profile for Au/Al_2O_3 is characterised by a positive peak (T_{max} = 461 K) where H_2 consumption matched that required for the reduction of Au^{3+} to Au^0, in agreement with the work of Gluhoi *et al*. [35] We observed an appreciable (10-fold) increase in H_2 chemisorption at reaction relative to ambient temperature (**Table 8.1**), indicating that uptake is an activated process, which is in line with the findings of van Bokhoven *et al*. [36-38]. Subsequent TPD analysis (see profile in **Figure 8.2(A)**) generated a broad H_2

release (from 700–1173 K) where H_2 desorbed exceeded the chemisorption measurements. This suggests the generation of surface hydrogen during TPR with the possible involvement of hydrogen spillover. The spillover phenomenon is well established for supported metals [39] where H_2 dissociates at metal sites generating H atoms that diffuse or "spillover" onto the support. This surface hydrogen can undergo a reverse diffusion/spillover from the support to the metal and participate in reaction [39]. Hydrogen spillover has been proposed for Au on a range of oxide (Al_2O_3, SiO_2, MgO, TiO_2, ZrO_2 and ZnO) carriers [25]. XRD analysis of the activated catalyst revealed four peaks (**Figure 8.2(BI)**) at 37.6°, 39.5°, 45.9° and 67.0° that correspond, respectively, to the (311), (222), (400) and (440) planes of γ-Al_2O_3 (**Figure 8.2(BII)**, JCPDS-ICDD 10-0425). The absence of any detectable signals (at 38.1°, 44.4°, 64.7° and 77.5°) due to Au (**Figure 8.2(BIII)**, JCPDS-ICDD 04-0784) suggests the occurrence of a well dispersed Au phase with particles below XRD detection (< *ca.* 5 nm) [40]. Indeed, the representative TEM image presented in **Figure 8.2(C)** confirms that Au is present at the nano-scale as pseudo-spherical particles. The histogram in **Figure 8.2(D)** shows a size distribution in the 1-8 nm range with a mean = 4.3 nm and a predominant component (95 %) ≤ 5 nm, which has been identified as crucial for significant hydrogenation activity over Au [41].

8.4.2 Gas Phase Hydrogenation of Nitrocyclohexane

8.4.2.1 Reaction Thermodynamics

Two approaches were taken in the thermodynamic analysis: (a) consideration of all species included in **Figure 8.1**; (b) analysis constrained to reduction leading to amine and ketone formation (steps A-D) without condensation (to CCA) and hydrogenation (to DCA). The first approach was taken to identify the thermodynamically favoured product(s) and the second to distinguish any preference (or selectivity) between oxime, amine and ketone as hydrogenation products. Under reaction conditions, NC is fully converted at equilibrium. The calculated selectivity dependence on temperature (for case (a)) is given in **Figure 8.3(A)**, where DCA (selectivity > 77%) predominates and the amine is a secondary product with a selectivity increase at higher temperatures. Under

thermodynamic control, the oxime or ketone is not formed. Omitting the condensation step (case (b)), amine selectivity approaches 100% where $T \leq 363$ K with the formation of ketone at higher reaction temperatures (**Figure 8.3(B)**). The thermodynamic analysis has revealed complete NC conversion (353-473 K) where the oxime (target product) is further reacted to generate amine (principally) and ketone with subsequent condensation. Catalytic control is therefore required to achieve selectivity to the oxime.

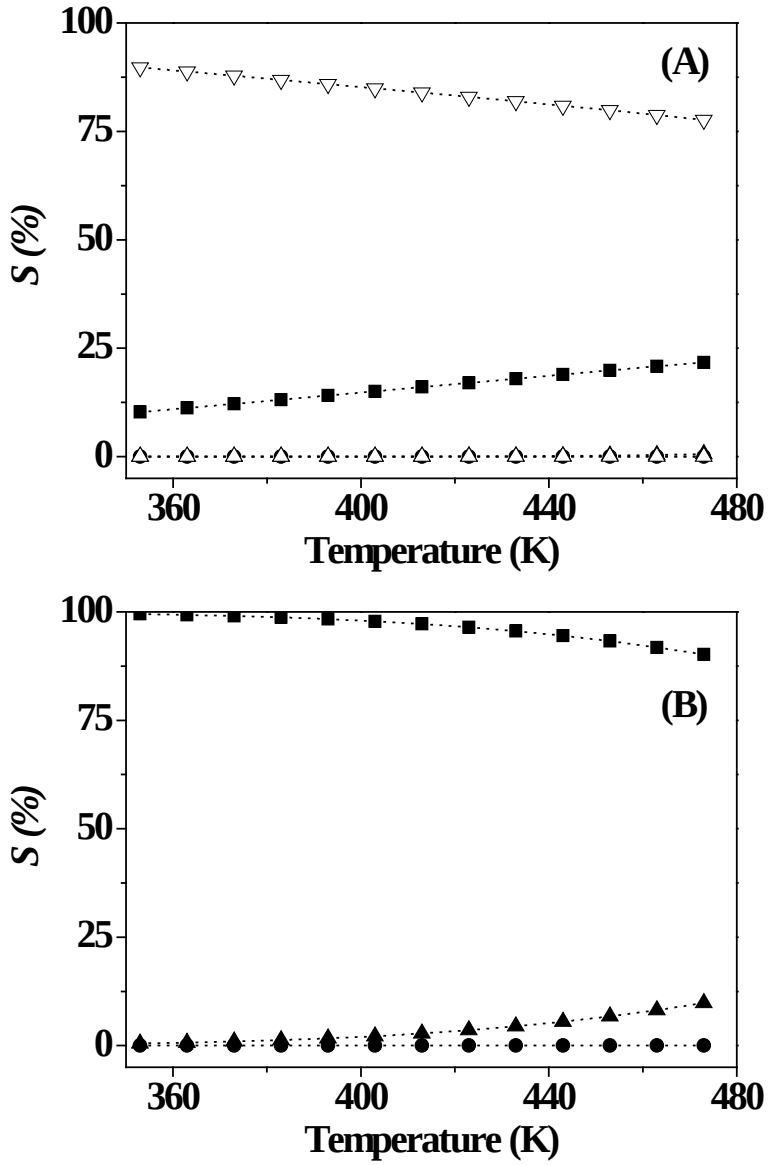

Figure 8.3: Product selectivity at the thermodynamic reaction equilibrium as a function of temperature: (A) considering all products presented in Figure 8. 1; (B) considering only products generated in steps A-D (excluding condensation reactions); oxime (●), amine (■), ketone (▲), DCA (▽) and CCA (△).

8.4.2.2 Catalytic Response over Au/Al_2O_3

The temporal dependence of NC fractional conversion (x) and product selectivity (S) is presented in **Figure 8.4(A)**. NC conversion exhibited an initial increase (first 3 h on-stream) before attaining steady state (and full carbon balance) with the formation of oxime as the principal product (S > 75%) and amine and ketone as by-products. Steady state conversion and the associated selectivity are used in this study as the basis for comparison of catalyst performance. The product distribution presented in **Figure 8.4(A)** deviates from the thermodynamic prediction (**Figure 8.3(A)**) where DCA predominates. Moreover, reaction over Au/Al_2O_3 resulted in partial NC conversion in contrast to complete conversion under thermodynamic control. We are not aware of any report in the literature that has examined thermodynamic limitations and has established explicit catalytic control. The results demonstrate that the catalytic action of Au/Al_2O_3 in gas phase continuous operation is far from the thermodynamic limits and can achieve high selectivity to the target oxime.

In order to investigate the intrinsic catalytic response, it is necessary to establish reaction conditions wherein transport constraints are minimised. The effect of gas hourly space velocity (*GHSV* between $2–6\times10^4$ h^{-1}) is shown in **Figure 8.4(B)**, where conversion invariance is indicative of minimal external mass and/or heat transport contributions. The *GHSV* was set at 2×10^4 h^{-1} for further testing, where conversion showed a proportional increase with increasing catalyst mass **Figure 8.4(C)**, demonstrating negligible interphase diffusional limitations. We have previously applied a pseudo-first order kinetic treatment for catalytic nitroarene hydrogenation systems [42] where, in excess H_2, the reactor/kinetic expression is given by

$$\ln\left[\frac{1}{(1-x)}\right] = k\left(\frac{n}{F}\right) \tag{8.7}$$

and the ratio n/F (molar Au to inlet hourly NC feed rate) has the physical significance of contact time. The linear relationships (between $\ln(1–x)^{-1}$ and n/F), shown in **Figure 8.4(D)** for two reaction temperatures (353 and 473 K), confirm applicability of pseudo-first order kinetics. The temperature dependence of product selectivity at a fixed NC conversion (x = 0.1) can be assessed from the entries in **Table 8.2**.

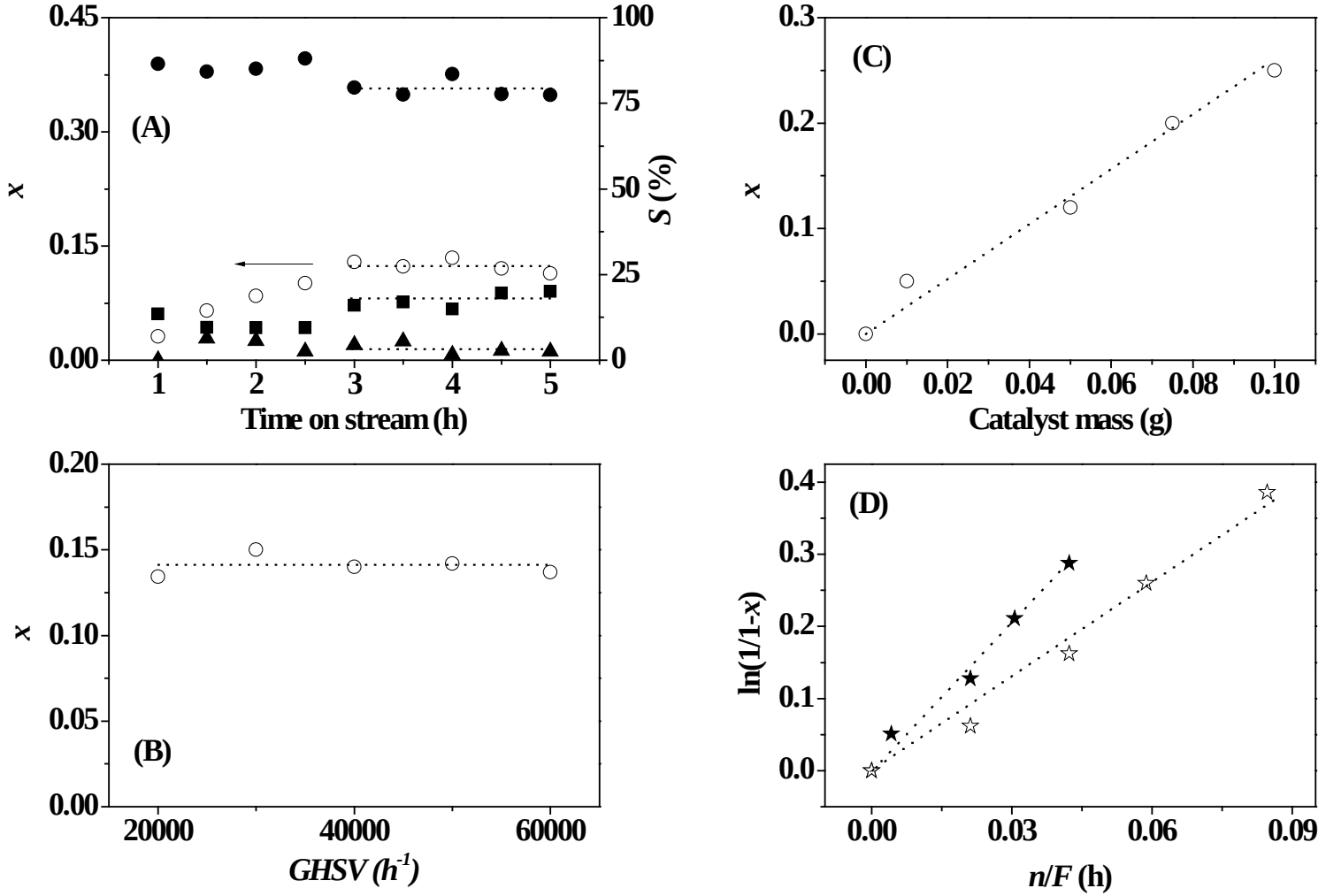

Figure 8.4: NC hydrogenation over Au/Al_2O_3 (n/F = 4.7×10^{-3}–8.5×10^{-2} h): (A) Temporal variation of NC conversion (x, ○) and selectivity (S) to oxime (●), amine (■) and ketone (▲) at 353 K; (B) Effect of gas hourly space velocity ($GHSV$) on NC conversion (x) at 353 K; (C): Variation of NC conversion (x) with increasing mass of catalyst at 473 K; (D): Applicability of pseudo-first order kinetics for reaction at 353 K (☆) and 473 K (★).

Table 8.2: Rate constant (*k*) and selectivity (at *x* = 0.1) for the reaction of nitrocyclohexane (NC) and cyclohexanone oxime over Au/Al_2O_3 at 353 and 473 K.

Reactant	353 K		473 K	
	k (h^{-1})	S (%)	k (h^{-1})	S (%)
Nitrocyclohexane	4.6	Oxime (80) Amine (18) Ketone (2)	7.0	Oxime (4) Amine (15) Ketone (67) DCA (14)
Cyclohexanone oxime	2.6	Amine (100)[a]	25	Ketone (83) Amine (11) DCA (6)

[a] $x = 0.03$ due to the low activity at 353 K

An increase in temperature elevated NC consumption rate, favouring ketone formation. In the parallel/sequential hydrogenation of NC, the participation of water (dissociated as OH and H) is required for the production of ketone *via* path D (**Figure 8.1**). Moreover, condensation was a feature of reaction at 473 K with the generation of DCA. The oxime selectivity achieved at 353 K is close to that reported (83%) for Au/Al_2O_3 [7] in batch liquid phase reaction. In order to gain some insight into reaction mechanism, the dependence of selectivity on NC conversion was examined and the results are presented in Figure 8.5. At 353 K, the oxime was the primary product where selectivity exceeded 80% at low conversion ($x < 0.1$), with secondary amine formation, trace ketone and no detectable condensation products (CCA or DCA). At this temperature, the reaction pathway was limited to hydrogenation steps (A-C, **Figure 8.1**). The observed shift in preferential amine production at the expense of oxime with increasing NC conversion ($x > 0.1$) is consistent with a ~~NC~~oxime→amine stepwise mechanism. In liquid phase reaction, the high selectivity (~ 80%) over Au/Al_2O_3 can be achieved at complete conversion, where however, pressurised system with H_2 (to a minimum of $P_{H2} = 0.6$ MPa) was essential and no reaction takes place at normal pressure [7]. The published data refer solely to liquid phase reaction where the highest temperature considered was 413 K [8]. Shimizu *et al*. have reported that 373 K was an optimum temperature for the transformation of NC to oxime [7]. In this study, reaction at 473 K (Figure 8.5(B))

generated ketone as principal product with a decline in selectivity at higher conversion in favour of amine and DCA; oxime formation was limited (S < 6%). This indicates that steps C and D have different temperature dependences and the latter was promoted to a far greater extent in moving from 353 to 473 K. Serna *et al*. noted that H_2 is required for the formation of cyclic ketone and direct hydrolysis of cyclohexanone by water was limited over Pt/TiO_2 [8]. Generation of the ketone favoured subsequent condensation with DCA formation. CCA was not detected in the product stream, suggesting a facile conversion (hydrogenation) to DCA.

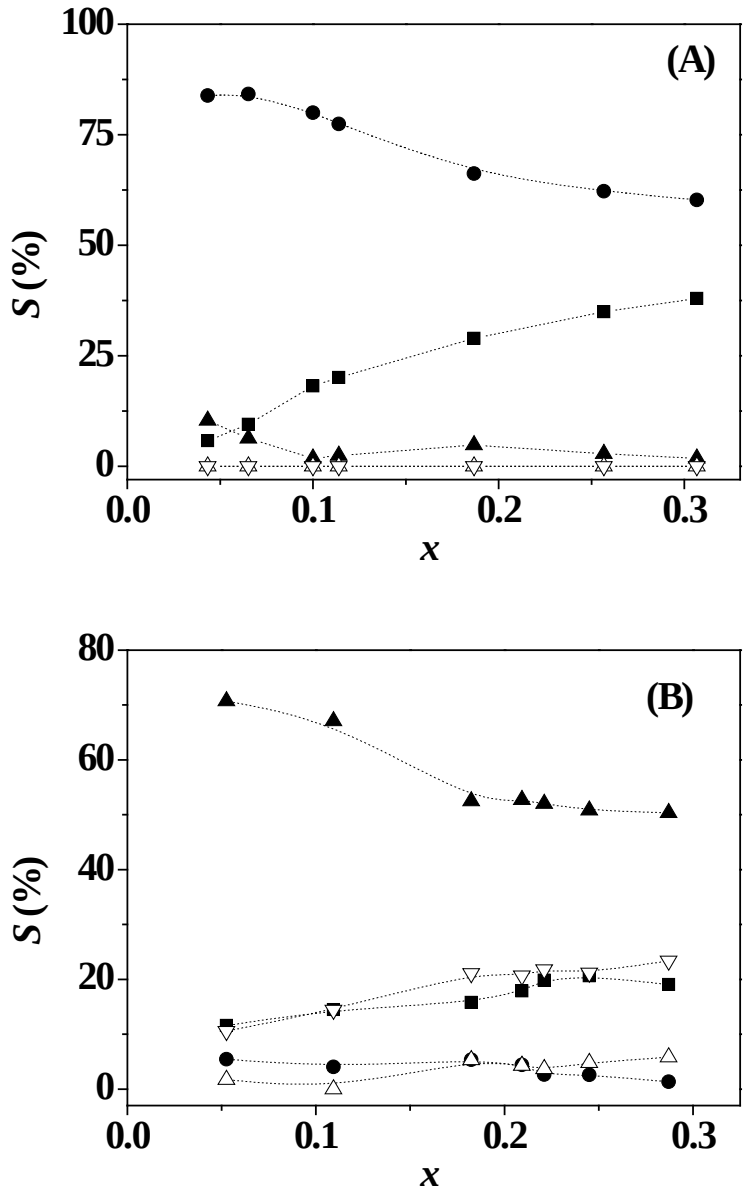

Figure 8.5: Variation of selectivity (S) with NC conversion (x) over Au/Al_2O_3 at (A) 353 K, n/F = 4.7–9.3×10^{-2} h and (B) 473 K, n/F = 0.5–4.7×10^{-2} h: oxime (●), amine (■), ketone (▲), DCA (▽), CCA (△).

Taking cyclohexanone oxime as reactant, reaction rate and product selectivity can be compared in **Table 8.2**. At 353 K, oxime consumption rate was lower than that of NC, which can account for the high selectivity to oxime obtained from the NC feed. The significant increase in oxime consumption rate relative to NC at 473 K is also consistent with the observed decrease in selectivity at the higher temperature. Moreover, product selectivity from the oxime coincided with that obtained from NC, *i.e.* preferential amine formation at 353 K with a shift at 473 K to ketone and secondary DCA production. The ketone can be formed by direct hydrolysis of the oxime [43,44] and/or hydrolysis of cyclohexylimine formed from oxime reduction [45,46]. Serna *et al.* [8], conducting reactions in the absence of hydrogen over Pt/TiO_2, demonstrated that ketone production involves cyclohexylimine as an intermediate. The relative surface concentration of oxime (to form the imine intermediate), reactive hydrogen and –OH (dissociated form of water) must influence product selectivity, as illustrated in **Figure 8.6**. Surface reactive –OH can result from reduction of NC and/or oxime (**Figure 8.1**). The surface hydrogen can react with imine to give the amine product (path (I), **Figure 8.6**) or with –OH to form water (path II), which can desorb from the catalyst, whereas ketone formation requires the combination of surface imine with –OH (path III). To test this hypothesis, a series of reactions at different hydrogen partial pressures (P_{H2}) were conducted at the same *n/F* and a temperature (353 K) at which there was no detectable condensation product. The decrease in hydrogen content in the feed can serve to limit surface hydrogen which should, in turn, inhibit paths I and II and lead to an increase in ketone selectivity. Lower P_{H2} delivered lower NC fractional conversion, as shown in **Figure 8.7**, with a critical switch from oxime to ketone as preferred product where $P_{H2} < 0.2$ atm. The highest selectivity (95%) to oxime was recorded at $P_{H2} = 0.33$ atm. Moreover, formation of amine was only observed at higher P_{H2} (> 0.7 atm) and is consistent with a NC →oxime→amine stepwise mechanism. The variation of product selectivity with P_{H2} demonstrates the critical role of interplay between surface imine, hydrogen and –OH.

8.4.3 Role of the Oxide Support

It is known that support properties influence Au catalytic performance in

hydrogenation applications [25,47]. For instance, Boronat *et al*. observed that Au/TiO_2 and Au/Fe_2O_3 outperformed Au/C and Au/SiO_2 in the hydrogenation of 3-nitrostyrene to 3-aminostyrene [30]. We have also demonstrated previously that the Au carrier can control selectivity in nitroarene hydrogenation [48]. Following on from that work, we have examined the catalytic action of Au on TiO_2, CeO_2 and ZrO_2.

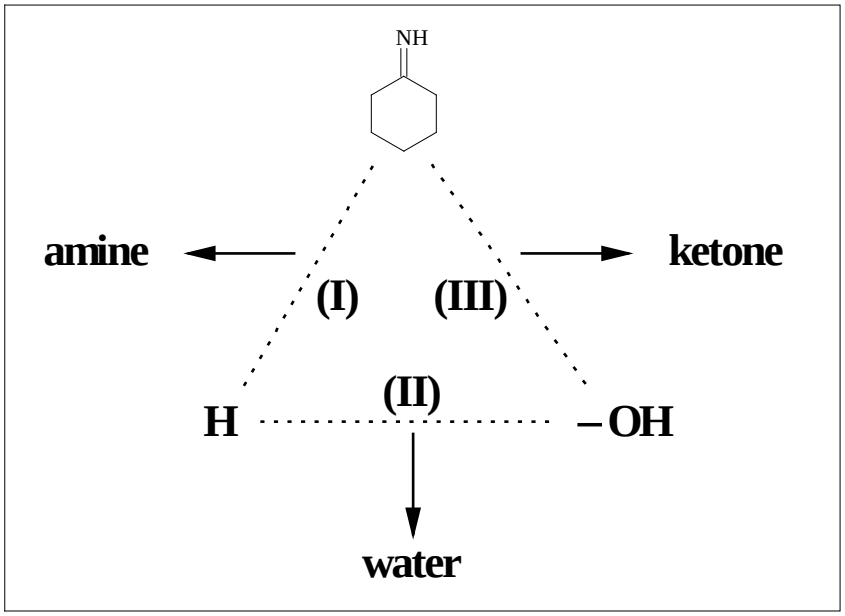

Figure 8.6: Scheme showing possible interaction between imine, surface reactive hydrogen (H) and –OH (dissociated form of water).

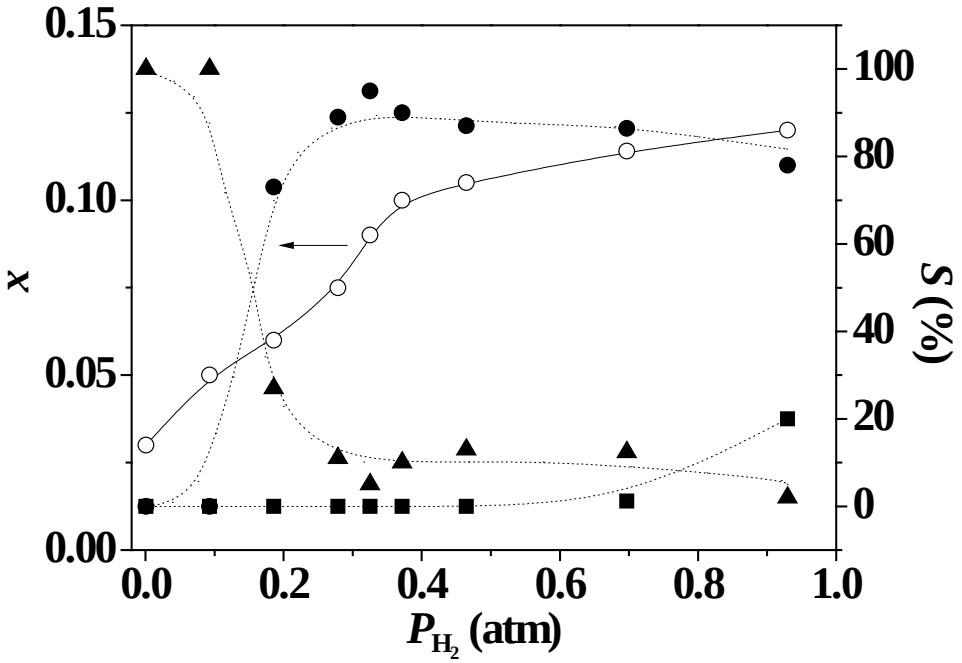

Figure 8.7: Effect of hydrogen partial pressure on NC conversion (*x*, ○) and product selectivity (*S*) at 353 K and $n/F = 4.7\times10^{-2}$ h; oxime (●), amine (■), ketone (▲).

8.4.3.1 Catalyst Characterisation

The BET surface area of the supports and activated (post-TPR) Au catalysts considered in this study are recorded in **Table 8.1**. In each case, the area was lower after Au inclusion, suggesting partial pore blockage; total pore volume correlated with BET areas. The TPR profiles for Au/TiO_2, Au/CeO_2 and Au/ZrO_2 are given in **Figure 8.8(A)** and associated H_2 consumption and T_{max} values recorded in **Table 8.1**. TPR treatment (up to 473 K) for each support (TiO_2, CeO_2 and ZrO_2) did not result in any detectable H_2 consumption, which is consistent with previous reports [19,48,49]. TPR of Au/ZrO_2 exhibited a T_{max} close to that recorded for Au/Al_2O_3 and comparable with the literature (483-503 K [50]) where the H_2 consumed can be attributed to a reduction of Au^{3+} to Au^0. Activation of Au/CeO_2 (T_{max} = 420 K close to 423 K given in [48]) and particularly Au/TiO_2 (T_{max} = 365 K close to 373-434 K given in [51,52]) required lower temperatures. It has been reported that the reducibility of supported Au prepared by deposition-precipitation decreases in the order Au/TiO_2 > Au/CeO_2 > Au/Al_2O_3 [53], which, on the basis of the measured T_{max}, matches the trend observed in this work. Hydrogen consumption during TPR of Au/TiO_2 and Au/CeO_2 exceeded that required for the reduction of the metal precursor, suggesting partial reduction of the supports. Campo *et al.* [54] established that the inclusion of Au enhanced reducibility of CeO_2, resulting in a shift in the reduction peak from 703 to 379 K with evidence for a similar effect in the case of Au/TiO_2 [48]. Partial reduction of oxide supports can generate oxygen vacancies, as has been proposed for Au/TiO_2 [51,55] and Au/CeO_2 [56,57]. From a consideration of the "actual" relative to "theoretical" H_2 consumption values recorded in **Table 8.1**, the degree of CeO_2 reduction is greater than that of TiO_2, which agrees with DFT analysis [58] and is also demonstrated by the higher oxygen uptake post-TPR (**Table 8.1**). This is significant as oxygen vacancies created during TPR can influence hydrogenation performance [34,59].

The total surface hydrogen was assessed by H_2-TPD analysis, where hydrogen released decreased in the order: Au/Al_2O_3 >> Au/ZrO_2 > Au/CeO_2 > Au/TiO_2. The greater H_2 desorption from Au/Al_2O_3 may result from the higher chemisorption capacity (**Table 8.1**), consistent with the proposal by Shimizu *et al.* [32] of facilitated dissociation

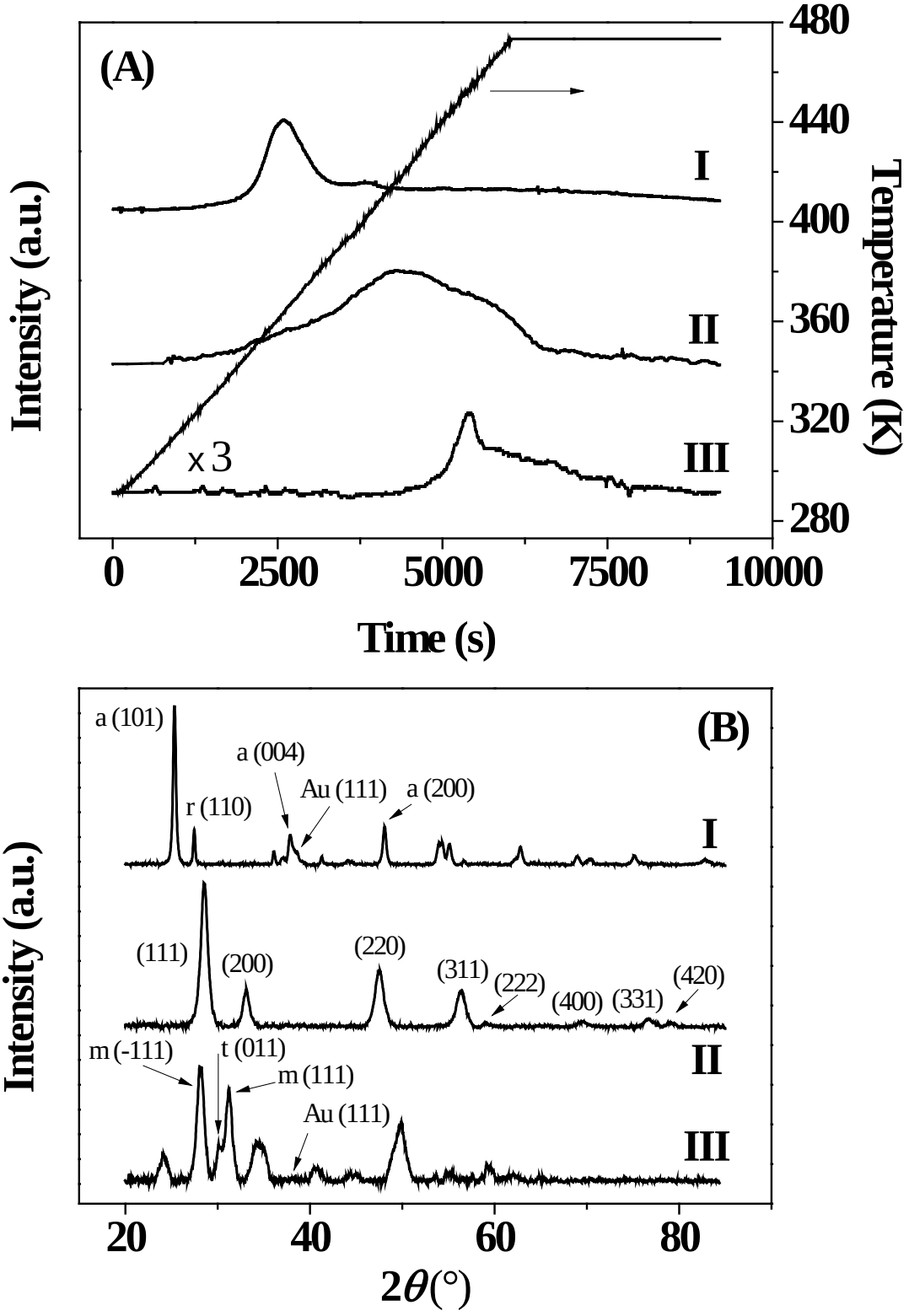

Figure 8.8: TPR profiles (A) and XRD patterns (B) for (I) Au/TiO_2, (II) Au/CeO_2 and (III) Au/ZrO_2: *m* denotes monoclinic phase; *t* denotes tetragonal phase; *a* denotes anatase phase; *r* denotes rutile phase.

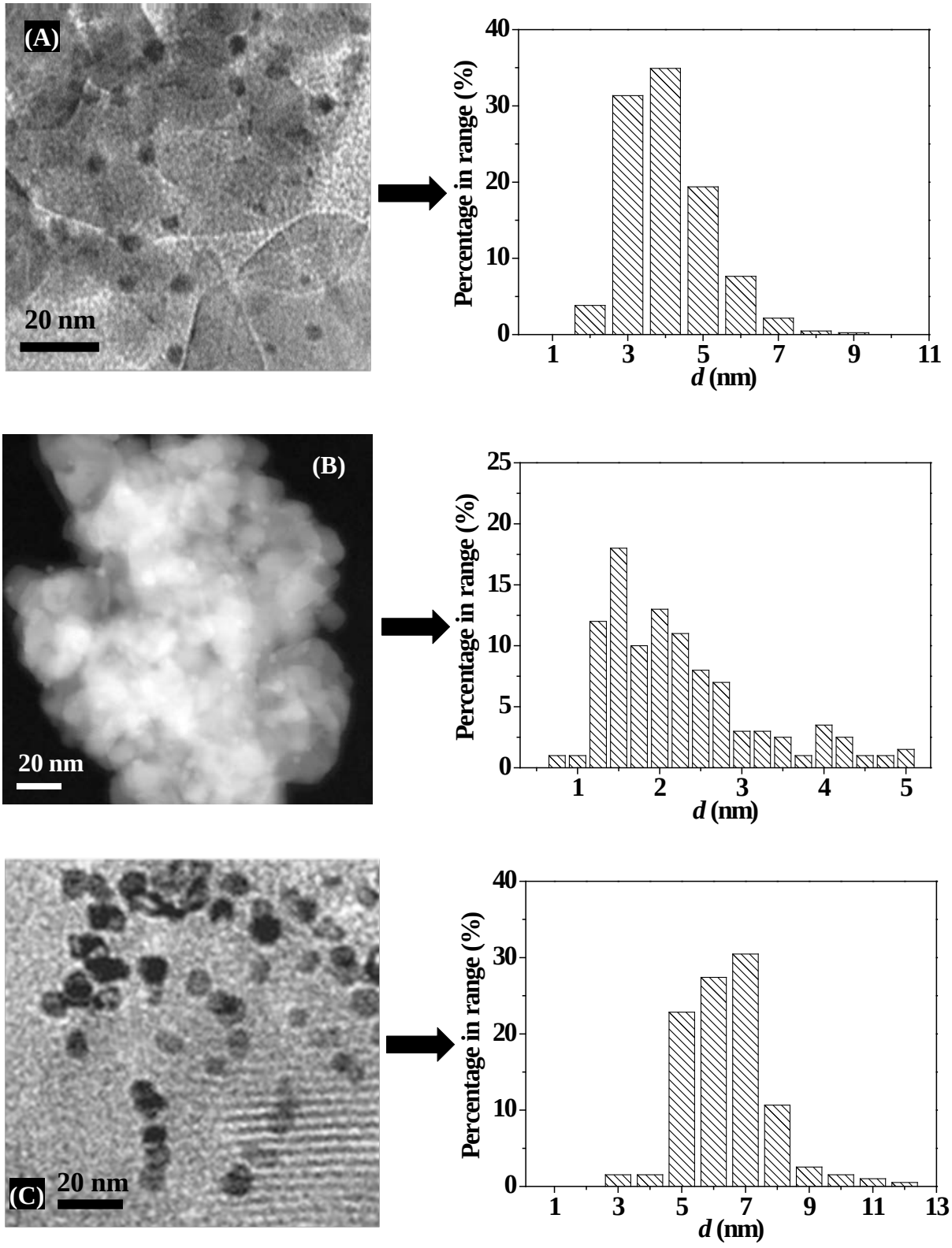

Figure 8.9: Representative STEM/TEM images of (A) Au/TiO_2, (B) Au/CeO_2 and (C) Au/ZrO_2 with associated Au particle size (*d*) distributions.

(to H^+/H^-) at the Au-Al_2O_3 interface. Enhanced surface hydrogen on Al_2O_3 can also be linked to the higher BET area, where surface oxygen groups (terminal hydroxyls) [60,61]

and Lewis acid sites [7,62] can act to accommodate hydrogen spillover from Au sites. The lower value for Au/CeO_2 relative to Au/ZrO_2 with similar surface area can be ascribed to H_2 consumption in CeO_2 reduction. The XRD peak assignments for Au/TiO_2 (**Figure 8.8(B)**, 2θ = 25.38°, 37.88° and 48.18°) match the (004), (101) and (200) planes of tetragonal anatase (JCPDS-ICDD 21-1272). The peak at 27.48° is due to tetragonal (110) rutile (JCPDS-ICDD 21-1276) with an anatase: rutile ≈ 5:1 that is characteristic of Degussa P25 for thermal treatment up to 923 K [63]. A weak signal at 38.1° can be attributed to Au (111) but the peak overlaps with an anatase signal and does not allow a calculation of Au size by standard line broadening analysis. The XRD pattern for Au/CeO_2 presents eight peaks in the range 2θ = 28.5°-79.0° that can be associated with the main planes of CeO_2 (JCPDS-ICDD 43-1002) where there was no observable peak(s) due to the supported Au phase. Analysis of Au/ZrO_2 presented the three characteristic peaks for monoclinic ((-111), (111)) and tetragonal (011) phases based on the JCPDS references (37-1484 and 50-1089) with again a weak signal (at 38.1°) due to Au. STEM/TEM measurements (see representative images in **Figure 8.9**) have revealed Au particles at the nano-scale (1-12 nm). Particle size distribution is illustrated by the histograms included in **Figure 8.9**; mean Au diameters (d_{TEM}) are given in **Table 8.1**. Gold on CeO_2 is characterised by a narrower distribution of smaller Au particles suggesting strong Au-CeO_2 interaction, possibly linked to support oxygen vacancies that result in a smaller mean Au size. There is evidence in the literature that vacancies can stabilise transition metal nano-particles and inhibit sintering [64]. Strong Au interaction with CeO_2 vacancies has been proposed to limit CO uptake [65]. Indeed H_2 chemisorption on Au/CeO_2 was measurably lower than uptake on the other catalysts (**Table 8.1**). Suppressed chemisorption is a feature of CeO_2 supported noble metals (Rh, Pd, Pt) [66] and Au on $Ce_xZr_{1-x}O_2$ [34], where the latter has been linked to low catalytic activity in $–NO_2$ hydrogenation.

8.4.3.2 Catalytic Performance

A comparison of support effect(s) was made at a common fractional NC conversion (x = 0.1) for reaction at 353 K. The resultant turnover frequencies (*TOF*, normalised with respect to Au dispersion, *i.e.* per Au surface atom) and product selectivities are given in

Table 8.3. With the exception of Au/CeO_2, *TOF* increased with decreasing mean Au size (from 7.0 to 4.3 nm). A similar response (over the 3-9 nm range) was observed for nitroarene hydrogenation [48,67]. Indeed, a dramatic dependence of activity on Au size has been reported for liquid phase NC hydrogenation where an increase in size (from 2.5 to 6 nm) resulted in a drop in conversion from 100 to 4.5% [7]. The available literature on hydrogenation over supported Au suggests that activity is limited by hydrogen activation, which is dependent on Au coordination [68], where smaller Au particles exhibit a greater preponderance of corner and edge sites that facilitate H_2 dissociative adsorption [14,38]. This has also been established by Corma *et al.* through theoretical DF calculations [69]. However, Au/CeO_2 with the smallest mean Au size (3.0 nm) deviates from this trend and delivered the lowest *TOF*. In previous work [48,67], we also recorded a significant drop in hydrogenation rate for Au particles ≤ 2 nm and attributed this to quantum size effects. For Au particles in the 1-3 nm size range, it has been reported that the electronic properties vary considerably with a switch from metal to semiconductor characteristics [70]. Claus and co-workers [71], studying the gas phase hydrogenation of acrolein over Au/TiO_2, linked an order of magnitude decrease in activity (400→ 41 mmol g_{Au}^{-1} s^{-1}) with decreasing Au particle size (down to 1.4 nm) to a transition from metallic to *non*-metallic character for small Au particles. Stronger metal-support interaction, via support oxygen vacancies can inhibit reactant activation/chemisorption and impact on catalysis [66]. Our chemisorption measurements indicate suppressed H_2 uptake on Au/CeO_2 under reaction conditions (**Table 8.1**), which must be linked to lower observed activity. There is no available *TOF*s from Au catalysts for comparison since Shimizu *et al*. have only provided conversion values [7]. However, the activity of Na doped Pt/TiO_2 (*TOF*: ~ 300 h^{-1} at P_{H2} = 4 bar and 383 K [8]) is more active than the Au samples considered in this work.

The hydrogenation selectivity results given in **Table 8.3** suggest three catalyst groupings: (i) Au/Al_2O_3 generated cyclohexanone oxime as the major product; (ii) Au/CeO_2 promoted near exclusive production of cyclohexanone; (iii) Au/TiO_2 and Au/ZrO_2 delivered cyclohexylamine and cyclohexanone as principal products (in varying proportions). Our results are consistent with earlier liquid phase work where Au/Al_2O_3 exhibited appreciably greater selectivity (83%) to the oxime when compared with

Au/TiO_2 (10%) [7]. As discussed in *section 8.4.2.2*, preferential oxime production over Au/Al_2O_3 can be attributed to a higher rate for step A relative to B (**Figure 8.1**) where the available surface hydrogen facilities consumption of reactive –OH (to form water that desorbs, step II in **Figure 8.6**). In the case of Au/CeO_2, metal/support interaction(s) limit(s) hydrogen activation and must inhibit steps I and II with the predominance of step III (**Figure 8.6**) favouring ketone formation. Both Au/TiO_2 and Au/ZrO_2 are essentially non-selective in terms of the oxime with contributions from the three steps in our proposed scheme (**Figure 8.6**). Under these reaction conditions, condensation (step E in **Figure 8.1**) only proceeds over Au/TiO_2. This is in line with the study of Shimizu *et al.* where the production of DCA and CCA was a feature of reaction over Au/TiO_2 at all conversions [7]. The contribution of Au/TiO_2 to successive condensation reactions (releasing water) has been established previously in reactions using ethanol as a model reactant [72]. Condensation over Au/TiO_2 can be attributed to the combined action of surface hydrogen and oxygen vacancies, where the former ensures amine production and the latter facilitates reaction between amine and ketone.

Table 8.3: Turnover frequency (*TOF*) and selectivity (at $x = 0.1$) for the reaction of nitrocyclohexane (NC) over the supported Au catalysts at 353 K.

Catalyst	TOF^a (h^{-1})	Selectivity (%)				
		Oxime	Amine	Ketone	CCA	DCA
Au/Al_2O_3	16.4	80	18	2	0	0
Au/TiO_2	9.1	6	34	40	0	20
Au/CeO_2	1.6	0	2	98	0	0
Au/ZrO_2	6.1	18	28	54	0	0

[a]calculated using Au dispersion obtained from TEM analysis

8.5 Conclusions

Activity and selectivity in gas phase NC hydrogenation over supported Au shows a dependence on the oxide (Al_2O_3, TiO_2, CeO_2 and ZrO_2) carrier. Thermodynamic analysis has revealed complete NC conversion at 353-473 K with dicyclohexylamine (selectivity > 77%) as the predominant product. Cyclohexylamine is generated with increasing selectivity at higher temperatures under thermodynamic control where cyclohexanone

oxime or cyclohexanone is not formed. Activation by TPR (to 473 K) resulted in precursor reduction ($Au^{3+} \rightarrow Au^{0}$) and excess H_2 consumption in the case of Au/TiO_2 and Au/CeO_2 that can be attributed to partial support reduction, which was measurably greater in the case of CeO_2. Hydrogen release by TPD exceeded that measured in pulse chemisorption, suggesting the occurrence of spillover hydrogen (during TPR). Mean Au particle size decreased in the order: Au/ZrO_2 (7.0 nm) > Au/TiO_2 (4.7 nm) > Au/Al_2O_3 (4.3 nm) > (Au/CeO_2) (3.0 nm). NC *TOF* was higher for smaller Au particles with the exception of Au/CeO_2. Gold on CeO_2 is characterised by a narrower distribution of smaller particles (1-5 nm) resulting from stronger support interaction via oxygen vacancies that suppresses H_2 chemisorption and lowers activity. Reaction over Au/Al_2O_3 is selective to the target oxime (maximum selectivity = 95%) at 353 K where an increase in temperature (to 473 K) elevates rate, favouring ketone formation with subsequent condensation. Varying H_2 partial pressure has demonstrated critical interplay between surface imine, H and –OH in determining selectivity. Selectivity to oxime is sensitive to surface hydrogen where amine and ketone formation are favoured at high and low coverage, respectively. Reaction over Au/CeO_2 generated cyclohexanone as the predominant product due to limited surface hydrogen whereas Au/TiO_2 and Au/ZrO_2 promoted both ketone and amine formation.

8.6 References

[8.1] K. Takagi, T. Ishida, *Oxidation of cyclohexane*, US Patent 3644526, (1972)

[8.2] H.X. Yuan, Q.H. Xia, H.J. Zhan, X.H. Lu, K.X. Su, *Catalytic oxidation of cyclohexane to cyclohexanone and cyclohexanol by oxygen in a solvent-free system over metal-containing ZSM-5 catalysts*, Appl. Catal. A: Gen., **304**, 178-184 (2006)

[8.3] Nanjing Delifei Technology Consulting Co. Ltd., *Device for recovering heat of oxidant solution in process of preparing cyclohexanone by oxidizing cyclohexane*, CN Patent 202170313, (2012)

[8.4] K. Weissermel, H.-J. Arpe, *Industrial Organic Chemistry 4th Edition*, Wiley-VCH, Weinheim, 2003

[8.5] H.-G. Liao, Y.-J. Xiao, H.-K. Zhang, P.-L. Liu, K.-Y. You, C. Wei, H.A. Luo, *Hydrogenation of nitrocyclohexane to cyclohexanone oxime over Pd/CNT catalyst*

under mild conditions, Catal. Commun., **19**, 80-84 (2012)

[8.6] S.K. Klitgaard, K. Egeblad, U.V. Mentzel, A.G. Popov, T. Jensen, E. Taarning, I.S. Nielsen, C.H. Christensen, *Oxidations of amines with molecular oxygen using bifunctional gold-titania catalysts*, Green Chem., **10**, 419-423 (2008)

[8.7] K.-I. Shimizu, T. Yamamoto, Y. Tai, A. Satsuma, *Selective hydrogenation of nitrocyclohexane to cyclohexanone oxime by alumina-supported gold cluster catalysts*, J. Mol. Catal. A: Chem., **345**, 54-59 (2011)

[8.8] P. Serna, M. Lopez-Haro, J.J. Calvino, A. Corma, *Selective hydrogenation of nitrocyclohexane to cyclohexanone oxime with H_2 on decorated Pt nanoparticles*, J. Catal., **263**, 328-334 (2009)

[8.9] DuPont, *Improvements in the production of oximes*, GB Patent 857902, (1961)

[8.10] R.E. Foster, A.F. Kirby, *Preparation of ketoximes*, GB Patent 860340, (1961)

[8.11] J.F. Knifton, *Homogeneous catalyzed reduction of nitrocompounds: II. Hydrogenation to oximes*, J. Catal., **33**, 289-298 (1974)

[8.12] A. Corma, P. Serna, *Chemoselective hydrogenation of nitro compounds with supported gold catalysts*, Science, **313**, 332-334 (2006)

[8.13] J.F. Knifton, *Homogeneous catalyzed reduction of nitro compounds. I. Synthesis of oximes*, J. Org. Chem., **38**, 3296-3301 (1973)

[8.14] G.C. Bond, *Chemisorption and reactions of small molecules on small gold particles*, Molecules, **17**, 1716-1743 (2012)

[8.15] N. Perret, X. Wang, L. Delannoy, C. Potvin, C. Louis, M.A. Keane, *Enhanced selective nitroarene hydrogenation over Au supported on β-Mo_2C and β-Mo_2C/Al_2O_3*, J. Catal., **286**, 172-183 (2012)

[8.16] M. Okumura, T. Akita, M. Haruta, *Hydrogenation of 1,3-butadiene and of crotonaldehyde over highly dispersed Au catalysts*, Catal. Today, **74**, 265-269 (2002)

[8.17] N. Perret, F. Cardenas-Lizana, M.A. Keane, *Selective hydrogenation of benzaldehyde to benzyl alcohol over Au/Al_2O_3*, Catal. Commun., **16**, 159-164 (2011)

[8.18] M.S. Ide, B. Hao, M. Neurock, R.J. Davis, *Mechanistic Insights on the Hydrogenation of α,β-unsaturated ketones and aldehydes to unsaturated alcohols*

over metal catalysts, ACS Catalysis, **2**, 671-683 (2012)

[8.19] X. Zhang, H. Shi, B.-Q. Xu, *Vital roles of hydroxyl groups and gold oxidation states in Au/ZrO_2 catalysts for 1,3-butadiene hydrogenation*, J. Catal., **279**, 75-87 (2011)

[8.20] P. Liu, H. Zhang, S. Liu, Z. Yao, F. Hao, K. You, H.A. Luo, *Nitrocyclohexane hydrogenation to ε-caprolactam over Pd/C and 2,4,6-trichloro-[1,3,5]-triazine in N,N-dimethylformamide*, React. Kinet. Mech. Catal., **107**, 383-391 (2012)

[8.21] C. Jiménez-González, P. Poechlauer, Q.B. Broxterman, B.-S. Yang, D. am Ende, J. Baird, C. Bertsch, R.E. Hannah, P. Dell'Orco, H. Noorman, S. Yee, R. Reintjens, A. Wells, V. Massonneau, J. Manley, *Key green engineering research areas for sustainable manufacturing: a perspective from pharmaceutical and fine Chemicals manufacturers*, Org. Process. Res. Dev., **15**, 900-911 (2011)

[8.22] X. Wang, S. Li, H. Wang, B. Liu, X. Ma, *Thermodynamic analysis of glycerin steam reforming*, Energy Fuels, **22**, 4285-4291 (2008)

[8.23] H. Wang, X. Wang, M. Li, S. Li, S. Wang, X. Ma, *Thermodynamic analysis of hydrogen production from glycerol autothermal reforming*, Int. J. Hydrogen Energy, **34**, 5683-5690 (2009)

[8.24] M. Hazewinkel, *Encyclopaedia of Mathematics*, Springer-Verlag, Berlin, 2002

[8.25] G.C. Bond, C. Louis, D.T. Thompson, *Catalysis by Gold*, Imperial College Press, London, 2006

[8.26] M.A. Keane, *Gas phase hydrogenation/hydrogenolysis of benzaldehyde and o-tolualdehyde over Ni/SiO_2*, J. Mol. Catal. A: Chem., **118**, 261-269 (1997)

[8.27] G. Tavoularis, M.A. Keane, *The gas phase hydrodechlorination of chlorobenzene over nickel/silica*, J. Chem. Technol. Biotechnol., **74**, 60-70 (1999)

[8.28] A. Corma, P. Serna, *Preparation of substituted anilines from nitro compounds by using supported gold catalysts*, Nature Protoc., **1**, 2590-2595 (2006)

[8.29] A. Corma, P. Serna, H. García, *Gold catalysts open a new general chemoselective route to synthesize oximes by hydrogenation of α,β-unsaturated nitrocompounds with H_2*, J. Am. Chem. Soc., **129**, 6358-6359 (2007)

[8.30] M. Boronat, P. Concepción, A. Corma, S. González, F. Illas, P. Serna, *A molecular mechanism for the chemoselective hydrogenation of substituted nitroaromatics with*

nanoparticles of gold on TiO_2 catalysts: a cooperative effect between gold and the support, J. Am. Chem. Soc., **129**, 16230-16237 (2007)

[8.31] M. Pietrowski, M. Wojciechowska, *The origin of increased chemoselectivity of platinum supported on magnesium fluoride in the hydrogenation of chloronitrobenzene*, Catal. Today, **169**, 217-222 (2011)

[8.32] K.-I. Shimizu, Y. Miyamoto, T. Kawasaki, T. Tanji, Y. Tai, A. Satsuma, *Chemoselective Hydrogenation of nitroaromatics by supported gold catalysts: mechanistic reasons of size- and support-dependent activity and selectivity*, J. Phys. Chem. C, **113**, 17803-17810 (2009)

[8.33] X. Wang, N. Perret, M.A. Keane, *The role of hydrogen partial pressure in the gas phase hydrogenation of p-chloronitrobenzene over alumina supported Au and Pd: a consideration of reaction thermodynamics and kinetics*, Chem. Eng. J., **210**, 103-113 (2012)

[8.34] X. Wang, N. Perret, J.J. Delgado, G. Blanco, X. Chen, C.M. Olmos, S. Bernal, M.A. Keane, *Reducible support effects in the gas phase hydrogenation of p-chloronitrobenzene over gold*, J. Phys. Chem. C, **117**, 994-1005 (2013)

[8.35] A. Gluhoi, X. Tang, P. Marginean, B. Nieuwenhuys, *Characterization and catalytic activity of unpromoted and alkali (earth)-promoted Au/Al_2O_3 catalysts for low-temperature CO oxidation*, Top. Catal., **39**, 101-110 (2006)

[8.36] E. Bus, J.A. van Bokhoven, *Hydrogen chemisorption on supported platinum, gold, and platinum-gold-alloy catalysts*, Phys. Chem. Chem. Phys., **9**, 2894-2902 (2007)

[8.37] C. Kartusch, J.A. van Bokhoven, *Hydrogenation over gold catalysts: The interaction of gold with hydrogen*, Gold Bull., **42**, 343-348 (2009)

[8.38] E. Bus, J.T. Miller, J.A. van Bokhoven, *Hydrogen chemisorption on Al_2O_3-supported gold catalysts*, J. Phys. Chem. B, **109**, 14581-14587 (2005)

[8.39] W.C. Conner, J.L. Falconer, *Spillover in heterogeneous catalysis*, Chem. Rev., **95**, 759-788 (1995)

[8.40] S. Díaz-Moreno, D.C. Koningsberger, A. Muñoz-Páez, *The "invisible" metal particles in catalysis*, Nucl. Instrum. Methods Phys. Res. B, **133** 15-23 (1997)

[8.41] J. Radnik, C. Mohr, P. Claus, *On the origin of binding energy shifts of core levels of supported gold nanoparticles and dependence of pretreatment and material*

synthesis, Phys. Chem. Chem. Phys., **5**, 172-177 (2003)

[8.42] F. Cardenas-Lizana, Z.M. de Pedro, S. Gomez-Quero, M.A. Keane, *Gas phase hydrogenation of nitroarenes: A comparison of the catalytic action of titania supported gold and silver*, J. Mol. Catal. A: Chem., **326**, 48-54 (2010)

[8.43] M.A. Camblor, A. Corma, H. Garcia, V. Semmer-Herledan, S. Valencia, *Active sites for the liquid-phase beckmann rearrangement of cyclohexanone, acetophenone and cyclododecanone oximes, catalyzed by beta zeolites*, J. Catal., **177**, 267-272 (1998)

[8.44] C. Ngamcharussrivichai, P. Wu, T. Tatsumi, *Liquid-phase Beckmann rearrangement of cyclohexanone oxime over mesoporous molecular sieve catalysts*, J. Catal., **227**, 448-458 (2004)

[8.45] P.N. Rylander, *Catalytic Hydrogenation in Organic Synthesis*, Academic Press, New York, 1979

[8.46] D.P. Curran, J.F. Brill, D.M. Rakiewicz, *A mild reductive conversion of oximes to ketones*, J. Org. Chem., **49**, 1654-1656 (1984)

[8.47] F. Cárdenas-Lizana, M. Keane, *The development of gold catalysts for use in hydrogenation reactions*, J. Mater. Sci., **48**, 543-564 (2013)

[8.48] F. Cardenas-Lizana, S. Gomez-Quero, N. Perret, M.A. Keane, *Gold catalysis at the gas-solid interface: role of the support in determining activity and selectivity in the hydrogenation of m-dinitrobenzene*, Catal. Sci. Tech., **1**, 652-661 (2011)

[8.49] S. Scire, S. Minico, C. Crisafulli, C. Satriano, A. Pistone, *Catalytic combustion of volatile organic compounds on gold/cerium oxide catalysts*, Appl. Catal. B: Environ., **40**, 43-49 (2003)

[8.50] X. Zhang, H. Shi, B.-Q. Xu, *Catalysis by gold: isolated surface Au^{3+} ions are active sites for selective hydrogenation of 1,3-butadiene over Au/ZrO_2 catalysts*, Angew. Chem. Int. Ed., **44**, 7132-7135 (2005)

[8.51] F. Cárdenas-Lizana, S. Gómez-Quero, M.A. Keane, *Exclusive production of chloroaniline from chloronitrobenzene over Au/TiO_2 and Au/Al_2O_3*, ChemSusChem, **1**, 215-221 (2008)

[8.52] V. Idakiev, T. Tabakova, Z.Y. Yuan, B.L. Su, *Gold catalysts supported on mesoporous titania for low-temperature water-gas shift reaction*, Appl. Catal. A:

Gen., **270**, 135-141 (2004)

[8.53] L. Delannoy, N. Weiher, N. Tsapatsaris, A. Beesley, L. Nchari, S. Schroeder, C. Louis, *Reducibility of supported gold (III) precursors: influence of the metal oxide support and consequences for CO oxidation activity*, Top. Catal., **44**, 263-273 (2007)

[8.54] B. Campo, C. Petit, M.A. Volpe, *Hydrogenation of crotonaldehyde on different Au/CeO_2 catalysts*, J. Catal., **254**, 71-78 (2008)

[8.55] T.-Y. Ma, J.-L. Cao, G.-S. Shao, X.-J. Zhang, Z.-Y. Yuan, *Hierarchically structured squama-like cerium-doped titania: synthesis, photoactivity, and catalytic CO oxidation*, J. Phys. Chem. C, **113**, 16658-16667 (2009)

[8.56] D. Widmann, R. Leppelt, R.J. Behm, *Activation of a Au/CeO_2 catalyst for the CO oxidation reaction by surface oxygen removal/oxygen vacancy formation*, J. Catal., **251**, 437-442 (2007)

[8.57] N.A. Joy, M.I. Nandasiri, P.H. Rogers, W. Jiang, T. Varga, S.V.N.T. Kuchibhatla, S. Thevuthasan, M.A. Carpenter, *Selective plasmonic gas sensing: H_2, NO_2, and CO spectral discrimination by a single Au-CeO_2 nanocomposite film*, Anal. Chem., **84**, 5025-5034 (2012)

[8.58] J. Graciani, J.J. Plata, J.F. Sanz, P. Liu, J.A. Rodriguez, *A theoretical insight into the catalytic effect of a mixed-metal oxide at the nanometer level: the case of the highly active metal/CeO_x/TiO_2(110) catalysts*, J. Chem. Phys., **132**, 104703 (2010)

[8.59] J. Xiong, J. Chen, J. Zhang, *Liquid-phase hydrogenation of o-chloronitrobenzene over supported nickel catalysts*, Catal. Commun., **8**, 345-350 (2007)

[8.60] J.A. Altham, G. Webb, *Radiochemical studies of chemisorption and catalysis: IX. The behavior of 14C-ethylene, 14C-propylene and tritium adsorbed on alumina- and silica-supported platinum catalysts*, J. Catal., **18**, 133-141 (1970)

[8.61] W.J. Ambs, M.M. Mitchell Jr, *Hydrogen spillover on platinum-alumina, effect of water*, J. Catal., **82**, 226-229 (1983)

[8.62] K.-I. Shimizu, Y. Miyamoto, A. Satsuma, *Size- and support-dependent silver cluster catalysis for chemoselective hydrogenation of nitroaromatics*, J. Catal., **270**, 86-94 (2010)

[8.63] T. Sekiya, T. Yagisawa, S. Kurita, *Annealing of anatase titanium dioxide under*

hydrogen atmosphere, J. Ceram. Soc. Jpn., **109**, 672-675 (2001)

[8.64] C.T. Campbell, C.H.F. Peden, *Chemistry - oxygen vacancies and catalysis on ceria surfaces*, Science, **309**, 713-714 (2005)

[8.65] C.J. Weststrate, R. Westerstrom, E. Lundgren, A. Mikkelsen, J.N. Andersen, A. Resta, *Influence of oxygen vacancies on the properties of ceria-supported gold*, J. Phys. Chem. C, **113**, 724-728 (2009)

[8.66] S. Bernal, J.J. Calvino, M.A. Cauqui, J.M. Gatica, C. Larese, J.A. Pérez Omil, J.M. Pintado, *Some recent results on metal/support interaction effects in NM/CeO_2 (NM: noble metal) catalysts*, Catal. Today, **50**, 175-206 (1999)

[8.67] F. Cardenas-Lizana, S. Gomez-Quero, N. Perret, M.A. Keane, *Support effects in the selective gas phase hydrogenation of p-chloronitrobenzene over gold*, Gold Bull., **42**, 124-132 (2009)

[8.68] L. McEwan, M. Julius, S. Roberts, J. Fletcher, *A review of the use of gold catalysts in selective hydrogenation reactions*, Gold Bull., **43**, 298-306 (2010)

[8.69] A. Corma, M. Boronat, S. Gonzalez, F. Illas, *On the activation of molecular hydrogen by gold: a theoretical approximation to the nature of potential active sites*, Chem. Commun., 3371-3373 (2007)

[8.70] Q. Guo, K. Luo, K.A. Davis, D.W. Goodman, *Initial growth of Au on oxides*, Surf. Interface. Anal., **32**, 161-165 (2001)

[8.71] P. Claus, A. Brückner, C. Mohr, H. Hofmeister, *Supported gold nanoparticles from quantum dot to mesoscopic size scale: effect of electronic and structural properties on catalytic hydrogenation of conjugated functional groups*, J. Am. Chem. Soc., **122**, 11430-11439 (2000)

[8.72] A.M. Nadeem, G.I.N. Waterhouse, H. Idriss, *The reactions of ethanol on TiO_2 and Au/TiO_2 anatase catalysts*, Catal. Today, **182**, 16-24 (2012)

CHAPTER 9

Gas Phase Selective Hydrogenation of Phenylacetylene to Styrene over Au/Al_2O_3

In previous chapters of the thesis, a series of nitro-compounds have been the organic reactant studied. In this chapter, carbon-carbon triple bond, *i.e.* phenylacetylene, hydrogenation has been investigated over alumina supported gold and palladium catalysts, where effects of temperature and hydrogen partial pressure are considered. This chapter is in preparation for publication (see publication No. 12). Co-author M.A.K. directed the project and co-wrote the chapter.

9.1 Introduction

Trace quantities of phenylacetylene can poison styrene polymerization catalysts [1,2]. The phenylacetylene content must be less than 10 ppm [3] and selective hydrogenation (to styrene) is viewed as a viable process solution [2,4]. High styrene selectivities have been achieved in batch liquid phase operations using Pd based catalysts [5,6]. Bacchi *et al.* reported 92% styrene yield for reaction over Pd complexes (with hydrazine ligands) [5] while the application of Pd/MCM-41 delivered a 96% yield [6]. Other transition metal (Ru [7], Pt [7], Rh [8] and Ni [9]) catalysts are active in this reaction with varying levels of selectivity. In terms of reaction pathway, it has been established (in liquid phase operation) that phenylacetylene undergoes consecutive reduction where styrene serves as an intermediate in the subsequent conversion to ethylbenzene [10-12]. Liu *et al.* have demonstrated by FTIR analysis that selectivity is sensitive to H_2/phenylacetylene ratio where styrene is favoured under H_2 lean conditions [12].

A switch from conventional batch liquid to continuous gas phase reaction presents process advantages in terms of higher throughput and enhanced productivity. Indeed, Goršek and Glavič in their assessment of production rate and energy integration

concluded that a continuous plant is more profitable than one employing batch reactions for all capacities [13]. Gas phase continuous operation circumvents down time (between batches) and the use of additional chemicals as solvents, hydrogen donors and derivatisation agents [14-16]. Reported gas phase phenylacetylene hydrogenation is limited to the work of Nilolaev *et al.* who examined the application of Au/Al_2O_3 in the conversion of phenylacetylene/styrene mixtures [17-19]. Selectivity to styrene was below 30% and activity was dependent on Au particle size (2.5-30 nm) [17,18]. There is considerable scope to enhance Au promoted styrene production in continuous operation. In previous work, we have demonstrated 100% selectivity in the hydrogenation of functionalised nitroarenes over oxide supported Au to target amine products [20-22] and in the conversion of benzaldehyde to benzyl alcohol [23]. We have now extended that work to consider the catalytic action of Au/Al_2O_3 in selective phenylacetylene → styrene, assessing the effects of temperature and H_2 partial pressure as critical process variables. Drawing on the published liquid phase catalytic work where supported Pd was the predominant catalyst system [4,6,24-27], we have employed Pd/Al_2O_3 as benchmark and correlate catalyst testing with structural characterisation.

9.2 Materials and Methods

9.2.1 Catalyst Preparation

A 1.1% w/w $Au/\gamma\text{-}Al_2O_3$ was prepared by deposition-precipitation. Urea, used as basification agent, was added (100-fold excess) to a solution of $HAuCl_4$ (4.4×10^{-2} M), the $\gamma\text{-}Al_2O_3$ support (Puralox, Condea Vista Co.) was introduced and the suspension stirred and heated to 353 K (2 K min^{-1}) for 3 h. The pH progressively increased to reach *ca.* 7 after 3 h as a result of urea decomposition

$$NH_2\text{-}CO\text{-}NH_2 + 3H_2O \xrightarrow{T=353K} 2NH_4^+ + 2OH^- + CO_2 \qquad (9.1)$$

The resultant solid was separated by centrifugation, washed repeatedly with deionised water (with centrifugation between each washing) until the washing water was Cl-free (based on the $AgNO_3$ test) and dried in He (45 cm^3 min^{-1}) at 373 K (2 K min^{-1}) for 5 h. For comparison purposes, a commercial (Sigma-Aldrich) 1.2 % w/w Pd/Al_2O_3 catalyst was

employed and used as received. The catalysts were sieved to 75 μm average particle diameter (ATM fine test sieves) and the Au and Pd loadings determined by inductively coupled plasma-optical emission spectrometry (ICP-OES, Vista-PRO, Varian Inc.) from the diluted extract of aqua regia.

9.2.2 Catalyst Characterisation

Nitrogen adsorption-desorption isotherms were measured at 77 K using the commercial automated Micromeritics Gemini 2390 system; samples were outgassed at 423 K under N_2 for 1 h prior to analysis. Specific surface areas were calculated using the standard BET method with mean pore size and cumulative pore volumes determined by BJH analysis of the desorption isotherms. Temperature programmed reduction (TPR) and H_2 chemisorption were recorded using the commercial CHEMBET 3000 (Quantachrome Instrument) unit; data acquisition/manipulation employed the TPR Win^{TM} software. The samples were loaded into a U-shaped quartz cell (100 mm × 3.76 mm i.d.) and heated in 17 cm^3 min^{-1} (Brooks mass flow controlled) 5% v/v H_2/N_2 to 573 K (Pd/Al_2O_3) or 603 K (Au/Al_2O_3) at 2 K min^{-1}. The effluent gas passed through a liquid N_2 trap and H_2 consumption was monitored by a thermal conductivity detector. Post-TPR, samples were swept with 65 cm^3 min^{-1} N_2 for 1.5 h, cooled to 423 K or 298 K and subjected to H_2 chemisorption by pulse (10-50 μl) titration.

Powder x-ray diffractograms (XRD) were recorded on a Bruker/Siemens D500 incident x-ray diffractometer using Cu Kα radiation. Samples were scanned at 0.02º $step^{-1}$ over the range $20º \leq 2\theta \leq 85º$ and the diffractograms were compared with JCPDS-ICDD reference standards (Au (Card No. 04-0784), Pd (05-0681) and γ-Al_2O_3 (10-0425)). Metal (Au and Pd) particle morphology and size were determined by transmission (TEM, JEOL JEM 2011) and scanning transmission electron microscopy (STEM, JEOL 2200FS) electron microscopy, employing Gatan DigitalMicrograph 1.82 for data acquisition/manipulation. Samples for analysis were prepared by dispersion in acetone and deposited on a holey carbon/Cu grid (300 Mesh). The surface area-weighted metal diameter (d_{TEM}) was calculated from

$$d_{TEM} = \frac{\sum_i n_i d_i^3}{\sum_i n_i d_i^2} \quad (9.2)$$

where n_i is the number of particles of diameter d_i and $\Sigma n_i > 200$. X-ray photoelectron spectroscopy (XPS) analysis was conducted on an Axis Ultra instrument (Kratos Analytical) under ultra-high vacuum (< 10^{-8} Torr) using a monochromatic Al Kα X-ray source (1486.6 eV). Analyser pass energy was 80 eV for survey (0–1000 eV) and 40 eV for high resolution spectra (Au $4f_{7/2}$ and Pd $3d_{5/2}$). The adventitious carbon 1*s* peak at 284.5 eV was used as internal standard to compensate for any charging effects. Spectra curve fitting and quantification were performed with the Casa XPS software, using relative sensitivity factors provided by Kratos.

9.2.3 Catalytic Procedure

Reactions were carried out at H_2 partial pressures in the range 1.5×10^{-3}– 0.88 atm (varied by dilution in He, total pressure = 1 atm), immediately after *in situ* activation (at 2 K min^{-1} to 573-603 K in 60 cm^3 min^{-1} H_2 for 1h) in a continuous flow fixed bed vertical glass reactor (i.d. = 15 mm, *l* = 600 mm) at 353-473 K. The catalytic reactor and operating conditions to ensure negligible heat/mass transport limitations have been fully described elsewhere [28,29] but features pertinent to this study are given below. A layer of borosilicate glass beads served as preheating zone, ensuring that the inlet phenylacetylene (or styrene) was vaporised and reached reaction temperature before contacting the catalyst. Isothermal conditions (±1 K) were ensured by diluting the catalyst bed with ground glass (75 μm). Temperature was continuously monitored by a thermocouple inserted in a thermowell within the catalyst bed. Phenylacetylene (or styrene) was delivered *via* a glass/teflon air-tight syringe and teflon line using a microprocessor controlled infusion pump (Model 100 kd Scientific) at a fixed calibrated flow rate. A co-current flow of H_2 (or H_2/He) was maintained at $GHSV = 2\times10^4$ h^{-1} with an inlet organic flow (*F*) of 0.6×10^{-4}–4.8×10^{-3} mol h^{-1}; molar metal (*n*) to *F* ratio spanned the range 2.3×10^{-5}–4.7×10^{-2} h. At the low partial pressures of phenylacetylene in the feed, thermochemical calculations have confirmed that the reactant is in the gas phase over the temperature range applied. In blank tests, passage of phenylacetylene (or styrene) in H_2

through the empty reactor or over the support alone did not result in any detectable conversion.

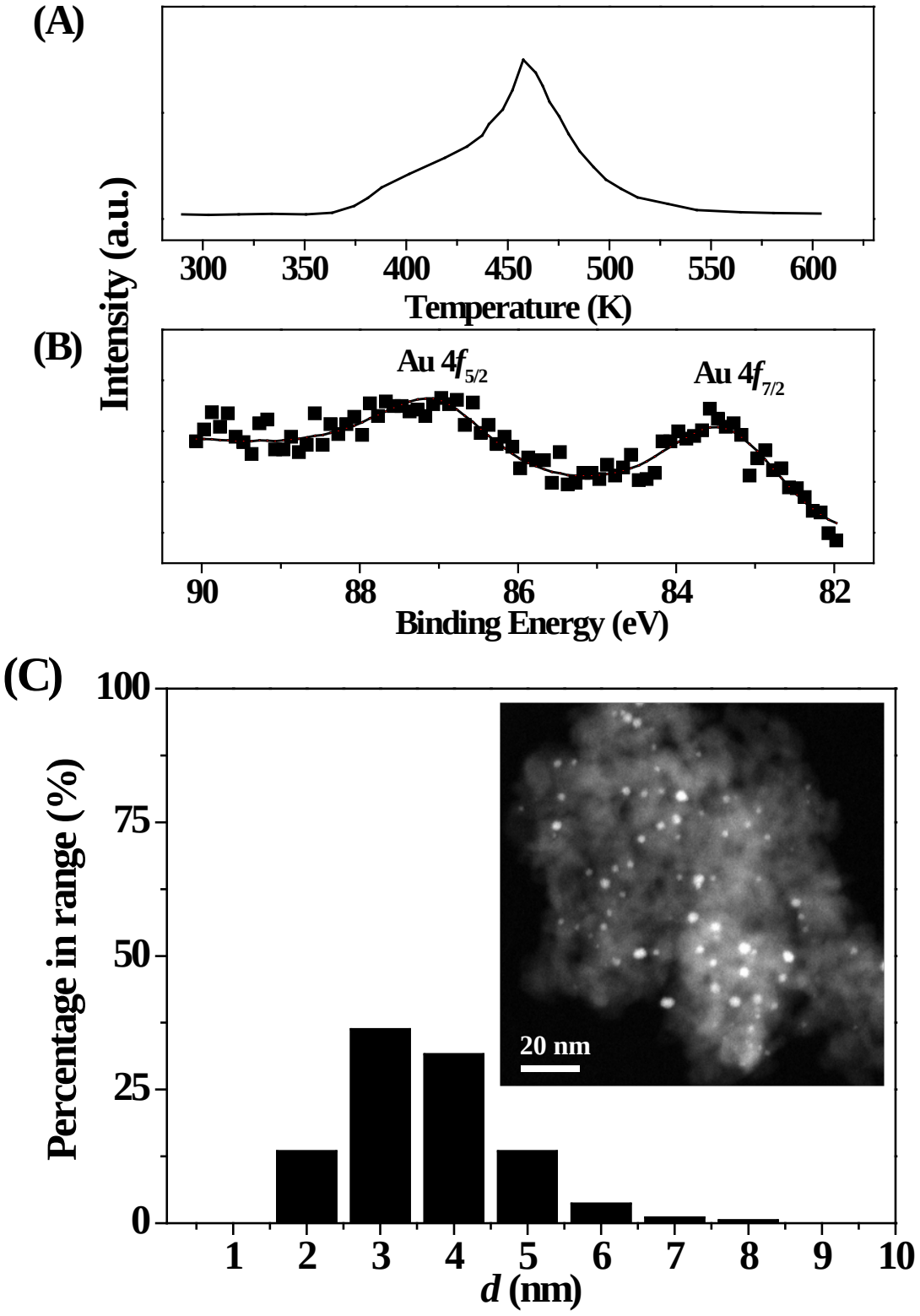

Figure 9.1: Au/Al_2O_3 characteristics: (A) TPR profile, (B) XPS spectrum over the Au 4*f* BE region and (C) representative STEM image (inset) with associated Au particle size (*d*) distribution histogram.

The reactor effluent was frozen in a liquid N_2 trap for subsequent analysis, using a Perkin-Elmer Auto System XL gas chromatograph equipped with a programmed split/splitless injector and FID, employing a DB-1 50 m × 0.20 mm i.d. 0.33 μm film thickness capillary column (J&W Scientific), as described elsewhere [30]. Phenylacetylene (Aldrich, ≥ 99.9%), styrene (Aldrich, ≥ 99.9%) and ethanol (Riedel-de Häen, ≥ 99.5%) as carrier were used without further purification. Repeated reactions with different samples from the same batch of catalyst delivered raw conversion and selectivity data that were reproducible to within ±6 %. Turnover frequency (*TOF*) was calculated based on Au and Pd dispersion obtained from TEM/STEM analysis.

9.3 Results and Discussion

9.3.1 Au/Al_2O_3

9.3.1.1 Catalyst Characteristics

Critical Au/Al_2O_3 characteristics are given in **Table 9.1**. The BET surface area (166 $m^2\ g^{-1}$), total pore volume (0.36 $cm^3\ g^{-1}$) and mean size (5.8 nm) are within the range (150–250 $m^2\ g^{-1}$, 0.27–0.75 $cm^3\ g^{-1}$ and 3.5–15 nm) reported for γ-Al_2O_3 supported metal systems [31,32]. Catalyst activation by temperature programmed reduction (TPR) generated the profile shown in **Figure 9.1(A)**, exhibiting a positive signal with T_{max} = 458 K. The associated H_2 consumption (87 μmol g^{-1}) matches that required for the reduction of the precursor to the metallic state (84 μmol g^{-1}), *i.e.* $Au^{3+} \rightarrow Au^0$. A single TPR peak has been reported previously for Au/Al_2O_3 at 434 K [33] and 503 K [34]. XPS measurements were conducted to probe Au electronic character and the resultant spectrum over the Au 4*f* binding energy (BE) region is given in **Figure 9.1(B)**. The extracted Au $4f_{7/2}$ BE (83.4 eV) is significantly lower than that reported for metallic Au (84.0 eV) [35], suggesting electron transfer from the support to generate electron rich $Au^{\delta-}$, as has been proposed for Au on Al_2O_3 [36,37].

Hydrogenation activity is dependent on H_2 activation where dissociative chemisorption occurs on low coordination Au sites [38]. Hydrogen uptake is enhanced with decreasing Au particle size at the nano-scale due to the preponderance of Au corner

Table 9.1: Physicochemical characteristics of Au/Al_2O_3 and Pd/Al_2O_3.

Catalyst	Metal loading (% w/w)	TPR T_{max} (K)	BET area ($m^2\ g^{-1}$)	Pore volume/mean size ($cm^3\ g^{-1}$)/(nm)	H_2 chemisorption (μmol g^{-1})	Mean particle size/range (nm)	XPS BE (eV)
Au/Al_2O_3	1.1	458	166	0.36/5.8	0.4[b]/4.4[c]	4.3/2-8	83.4[d]
Pd/Al_2O_3	1.2	355[a]	156	0.46/9.2	33.8[b]/22.6[c]	3.0/1-6	334.9[e]

[a]associated with H_2 release in Pd hydride decomposition; [b]at 298 K; [c]at 423 K; [d]Au $4f_{7/2}$; [e]Pd $3d_{5/2}$

Table 9.2: Temperature dependence of turnover frequency (*TOF*), associated selectivities (*S*) at a common fractional conversion ($x = 0.1$), values of the *L* and *M* parameters and rate constant ratios (k_1/k_2 and k_3/k_2 see Figure 9.2) obtained from the fit (see Eqs (9.7)-(9.11) and Figure 9.3(B)) of product composition from phenylacetylene and styrene reaction over Au/Al_2O_3 and Pd/Al_2O_3.

Catalyst	Temperature (K)	Phenylacetylene feed						Styrene feed	
		TOF (s^{-1})	*S* (%)	*L*	*M*	k_1/k_2	k_3/k_2	*TOF* (s^{-1})	*S* (%)[a]
Au/Al_2O_3	353	1.5×10^{-2}	styrene (100)	0.93	0.07	0.07	0.08	7×10^{-4}	100
Au/Al_2O_3	473	13×10^{-2}	styrene (90); ethylbenzene (10)	0.99	0.83	0.01	0.84	9×10^{-3}	100
Pd/Al_2O_3	353	0.9	styrene: (88); ethylbenzene (12)	0.99	2.54	0.01	2.57	22	100
Pd/Al_2O_3	473	5.6	styrene (82); ethylbenzene (18)	0.51	2.51	0.94	4.87	28	100

[a]ethyl benzene was the only product

and edge sites [39]. XRD analysis (diffractogram not shown) only revealed peaks due to the support, suggesting a well dispersed supported Au phase. We have applied STEM analysis to determine Au size (distribution and mean) and the representative image (**Figure 9.1(C)**) demonstrates the occurrence of pseudo-spherical Au particles in the size range 2-8 nm with a surface area weighted mean size of 4.3 nm; see size distribution histogram in **Figure 9.1(C)**. Hydrogen uptake measured at ambient temperature (**Table 9.1**) was low suggesting limited capacity to chemisorb H_2, as has been noted elsewhere for a range of Au systems [25,40,41]. Uptake was appreciably higher at 423 K (median reaction temperature), indicating that H_2 chemisorption on supported Au is an activated process. Although we could find no reported chemisorption values to relate to our measurements, van Bokhoven and co-workers [39,42] and Lin *et al*. [43] have proposed enhanced H_2 activation on Au/Al_2O_3 and Au/TiO_2, respectively, at higher temperatures.

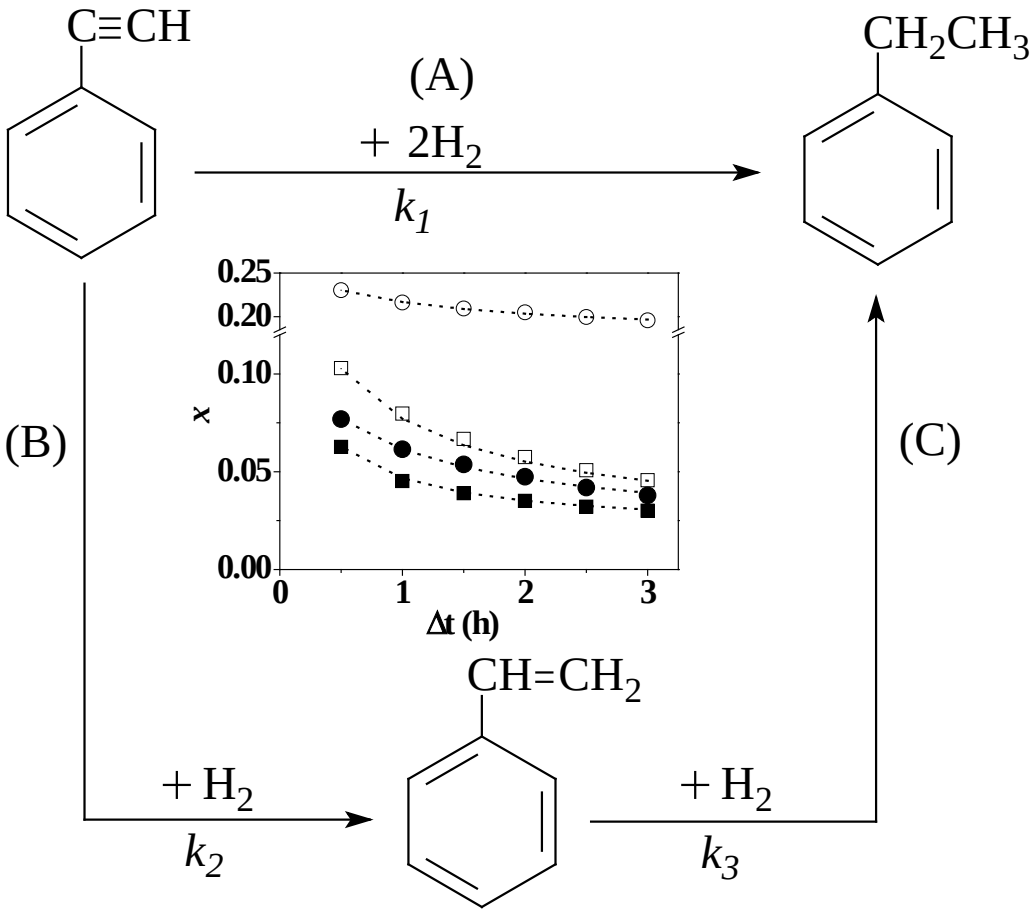

Figure 9.2: Reaction pathways in the hydrogenation of phenylacetylene. Inset: variation of phenylacetylene fractional conversion (*x*) with time-on-stream over Au/Al_2O_3 (■: $n/F = 9.3\times10^{-3}$ h, □: $n/F = 1.4 \times 10^{-3}$ h) and Pd/Al_2O_3 (●: $n/F = 9.4 \times 10^{-5}$ h, ○: $n/F = 4.7 \times 10^{-5}$ h) at 353 K (solid symbols) and 473 K (open symbols): H_2/phenylacetylene > 60; lines represent fit to eq. (9.3).

9.3.1.2 Catalytic Response

The consecutive phenylacetylene hydrogenation to ethylbenzene *via* styrene [10-12] is shown in **Figure 9.2** (reaction *via* steps B and C), which also includes a parallel direct route (step A). Fractional phenylacetylene conversion (x) is illustrated as a function of time on-stream at two reaction temperatures in the inset to **Figure 9.2**. The temporal variation in activity can be expressed in terms of the empirical relationship [33,37]

$$\frac{(x - x_0)}{(x_{3h} - x_0)} = \frac{\Delta t}{(\beta + \Delta t)} \tag{9.3}$$

where x_{3h} represents conversion after 3 h on-stream and β is a time scale fitting parameter. Fit convergence yielded x_0 (initial conversion), which was used to obtain the turnover frequencies (*TOF*, rate normalised per surface Au site) given in **Table 9.2**. Reaction over Au/Al_2O_3 delivered exclusive styrene production at 353 K (x = 0.1). This is a significant result as there has been no reported instance of 100% styrene selectivity in gas phase continuous operation. An increase in reaction temperature (from 353 to 473 K) resulted in an order of magnitude increase in *TOF*, generating styrene as principal product with secondary formation of ethylbenzene (**Table 9.2**). A shift in selectivity to ethylbenzene at higher temperatures (up to 343 K) has also been observed in the liquid phase over carbon supported Pd and Pt catalysts [3,44]. The extended activity/selectivity response is shown in **Figure 9.3**. High styrene selectivity (> 90%) was maintained at 353 K but there was a clear decline at 473 K with increasing conversion, consistent with a stepwise mechanism (steps B and C in **Figure 9.2**). Styrene and ethylbenzene were the only detected products with no evidence of dealkylation (to toluene) or condensation steps as reported for reaction over Ni and Ni-Pd catalysts [9]. We can note high alkene selectivities obtained with Au/Al_2O_3 in the hydrogenation of acetylene [45,46], propyne [47] and 1,3-butadiene [48]. Use of styrene as reactant generated ethylbenzene as the sole product but with an appreciably lower *TOF* relative to that recorded with phenylacetylene as feed (**Table 9.2**). This can account for the observed styrene selectivity from phenylacetylene where subsequent hydrogenation proceeded at a far lower rate. As both phenylacetylene and styrene act as Lewis bases, interaction with the Lewis acid-base sites on Al_2O_3 ($Al^{\delta+}$–$O^{\delta-}$) can lead to dissociative adsorption through the terminal carbon atom at $Al^{\delta+}$ with a proton

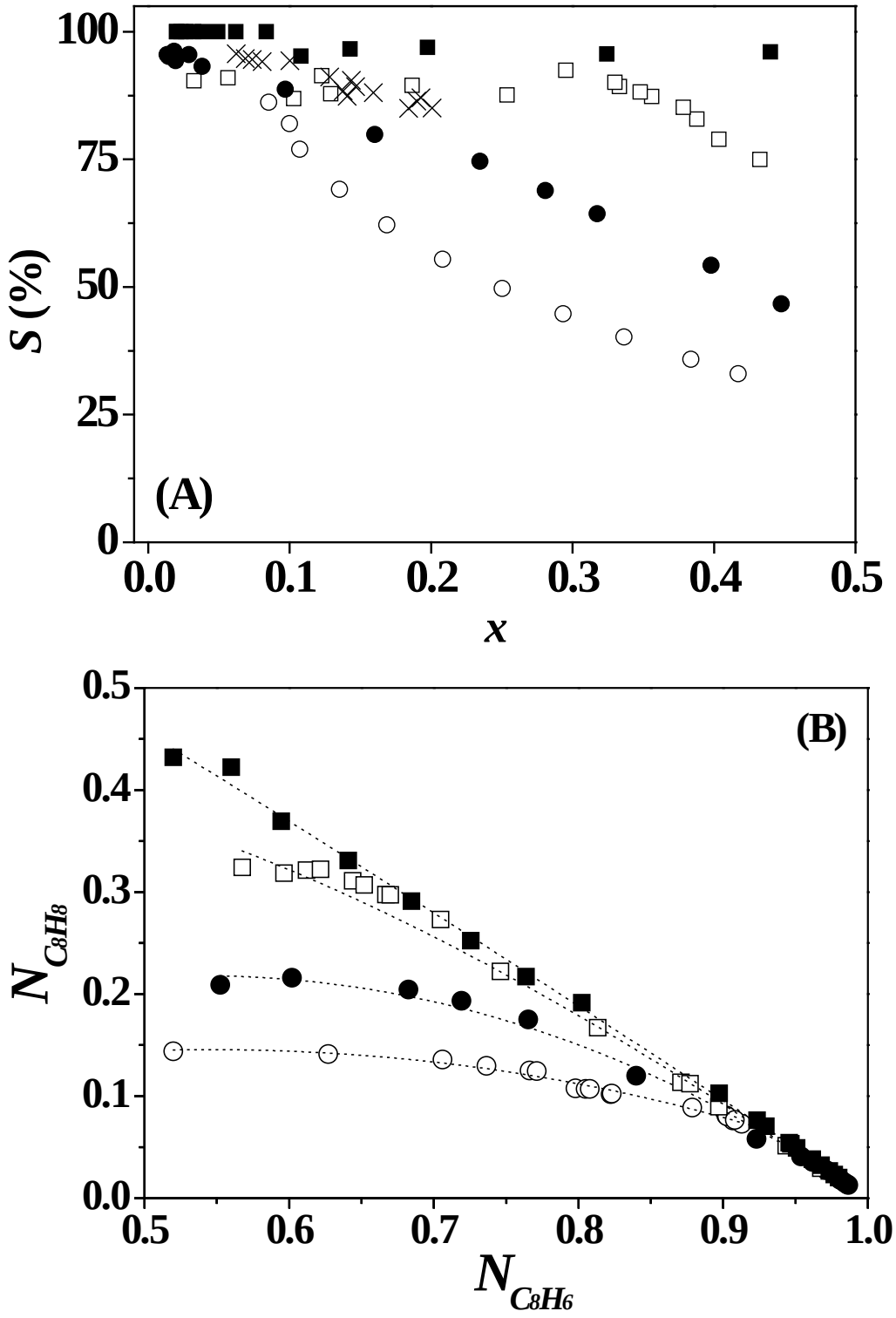

Figure 9.3: (A): Variation of styrene selectivity (*S*) with phenylacetylene fractional conversion (*x*) over Au/Al_2O_3 (■, □) and Pd/Al_2O_3 (●, ○) at 353 K (solid symbols) and 473 K (open symbols), where H_2/phenylacetylene > 60. Note: × represents *S* over Pd/Al_2O_3 at 473 K where molar H_2/phenylacetylene = 1. (B) Dependence of styrene mole fraction (N_{C8H8}) on phenylacetylene mole fraction (N_{C8H6}) for reaction over Au/Al_2O_3 and Pd/Al_2O_3 (symbols as above); lines represent fit to the consecutive/parallel mechanism (see Eqs (9.7)-(9.11), $R^2 > 0.98$).

bonded to the adjacent $O^{\delta-}$. Ivanov *et al.* have provided evidence from DRIFTS analysis for this mode of bonding using acetylene as a probe molecule [49]. While there is no clear consensus regarding structure sensitivity in alkyne hydrogenation, there is some evidence that the geometric and electronic properties of nano-scale Au can influence phenylacetylene hydrogenation, where smaller Au size favours higher activity and styrene selectivity [18]. Nikolaev and Smirnov [17] have proposed a preferential adsorption of phenylacetylene relative to styrene on Au edge and corner sites that are prevalent with decreasing Au particle size. DFT calculations have demonstrated stronger interaction of propyne (compared with propylene) with nano-sized Au, resulting in high (80–90%) associated selectivity to propylene in the hydrogenation of propyne+propylene mixtures over Au/CeO_2 [47]. Moreover, Jia *et al.* have recorded greater acetylene uptake than ethylene on Au/Al_2O_3, which was linked to enhanced (by a factor of 2000) acetylene hydrogenation rates [45].

9.3.2 Pd/Al_2O_3

9.3.2.1 Catalyst Characteristics

The commercial Pd/Al_2O_3 sample used as benchmark exhibited comparable BET area and pore volume with a higher mean pore size when compared with the laboratory synthesised Au/Al_2O_3 (**Table 9.1**). The TPR profile (**Figure 9.4(A)**) presents a single negative (H_2 release) peak at 355 K that can be attributed to the decomposition of *β*-Pd hydride, which is generated by H_2 absorption at partial pressure in excess of 0.02 atm [50-52]; a pressure of 0.05 atm was used in this study. Hydride composition (H/Pd) is dependent on Pd particle size [53,54] and the value recorded (0.1) is significantly lower than that which characterises bulk Pd (0.7) [51], suggesting the formation of Pd particles at the nano-scale. Indeed, Mendez *et al.* [55] have reported an equivalent hydride composition for 0.66% w/w Pd/Al_2O_3 with a mean Pd particle size of 2.0 nm. As in the case of Au/Al_2O_3, the XRD pattern for Pd/Al_2O_3 (not shown) did not exhibit any characteristic peak for Pd metal, suggesting Pd particle formation < 5 nm [56]. This was confirmed by TEM analysis (see representative image and size distribution histogram in **Figure 9.4(B)**) with particles in the 1-6 nm size range and a surface area-weighted mean

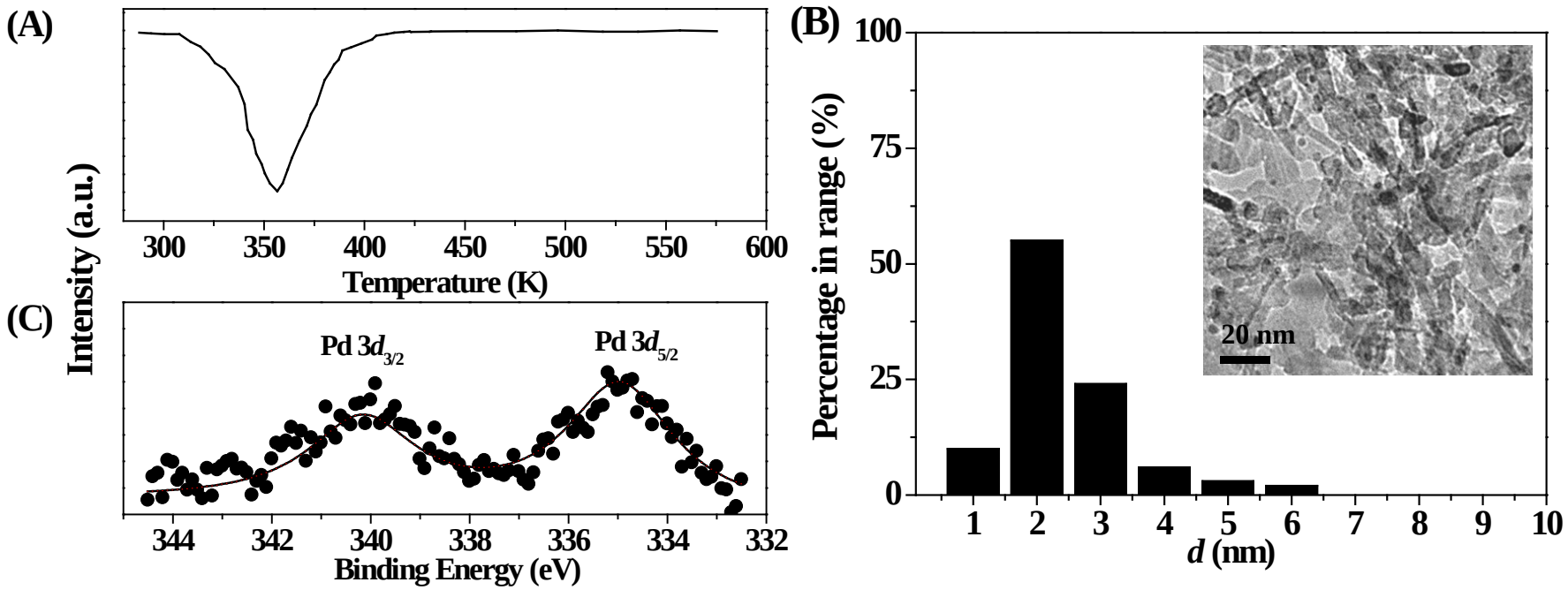

Figure 9.4: Pd/Al_2O_3 characteristics: (A) TPR profile, (B) representative TEM image (inset) with associated particle size (*d*) histogram and (C) XPS spectrum over Pd 3*d* BE region.

of 3.0 nm. Ambient temperature H_2 chemisorption on Pd/Al_2O_3 was significantly greater than that recorded for Au/Al_2O_3 (**Table 9.1**), which agrees with the general consensus that a higher activation barrier exists for H_2 chemisorption on Au relative to group 10 metals [40]. In contrast to Au/Al_2O_3, H_2 chemisorption on Pd/Al_2O_3 was suppressed at the higher temperature, an effect that has been reported for Pd [57], Pt [40,58] and Rh [59] systems. As H_2 dissociation on Pd is exothermic, elevated temperatures serve to limit uptake [39,40] whereas adsorption on supported Au is an activated process, favoured by increased temperature. The XPS spectrum over the Pd 3*d* BE region is shown in **Figure 9.4(C)** and the associated BE value (for $3d_{5/2}$) is given in **Table 9.1**. The Pd $3d_{5/2}$ core level BE (334.9 eV) is 0.4 eV lower than the metallic Pd reference (335.3 eV) [60], suggesting electron transfer from the support to generate $Pd^{\delta-}$, which is consistent with the literature [61,62].

9.3.2.2 Catalytic Response

Representative time on-stream conversion profiles are given in the inset to **Figure 9.2**, where a temporal decrease in conversion is again evident. The experimentally determined *TOF* values, which far exceed those obtained with Au/Al_2O_3, exhibited an increase at elevated reaction temperature (**Table 9.2**). The high activity exhibited by supported Pd has been exploited in industrial catalysis for alkyne hydrogenation [47,63] and application in acetylene hydrogenation has been considered to a far greater extent than the conversion of phenylacetylene [12,44]. Supported Pd in the metallic state has been proposed as the active site for C≡C hydrogenation [47,63] where activity and selectivity in conversion of phenylacetylene has shown a dependence on Pd particle size [64]. We should note that structure "insensitivity" has also been reported for reaction over pumice supported Pd [65]. The greater rate delivered by Pd/Al_2O_3 can be attributed to increased reactive surface hydrogen as established from the chemisorption measurements (**Table 9.1**). In order to probe this effect further, phenylacetylene hydrogenation over Pd/Al_2O_3 was conducted at lower H_2 partial pressure, corresponding to an inlet molar H_2/phenylacetylene = 1, which should serve to limit the available hydrogen for reaction. The resultant *TOF* (0.11 s^{-1} at 473 K) approached that recorded for Au/Al_2O_3 (at H_2

partial pressure = 0.87 atm, **Table 9.2**), demonstrating the critical role of hydrogen activation.

Reaction over Pd/Al_2O_3 was non-selective with significant ethylbenzene formation that was favoured by higher temperature and increasing conversion, as shown in **Figure 9.3(A)**. A comparison of selectivity in the sequential/parallel reaction mechanism that applies here (**Figure 9.2**) is only meaningful at a common level of conversion (x = 0.1 in **Table 9.2**), which establishes enhanced selectivity to styrene over Au/Al_2O_3. Conversion of a styrene feed over Pd/Al_2O_3 generated higher *TOF* relative to the phenylacetylene, representing a marked deviation from the catalytic response for Au/Al_2O_3 and can account for increased ethylbenzene production. Indeed, greater reactivity of styrene than phenylacetylene has been observed elsewhere for reaction over Ni [66] and Pd [12] catalysts. It is widely accepted that the conversion of alkenes to alkanes over Pd catalysts proceeds at a greater rate than the alkyne → alkene step [12,47,63]. The capacity of Pd sites to activate both C≡C and C=C has been demonstrated by DFT calculations [47] and is quite distinct from preferential C≡C activation on Au. Moreover, the generation of $Pd^{\delta-}$ (from XPS analysis) may result in more effective interaction with styrene as a weaker Lewis base than phenylacetylene. A decrease in inlet H_2 partial pressure to a molar H_2/phenylacetylene ratio = 1 (stoichiometry for styrene formation) shifted the selectivity/activity profile to overlap with that shown by Au/Al_2O_3 in excess H_2 (**Figure 9.3)**. The lower H_2 chemisorption capacity for Au/Al_2O_3 (**Table 9.1**) must contribute to styrene selectivity by limiting the degree of consecutive hydrogenation to ethylbenzene. It should be noted that was no detectable activity for reaction over Au/Al_2O_3 at H_2/phenylacetylene = 1. Under conditions of excess H_2, phenylacetylene conversion to ethylbenzene is facilitated by styrene activation at Pd sites. Selectivity to the alkene can, however, be imposed by limiting the H_2 supply to the stoichiometry for styrene formation.

In accordance with the pathways given in **Figure 9.2**, the steps involved in phenylacetylene hydrogenation are represented by

$$C_8H_6 + 2H_2 \xrightarrow{k_1} C_8H_{10} \tag{9.4}$$

$$C_8H_6 + H_2 \xrightarrow{k_2} C_8H_8 \tag{9.5}$$

$$C_8H_8 + H_2 \xrightarrow{k_3} C_8H_{10} \tag{9.6}$$

and

$$\frac{dN_{C_8H_6}}{d\left(n/F_{C_8H_6}\right)} = -\left(k_1 + k_2\right) \times N_{C_8H_6} \tag{9.7}$$

$$\frac{dN_{C_8H_8}}{d\left(n/F_{C_8H_6}\right)} = k_2 \times N_{C_8H_6} - k_3 \times N_{C_8H_8} \tag{9.8}$$

$$\frac{dN_{C_8H_{10}}}{d\left(n/F_{C_8H_6}\right)} = k_3 \times N_{C_8H_8} + k_1 \times N_{C_8H_6} \tag{9.9}$$

where N_i represents the molar fraction of the ith compound and k_j is the pseudo-first order rate constant of step j. From a combination of Eqs (9.7) and (9.8)

$$\frac{dN_{C_8H_8}}{dN_{C_8H_6}} = -L + M \times \left(\frac{N_{C_8H_8}}{N_{C_8H_6}}\right) \tag{9.10}$$

with

$$L = \frac{k_2}{k_1 + k_2} \quad \therefore \quad M = \frac{k_3}{k_1 + k_2}$$

which when integrated gives

$$N_{C_8H_8} = \frac{L}{1-M} \times \left(N_{C_8H_6}{}^{M} - N_{C_8H_6}\right) + C \tag{9.11}$$

where C is a constant and the values of L and M can be determined by non-linear mathematical fitting. The applicability of this parallel/consecutive mechanism can be assessed from the entries in **Figure 9.3(B)**, where it can be seen that the model provides a more than adequate fit to the experimental data. The rate constant ratios (k_1/k_2 and k_3/k_2) obtained from the L and M parameters are given in **Table 9.2** for Au/Al_2O_3 and Pd/Al_2O_3 at the two reaction temperatures. A strictly consecutive reaction network should yield a value of L close to unity ($k_1 = 0$) where lower L values reflect increased contribution due to the direct conversion of phenylacetylene to ethyl benzene. Reaction over Au/Al_2O_3 at 353 K proceeded in a predominantly stepwise fashion (L approaching unity) where the high styrene selectivity results from the far lower rate of subsequent hydrogenation ($k_2 >> k_3$). Stepwise hydrogenation was also favoured at the higher reaction temperature (L = 0.99) but styrene hydrogenation was promoted to a greater extent (marked increase in k_3/k_2), which can explain the observed ethylbenzene formation. In the case of Pd/Al_2O_3,

phenylacetylene hydrogenation followed consecutive steps at 353 K but, in contrast to Au/Al_2O_3, the rate of styrene hydrogenation far exceeded the phenylacetylene → styrene step resulting in significant ethylbenzene production. Reaction at 473 K favoured a concerted conversion of ethylbenzene ($k_1 \approx k_2$) and styrene reduction ($k_3 >> k_2$) leading to increased ethylbenzene selectivity (**Figure 9.3** and **Table 9.2**). It should be noted that single step direct phenylacetylene → ethylbenzene has been proposed for reaction over Pd/pumice [65] and Pd/C [44]. Operation at H_2/phenylacetylene = 1 (at 473 K) over Pd/Al_2O_3 generated $k_1/k_2 = 0.05$ and $k_3/k_2 = 1.14$, which approaches the values recorded for Au/Al_2O_3 (see **Table 9.2**). Selectivity exhibited by Au/Al_2O_3 can be linked to the preferential adsorption/activation of phenylacetylene and lower reactivity of styrene. In contrast, both phenylacetylene and styrene are activated on Pd/Al_2O_3 where the alkene exhibits higher reactivity but selectivity can be tuned by altering the inlet H_2/phenylacetylene.

9.4 Conclusions

We have established a distinct catalytic response for alumina supported Au and Pd in the gas phase continuous hydrogenation of phenylacetylene. Charge transfer from Al_2O_3 to nano-scale Au (2-8 nm) and Pd (1-6 nm) generates an electron rich metal phase. Pd/Al_2O_3 exhibited a greater capacity for H_2 uptake under reaction conditions and delivered an appreciably higher *TOF*. Kinetic analysis has revealed stepwise phenylacetylene hydrogenation in excess H_2 over Au/Al_2O_3 with 100% selectivity to styrene at 353 K that is attributed to preferential adsorption/activation of phenylacetylene relative to styrene and further hydrogenation is limited by the available surface hydrogen. An increase in temperature (to 473 K) raised *TOF* with the promotion of sequential styrene hydrogenation to ethylbenzene. Stepwise hydrogenation also prevailed over Pd/A_2O_3 at the lower temperature but surface activation of styrene coupled with enhanced H_2 dissociation generated significant ethylbenzene. Increased reaction temperature favoured parallel direct phenylacetylene hydrogenation with increased ethylbenzene selectivity. Lowering the inlet H_2/phenylacetylene ratio to 1 delivered an activity/selectivity response over Pd/A_2O_3 approaching that for Au/A_2O_3, demonstrating

the critical role of hydrogen supply in determining catalyst performance.

9.5 References

[9.1] F. Arena, G. Cum, R. Gallo, A. Parmaliana, *Palladium catalysts supported on oligomeric aramides in the liquid-phase hydrogenation of phenylacetylene*, J. Mol. Catal. A: Chem., **110**, 235-242 (1996)

[9.2] S. Domínguez-Domínguez, A. Berenguer-Murcia, D. Cazorla-Amorós, A. Linares-Solano, *Semihydrogenation of phenylacetylene catalyzed by metallic nanoparticles containing noble metals*, J. Catal., **243**, 74-81 (2006)

[9.3] C. Li, Z. Shao, M. Pang, C.T. Williams, C. Liang, *Carbon nanotubes supported Pt catalysts for phenylacetylene hydrogenation: effects of oxygen containing surface groups on Pt dispersion and catalytic performance*, Catal. Today, **186**, 69-75 (2012)

[9.4] S. Dominguez-Dominguez, A. Berenguer-Murcia, B.K. Pradhan, A. Linares-Solano, D. Cazorla-Amoros, *Semihydrogenation of Phenylacetylene Catalyzed by Palladium Nanoparticles Supported on Carbon Materials*, J. Phys. Chem. C, **112**, 3827-3834 (2008)

[9.5] A. Bacchi, M. Carcelli, M. Costa, A. Leporati, E. Leporati, P. Pelagatti, C. Pelizzi, G. Pelizzi, *Palladium(II) complexes containing a P, N chelating ligand Part II. Synthesis and characterisation of complexes with different hydrazinic ligands. Catalytic activity in the hydrogenation of double and triple C-C bonds*, J. Organomet. Chem., **535**, 107-120 (1997)

[9.6] S. Dominguez-Dominguez, A. Berenguer-Murcia, A. Linares-Solano, D. Cazorla-Amoros, *Inorganic materials as supports for palladium nanoparticles: Application in the semi-hydrogenation of phenylacetylene*, J. Catal., **257**, 87-95 (2008)

[9.7] C. Li, Z. Shao, M. Pang, C.T. Williams, X. Zhang, C. Liang, *Carbon nanotubes supported mono- and bimetallic Pt and Ru catalysts for selective hydrogenation of phenylacetylene*, Ind. Eng. Chem. Res., **51**, 4934-4941 (2012)

[9.8] X.-Y. Quek, Y. Guan, E.J.M. Hensen, *Structure sensitivity in the hydrogenation of*

unsaturated hydrocarbons over Rh nanoparticles, Catal. Today, **183**, 72-78 (2012)

[9.9] M.D. Navalikhina, N.E. Kavalerskaya, E.S. Lokteva, A.A. Peristyi, E.V. Golubina, V.V. Lunin, *Selective hydrogenation of phenylacetylene on Ni and Ni-Pd catalysts modified with heteropoly compounds of the Keggin type*, Russ. J. Phys. Chem. A, **86**, 1800-1807 (2012)

[9.10] F. Bautista, J. Campelo, A. Garcia, D. Luna, J. Marinas, R. Quiros, A. Romero, *Influence of surface support properties on the liquid-phase selective hydrogenation of phenylacetylene on supported nickel catalysts*, Catal. Lett., **52**, 205-213 (1998)

[9.11] T. Vergunst, F. Kapteijn, J.A. Moulijn, *Optimization of geometric properties of a monolithic catalyst for the selective hydrogenation of phenylacetylene*, Ind. Eng. Chem. Res., **40**, 2801-2809 (2001)

[9.12] W. Liu, C. Otero Arean, S. Bordiga, E. Groppo, A. Zecchina, *Selective phenylacetylene hydrogenation on a polymer-supported palladium catalyst monitored by FTIR spectroscopy*, ChemCatChem, **3**, 222-226 (2011)

[9.13] A. Goršek, P. Glavič, *Design of batch versus continuous processes: part I: single-purpose equipment*, Chem. Eng. Res. Des., **75**, 709-717 (1997)

[9.14] W. Wang, Y. Zheng, J. Lin, Y. She, K.J. Fu, *Time-resolved IR study of gas-phase reactions of benzene with Group VIB metal pentacarbonyls and tetracarbonyls*, J. Phys. Chem., **97**, 11921-11928 (1993)

[9.15] A. Goossens, J. Schoonman, M. Yoshimura, *Gas-phase synthesis of nano-structured semiconductors*, Eur. J. Solid State Inorg. Chem., **32**, 779-786 (1995)

[9.16] J.K. Laerdahl, E. Uggerud, *Gas phase nucleophilic substitution*, Int. J. Mass. Spectrom., **214**, 277-314 (2002)

[9.17] S.A. Nikolaev, V.V. Smirnov, *Synergistic and size effects in selective hydrogenation of alkynes on gold nanocomposites*, Catal. Today, **147**, S336-S341 (2009)

[9.18] S. Nikolaev, V. Smirnov, *Selective hydrogenation of phenylacetylene on gold nanoparticles*, Gold Bull., **42**, 182-189 (2009)

[9.19] S. Nikolaev, N. Permyakov, V. Smirnov, A. Vasil'kov, S. Lanin, *Selective hydrogenation of phenylacetylene into styrene on gold nanoparticles*, Kinet. Catal.,

51, 288-292 (2010)

[9.20] X. Wang, N. Perret, M.A. Keane, *The role of hydrogen partial pressure in the gas phase hydrogenation of p-chloronitrobenzene over aluminasupported Au and Pd: a consideration of reaction thermodynamics and kinetics*, Chem. Eng. J., **210**, 103-113 (2012)

[9.21] X. Wang, N. Perret, J.J. Delgado, G. Blanco, X. Chen, C.M. Olmos, S. Bernal, M.A. Keane, *Reducible support effects in the gas phase hydrogenation of p-chloronitrobenzene over gold*, J. Phys. Chem. C, **117**, 994-1005 (2013)

[9.22] F. Cárdenas-Lizana, M. Keane, *The development of gold catalysts for use in hydrogenation reactions*, J. Mater. Sci., **48**, 543-564 (2013)

[9.23] N. Perret, F. Cárdenas-Lizana, M.A. Keane, *Selective hydrogenation of benzaldehyde to benzyl alcohol over Au/Al_2O_3*, Catal. Commun., **16**, 159-164 (2011)

[9.24] A. Mastalir, Z. Kiraly, F. Berger, *Comparative study of size-quantized Pd-montmorillonite catalysts in liquid-phase semihydrogenations of alkynes*, Appl. Catal. A: Gen., **269**, 161-168 (2004)

[9.25] E.V. Starodubtseva, M.G. Vinogradov, O.V. Turova, N.A. Bumagin, E.G. Rakov, V.I. Sokolov, *Palladium(0) supported on carbon nanotubes as an efficient catalyst of the CC bond hydrogenation*, Catal. Commun., **10**, 1441-1442 (2009)

[9.26] P. Weerachawanasak, O. Mekasuwandumrong, M. Arai, S.-I. Fujita, P. Praserthdam, J. Panpranot, *Effect of strong metal-support interaction on the catalytic performance of Pd/TiO_2 in the liquid-phase semihydrogenation of phenylacetylene*, J. Catal., **262**, 199-205 (2009)

[9.27] J. Panpranot, K. Phandinthong, T. Sirikajorn, M. Arai, P. Praserthdam, *Impact of palladium silicide formation on the catalytic properties of Pd/SiO_2 catalysts in liquid-phase semihydrogenation of phenylacetylene*, J. Mol. Catal. A: Chem., **261**, 29-35 (2007)

[9.28] M.A. Keane, *Gas phase hydrogenation/hydrogenolysis of benzaldehyde and o-tolualdehyde over Ni/SiO_2*, J. Mol. Catal. A: Chem., **118**, 261-269 (1997)

[9.29] G. Tavoularis, M.A. Keane, *The gas phase hydrodechlorination of chlorobenzene over nickel/silica*, J. Chem. Technol. Biotechnol., **74**, 60-70 (1999)

[9.30] G. Yuan, M.A. Keane, *Aqueous-phase hydrodechlorination of 2,4-dichlorophenol over Pd/Al_2O_3: Reaction under controlled pH*, Ind. Eng. Chem. Res., **46**, 705-715 (2007)

[9.31] Z. Zhang, T.J. Pinnavaia, *Mesoporous γ-alumina formed through the surfactant-mediated scaffolding of peptized pseudoboehmite nanoparticles*, Langmuir., **26**, 10063-10067 (2010)

[9.32] M. Trueba, S.P. Trasatti, *γ-Alumina as a support for catalysts: a review of fundamental aspects*, Eur. J. Inorg. Chem., **2005**, 3393-3403 (2005)

[9.33] F. Cárdenas-Lizana, S. Gómez-Quero, G. Jacobs, Y. Ji, B.H. Davis, L. Kiwi-Minsker, M.A. Keane, *Alumina supported Au-Ni: surface synergism in the gas phase hydrogenation of nitro-compounds*, J. Phys. Chem. C, **116**, 11166-11180 (2012)

[9.34] C.K. Costello, J. Guzman, J.H. Yang, Y.M. Wang, M.C. Kung, B.C. Gates, H.H. Kung, *Activation of Au/γ-Al_2O_3 catalysts for CO oxidation: Characterization by X-ray absorption near edge structure and temperature programmed reduction*, J. Phys. Chem. B, **108**, 12529-12536 (2004)

[9.35] M. Baron, O. Bondarchuk, D. Stacchiola, S. Shaikhutdinov, H.J. Freund, *Interaction of gold with cerium oxide supports: CeO_2(111) thin films vs CeOx nanoparticles*, J. Phys. Chem. C, **113**, 6042-6049 (2009)

[9.36] F. Wang, G. Lu, *Control Reaction Path of CO oxidation by regulating the oxidation state of Au species*, Catal. Lett., **134**, 72-77 (2010)

[9.37] N. Perret, X. Wang, L. Delannoy, C. Potvin, C. Louis, M.A. Keane, *Enhanced selective nitroarene hydrogenation over Au supported on β-Mo_2C and β-Mo_2C/Al_2O_3*, J. Catal., **286**, 172-183 (2012)

[9.38] M. Boronat, P. Concepción, A. Corma, S. González, F. Illas, P. Serna, *A molecular mechanism for the chemoselective hydrogenation of substituted nitroaromatics with nanoparticles of gold on TiO_2 catalysts: a cooperative effect between gold and the support*, J. Am. Chem. Soc., **129**, 16230-16237 (2007)

[9.39] E. Bus, J.T. Miller, J.A. van Bokhoven, *Hydrogen chemisorption on Al_2O_3-supported gold catalysts*, J. Phys. Chem. B, **109**, 14581-14587 (2005)

[9.40] G.C. Bond, C. Louis, D.T. Thompson, Catalysis by Gold, Imperial College Press,

London, 2006.

[9.41] X. Wang, N. Perret, M.A. Keane, *Gas phase hydrogenation of nitrocyclohexane over supported gold catalysts*, Appl. Catal. A: Gen., **467**, 575-584 (2013)

[9.42] C. Kartusch, J. van Bokhoven, *Hydrogenation over gold catalysts: the interaction of gold with hydrogen*, Gold Bull., **42**, 343-348 (2009)

[9.43] S. Lin, M.A. Vannice, *Gold dispersed on TiO_2 and SiO_2: adsorption properties and catalytic behavior in hydrogenation reactions*, Catal. Lett., **10**, 47-61 (1991)

[9.44] S.D. Jackson, L.A. Shaw, *The liquid-phase hydrogenation of phenyl acetylene and styrene on a palladium/carbon catalyst*, Appl. Catal. A: Gen., **134**, 91-99 (1996)

[9.45] J. Jia, K. Haraki, J.N. Kondo, K. Domen, K. Tamaru, *Selective hydrogenation of acetylene over Au/Al_2O_3 catalyst*, J. Phys. Chem. B, **104**, 11153-11156 (2000)

[9.46] A.C. Gluhoi, J.W. Bakker, B.E. Nieuwenhuys, *Gold, still a surprising catalyst: Selective hydrogenation of acetylene to ethylene over Au nanoparticles*, Catal. Today, **154**, 13-20 (2010)

[9.47] Y. Segura, N. Lopez, J. Perez-Ramirez, *Origin of the superior hydrogenation selectivity of gold nanoparticles in alkyne + alkene mixtures: triple- versus double-bond activation*, J. Catal., **247**, 383-386 (2007)

[9.48] S. Schimpf, M. Lucas, C. Mohr, U. Rodemerck, A. Brückner, J. Radnik, H. Hofmeister, P. Claus, *Supported gold nanoparticles: in-depth catalyst characterization and application in hydrogenation and oxidation reactions*, Catal. Today, **72**, 63-78 (2002)

[9.49] A.V. Ivanov, A.E. Koklin, E.B. Uvarova, L.M. Kustov, *A DRIFT spectroscopic study of acetylene adsorbed on metal oxides*, Phys. Chem. Chem. Phys., **5**, 4718-4723 (2003)

[9.50] R. Gopinath, N. Seshu Babu, J. Vinod Kumar, N. Lingaiah, P. Sai Prasad, *Influence of Pd precursor and method of preparation on hydrodechlorination activity of alumina supported palladium catalysts*, Catal. Lett., **120**, 312-319 (2008)

[9.51] S. Gómez-Quero, F. Cárdenas-Lizana, M.A. Keane, *Effect of metal dispersion on the liquid-phase hydrodechlorination of 2,4-dichlorophenol over Pd/Al_2O_3*, Ind. Eng. Chem. Res., **47**, 6841-6853 (2008)

[9.52] N.S. Babu, N. Lingaiah, R. Gopinath, P.S. Sankar Reddy, P.S. Sai Prasad,

Characterization and reactivity of alumina-supported Pd catalysts for the room-temperature hydrodechlorination of chlorobenzene, J. Phys. Chem. C, **111**, 6447-6453 (2007)

[9.53] N.K. Nag, *A study on the formation of palladium hydride in a carbon-supported palladium catalyst*, J. Phys. Chem. B, **105**, 5945-5949 (2001)

[9.54] G. Fagherazzi, A. Benedetti, S. Polizzi, A. Mario, F. Pinna, M. Signoretto, N. Pernicone, *Structural investigation on the stoichiometry of β-PdH_x in Pd/SiO_2 catalysts as a function of metal dispersion*, Catal. Lett., **32**, 293-303 (1995)

[9.55] C.M. Mendez, H. Olivero, D.E. Damiani, M.A. Volpe, *On the role of Pd β-hydride in the reduction of nitrate over Pd based catalyst*, Appl. Catal. B: Environ., **84**, 156-161 (2008)

[9.56] D.H. Kim, Y.-H. Chin, G.G. Muntean, A. Yezeretz, N.W. Currier, W.S. Epling, H.-Y. Chen, H. Hess, C.H.F. Peden, *Relationship of Pt particle size to the NOx storage performance of thermally aged $Pt/BaO/Al_2O_3$ lean NO_x trap catalysts*, Ind. Eng. Chem. Res., **45**, 8815-8821 (2006)

[9.57] V.V. Bhat, C.I. Contescu, N.C. Gallego, *Kinetic effect of Pd additions on the hydrogen uptake of chemically-activated ultramicroporous carbon*, Carbon, **48**, 2361-2364 (2010)

[9.58] E. Bus, J.A. van Bokhoven, *Hydrogen chemisorption on supported platinum, gold, and platinum-gold-alloy catalysts*, Phys. Chem. Chem. Phys., **9**, 2894-2902 (2007)

[9.59] C.-M. Lu, I. Wang, S.-C. Chou, C.-T. Yeh, *Hydrogenation of benzene over rhodium-copper alloy crystallites supported on alumina*, Chinyi J., **19**, 119-131 (2001)

[9.60] H. Liu, M. Liang, C. Xiao, N. Zheng, X. Feng, Y. Liu, J. Xie, Y. Wang, *An excellent Pd-based nanocomposite catalyst for the selective hydrogenation of para-chloronitrobenzene*, J. Mol. Catal. A: Chem., **308**, 79-86 (2009)

[9.61] K. Sun, J. Liu, N. Nag, N.D. Browning, *Studying the metal-support interaction in Pd/γ-Al_2O_3 Catalysts by atomic-resolution electron energy-loss spectroscopy*, Catal. Lett., **84**, 193-199 (2002)

[9.62] N. Tsud, V. Johanek, I. Stara, K. Veltruska, V. Matolin, *CO adsorption on palladium model catalysts: XPS Pd/Al_2O_3 interaction study*, Surf. Sci., **467**,

169-176 (2000)

[9.63] A. Borodzinski, G.C. Bond, *Selective hydrogenation of ethyne in ethene-rich streams on palladium catalysts. part 1. effect of changes to the catalyst during reaction*, Catal. Rev., **48**, 91-144 (2006)

[9.64] G. Carturan, G. Facchin, G. Cocco, S. Enzo, G. Navazio, *Influence of metal dispersion on selectivity and kinetics of phenylacetylene hydrogenation catalyzed by supported palladium*, J. Catal., **76**, 405-417 (1982)

[9.65] D. Duca, L.F. Liotta, G. Deganello, *Selective hydrogenation of phenylacetylene on pumice-supported palladium catalysts*, J. Catal., **154**, 69-79 (1995)

[9.66] X. Chen, A. Zhao, Z. Shao, C. Li, C.T. Williams, C. Liang, *Synthesis and catalytic properties for phenylacetylene hydrogenation of silicide modified nickel catalysts*, J. Phys. Chem. C, **114**, 16525-16533 (2012)

CHAPTER 10

Summary and Future Work

The main goal of this thesis is to investigate the application of Au catalysts in sustainable hydrogenation processing, where enhanced catalytic performance was achieved by systematic optimisation of catalyst structural properties and control of reaction conditions. This has been facilitated through a consideration of reaction thermodynamics, kinetics and catalyst deactivation. All the reactions were conducted under relatively mild reaction conditions (353-493 K, 1 atm) in continuous flow gas phase operation. The benefits of continuous processing relative to standard batch operation have been demonstrated. The results establish clean catalytic routes to high value products (amines, oxime and styrene) that find a range of applications in the fine chemicals sector. The main findings of this work are highlighted in this Chapter and future research directions are proposed.

10.1 General Conclusions

Thermodynamic equilibrium analysis of aromatic nitro-compound (*p*-chloronitrobenzene) hydrogenation has demonstrated that the possible hydrogenation and hydrogenolysis reactions are exothermal ($\Delta H_{423K} < 0$). Each step is thermodynamically favourable ($\Delta G_{423K} < 0$) with the exception of cyclohexene production. Under thermodynamic control, reaction temperature (373-473 K) has a negligible effect on product distribution, which is sensitive to $H_2/–NO_2$ in the stoichiometric range (1-8) where, at $H_2/–NO_2 \geq 10$, cyclohexane is the preferred product. Reaction over Au/Al_2O_3 and Pd/Al_2O_3 delivered a product composition far removed from thermodynamic equilibrium where Au/Al_2O_3 promoted sole formation of *p*-chloroaniline at 373-473 K and each inlet H_2/*p*-chloronitrobenzene. Reaction over Pd/Al_2O_3 generated nitrobenzene and aniline (combined hydrodechlorination and hydrogenation) with increased selectivity to nitrobenzene at lower $H_2/–NO_2$. Utilisation

of a reducible ($Ce_{0.62}Zr_{0.38}O_2$) oxide as Au carrier resulted in hydrodechlorination to aniline. This is attributed to the action of oxygen vacancies formed *via* support reduction that is favoured by higher activation/reduction temperature.

Taking Au/Al_2O_3 as a representative catalyst, a temporal decline in activity was observed that was more pronounced at H_2/*p*-chloronitrobenzene < 20. The spent catalyst exhibited equivalent BET area/pore characteristics, Au particle size and electronic character relative to activated unused Au/Al_2O_3. A significant carbon content (6.3% w/w) post-reaction was in evidence, which hindered H_2 chemisorption capacity under reaction conditions, leading to suppressed hydrogenation activity. Catalyst regeneration by oxidative/reduction treatment resulted in a near complete restoration of the initial hydrogenation activity and exclusive selectivity to *p*-chloroaniline.

Comparison of batch liquid and gas phase continuous modes has established clear advantages for the latter in terms of productivity and lower associated E-Factor. Hydrogenation activity can be substantially enhanced using water as solvent (relative to alcohol). This is significant with respect to sustainability and the application of “green chemistry”. Moreover, supported Au has shown 100% selectivity in the gas phase hydrogenation of *p*-nitrobenzonitrile to *p*-aminobenzonitrile, outperforming benchmark Ni and Pd catalysts that are non-selective. Employing Mo_2C as an active Au and Au-Pd carrier has promoted catalytic activity in the hydrogenation of nitrobenzene, *p*-chloronitrobenzene, and *p*-nitrobenzonitrile, where the inclusion of Pd as promoter elevated activity while maintaining 100% selectivity.

Further applications of Au catalysts in hydrogenation focused on the conversion of an aliphatic nitro-compound and selective C≡C reduction. Cyclohexanone oxime synthesis from nitrocyclohexane has been established over Au/Al_2O_3 with selectivity up to 95%. Catalyst performance in this application is sensitive to the support where use of ZrO_2, TiO_2 and CeO_2 delivered a quite distinct product composition that can be attributed to differences in surface properties. Exclusive styrene generation from selective phenylacetylene hydrogenation has been achieved over Au/Al_2O_3, outperforming Pd/Al_2O_3 which promoted catalysing full reduction of phenylacetylene to ethylbenzene.

10.2 Future Directions

10.2.1 Coupling of Dehydrogenation with Hydrogenation: H_2 Utilisation

In this thesis, compressed hydrogen gas (delivered at 1 atm) was employed in the gas phase hydrogenation reactions. The benefits over hydrogen donors used in conventional batch systems has been noted (see **Chapter 5**). Moreover, operation of the latter systems at high H_2 pressure is a safety concern while the use of hydrogen donors necessitates additional separation stages, often under reflux conditions that impacts on overall process sustainability. Use of a diluted hydrogen (sub-atmospheric) feed serves to improve atom efficiency (see **Chapter 2 & 5**) but a significant component remains unreacted. This can be addressed by incorporating a recycle loop. Nevertheless, hydrogen is not a renewable resource and alternative sources must be considered for a step change increase in efficiency. One possibility is the coupling a dehydrogenation reaction to generate hydrogen *in situ* for the hydrogenation reaction. The critical practical issue here is that the dehydrogenation product must have intrinsic value, does not undergo secondary reaction with the hydrogenation reactant and/or product and is readily separated downstream. The work in this thesis has established ultra-selectivity for supported Au in the hydrogenation of a range of functionalised nitro-compounds. However, the reaction rate falls below that achieved with conventional (but non-selective) transition metal catalysts. Coupling of dehydrogenation to deliver hydrogen *in situ* may result in increased selective hydrogenation rate, which can close one of the remaining sustainability gaps in the application of Au catalysts in hydrogenation. This will require a scoping exercise to identify the dehydrogenation reaction that can take place over Au (or Au based bimetallics) under conditions where 100% $–NO_2$ hydrogenation selectivity can be maintained.

10.2.2 Selective Oxidation of Glycerol using Au Catalysts

Fossil fuels (coal, petroleum crude oil and natural gas) have been predominant as the source of thermal energy, fuels and chemicals. Fossil fuel reserves are finite and the increasing energy demands has already resulted in serious reserves depletion and

environmental degradation. One progressive response is the use of biomass as an alternative energy resource that has the advantage of a plentiful and renewable supply. A promising substitute standard fuel substitute is biodiesel, which is now produced conventionally *via* transesterification of vegetable/animal oils or waste fats with alcohols, producing glycerol as an inevitable by-product. While glycerol is commonly used in pharmaceuticals, cosmetics, soaps, toothpastes or as sweetener there is a pressing requirement to extend its uses and capitalise on the surplus glycerol. Selective oxidation of glycerol can generate glyceric acid, tartronic acid, dihydroxyacetone, glycolic acid or mesoxalic acid, all of which exhibit high commercial value. Application of supported Au catalysts in oxidation predates the hydrogenation work. The work presented in this thesis can extended to assess commonality and deviations in terms of structure/performance in oxidation relative to hydrogenation. Hydrogenation of a biomass resource can consider the conversion of furfural (to furfuryl alcohol) as a route to an intermediate to a wide range of fine chemicals. Gold catalysis to produce value-added products from biomass will undoubtedly grow in importance in the near future.

10.2.3 Catalytic Hydrogenation (Conversion) of Carbon Dioxide (CO_2) *to Valuable Chemicals*

Increasing CO_2 emissions are inextricably linked to negative ecological and environmental impacts and the occurrence of global warming and climate change. Carbon dioxide capture and storage can only be considered as short term solutions. This does not make use of CO_2 as a potential resource. Carbon dioxide utilisation must draw on innovations in catalysis. Hydrogenation of CO_2 offers one possibility as a route to formic acid, formaldehyde and methanol. Supported Au catalysts have a role to play here where the selective production of amines can be coupled with reaction with CO_2. This will require a programme of catalyst testing with kinetic analysis where *in situ* spectroscopic (DRIFTS FTIR) analysis should provide critical in determining the surface requirements for CO_2 insertion/utilisation.